UNIVERSIDADE DE SANTIAGO DE COMPOSTELA

Thermomagnetic Properties at the Nanoscale

by

David Serantes Abalo

A thesis submitted in partial fulfillment for the degree of Doctor of Philosophy

in the

Faculty of Physics

Applied Physics Department

29^{th} January, 2011

ISBN 978-84-9887-765-6 (Edición digital PDF)

Declaration of the Advisor

I, DANIEL BALDOMIR FERNÁNDEZ, professor of the Applied Physics Department at the Universidade de Santiago de Compostela

DECLARE THAT:

- This thesis titled '*Thermomagnetic Properties at the Nanoscale*' and the work presented in it was carried out by DAVID SERANTES ABALO under my advising.
- The thesis is submitted in partial fulfillment for the degree of Doctor of Philosophy in the Applied Physics Department at the Universidade de Santiago de Compostela.

Signed:

Date: 29^{th} January, 2011

Declaration of Authorship

I, DAVID SERANTES ABALO, declare that this thesis titled, '*Thermomagnetic Properties at the Nanoscale*' and the work presented in it are my own. I confirm that:

- This work was done wholly or mainly while in candidature for a research degree at this University.
- Where any part of this thesis has previously been submitted for a degree or any other qualification at this University or any other institution, this has been clearly stated.
- Where I have consulted the published work of others, this is always clearly attributed.
- Where I have quoted from the work of others, the source is always given. With the exception of such quotations, this thesis is entirely my own work.
- I have acknowledged all main sources of help.
- Where the thesis is based on work done by myself jointly with others, I have made clear exactly what was done by others and what I have contributed myself.

Signed:

Date: 29^{th} January, 2011

Acknowledgements

First of all, I would like to thank Prof. Daniel Baldomir. Of course, for giving me the opportunity to start my scientific career and for his continuous guidance and good advices through all of these years, without which it would have been impossible to do this thesis. But also, and not less important, for his faithful support no matter the tough occasions we had to go through.

I would like to express my gratitude to the collaborators whose contribution, either in the form of a co-authorship or from very fruitful conversations, helped me during my research. In this regards, I am very grateful to Profs. J. Rivas, F. Rivadulla and C. Vázquez, from the Universidade de Santiago de Compostela (Spain); to Prof. C.E. Hoppe, from the Universidad Mar del Plata (Argentina); to Profs. B. Hernando, V.M. Prida, and J.L. Sánchez-Llamazares, from the Universidad de Oviedo (Spain); to Profs. J. González and A. Zhukov, from the Universidad del País Vasco (Spain); to Dr. V. Salgueiriño-Maceira, from the Universidade de Vigo (Spain); to Prof. Ó. Iglesias and Dr. C. Martínez-Boubeta, from the Universitat de Barcelona (Spain); and to Dr. M. Cerchez, from the Universität Düsseldorf (Germany).

Special thanks must go to Prof. Michael Farle and the other members of the group for their warmth during my stay in the Universität Duisburg-Essen (Germany).

My gratitude also to Manuel Pereiro, for helping me in every step of the several problems of the beginner and for his unconditional friendship. I was very fortunate to have the occasion to share with him these years.

I owe a lot to Prof. Javier Castro, always open to discuss about new ideas and able to supply me with the most appropriate references; and should not forget my group mates, Moisés, Víctor, Jorge, Alberto, Antía and Iván, with whom I've shared 5 years working, learning and enjoying together.

I would like to thank all the people in the CESGA (Centro de Supercomputación de Galicia), specially Carlos Mouriño and Andrés Gómez, and the people in the IIT (Instituto de Investigacións Tecnolóxicas) led by Prof. Juan Arias.

Last but not least, I would like to thank my parents, Carmiña and Pepe, for being the perfect model every child would need to look at; to my sister Carmela, and to Catuxa for their love and support. No words can say how much I owe them.

Contents

A meus avós.

1 Introduction to the Thesis

1.1 Motivation

Nanosized magnetic materials exhibit a rich variety of magnetic phenomena in comparison with the bulk counterparts, what gives place to a novel range of applications of great importance to improve daily human activities as high-density magnetic recording storage or biomedical applications [1]. The origin of these special magnetic properties is found on the reduced dimensionality [2]: when the size of the material reaches the order of nanometers the influence of the surface atoms becomes very comparable (or even higher) to the bulk contribution, the defects due to the broken symmetry may be of significant importance, and other physical effects may also become very relevant when the size reaches the order of characteristic length scales of the material (as for example the domain size). The properties observed in such reduced dimensions are strongly sensitive to small size, shape, composition, etc dependence, what defines the different magnetic structures (nanoparticles, nanowires, thin films, etc) as forming specific research fields based on their differentiated proper characteristics [3]. The goal of this thesis is to investigate the thermomagnetic properties of nanostructured systems in the single-domain range, motivated by the unusual magnetic properties that common materials exhibit in nanoscaled dimensions.

One of the most remarkable magnetic properties arising in these reduced dimensions is the so-called *superparamagnetism*. Superparamagnetic (SPM) phenomena is the paramagnetic-like temperature dependence that occurs in single-domain magnetic entities above a characteristic threshold named *blocking temperature*, and its

special features are determined by the complex interplay between the magnetic parameters ruling the system (magnetic moment, anisotropy, applied field, etc). Understanding the SPM properties of nanosized systems is of primordial importance both for the basic theoretical knowledge [4] and for specific-designed applications (as for example the increase of the storage information capacity of hard drives [5], or the development of well-controlled biomedical applications [6]). Because of this a big effort has been devoted to the study of SPM systems in the last years, aimed to understand its underlying physical mechanisms.

However, the investigation of SPM properties is a complex task due to its strong dependence on several uncontrolled parameters, which mask the physical origin of the magnetic behaviour and hence makes very difficult to achieve a precise characterization. The high parameter-dispersion degree found in real systems, arising from the large dispersion of parameters (particle size, anisotropy, shape) and uncontrolled interparticle interactions, results in a complex physical problem non-solvable by analytical methods. To investigate such complex scenario it is very common the use of computational techniques, which allow a precise control of the physical parameters governing the system.

SPM phenomena occupies a central role amongst the thermomagnetic properties in single-domain magnetic systems, and so under this basis and due to its importance both from the theoretical and applied point of view, in this thesis we[1] have systematically investigated its properties as a function of the main magnetic parameters ruling the SPM response. To reach such an objective we have mainly focused on systems of magnetic nanoparticles randomly distributed, the most usual experimental situation, but also other specific situations as particle chains were analyzed. In order to achieve a good control of the magnetic parameters ruling the magnetic response of the system we have used a Monte Carlo (MC) method based on the Metropolis algorithm, a very useful tool for studying such magnetic nanostructures: on the one hand, with a MC method the characteristics of the system are perfectly controlled and, on the other hand, we can face the study of problems with no analytical solution as for example the magnetic dipolar interaction. This is the main objective of the present work: with the help of a MC technique we can study different nanostructured systems, as randomly distributed nanoparticle systems or chain-like nanoparticle assemblies, and to investigate how their different parameters (magnetic anisotropy, size, shape, interparticle interactions, etc) influence its magnetic behaviour.

[1] In this thesis "we" will sometimes refer to the author and sometimes to the author and co-authors. This will always be suitable, as per the traditions of written physics.

In parallel to the study of the basic magnetic properties of such systems we have also carried out the detailed analysis of a very special thermomagnetic feature, the so-called *magnetocaloric effect* (MCE). The MCE is defined as the temperature variation of a magnetic material under the applying or removal of an external magnetic field, and it is very important for technological applications as magnetic refrigeration (lowering the temperature by means of an adiabatic magnetic field variation) and hyperthermia treatment (killing of the malignant tumoural cells by selectively rising their temperature). The MCE, like any other magnetic effect when reduced to the nanoscale level, is subjected to new and uncontrolled properties due to the special properties of nanoscaled systems and therefore its properties are still to be understood in the nanometer range, for the influence of different parameters is the subject of much controversy. In order to gain further knowledge about the MCE in nanoscaled dimensions, we have carried out a systematic study of the magnetocaloric properties of the system complementary to the theoretical one.

This thesis is organized as follows. The above three aspects *superparamagnetism*, *MC method* and *MCE*, constitute the main guiding lines in our work and so their general properties will be priorly accounted before the description of our research results. Their characteristics are described in SECTIONS 1.2, 1.3, and 1.4, respectively. Next, in CHAPTER 2 we present our results about the general SPM properties and MCE in randomly distributed nanoparticle systems as a function of the main parameters ruling its behavior. This analysis is based on the assumption that the system can be described in a first -however quite good- approximation by the Zeeman, anisotropy, and dipolar interaction energies. The influence of dipolar interaction has been the center of much investigation for several years due to the dissimilar (even contradictory) results reported in the literature; in this aim we have performed an insightful study about its influence on the magnetic response on the nanoparticle system, introduced as proportional to the sample concentration. We have found the existence of a general scaling parameter able to describe its influence, similarly to the normalization of the magnetic field by the dipolar field of the particles. Such feature has been carefully analyzed, and its implications regarding other results reported in the literature have been thoroughfully investigated. These results are described in CHAPTER 3. Other spatial arrangement of the nanoparticles is investigated in CHAPTER 4, where the particles align in chain-like structures. As in the previous factors, both the SPM properties and MCE are investigated, finding in this case very special features related to the ordering properties of the system as driven by the anisotropy axes orientation. Regarding the MCE, we have found the existence of an optimizing field value, which displays features of a phase transition.

These first 3 chapters constitute the core of our investigation as related to SPM properties and MC simulations.

Along this thesis, however, we have not only analyzed superparamagnetism and MCE in nanoparticle systems by using Monte Carlo simulations. Additionally, we have spread our interest into other nanomagnetic systems, being in close contact with experimental groups that provided us with the opportunity to extend our knowledge into other scenarios. In this regards, it is worth to mention the close relationship between the magnetic response of the nanoparticle chains and that of magnetic nanowires (see CHAPTER 4). Results concerning experimental data are reported in CHAPTER 5, where the magnetocaloric properties of NiMn-based Heusler-based alloys in ribbon shape are reported for different ribbon compositions, and in CHAPTER 6, where it is proposed a theoretical approach to describe the anomalous deviation from the Curie-Weiss-like behaviour measured experimentally in FePt nanoparticles.

1.2 Superparamagnetism

The term *superparamagnetism* refers to the magnetic phenomena observed in fine magnetic particle systems exhibiting close similarities to atomic paramagnetism. Basically, single-domain magnetic nanoparticles can be characterized by their large total magnetic *supermoment*, which exhibits a paramagnetic-like decay of the magnetization with temperature above a characteristic threshold named *blocking temperature*, T_B. This particular temperature, unlike the *Curie* temperature T_C, is extremely dependent on the experimental observational time-window and this characteristic gives place to a complex theoretical frame with especial experimental features. In what follows we briefly introduce the conditions for the existence of superparamagnetism and its basic characteristics; for a more exhaustive description, see for example the reviews by D. Kechrakos [7], O. Petracic [8], M. Knobel et al. [9], J.L. Dormann et al. [4].

1.2.1 Single-domain particles

Superparamagnetic (SPM) phenomena is observed upon reduction of the size of ferromagnetic (FM) materials[2] down to the single-domain range: in a FM magnetic

[2] By *ferromagnet* we mean any magnetic configuration resulting in a net total magnetic moment; we are not interested in the atomic arrangement, to be ferro-, ferri-, canted, or any other ferromagnetic variation. The important characteristic it the existence of net configuration in absence of applied magnetic field.

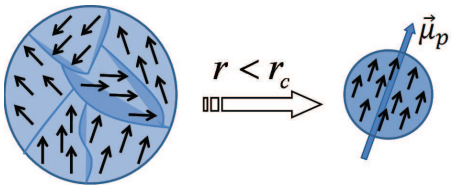

Figure 1.1:
Scheme illustrating the transition from the multi-domain configuration to the single-domain one upon size reduction.

material, multiple magnetic domains exist as a result of the balance between the exchange interaction energy favouring the parallel alignment of neighbouring atomic moments (thereby forming magnetic domains), and the magnetostatic interaction energy forcing their breaking into smaller domains with tendency to antiparallel orientation. The domain size is determined by the relative counterbalance between both energies. With decreasing size of the magnetic system, there is a critical value (r_c for the radius of a spherical particle) below which the magnetostatic energy no longer allows for the breaking of the system into smaller domains and so the system is composed of a *single domain*, as illustrated in FIGURE 1.1. Typical values are $r_c \approx 15$ *nm* for Fe and $r_c \approx 35$ *nm* for Co [4].

Assuming coherent rotation of the domain atomic moments, the particle is therefore characterized by its total magnetic *supermoment*, $\vec{\mu}_p$, resulting from the total magnetization of the particle. In first approximation, considering uniform magnetization (so neglecting surface effects) it can be described as proportional to the particle volume V and saturation magnetization M_S as

$$|\vec{\mu}_p| = M_S V \tag{1.1}$$

As mentioned above, the SPM response in magnetic nanoparticles is observed above the so-called blocking temperature T_B, a proper feature of SPM systems that differentiates them from atomic paramagnetism. The origin of T_B relays on the magnetic anisotropy present in the nanoparticles (in oppoxsition to atomic moments) due to their finite size, which tends to orientate the particle supermoment along some preferential direction. The magnetic anisotropy energy E_A found in a magnetic nanoparticle can have different origins (crystal, shape, surface, etc) giving place to very complex scenarios, and so for the sake of simplicity we have focused on the simplest *uniaxial* anisotropy case.[3] So, from now on we consider the different anisotropy contributions as comprised in an *effective* uniaxial anisotropy term, $\vec{K}_{\text{eff}}$, as illustrated in FIGURE 1.2(a).

[3]For details about the different anisotropy sources see for example Ref. [4].

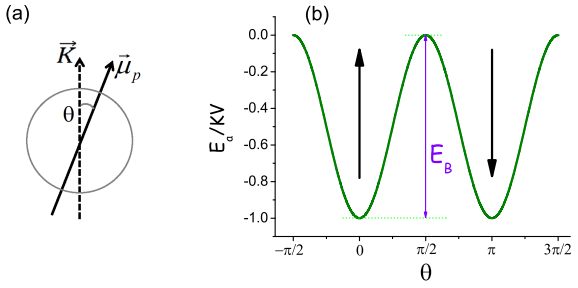

Figure 1.2:
(a) Schematic drawing of the uniaxial magnetic anisotropy K and magnetic supermoment of a single-domain nanoparticle, and (b) the corresponding uniaxial anisotropy wells.

If we consider the magnetic anisotropy to be proportional to the particle volume as $\vec{K}_{\text{eff}} = KV\hat{n}$, with K the *effective* uniaxial anisotropy constant (per unit volume) and $\hat{n}$ the unitary vector describing the easy-magnetization anisotropy direction, then the energy term for the i-particle can be written as

$$E_A^{(i)} = -KV_i \left(\frac{\vec{\mu}_i \cdot \hat{n}_i}{|\vec{\mu}_i|} \right)^2 = -KV_i \cos^2\theta \tag{1.2}$$

being θ the angle between the magnetic supermoment of the particle and the easy anisotropy axis. The moment of the particle has therefore two preferred orientation, equally probable, along the easy-magnetization anisotropy axis direction. Both directions are separated by an energy barrier E_B of height KV. The energy spectra corresponding to this uniaxial anisotropy energy is illustrated in FIGURE 1.2(b).

The system we have constructed up to now is that of homogeneous magnetic nanoparticles characterized by their size V, saturation magnetization M_S, and uniaxial magnetic anisotropy energy K. This very simple scenario describes reasonably well many experimental situations, and so from now on we focus on the magnetic properties of a system of such particles as a function of temperature (T) and magnetic field ($\vec{H}$). Real systems are usually characterized by randomness in their spatial distribution and in the easy-axes orientation that strongly influence the properties of the system as determined by interparticle-interactions and applied magnetic field. These analysis are however quite complex and will be undertaken in CHAPTER 2. For the sake of simplicity we consider for the moment a non-interacting particle system (so spatial distribution concerns are avoided) and equal particles (parallel aligned anisotropy axes), so that the particles are equivalent to each other and the system can be studied under a single-particle perspective.

1.2.2 Thermal relaxation and blocking temperature (T_B)

The influence of the temperature (T) on the magnetic properties of the particles can be easily figured out in the high- and low-T limit cases. At very high T, the

thermal energy is much larger than the anisotropy barrier ($k_BT >> E_B$, with k_B the Boltzmann constant) and so the magnetic anisotropy plays a negligible influence on the orientation of the particles' moments. In this case a paramagnetic-like dependence of the magnetization with T is expected and the particles are in the *superparamagnetic state* (SPM state). On the contrary, at very low T the particle moment remains confined along the anisotropy direction (local energy minimum) because the thermal energy being unable to switch its orientation out of that minimum ($k_BT << E_B$). When this happens the particles are said to be in the *blocked state* (BL state).

Thermal energy promotes the fluctuation of the magnetic moments, its influence varying between the rapid motion at very high temperatures and the practically steady state at very low T. Hence, to understand how thermal energy influences the magnetic behavior of the particles it is necessary to understand the dynamics of the particle moments as a function of T. The influence of thermal fluctuation on the orientation of the particles' supermoments was first described by Néel [10], who proposed that the thermal fluctuations could promote the jumping of the magnetic moment of the particles from one anisotropy well to the other, introducing the average time τ for thermal activation (often called *relaxation time*) over the anisotropy barrier to follow an Arrhenius law

$$\tau = \tau_0 e^{\frac{E_B}{k_B T}} \tag{1.3}$$

where τ_0 directly depends on the material parameters (K, M_S, etc) and is of the order of $10^{-11} - 10^{-9} s$. Under this description, it therefore points out that the measuring time τ_m will be a key-point on determining the magnetic state of the system: if the measuring time is large in comparison with the characteristic reversal time of the particles, $\tau_m >> \tau$, then the particle moment will fluctuate rapidly from one well to the other in a paramagnetic-like fashion, i.e. the particle will be in the SPM state. However, if $\tau_m << \tau$, during the measuring time the particle moment will remain blocked along one anisotropy well, i.e. the particle is said to be in the BL state. Macroscopically, the SPM state is completely reversible upon temperature and field variations, whereas the BL is characterized by its hysteretic behavior, proper of ferromagnets. The limit between both states is found at $\tau_m \equiv \tau$, and serves for the definition of the so-called *blocking temperature* T_B, as illustrated in FIGURE 1.3 and obtained from Eq.(1.3)

$$T_B = \frac{KV}{k_B \ln(\tau_m/\tau_0)} \tag{1.4}$$

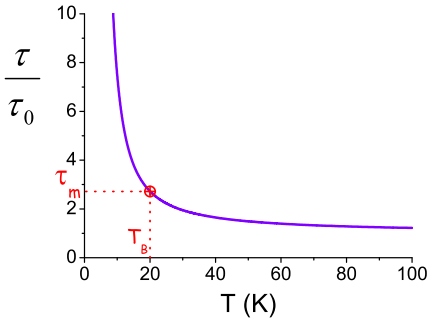

Figure 1.3:
Relaxation time τ *vs* T, and indication of T_B for a certain τ_m.

As Eq.(1.4) shows, T_B depends both on the intrinsic particle parameters and on the external ones as the measuring time. Therefore, by varying the external influences of the systems (temperature, measuring time, applied field) we may tune its response. From the trends obtained we can extract information about the characteristics of the system, and so information for the design of technological applications.

Eq.(1.4) highlights that the value of τ_m is decisive in determining T_B and so the magnetic response of the system in a given time-scale (for example, for information storage-related applications, very large time scales have to be considered; however, for magnetic recording speed very short ones must be achieved). Since τ_m is determined by the experimental technique, its value has to be chosen with respect to the information and uses concerning our purposes. Along this thesis, our interest has been focused on quasi static process and so associate T_B with the one obtained in dc-thermomagnetization measurements, in which the measuring time is very large large ($\tau_m \approx 100s$) in comparison with the characteristic time τ_0 of the particles and so we can talk of static measurements. Other measurement techniques involving much shorter measuring times are associated to *dynamic* measurements, not considered in this thesis.[4]. We have mainly focused on data obtained following the standard *zero field cooling* (ZFC) and *field cooling* (FC) protocols, in which the system is perturbed under a low magnetic field for measuring the evolution of its magnetization with temperature. Previous to describing such processes and its characteristics, we shall analyze the effect of the magnetic field on the single-domain magnetic nanoparticles' properties.

[4]For a recent review on the dynamic properties of SPM systems see for example the work by P.E. Jonsson [11]; other measurement techniques associated to different time scales are analyzed in Ref. [4]

1.2.3 Field dependence

When an external magnetic field is applied over the nanoparticles, it tries to align their magnetic moments along its direction. Therefore, except if applied perpendicularly to the easy anisotropy axis, it will favour the occupancy of one of the anisotropy energy wells over the other. The orientation of the magnetic moment of a particle i is then governed by the competition among its uniaxial (E_A) and Zeeman (E_Z) energies

$$E^i = E_A^{(i)} + E_Z^{(i)} = -KV_i \left(\frac{\vec{\mu}_i \cdot \hat{n}_i}{|\vec{\mu}_i|} \right)^2 - \vec{\mu}_i \cdot \vec{H} \tag{1.5}$$

The influence of the external field in the orientation of the magnetic supermoments, assuming coherent rotation of the atomic magnetic moments and the field applied at a certain angle θ_0 with respect to the easy anisotropy axis, is known as the *Stoner-Wohlfart model* [12] after the authors who first considered and solved this problem. They ignored thermal effects and so could solve it from minimal energy arguments, not taking into account time-dependence as related to temperature. In this introduction section, however, we are mainly interested in giving an overall description of the SPM features, as how the magnetic field will affect the orientation of the magnetic moments with temperature in relation to the anisotropy energy barrier and its influence on T_B. Therefore, we do not discuss now the orientation of the field at different angles and focus, for the sake of simplicity, on the simple case of the field applied parallel to the easy anisotropy axis ($\vec{H} \| \hat{n}_i$). Note that in this context of non-interacting particles, applying the magnetic field at a certain angle with respect to the easy axis is equivalent to consider only its projection along the axis. Since we are under the assumption of non-interacting and equivalent particles, we can apply single-particle considerations and simplify the i subindex in Eq.(1.5), which taking into account Eq.(1.1), reads

$$E = -KV \cos^2 \theta - M_S V H \cos \theta \tag{1.6}$$

Eq.(1.6) has two local energy minima at $\theta = 0, \pi$ with values $E_{min} = -KV \pm M_S V H$, and a maximum a $\theta = \pi/2$ with value $E_{max} = KV(HM_S/2K)^2$. The $\theta = 0$ value stands for the parallel orientation of the particle moment with respect to the magnetic field ($\uparrow\uparrow$), whereas the $\theta = \pi$ value stands for the antiparallel one ($\uparrow\downarrow$). This difference in the energy wells described by FIGURE 1.2 corresponds therefore to different energy barriers depending on the orientation of the particle moment with respect to the applied field, which we shall call $E_B^{\uparrow\downarrow}$ and $E_B^{\uparrow\uparrow}$ for the antiparallel and parallel cases, respectively. Introducing the *anisotropy field* of the particles as

$$H_A = \frac{2K}{M_S} \tag{1.7}$$

we calculate these energy barriers as the difference between the minima and maximum energies, obtaining

$$E_B^{\uparrow\downarrow} = KV\left(1 - \frac{H}{H_A}\right)^2 \tag{1.8}$$

and

$$E_B^{\uparrow\uparrow} = KV\left(1 + \frac{H}{H_A}\right)^2 \tag{1.9}$$

The difference in the height of the energy barriers indicates also a change in the characteristic relaxation time of the particles, since it depends now on the relative orientation of the magnetic dipoles with respect to the field: particles antiparallel-oriented with respect to the field have a smaller energy barrier in comparison to the solely-anisotropy one and so a smaller thermal energy is enough to overcome it, whereas the parallel-oriented particles are now confined into a deeper anisotropy well and so a higher thermal energy is necessary to promote the jumping of its magnetic moments. This influence of the magnetic field on the energy wells of FIGURE 1.2 is shown in FIGURE 1.4 (left panel), as well as its implications into the relaxation time of the particles (right panel).

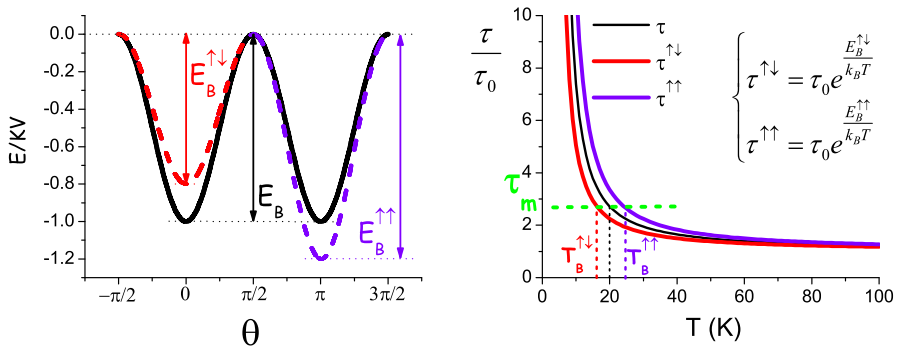

Figure 1.4:
Anisotropy energy wells (left panel) and relaxation time (right panel) of the particles as influenced by the magnetic field.

FIGURE 1.4 illustrates the importance of the strength of the applied magnetic field on determining the magnetic properties of SPM systems, and also serves as a definition of *small field* as referred to magnetic nanoparticles in comparison with

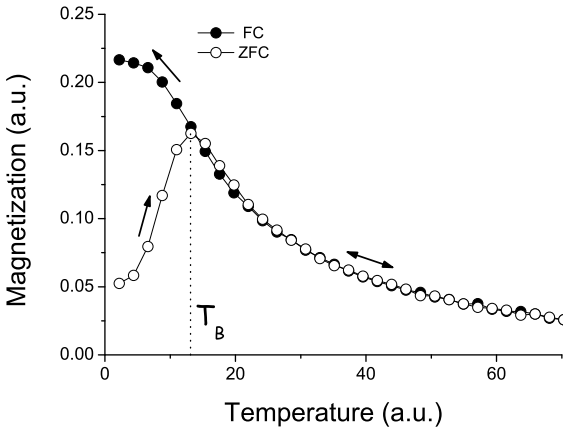

Figure 1.5: Typical ZFC and FC magnetization curves *vs* temperature. Vertical dotted line stands for the maximum of the ZFC curve, usually associated to T_B.

their anisotropy field: the ratio H/H_A must be as smaller as possible so that the system keeps as closer as possible to the ideal SPM conditions.

1.2.4 Thermomagnetic measurements

Once we have gone through how a magnetic field $\vec{H}$ influences the properties of the particles we can undertake the description of the *ZFC* and *FC* measurements. In both processes the temperature evolution of the total magnetization of the system is recorded following different thermomagnetic histories, and it is this different history what highlights reversibility (no-hysteresis) and irreversibility (hysteresis) for differentiating the anhysteretic SPM state from the hysteretic BL state.[5] In a ZFC process, the system is first cooled down in zero field until a very low T is reached, and afterwards a small field is applied and the magnetization is recorded while heating the sample up. The FC curve is obtained by measuring the magnetization of the sample while cooling under low magnetic field (same field strength for both ZFC and FC processes, and low to minimize the disturbance of the system; further analysis in this regards is presented in Section 2.2). Typical ZFC/FC curves are shown in Figure 1.5.

The ZFC and FC curves shown in Figure 1.5 display the usual features found in SPM systems: i) both curves coincide at high temperatures in a PM-like dependence; ii) with decreasing T both curves grow until a certain temperature range is reached where the curves start to diverge, the FC curve still growing although

[5] Although for evaluating magnetic hysteresis, measuring M(H) cycles could seem a better choice, they are not appropriate for determining the value of T_B, since it would be necessary to measure a large amount $M(H)$ isotherms to identify T_B, whereas $M(T)$ measurements give a continuous temperature range to more precisely obtain it from a single curve.

at a lower rate while the ZFC exhibits a maximum and decreases below it. This maximum in the ZFC curve is generally associated in the literature to T_B [7], as indicated in the figure, since such maximum roughly differentiates two main temperature regimes: a high-temperature one where both curves essentially coincide and exhibit a PM-like temperature dependence, from a low-temperature regime where both curves clearly diverge. However, a detailed view of the curves reveals that a $1/T$ PM-like decrease right above T_B is not observed in the ZFC curve, and a slight difference between the ZFC and FC one is perceived. These features indicate that a true SPM behavior is not exhibited right above the maximum, but only at higher temperatures the ZFC curve perfectly overlaps the FC one and exhibits a well-defined PM-like temperature dependence. The reason why the ideal SPM behavior is not observed right at $T > T_B$ is found on the inverse of the relaxation time τ, which gives the probability of the particle to overcome the anisotropy energy barrier along the temperature

$$p(T) = \tau_0^{-1} e^{\frac{-E_B}{k_B T}} \tag{1.10}$$

The features displayed in FIGURE 1.4 concerning the different height of the anisotropy wells as influenced by the external field, must be taken into account too when analyzing the physical trend followed in the ZFC magnetization curve. The initial state of the ZFC process starts with no net magnetization after cooling in zero field. If naming *parallel* particles those with $E_Z < 0$, and *antiparallel* particles those with $E_Z > 0$, then when the field is applied parallel particles will rapidly align with the field, while the antiparallel ones will progressively overcome the energy barrier with the increasing thermal energy and also align with the field. This process leads to a continuous increase of the magnetization, as illustrated in FIGURE 1.5, until the thermal energy overcomes $E_B^{\uparrow\downarrow}$, and so no longer reversal magnetization takes place. This is not so simple however, since the thermal energy does not induce the alignment of more particles, but counterbalances their orientation, inducing thermal fluctuations. As the thermal energy is now comparable to the energy of the deeper anisotropy well, inverse reversal mechanism overcoming has a higher appreciable probability to occur. This frame stands so for the expected further decrease in the magnetization, although not yet accomplished full PM-like behavior. In fact, pure PM-like behavior would only be observed for $k_B T >> E_B$. It is important to emphasize these aspects when dealing with the magnetic properties of SPM systems, remarking that T_B defines only a characteristic temperature value, of enormous

interest for characterizing the system but not equivalent to a phase transition[6].

Because of the above reasons, some authors do not associate directly the maximum in the curves to T_B and prefer a different definition [9]. Although we understand such discrepancy and share the necessity of finding a more precise formalism for relating the shape of the ZFC curves to the particles' characteristics, we will along this thesis associate the maximum of the ZFC curve with T_B, both because of simplicity and to facilitate the comparison of our results with experimental data. Thus, in our studies we will concentrate in analyzing the maximum of the ZFC curves under different influences (field, anisotropy, dipolar interactions), aiming to understand the basic properties of the system. It is important to remind here that all the properties described up to now correspond to the simplest single-particle scenario, where all the particles have been treated as equivalent to each other because of been non-interacting and with parallel-aligned easy anisotropy axes, as illustrated in FIGURE 1.6.

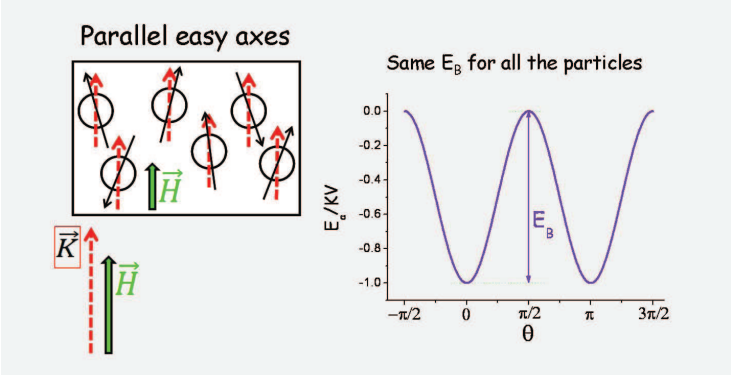

Figure 1.6:
Schematic drawing of the ideal simplest model of non-interacting and parallel aligned easy axes along the applied field.

However, real systems are usually characterized by a random distribution of the anisotropy easy axes, what would be equivalent to a distribution of the heights of the energy barriers along the field direction, as schematized in FIGURE 1.7, giving

[6]There has been much discussion in the literature about whether strong dipolar coupling among the particles could lead to a phase-transition character at T_B. This aspect will be further discussed in SECTION 2.4. The importance of p(T) in the shape of the ZFC curve will be discussed in more detail in SECTION 2.5

place to a extraordinarily complex scenario. Furthermore, one of the main objectives of our work is to reach a comprehension of the role played by interparticle dipole-dipole interactions on the magnetic properties of a nanoparticle system as described above. We shall not extend here in describing this interaction, which will be intensively analyzed later, a general approach presented in SECTION 2.4 and a more exhaustive one in CHAPTER 3. In brief, magnetic dipole-dipole interactions are long-range and anisotropic, resulting so in a complex interplay with the anisotropy barriers. Low-interacting conditions can be described by mean-field approximations in which the single-particle barriers are slightly modified by the interaction energy; however, strongly-interacting conditions ruled by collective effects cannot be described under that approach, and so the use of computational techniques becomes an indispensable tool for treating systems with so many freedom degrees. Computational techniques allow us to deal with perfectly controlled systems and the exact treatment of the interactions among particles. There are two main computational approaches for dealing with the magnetic properties of interacting nanoparticle systems, namely the *Monte Carlo* (MC) and *Langevin Dynamics* (LD) methods. Both methods are complementary for the study of nanoparticle system: MC simulations are very adequate to treat long-time (static) magnetic properties in complex interacting systems [13] but do not have associated a physical time; LD methods, on the contrary, are very precise for modeling the dynamics of the magnetic moments [14] but cannot treat static processes.[7] As mentioned above we have focused our research on static measurements, and therefore we have used for such a purpose a MC method described in SECTION 1.3.

Finally, it is worthy to recall again the several simplifications assumed in this introduction to *superparamagnetism*, were we have considered very simple and ideal characteristics for the particles. In real systems there are always several dispersive -often uncontrolled- characteristics (inhomogeneities in the particles' composition; temperature-dependent K, M_S; size/anisotropy distribution; etc), characteristics all that confer additional uncontrolled degrees of freedom to the already very complex system, and so make very hard to interpret the magnetic measurements in order to characterize their properties. That is the reason why we had to focus on a very simple scenario which, on the other side, it is already complex enough to make absolutely necessary the use of computational techniques for its study.

[7] There have been important approaches trying to relate the more physical LD-time to the MC *time steps*, see for example the works by U. Nowak et al. [15] and X.Z. Cheng et al. [16].

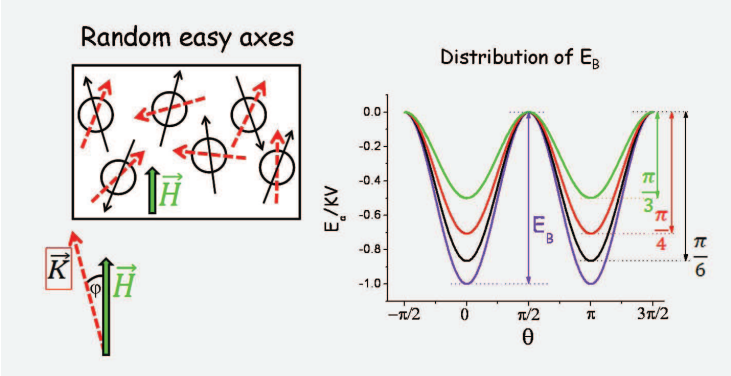

Figure 1.7:
Schematic drawing of the usual random easy axes distribution, and the modulation of the energy barrier height along the field direction.

1.3 Monte Carlo method

Monte Carlo (MC) methods are a type of numerical simulation techniques based on the generation of random numbers [17]. MC methods are utilized to solve complex problems with large freedom degrees: the features of a particular problem are represented by probabilities, and the MC technique consists on generating large amounts of random numbers and counting the fraction of them obeying some conditions. The way of counting and the conditions imposed define the *numerical algorithm*. A simple example to illustrate the functioning of a MC method is the calculus of π from the area of a circle. If placing a circle of radius r into a square of side $2r$ and randomly generating N-points into the square, the fraction of them laying inside the circle (n_{circle}) will be equal to the proportion between areas, and so it is easy to obtain $\pi = 4\frac{n_{circle}}{N}$. The MC calculation of the area will be more precise the larger the amount of points (events) generated, as illustrated in FIGURE 1.8.

The two drawings in FIGURE 1.8 stand for two examples of random generation of events (N=100 and N=1000) into the square with the circle held inside. The graph shows the fraction between points laying in each geometrical figure as a function of the amount of random events generated, pointing out that the precision to determine π from the random points areal ratio grows rapidly with N.

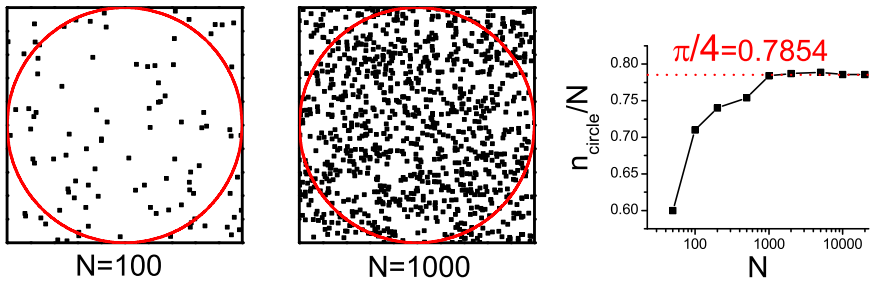

Figure 1.8:
Use of random events to calculate the value of π from the area of a circle, and the importance of the amount of events in the precision in the result.

1.3.1 Metropolis algorithm

Along this thesis we have used a MC method to simulate the magnetic properties of a magnetic nanoparticle system with a large amount of freedom degrees as described in SECTION 1.2. Specifically, we want to know how the orientation of the magnetic moments of the particles evolves as a function of different parameters (namely temperature, applied magnetic field and interparticle dipolar interactions), i.e. how they behave as a function of the different energies involved. To simulate such processes we impose to the system some known conditions and determine its configuration from a random generation of events as evaluated under those conditions. The processes we simulate are essentially quasi static, and so the conditions ruling the system can be based on minimizing-energy arguments on the following manner: i) the system energy of the system under certain conditions is evaluated, ii) an external parameter is varied and the energy is reevaluated, and iii) the difference in energy is used to construct a probability function, and the change of configuration of the system is accepted or not from the random generation of events applied to such probability under a given algorithm.

It turns out that this problem is much more complex than calculating π from the ratio between the areas of the circle and square as described above, where the randomly generated events are equally probable and so the algorithm for solving the problem is just to count 1 if the points lay inside the circle and 0 otherwise. If we apply the same procedure to simulate the orientation of the magnetic moments with temperature, i.e. if we randomly generate new possible orientations and evaluate its feasibility to occur, we will find that most of the trials are highly improbable and so rejected, and only those with energy comparable to the previous state will have some chance of being accepted. For example, for simulating the new possible orientation

of a particle' magnetic moment, initially at an angle θ_i (Eq.(1.6)), the new trial configuration θ_f can be chosen totally at random, unrelated to θ_i, or by considering a slight variation after the actual configuration, so that $\theta_f = \theta_i + \delta\theta$, with $\delta\theta$ small. In the first case many trials will be very unfavorable and so rejected, while for the latter a higher acceptance ratio is expected. It becomes therefore crucial, in order to avoid the wasting of computational time and optimizing the simulation, to be able to select the new trial configurations among the most likely probable paths. This can be done if considering a Markov chain of events (configuration of one state depends only on the previous one), with the trial state being close in energy to the current one.

The key-points for treating the present problem are, therefore, i) the selection of the trial configurations in an efficient way, and ii) the choosing of an adequate implementation of the change from the initial state with energy E_i to the trial next state with energy E_f. Assuming classical Boltzmann distribution, the probability of a magnetic moment to have energy E at a temperature T is proportional to $exp(-E/k_B)$, $p(E) \propto e^{-E/k_BT}$. Consequently, if considering the orientation of the magnetic moments to be markovian the evolution from state E_i to state E_f will be proportional to the rate between final and initial states probabilities, $r_{i\to f} = p(E_f)/p(E_i) = e^{-\Delta E/k_BT}$, with $\Delta E = (E_f - E_i)$[8]. The motion of the magnetic moment of a nanoparticle from the initial state with energy E_i to the final state with energy E_f is often described by means of the *Metropolis algorithm* [19][9]: if $\Delta E < 0$ the new configuration is more stable energetically, the move to the new state is accepted and its energy changes to E_f, whereas if $\Delta E > 0$, although small, the move has still some probability $e^{-\Delta E/k_BT}$ to occur. To compute this probability a random number n with value between 0 and 1 is generated and, if $n < r_{i\to f}$ the new conformation of the system is accepted and so it has now energy E_f, while if $n < r_{i\to f}$ it is rejected and the energy remains still E_i. The Metropolis algorithm for the probability of a ΔE configuration change is expressed as

[8]This way of choosing the possible next configuration of the system as being energetically close to the actual one is named *importance sampling*, and is based on the *detailed balance* reversibility condition. This approach works very well for describing quasi-static thermodynamic processes, as intended in this work, although much care has to be taken if dealing with dynamic properties. For further details about this topic, see for example: O. Iglesias *Doctoral Thesis* [18], Chapter 5.

[9]The choice of this algorithm was motivated by its suitability to describe static properties of magnetic nanoparticle systems, as intended in this work. Other transition probability algorithms as Glauber dynamics could provide similar results for simulating ZFC/FC magnetization curves (different for simulating dynamic processes) [20]. Glauber dynamics, originally applied to the 1D-Ising model, mainly differs from Metropolis in that minimizing the energy is not always accepted as change. For more details on this and other algorithms as heat-bath see for example the work by K. Binder [17]. It is also interesting to note Ref. [21], where the governing algorithm is constructed as a combination of different MC trial-step choices.

$$min\left[1, e^{-\Delta E/k_B T}\right] \tag{1.11}$$

We have used Metropolis MC to simulate the evolution of the magnetization of a system of magnetic nanoparticles as a function of temperature and magnetic field. The program is based on a well-tested code (see for example Refs. [13, 22–24]) developed in the groups of Prof. José Rivas and Prof. Armin Bunde, (from the Universidade de Santiago de Compostela (Spain) and Justus-Liebig-Universitt Giessen (Germany), respectively), whose characteristics have been maintained. The simulated system consists on an assembly of N-particles contained inside a unit cubic cell (side L), which is replicated by using periodic boundary conditions in order to resemble a large and homogeneous system. The simulations are always done in two parts: in the first one the spatial distribution of the particles is set, and in the second part the particles are characterized by their attributes (size, anisotropy, magnetic moment) and the evolution of the system is simulated as a function of the desired parameters. The positions set in the first part are kept fixed during the simulation of the magnetic properties. Next we give a brief description of the generalities of the MC method, emphasizing some improvements added to the code.

1.3.2 Spatial arrangement

The procedure used to achieve the spatial distribution of the particles varies depending on the type of system we want to simulate: for ordered structures (chains of particles, crystalline structures) the particles are directly placed into the unit cubic cell under the desired structure, whereas for setting the spatial arrangement of liquid-like systems (frozen ferrofluids, solid matrices) a relaxation algorithm has to be used.

In FIGURE 1.9 we show some chain-like structures obtained by directly placing the particles into desired regular positions. They resemble one-dimensional columnar parallel chains of magnetic nanoparticles under different spatial arrangement (square, hexagonal) and different lengths along the X-axis. The study of such type of structures is at the center of much research nowadays for the basic study of the competition between the enhanced anisotropy and magnetostatic interactions [25–27]. Simulations as the above mentioned offer a good analogy to the behavior of ferromagnetic nanowires [28], aspect we intend to use for elucidating the different properties between the typical self-assembled hexagonal-lattice distribution and the more interesting for technological applications square-lattice one, as well as the chain-length role [29].

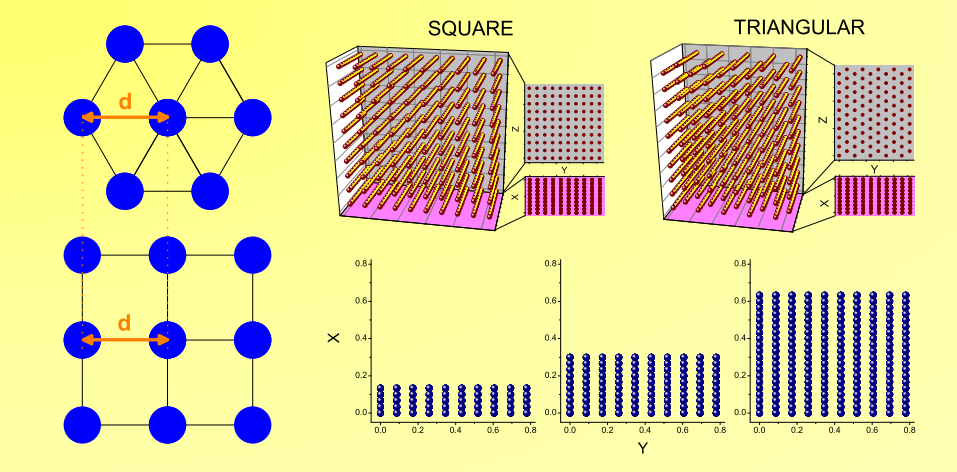

Figure 1.9:
Scheme of parallel-aligned chain-like structures hexagonally and squared distributed, and different lengths.

For simulating disordered systems as ferrofluids with liquid-like structure [30] the positions of the particles are not directly generated and so we use a Lennard-Jones pair potential (v_{LJ}) to distribute the particles. During the simulation the particles can move freely in space, but their trial positions are markovian-linked to the actual one and so the liquid-like structure is more quickly obtained. An example of liquid-like structure is shown in FIGURE 1.10, together with the corresponding correlation function.

For treating the long-range dipolar interactions the Ewald summation is used as in Ref. [13], considering for simulating long and homogeneous systems periodic boundary conditions over repetition of the unit cubic cell. The positions of the particles and their relative interdistances are calculated and storage for the next part of the simulations, in which remain constant throughout.

1.3.3 Superparamagnetic (SPM) properties

Once the spatial distribution of the particles is achieved the next step is to characterize them with their main physical properties, namely volume, magnetic moment and magnetic anisotropy. Following the model described in SECTION 1.2, magnetic anisotropy is considered of uniaxial type, and both magnetic moment and anisotropy are assumed to be proportional to the particle volume, and so the important parameters to characterize the particles are their volume and the orientation of the magnetic moment and easy-anisotropy axis.

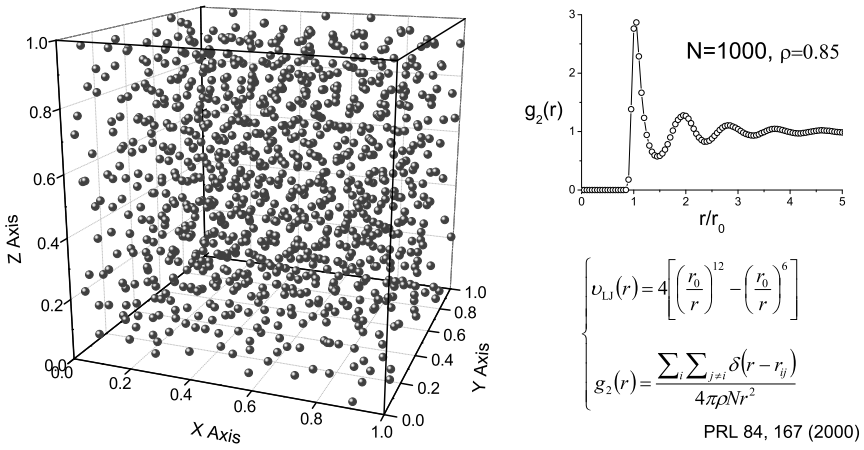

Figure 1.10:
Liquid-like distribution of N=1000 particles into a unit cubic cell and correlation function $g_2(r)$. Both the correlation function and Lennard-Jones pair potential are also indicated.

The volume is taken into account by means of the related sample concentration of the system c, preferable to determine experimentally and so better to compare with experimental results. Since one of the main objectives of this thesis is the study of the magnetic dipolar interactions, in all results presented here the system is always considered as monodisperse, in order to have the less uncontrolled parameter-dispersity as possible. If defining c as the fraction of the volume occupied by all the particles ($\sum_i^N V_i$) over the total system volume ($V_T = L^3$), then the relationship between particle size and volume sample concentration is

$$c = \frac{\sum_i^N V_i}{L^3} \equiv \frac{NV}{L^3} \tag{1.12}$$

The orientation of the anisotropy easy axes of the particles is a parameter that remains fixed along the whole simulation process, and hence its value must be carefully selected due to its strong influence on the magnetic properties of the system. For studying SPM properties we have assumed a random easy-axes distribution[10] as schematized in FIGURE 1.7, constraint that works quite well for describing real systems as frozen ferrofluids or solid matrices [31]. Once the easy axes are placed, the simulation of the magnetic evolution of the magnetic moments of the particles

[10] Other scenarios are considered in SECTION 3.3.3 and CHAPTER 4, in which the particles' easy-axes are parallel-aligned (also the spatial distribution are different, the particles being placed in a simple cubic net and forming chains, respectively).

can start, whose initial orientation can also be randomly distributed. The magnetic properties of the particles are contained on their magnetic moment $\vec{\mu}$ and magnetic anisotropy $\vec{K}$, under the *temperature/magnetic field* constraints applied to the system, which determine its energy. In real systems, the evolution between an initial state with energy E_i and a final state with energy E_f occurs at a certain time interval, in which the event (reorientation of the magnetic moments in this case) can be described by a probability distribution function. These time-dependent processes can be simulated by giving the system a certain amount of chances to occur, i.e. *attempts* to change the configuration. These attempts define the *computational time* and are called *Monte Carlo steps*. The MC step constitutes, therefore, the computational equivalence to real time units. In our simulations one MC step is defined as N trials given to a system of N-particles to change its configuration.

The simulation of a physical process in our simulations consists in varying a desired magnitude (temperature, magnetic field) under a certain protocol and evaluating the energy in the new state after a certain number of MC steps, accepting or neglecting the new configuration under the chosen algorithm (Metropolis in our case). For example, to simulate a ZFC process in a system of N-particles the system is cooled down from a high temperature in regular temperature intervals every a certain fix amount of MC steps in zero field down to a very low temperature. In every MC step, one particle is selected at random and a new orientation of its magnetic moment is generated and accepted under the Metropolis algorithm $min\left[1, e^{-\Delta E/k_B T}\right]$. This is repeated N-times in each MC step. Once the very low temperature is reached, a small magnetic field is applied and the process continues now while heating the sample[11]. The same procedure applies for simulating the magnetization *vs* magnetic field M(H) curve, just the parameter to vary after a certain amount of MC steps being different. A M(H) curve is simulated by initially cooling the system down to the desired temperature (in zero field for our simulations), and once it is reached, a small field is applied and increased in regular intervals of field/MC steps up to a high field H_{max}. Then, the field is decreased in the same manner until $-H_{max}$ is reached, and finally increased again until reaching once more H_{max} and having completed the cycle. To illustrate the features of the MC steps resembling real time units, we show in FIGURE 1.11 some ZFC (left panel)

[11] A thermalization is applied before any thermomagnetic simulation (ZFC, FC, magnetization vs. field) in order to rapidly reach a stable configuration. The reason for doing this is to reduce the initial instability of the system right after randomly generating the orientation of the magnetic moments and easy-anisotropy axes, which would take a vary large amount of MC steps to stabilize during the simulation process. Instead, if the system is initiated at a very high temperature and cooled in large temperature jumps down to the starting process temperature the system relax rapidly and reaches a energetically stable configuration more easily.

and M(H) (left panel) curves for fixed temperature and magnetic field variations, but different MC steps, corresponding to a system of non-interacting particles as that shown in FIGURE 1.10.

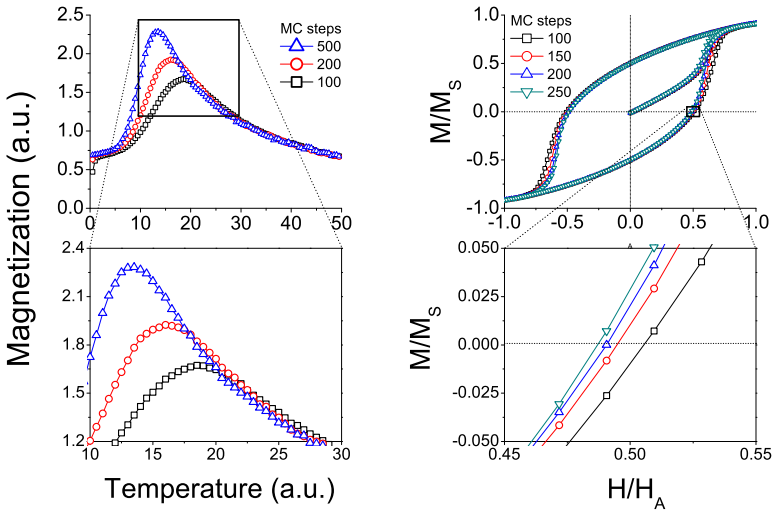

Figure 1.11:
Left panel: ZFC processes simulated for a fixed temperature interval variation, but different MC steps (100, 200, and 500). Right panel: M(H) simulated processes simulated for a fixed magnetic field interval variation, but different MC steps (100, 150, 200, and 250). In both cases, top panel shows the complete processes, while bottom panel shows a magnification of the more remarkable aspects of the simulation (maximum of the ZFC and coercive field, respectively).

Left panel of FIGURE 1.11 shows that the curves peak at lower temperatures for larger amount of MC steps, what reproduces the physical behavior described by Eq.(1.4): if relating the amount of MC steps with the experimental measuring time τ_m, then the longer is the time interval (amount of MC steps), the smaller it T_B. The behavior observed in the M(H) curves of FIGURE 1.11 (right panel) indicates a decrease in the coercive field for larger time intervals (higher amount of MC steps), also as expected since the FM-like behavior represented by the area in the M(H) curves is time-dependent, as discussed in SECTION 1.2, and tends to disappear for very large times (MC steps). However, it is important to indicate here that, although the physical tendency coincides with the expected in both kind of simulations, there is not a well-established relationship between MC steps and real time units and some scaling must be taken in this aim [15, 16]. As mentioned above, time-dependent processes in systems of magnetic nanoparticles are described better by means of the Landau-Lifshitz-Gilbert dynamic equation [14].

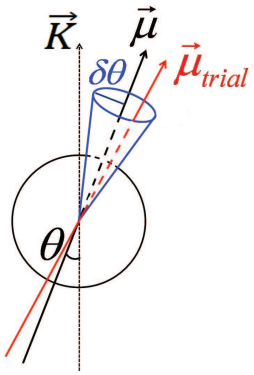

Figure 1.12: Schematic drawing of the $\delta\theta$-cone used to generate the new trial orientation $\vec{\mu}_{trial}$.

1.3.4 Trial *computational time* steps

It turns out from the above description of the MC technique that the choosing of the *trial* new configuration with energy E_f is of primordial importance: its value determines the acceptation rate of the algorithm and so the velocity and feasibility of the simulations. In our simulations we use the so-called *solid angle restriction scheme* [20]: the new trial orientation $\vec{\mu}_{trial}$ is randomly generated inside a cone of angle $\delta\theta$ around the current orientation $\vec{\mu}$. FIGURE 1.12 illustrates this choice of the new trial orientation inside a cone of angle $\delta\theta$ around the current orientation of the magnetic moment.[12]

The $\delta\theta$-value directly rules the speed of the magnetic moments' movement, and so its magnitude must be carefully selected in order to ensure the adequacy of the simulations to resemble physical processes: if $\delta\theta$ is too small the system will evolve very slowly to the quasi-equilibrium configuration, and we could be unable to resemble the physical process (too many MC steps would be necessary, not affordable by the computational resources available to us). If $\delta\theta$ is too large, the system can relax too fast and the features we are interested in simulating can be diluted and hence become unobservable. In FIGURE 1.13(a), we show the ZFC curves of the same system obtained for different values of $\delta\theta$. It is observed a tendency similar to that show in FIGURE 1.11, with the curves exhibiting a larger peak at decreasing temperature for larger $\delta\theta$-values. These results support our arguments on the functioning of the trial steps as *computational time* for reproducing real time-dependent processes.

[12] For more information about other MC-step trial schemes and its influence on the simulation results see for example Refs. [20, 21].

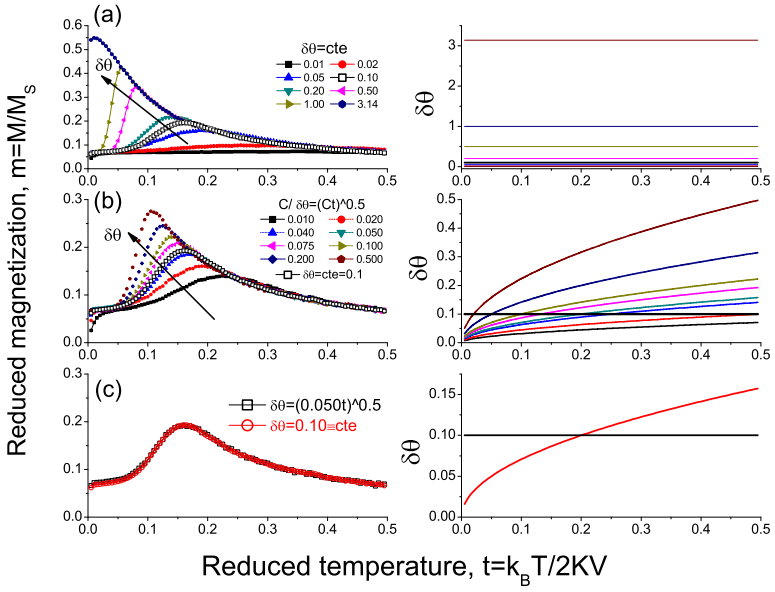

Figure 1.13:
ZFC processes as a function of $\delta\theta$. (a) corresponds to different $\delta\theta$-values constant with temperature, (b) shows different temperature-dependence for $\delta\theta$, and in (c) we compare the $\delta\theta$=0.1=cte case, with being temperature-dependent as $\delta\theta = (0.05t)^{1/2}$. In all cases, panels on the right show the temperature evolution of $\delta\theta$ and the $\delta\theta$=0.1=cte case is shown for the comparison.

The results plotted in FIGURE 1.13 indicate a strong dependence of the simulated results on $\delta\theta$, emphasizing so that much care must be taken if trying to extract time-related information about the system from the simulations: those depend not only on the artificial *MC step*, but also on the trial angle chosen. As pointed out at the beginning of this subsection, the Monte Carlo technique is very successful for analyzing quasi-static processes, and so we have focused in this thesis on the more reliable aspects of the simulations, i.e., quasi-static analysis of complex processes with large freedom degrees. In this regards, it must be noted that for all the simulations presented here, the choice of a given amount of Monte Carlo steps was set according to computational limitations rather than for any specific time-dependent analysis purposes.[13]

[13]Some time-dependent processes were analyzed in particular cases, but only to check the adequate evolution of the system while relaxing. It is also worth to point out that, in general, the results obtained by the Monte Carlo method are strongly dependent on the computational resources available. In this regards, along this thesis we have accomplished the simulation of very large systems up to 1000 particles (even reaching 8000 very recently), being notable the evolution

FIGURE 1.13 displays also some simulations in which the $\delta\theta$-value is considered to be temperature-dependent, in the same way as described in Refs. [15, 16]. The reason for including such dependence is not related to any effort concerned to use realistic times from the MC steps or to reach more accurate time-dependence results (Figs. 1.11 and 1.13(a) illustrate that it constitutes a very complex task). Instead, our motivation was simply to provide the simulations with a more realistic character: it seems to us more physical to make the thermal fluctuations to be larger at larger temperatures, as argued next: the analogy between the time-dependence or real experiments and simulations is introduced by means of *attempts* to change the configuration, which are generated randomly into the cone of angle $\delta\theta$. Under this assumption, the *movement* of the magnetic moments is resembled by giving the system a certain amount of MC steps to change its configuration. The matter is: in a real system, the magnetic moments fluctuate because of the thermal energy and consequently fluctuations are reduced the smaller the temperature. In order to reproduce this characteristic in the simulations, it appears very reasonable to us to include a temperature-dependence in the value of $\delta\theta$, since it is the tool used to resemble the thermal-flucuations found in real systems. It is worth no note here that although there is no intention on analyzing time-dependence in our simulations, however the temperature-dependence expression used has been intensively analyzed and discussed in such a purpose by Nowak et al. [15] and Cheng et al. [16]. The temperature dependence of $\delta\theta$ can be, following Refs. [15, 16][14] and in usual computational reduced temperature units[15] $t = k_B T/2KV$, written as $\delta\theta = (Ct)^{1/2}$, with C a constant value proportional to the particle inner characteristics (size, magnetic moment and anisotropy) and to the dynamics of the system (gyromagnetic ratio, damping parameter, measuring time). The results plotted in FIGURE 1.13(b) show that for values of C of the order of 0.050, not large variations are considered in comparison with the $\delta\theta = 0.10$ case, as shown in FIGURE 1.13. We arbitrarily choose the $\delta\theta = 0.050t$ dependence value for taking into account temperature-dependence of $\delta\theta$. As a general rule, in our simulations we have considered the $\delta\theta = 0.10$ trial cone, and only very recently the temperature dependence of $\delta\theta$ has been considered.

from the very initial simulations with 64 particles. This would have been impossible without the invaluable help of the Centro de Supercomputation de Galicia and the great staff working there.

[14] Both works have the same temperature-dependence of the trial cone angle and differ on the introduction of the dependence on the damping parameter α, a phenomenological experimental value difficult to determine and important for time-dependent studies. Hence, in our simulations we do discuss its influence and consider only its phenomenological influence into the thermal fluctuations.

[15] The temperature units and the motivation for their use will be discussed in CHAPTER 2. For the moment, it is enough to know that they are more interesting from the theoretical point of view, and more adequate for simulation purposes.

For every calculation described on the next sections the way of choosing $\delta\theta$ will be properly described.

To summarize, we use a MC technique to simulate the magnetic properties of magnetic nanoparticle systems as described in SECTION 1.2. The simulations consist on two parts: on the first one, the spatial arrangement of the particles is set, which will be kept fixed afterwards. On the second part, the particles are characterized with their magnetic moment and anisotropy easy axes (which is also kept fixed afterwards), and their energies evaluated under certain *magnetic field/temperature* conditions. The analogy to temporal variation is accounted by means of MC steps. As discussed at the beginning of the subsection, the results from the MC method will be more precise the larger amount of events generated. In this aim, we will consider different configurations of the system under the same conditions and average the results. To describe our simulations we have to give the following details:

1. System size: amount of particles N that constitutes the system.
2. Type of process: ZFC, FC, or M(H) curves.
3. Characteristics of the particles: size, magnetic moment, and anisotropy.
4. Energies governing the system (physical model considered).
5. Step size: $\delta\theta = 0.10 = cte$, or $\delta\theta = (0.050t)^{1/2}$.
6. MC-step variation rate of the considered magnitude (temperature, magnetic field).
7. Amount of configurations to average the results.

Finally, it is worthy to point out some very important advantages of MC method to study complex systems with large parameter-dispersion degrees. On one hand, it is clear that the main limitation of any computational technique is the assumption of idealizations. This is its main drawback, and may hinder its usefulness to simulate real systems if being incapable of reproducing some relevant real properties. But, if the difficulties are overcome and a description of the experimental characteristics is properly accomplished (and being aware of the assumed limitations), the computational technique becomes at this point a very powerful tool that allows us to reach a very deep insight into the properties of the simulated system. The reason for this advantage relies on its working kernel very essence: in the MC technique, each constituent of the system is independently characterized and identified, and consequently its characteristics are perfectly controlled. Thereby, the MC method

allows us not only to analyze the system from its macroscopic constituents, but also from the inner microscopic data at each parameter-variation.

Let us particularize this for our simulations of the magnetic properties of the nanoparticle system. As illustrated in SECTION 1.3.3, we can use the MC to simulate the total magnetization of the system under the influence of a desired parameter as a function of temperature/magnetic field variation, i.e. we can analyze its properties from the *macroscopic* point of view. But, as it is inherent to the MC technique the need to control at each step the orientation of each magnetic moment, we may also analyze at each configuration its inner properties, i.e. we can have the *microscopic* analysis. In this aim, we have worked out the original code and included several modifications in order to have all this information available to us at desire. The main characteristics considered have been: i) to record the evolution of each magnetic moment with parameter-variation, so that we may, for example, know at each temperature during a ZFC/FC process how many magnetic moments are parallel or antiparallel to the field, and their relative orientation with each other (see CHAPTER 4); ii) to analyze the different energetic contributions separately, so that direct comparison between the different energy sources can be evaluated (see CHAPTER 3); iii) to analyze the magnetic dipolar fields, in order to obtain histograms as a function of a parameter-variation. As discussed in CHAPTER 3, this may result a invaluable tool for understanding the unsolved question of the magnetic dipolar field influence. These improvements added to the code will be introduced during the next chapters, properly discussed and explained when needed.

1.4 Magnetocaloric effect (MCE)

The *magnetocaloric effect* (MCE) is the temperature change experimented by a magnetic material (ΔT_{ad}) when subjected to an adiabatic magnetic field variation. The magnitude and sign of ΔT_{ad} depend strongly on both the characteristics of the system (chemical composition, structure, shape, etc) and on the experimental conditions (temperature, magnetic field, time, pressure, thermal history, etc), providing a rich scenario for technological applications. The $\Delta T_{ad} < 0$ case allows for the so-called *magnetic refrigeration* (MR) [32], a cooling technology with remarkable advantages over conventional vapour-gas compression refrigeration: it is an environmental-friendly technology (no need of hazardous harmful gases) with higher energy efficiency [33] (over 20% of the Carnot cycle than the best compression-gas

based refrigerators[16]). On the other hand, the $\Delta T_{ad} > 0$ case finds a very promising application in the use of magnetic nanoparticles as hyperthermia agents for cancer treatment, as substitute/complimentary of usual radio- and chemo-therapy treatments [34]. The temperature rise created by the radiotherapy treatment is very aggresive to the neighbouring non-tumoral cells, provocating harmful secondary effects very unconvenient for the patient. This damage can be diminished (ideally totally removed) by selectively heating the malignant cells through direct injection of magnetic nanoparticles into the tumour and rising its temperature by means of an external field variation, maintaining undamaged the neighbouring healthy cells.

These MCE-based applications remain, however, still at an early stage. Despite the great success of MR as an alternative to room-temperature vapour-gas compressing technology, with several artifacts reported during the last years demonstrating the achievement of competitive cooling values [35], magnetic refrigerators are not of common use yet. The reasons for this slow down in the development of MR are not engineering-related technological difficulties, but instead commercial ones: the working magnetic substances of those prototypes are very expensive, making inviable its industrial production for commercial purposes [33]. Similarly, much effort has to be done in the field of hyperthermia before it may become a common medical technique, since the role of different key-parameters that determine the power of the temperature rising (dipole-dipole interparticle interactions; type of magnetic anisotropy; size polydispersity; etc) remains uncontrolled/misunderstood, and must consequently be addressed for optimizing the hyperthermia efficiency [34, 36].

Therefore, from a general point of view there are two main research aspects concerning the MCE: one is that of basic investigation for magnetic materials exhibiting appropriate ΔT_{ad} values at desired conditions, and the other deals with the design of the working conditions for its implementation into technological devices for commercial purposes. In this Thesis we have dealt exclusively with the basic-research side, i.e. we have analyzed the MCE under different conditions (magnetic field, type of material, spatial arrangement, etc) but no attention has been paid to the engineering design[17].

Our investigation has been focused on the study and characterization of the MCE in nanostructures, an innovative research line amidst the majority of current MCE-related studies. At present most MCE studies aiming cooling objectives deal with bulk systems, seeking for good (and cheap) magnetic substances suitable to be

[16] It is stimated that 15% of the energy comsumption worldwide involves the use of refrigeration, and so it points out the importance of implementation improvements [33].

[17] For more information is this regard, see for example the recent review by Bjørk et al. [35] and references therein.

used as working agents in room-temperature devices alternative to compression-gas cooling artifacts [37]. For this intention of large-scale refrigeration devices, large systems in bulk phase present very good magnetocaloric properties (around the first- and second-order magnetic phase transitions) and as a result, little attention has been paid to the MCE in low-dimensionality systems as to refrigeration concerns [38].

Our motivation to investigate the MCE at the nanoscale arises from the rapid development of micro- and nano-devices occurring nowadays in practically every branch of science. This nanominiaturization process brings together new technological requirements, as the need of efficient cooling technologies able to work in these low dimensions, and in this context of nanoscale-refrigeration nanostructuring seems rather appropriate [39]. Furthermore, it is clear that for hyperthermia applications the working substance must be in the *nm*-range due to the micro- or nano-size of the cells and blood vessels, what gives additional interest to the study of the MCE in nanosized dimensions. Our search has been mainly focused on randomly distributed single-domain particle entities (0D-structures), and also more complex arrangements as particle chains (1D-structures) and ribbons (2D-structures) have been investigated. Next we briefly introduce the basic characteristics of the MCE, with the purpose of giving the fundamental details necessary to understand our work. It is important to emphasize here that our interest is only centered in the evaluation of the MCE, and consequently no theoretical considerations concerning the MCE have been undertaken. For further information about the thermodynamics of the MCE and current state of the art, see for example Refs. [33, 35, 37, 38, 40].

1.4.1 Magnetic entropy change ΔS_M

To characterize the MCE we want to know ΔT_{ad} as a function of the magnetic field variation. However, direct measurements of ΔT_{ad} are very complex to determine experimentally, and so for the sake of simplicity most authors prefer to report the *isothermal magnetic entropy change* ΔS_M, easily obtained from indirect measurements. ΔS_M and ΔT_{ad} are directly related[18]: isothermal application of a magnetic field reduces the magnetic entropy of the system and, complementary, adiabatic magnetizing results in a temperature decrease [32].

[18]For the sake of simplicity we focus on the explanation of the process when a magnetic field is applied. Removal of the magnetic field results in the same reasonings, just changing the sign of ΔS_M and ΔT_{ad}.

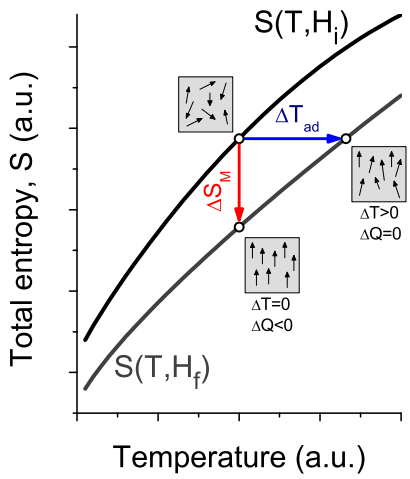

Figure 1.14:
Two isofield curves in the *total entropy vs temperature* diagram. Adiabatic field variation $\Delta H = H_f - H_i$ results in a temperature increase ΔT_{ad} (horizontal blue arrow), whereas isothermal variation of the same ΔH-value results in a magnetic entropy change ΔS_M (vertical red arrow). The drawings represent the magnetic configuration of the system in each $S(T, H)$-state.

A more detailed explanation is as follows: if splitting the total entropy of the system in two terms, the magnetic contribution and the associated to temperature[19], then i) the adiabatic application of a magnetic field reduces the magnetic part of the entropy and consequently, since the total entropy is constant, the entropy term associated to the temperature (and so the temperature) increases; ii) the isothermal application of the magnetic field reduces the magnetic part of the entropy and, since no temperature change occurs, then the total entropy decrease is equal to the magnetic entropy decrease. Therefore, ΔS_M and ΔT_{ad} are two magnitudes representing two quantitative characteristics of the MCE, and both are function of the initial temperature and magnetic field change. In FIGURE 1.14 it is illustrated the change in the magnetic system under a field variation $\Delta H = H_f - H_i$, both for the isothermal and adiabatic processes.

FIGURE 1.14 illustrates the basic features of the MCE: application of a magnetic field, which orders the system, causes a temperature rise if applied adiabatically and, alternatively, results in a heat release (expressed as $\Delta Q < 0$ in the figure) if applied isothermally. Analogously, the adiabatic removal of the magnetic field results in a decrease of the temperature, and in a heat absorb if removed adiabatically.

The combination of applied/removal magnetic fields under adiabatic/isothermal conditions can be used to directly design a refrigeration process based on the Carnot cycle. Regarding room-temperature MR, other thermodynamic cycles based on

[19] In bulk systems, the entropy terms associate to temperature are the lattice and electronic contributions [32, 41]; for the sake of simplicity we do not consider which are the actual contributions in nanoparticle systems (which we attribute to vibronic and rotationary modes), and just compute the magnetic part of the total entropy.

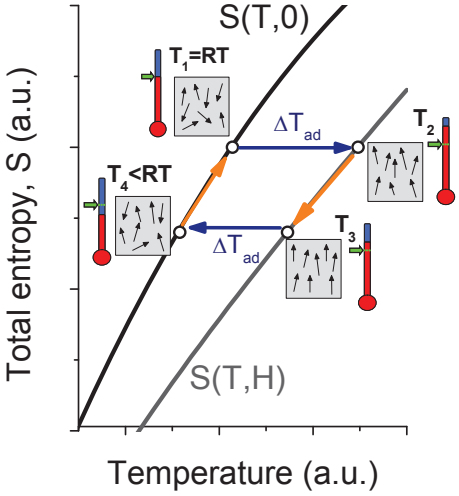

Figure 1.15:
$S-T$ diagram of the magnetic Brayton cycle.

different paths on the $S-T$ diagram of FIGURE 1.14 are preferable based on their ease to operate [41], the so-called Brayton and Ericsson cycles: the Ericsson cycle is composed of two isothermal and two isofield processes, whereas the Brayton cycle follows two isofield and two adiabatic processes. In FIGURE 1.15 it is shown the Brayton cycle, with the purpose to illustrate a magnetic-refrigeration process. For more information about these and other thermodynamic cycles suitable for implementation of MR see for example Refs. [37, 40].

MR process based on the Brayton cycle: if starting at a temperature $T_1 = RT$ (room temperature), the adiabatic application of a magnetic field increases the magnetic order of the system and reduces so its magnetic entropy. Hence, as the total entropy is constant, this decrease of the magnetic part of the entropy is counterbalanced by an increase of the entropy associated to the temperature, resulting in a temperature rise of the system up to T_2, with $T_2 > T_1$. Now, if the system is put in contact again with the environment (while maintaining applied the field), its temperature will drop to T_3 and the total entropy will decrease. Ideally we would like to have $T_3 = RT$, although in real refrigeration cycles this might take a too long time. The next step is the removal of the magnetic field under adiabatic conditions, what results now in a rise of the magnetic entropy. As the process is adiabatic, this increase of the magnetic entropy implies a decrease of the temperature part of the entropy, and so on a temperature decrease of the sample, down to T_4. The efficiency of a magnetic refrigerator based on the Brayton cycle will depend on the attained difference $\Delta T = T_4 - T_1$.

1.4.2 Measurement and units of ΔS_M

At equilibrium[20], the value of ΔS_M for a magnetic field change ΔH and temperature T is usually obtained from magnetization *vs* temperature/magnetic field measurements. Taking into account the Maxwell relation [43]

$$\left(\frac{\partial S}{\partial H}\right)_T = \left(\frac{\partial M}{\partial T}\right)_H \tag{1.13}$$

where M is the projection of the magnetization of the system along the magnetic field direction, the isothermal entropy change for a magnetic system at constant pressure and volume can be obtained as

$$\Delta S_M\left(T, \Delta H\right) = \int_{H_i}^{H_f} \left(\frac{\partial M\left(T, H\right)}{\partial T}\right)_H dH \tag{1.14}$$

For magnetic measurements made at discrete field and temperature intervals, Eq.(1.14) can be numerically approximated to

$$\Delta S_M = \sum_i \frac{M_{i+1} - Mi}{T_{i+1} - T_i} \Delta H_i \tag{1.15}$$

where M_{i+1} and M_i are the magnetization values measured in a magnetic field H, at the temperatures T_{i+1} and T_i, respectively. From Eqs.(1.14,1.15), it is evident that the MCE is directly proportional to the size of the magnetic moments and to the applied magnetic field, and, very important, to the ratio $\partial M/\partial T$. This is the reason why the MCE is usually investigated in bulk systems around the phase transformation, where a large change of the magnetization occurs, and on SPM materials, which exhibit large magnetic moments [40]. The applied field is desirable to be low, such that it does not need a high energy supply or that it can even be implemented by permanent magnets.

To obtain the ΔS_M values, Eq.(1.15) can be applied both to $M(H)$ and $M(T)$ thermomagnetic measurements. Most authors dealing with bulk systems prefer to evaluate the MCE from $M(H)$ measurements, which provide a systematic field dependence of ΔS_M. However, when dealing with nanosized materials other factors must be taken into account. The suitability of a magnetic material as working substance for a MR system is not only defined by its ΔS_M value, but it also of primary importance its capability to exhibit such MCE under cyclic applications

[20] In what follows we use a Maxwell relation to correlate the MCE and thermomagnetic measurements. It is important to note that Maxwell relations can only be correctly applied under equilibrium conditions in homogeneous systems; otherwise, the MCE might be overestimated [42].

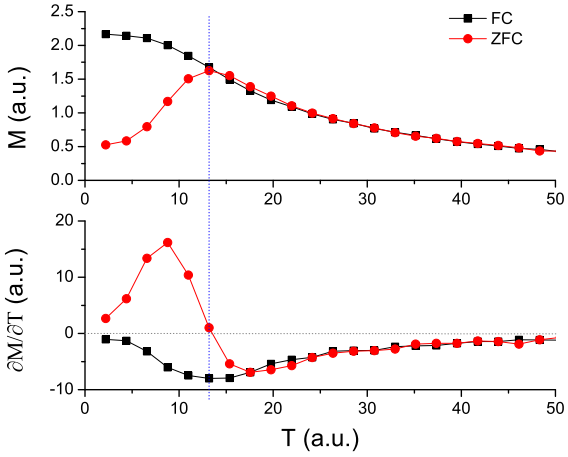

Figure 1.16: FC/ZFC curves and the corresponding $\partial M/\partial T$ values.

and removals of the magnetic field field, i.e. *reversibility* of the magnetocaloric properties is also fundamental for MR purposes.

In this regards, SPM nanoparticle systems exhibit a complex behavior, with its high-temperature reversible temperature range being strongly dependent on both the characteristics of the material and on experimental conditions, what makes necessary to elucidate such regimes prior to the MCE assessment. Since the reversible and irreversible temperature regimes are straightforward determined from $M(T)$ curves under the ZFC protocol (reversibility roughly above the maximum[21]), we have chosen to use these measurements to obtain ΔS_M. In addition, such protocol is also of high interest to study theoretical properties of single-domain entities, what provides us additional data for theoretical analysis. In FIGURE 1.16 we show the FC/ZFC processes shown in FIGURE 1.5 and the corresponding $\partial M/\partial T$ values to illustrate the reversible/irreversible characters of the different temperature regimes.

In FIGURE 1.16 we observe that the $\partial M/\partial T$-curves from the ZFC and FC processes overlap only in the high-temperature SPM range, and split at low temperatures, where have different sign. A splitting between both curves is also appreciated right above the maximum of the curve, where although of the same sign, the value obtained from the FC curves overestimates the one from the ZFC one. Therefore, the magnetic measurement we will use to obtain $\partial M/\partial T$ is the ZFC process, to avoid overestimation of the MCE. Also, the ZFC process corresponds to typical low-field $M(H)$ measurements if reaching the desired temperature in zero field (see Ref. [44] for an illustrative example). The negative value of $\partial M/\partial T$ observed

[21] This approximation works well for systems highly monodisperse; polydispersity of any type (size, shape, anisotropy, etc) would make necessary to reconsider this approximation.

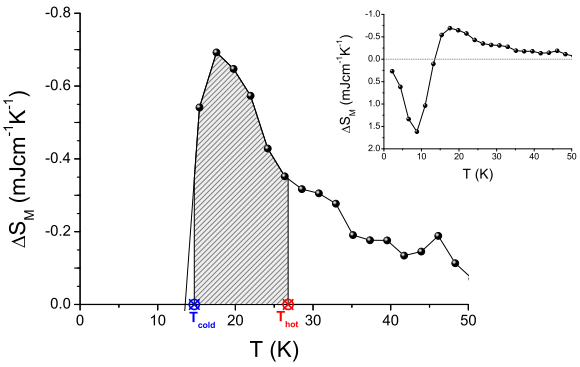

Figure 1.17: ΔS_M *vs* temperature. The dashed area indicates the temperature range between temperatures T_{cold} and T_{hot}. Inset shows the total temperature range of the ΔS_M curve.

at high temperatures is the appropriate for MR, as shown in FIGURE 1.15. The positive sign observed at low temperatures is adequate for hyperthermia purposes; however, since in this Thesis we have mainly focused on the refrigeration aspects of the MCE, most of the results reported will be focused on negative ΔS_M values. In FIGURE 1.17, we show the corresponding ΔS_M in the reversible temperature range obtained from FIGURE 1.16.

In FIGURE 1.17, we observe that the ΔS_M curve exhibits a peak (ΔS_M^{max}) where the MCE is therefore maximized. For MR purposes, the aim is to find materials with the largest possible ΔS_M^{max}, and to have such value at room temperature. The ΔS_M curve shows irregularities on its shape reflecting the accuracy errors coming from the uncertainty of magnetic moment, temperature, and applied magnetic field. Typically the errors are estimated to be $3-10\%$ [45]. The inset of FIGURE 1.17 displays a mach larger absolute ΔS_M for the low-temperature range below the maximum of the ZFC curve, which although for MR purposes is not interesting because of being irreversible, it has high qualities for hyperthermia purposes.

Finally, it is worth to mention that, although most authors report the MCE as ΔS_M using $Jkg^{-1}K^{-1}$ units, those are not the most appropriate from the engineering point of view of MR design, for which the cooling capacity must be known *per unit volume* [38]. That is the reason why in our investigations, we have preferably used $Jcm^{-3}K^{-1}$ volumetric units when possible.

1.4.3 Refrigerant capacity

From the results shown in FIGURE 1.17 it could be inferred that the most appropriated conditions for MR-systems based on the MCE are those at which ΔS_M is maximized. However, to appropriately choose a magnetic material for MR, not only

the ΔS_M value must be considered, but also other parameters as the working temperatures for a thermodynamic cycle have to be taken into account, whose adequacy and efficiency are reflected on the shape of the ΔS_M curve. Such characteristics are properly accounted by means of the refrigerant capacity (RC), a MCE parameter that quantifies the amount of heat that can be transferred in one thermodynamic cycle [38]. It is evaluated as

$$RC = \int_{T_{cold}}^{T_{hot}} \left[\Delta S_M\left(T\right)\right]_{\Delta H} dT \tag{1.16}$$

where T_{cold} and T_{hot} are the temperatures of the cold and hot reservoirs, respectively, usually defined as the temperatures at half maximum peak of the entropy curve. The shaded area in FIGURE 1.17 represents an example of the RC. Hence, depending on the MR requirements of the desired system not only the maximum magnetic entropy attained is important, but also how the temperature working range must be considered in the shape of the entropy curve.

2

Random nanoparticle systems

In this chapter we study the magnetic and magnetocaloric properties of randomly distributed single-domain magnetic nanoparticle systems as a function of the main parameters ruling its magnetic behavior: magnetic field, dipolar interparticle interactions, and magnetic anisotropy. The role played by each one of these parameters and their common interplay gives place to a complex problem with a large amount of dispersion degrees, and therefore to undertake such problem we have used a computational technique that allowed us to eliminate uncontrolled dispersion aspects. In what follows we briefly introduce the model used, and in the next subsections the influence of each parameter is analyzed. Finally, some considerations about the importance of ZFC/FC measurements for dealing with nanoparticle systems and the usefulness of having an analytical approach are discussed, special attention paid to the limits of such type of approaches.

2.1 Simple model with 3 energies: E_A, E_Z, E_D

The model used in our simulations is the same as in Ref. [12], in which it is considered a system of magnetic nanoparticles distributed in a liquid-like arrangement. Initially, every particle position moves freely and interacts by a standard Lennard-Jones pair potential with periodic boundary conditions, where the long-range interactions were characterized by using a Ewald's summation for an infinite sphere surrounded by vacuum [13]. Once the liquid-like arrangement is obtained the positions of the particles are kept fixed, resembling a frozen ferrofluid. As described in Section 1.2, in the SPM theory it is assumed single domain magnetic particles with inner coherent magnetization of the magnetic moments, what results in a total

absolute magnetic moment of the i-particle of $|\vec{\mu}_i| = M_S V_i$. We assume a monodisperse system, since polydispersion has a moderate importance in our present study. This working assumption is borne out by recent experimental works [46].

The energy of each particle is considered to have three sources: anisotropy (E_A), Zeeman (E_Z), and dipolar interaction (E_D). The anisotropy of the particles is considered to be uniaxial for the sake of simplicity, and hence the anisotropy energy of the i-particle is given by $E_A^{(i)} = -KV\cos^2\theta_i$ (Eq.(1.2)), where K, V are the same for all particles (monodispersity assumption). The Zeeman energy is described by the usual relation of the coupling of the magnetic moment to a magnetic field $\vec{H}$, i.e. $E_A^{(i)} = -M_S V H\cos\theta_i$, and the dipolar interaction energy between two particles i and j is given by

$$E_D^{(i,j)} = \frac{1}{2}\sum_{j\neq i}^{N}\left(\frac{\vec{\mu}_i\cdot\vec{\mu}_j}{r_{ij}^3} - 3\frac{(\vec{\mu}_i\cdot\vec{r}_{ij})(\vec{\mu}_j\cdot\vec{r}_{ij})}{r_{ij}^5}\right) \tag{2.1}$$

with $\vec{r}_i$ and $\vec{r}_j$ the positions of the particles i, j, respectively, and $\vec{r}_{ij}$ the vector distance connecting them. Adding up E_A, E_Z, E_D and extending the summation to all the particles, the total energy of the system results in

$$E_T = \sum_i \left(E_A^{(i)} + E_Z^{(i)} + E_D^{(i,j)}\right) \tag{2.2}$$

For the simulation procedure we use a Monte Carlo method based on the Metropolis algorithm, as described in Section 1.3: in every step a particle i is chosen at random and a new orientation of its magnetic moment is generated; the attempted new orientation is accepted with probability $min[1, exp(-\Delta E/k_B T)]$, where ΔE is the energy difference between attempted and present orientation, and k_B is the Boltzmann factor. After each trial, the time is incremented by N^{-1}, so that in one time unit (one MC step) N attempts are made (being N the number of particles in the simulated sample)[1].

All results are presented in reduced units. The applied magnetic field is introduced by means of the reduced field $h = H/H_A$, with $H_A = 2K/M_S$ the anisotropy field of the particles. The dipolar interaction strength, introduced by means of the sample concentration c, is often presented as normalized by $c_0 = 2K/M_S^2$, a unitless parameter which meaning will be intensively discussed in Chapter 3. Temperature

[1] The amount of particles used in our simulations varied significantly depending on the available resources, starting with N=64 -and even less- at the very beginning of the Thesis period, to N=1000 -and even more- very recently. It must be noted that the results are not presented ordered by making time, but instead to share a common theme is the chosen pattern.

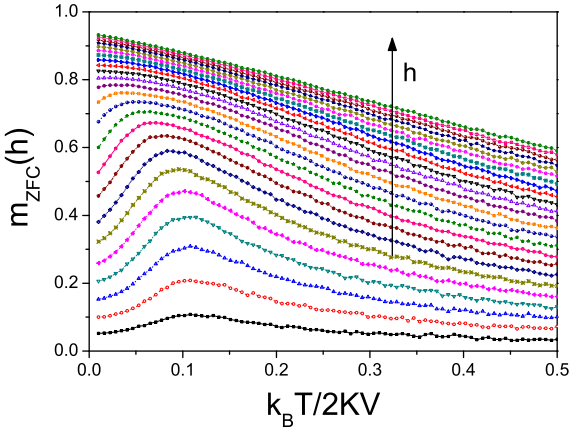

Figure 2.1:
ZFC curves for increasing h-values, with $0.10 \leq h \leq 1.20$. The arrow indicates the direction of increasing field.

is treated in reduced units of $t = k_B T/2KV$, and the magnetization of the sample (M) is given in normalized units of $m = M/M_S$.

2.2 Field dependence

As discussed in previous SECTION 1.2, the magnetic properties of SPM nanoparticle systems are strongly dependent on the strength of the applied magnetic field, which modifies the height of the anisotropy barrier and hence the relaxation characteristics. Its strength is also the key-point for the MCE (directly proportional to the magnitude of the field, as indicated by Eq.(1.14)), and therefore it is of great interest to understand its role on the magnetic response of nanoparticle systems. In this section we investigate the influence of the applied magnetic field both the SPM properties and MCE of a system of single-domain nanoparticle systems.

2.2.1 SPM properties

We have simulated ZFC processes under different values of the applied magnetic field (see Ref. [47] for computational details). In FIGURE 2.1, the reduced magnetization of the ZFC processes is plotted for different values of the reduced field h, with $0.10 \leq h \leq 1.20$. The sample concentration (which accounts for the strength of the dipolar interaction) is kept fixed for all the simulations ($c/c_0 = 0.064$).

The maxima of the curves of FIGURE 2.1 continually grow with increasing fields, as expected. However, its position with the temperature follows a non-monotononic tendency, shifting to lower temperatures in the high-field range (what corresponds to a lowering of the wall energy barrier), but displaying however a more complex behaviour at low fields, where it does not follow a well defined tendency. We analyze

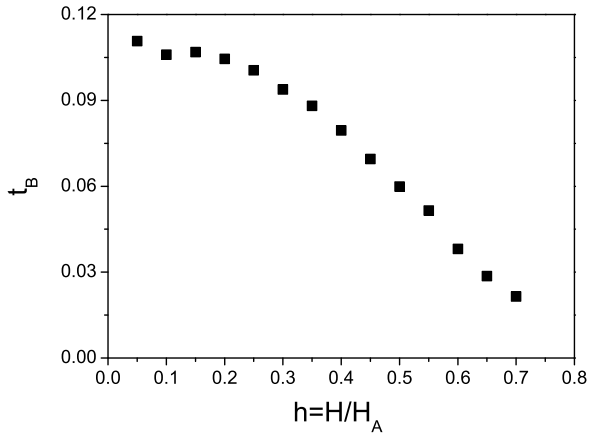

Figure 2.2:
t_B *vs* h corresponding to the curves shown in FIGURE 2.1.

in detail this behaviour from the field dependence of the blocking temperature for SPM system, usually described by

$$T_B(H) = \frac{KV}{k_B \ln\left(\frac{\tau_m}{\tau_0}\right)} \left[1 - \left(\frac{H}{H_A}\right)\right]^{\alpha} \tag{2.3}$$

where the exponent α depends on the easy-axis orientation and is close to 3/2 for random systems (see Ref. [48]). Following Eq.(2.3), we would expect the maximum of the curves to continually decrease with increasing magnetic field, to finally dissapear for $h = 1$ (applied magnetic field enough to overcome the anisotropy field of the particles). We represent in FIGURE 2.2 the maximum of the ZFC curves *vs* h.

We observe in FIGURE 2.2 an overall decrease of t_B with increasing h, in agreement with the lowering of the anisotropy barrier by the magnetic field predicted by Eq.(2.3). At very low fields, however, an anomalous behaviour is observed: t_B slightly decreases and then increases, before the monotonic decrease-range is reached. This behaviour reproduces the change from a bell-like shape to a monotonically decreasing behaviour that has been reported for increasing dipolar interactions [49]. Another important feature observed in FIGURE 2.2 is that the values of t_B are plotted only for values of $h \leq 0.7$: for larger fields, the peak of the ZFC curve disappears. This is an important point that runs contrary to the behaviour predicted by Eq.(2.3), pointing out limitations of such equation on describing the $H \to H_A$ limit case. Such failure may have its origin on the presence of the dipolar interactions, which are not taken into account. This matter is further studied in SECTION 2.4.

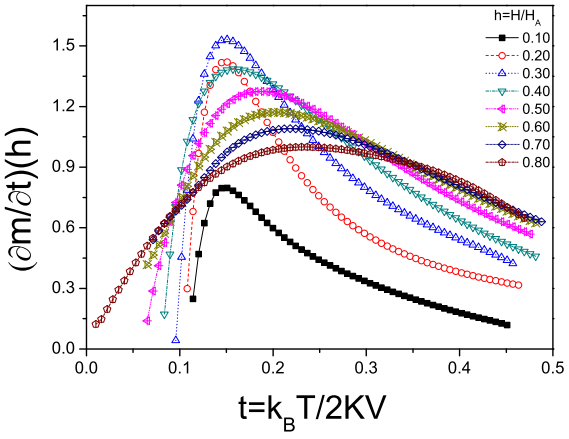

Figure 2.3: $\partial m/\partial t$ *vs* h obtained from ZFC processes. The values are calculated only for $t > t_B$, where the system is reversible.

2.2.2 MCE

We study now the field-dependence of the MCE. The magnetic entropy variation, which for a discrete magnetic field and temperature variation is described by Eq.(1.15), in reduced units reads

$$\Delta s_m = \sum_i \Delta s_i = \sum_i \frac{m(t_{i+1}, h) - m(t_i, h)}{t_{i+1} - t_i} \Delta h_i \tag{2.4}$$

where $m(t_i, h)$ is the reduced magnetization at the reduced temperature t_i under a reduced magnetic field h. $m(t_i, h)$ is defined as the projection of the total magnetization of the system along the magnetic field direction, normalized as $m = M/M_S$. Before calculating the related entropy change for the different conditions of applied field we analyze the $(\partial m/\partial t)$-ratio *vs* t. The reason for doing this specific analysis is to obtain an insightful characterization of the magnetocaloric properties of the system, which are proportional to $(\partial m/\partial t)(h)$. The results are plotted in FIGURE 2.3.

From FIGURE 2.3, we observe that all curves (for the different magnetic fields applied) are characterized by the existence of a maximum, and that the overall shape of the curves broadens with increasing field. A remarkable characteristic is the existence of an absolute maximum in $(\partial m/\partial t)$ for $h^* = 0.3$, at $t = 0.151$. This h^*-parameter marks also a distinct evolution in the shape of the $(\partial m/\partial t)(h)$ curves: for fields $h < h^*$ the overall shape of the curves consists on a relatively narrow peak that shifts very slightly to higher temperatures for increasing values of the applied field; for fields $h > h^*$, the overall shape of the curves broadens and shifts to higher temperatures more rapidly than at low fields. The positions of the peaks *vs* reduced temperature, as well as their relative height, are plotted in FIGURE 2.4.

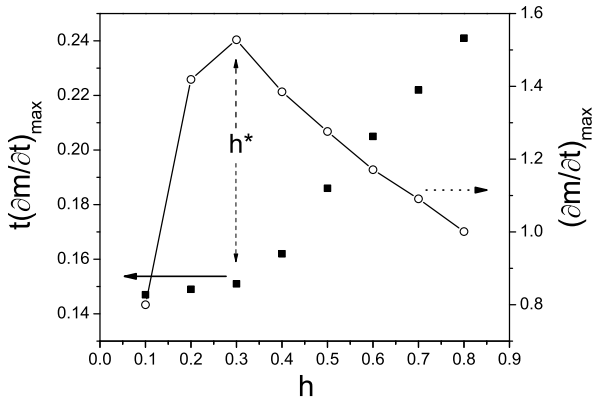

Figure 2.4: $(\partial m/\partial t)_{max}$ and $t(\partial m/\partial t)_{max}$ *vs* h. Vertical dotted line stands for h^*.

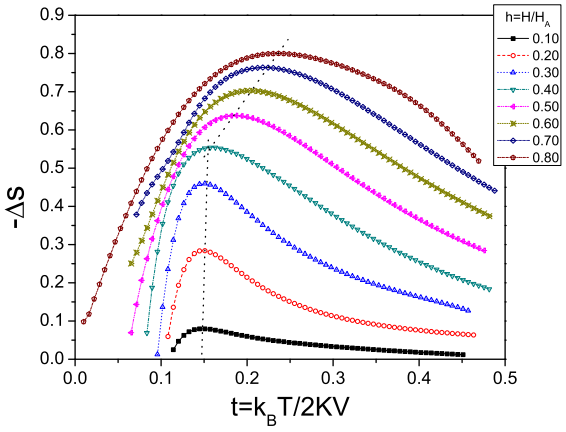

Figure 2.5: $-\Delta s_m$ *vs* h. The Δs_m-values are calculated for $t > t_B$, where the system is reversible.

In FIGURE 2.4 are shown the maximum values of $\partial m/\partial t$, i.e. $(\partial m/\partial t)_{max}$, for the different applied fields (empty circles), as well as the reduced temperatures at which those maxima occur, i.e. $t(\partial m/\partial t)_{max}$ (filled squares). Two different trends are observed: by one aside, at low fields ($h < h^*$) a tiny increase of the magnetic field results in a high enhancement of $\partial m/\partial t$ while the correspondent reduced temperature experiences a tiny increase. On the other side, for $h > h^*$, $\partial m/\partial t$ decreases with increasing field, and the temperature position rapidly grows with the field. We observe now how these different field range of $\partial m/\partial t$ translate onto the Δs_M *vs* h diagram, shown in FIGURE 2.5.

In FIGURE 2.5 it is observed an overall enhancement of Δs_m for increasing fields, evolving from a narrow peak at low fields to a fast broadening of the peaks at high fields ($h > h^*$). Also, the same tendency of FIGURE 2.3 is observed in the peak position of the curves: for fields $h < h^*$, the position of the peak slightly shifts to higher temperatures with increasing field, while for fields $h > h^*$ the temperature of

the maxima rapidly grows with increasing fields. This characteristic of the entropy curves for fields larger than h^*, i.e. large entropy change over a wide range of temperatures, results specially interesting for Micro- and Nano Electro Mechanical Systems applications [39]: the working temperature can be adjusted by varying the applied field without large ΔS_M variation, since the entropy does not vary much around the peak for fields larger than h^*.

The dotted lines drawn in FIGURE 2.5 signal the tendency followed by the maximum of the entropy curves, the same as pointed out in FIGURE 2.4: for fields $h < h^*$, Δs_M^{max} occurs at essentially constant (slightly higher) temperatures and enhances much its relative value, whereas for fields $h > h^*$, Δs_M^{max} occurs at higher temperatures but a smaller relative enhancement takes place. The height of the maximums, which rapidly grows with increasing field at low values of it, slows however down for larger fields.

Conclusions We have found that for a system of randomly distributed magnetic nanoparticles the magnetic entropy change always increases with the magnetic field (as expected [50]), and furthermore, we demonstrate the existence of an optimizing magnetic field h^* at which the $\partial m/\partial t$ ratio exhibits a maximum. This particular value of the magnetic field marks also two different ways of behaviour of the entropy: for fields $h < h^*$ the entropy curve is narrow, rapidly grows with larger fields and its temperature position remains essentially unchanged. On the contrary, for fields $h > h^*$ the entropy peak broadens with increasing field and rapidly shifts to higher temperatures, growing however at a lower rate with the magnetic field. The magnetic field h^* signals the more efficiency conditions for a MCE implementation, essential for reducing energy consumption.

2.3 Role of the magnetic anisotropy

In the previous section we have analyzed the field-dependent SPM properties and MCE of a system of magnetic nanoparticles, where the characteristics of the particles (size, anisotropy, sample concentration, etc) were kept fixed and no attention was paid to their influence. However, it is important to remark that the MCE study was carried out in the high-temperature SPM range (were the system is reversible), and that such temperature range is directly determined by the magnetic anisotropy of the particles, as analyzed in SECTION 1.2. Therefore, both for MCE-related purposes and for basic-magnetism research it is of primordial importance to understand the role played by the magnetic anisotropy and its relative interplay

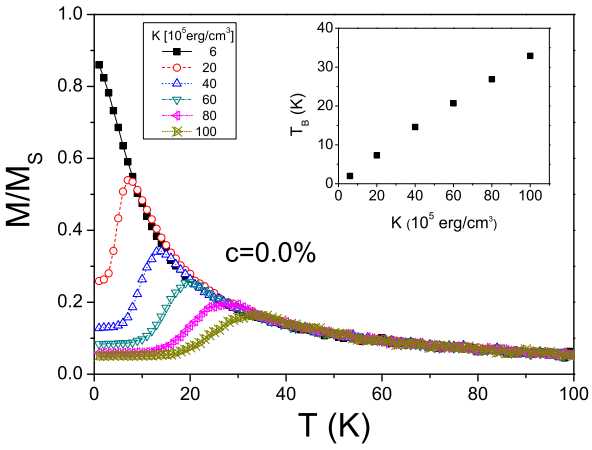

Figure 2.6:
ZFC processes for increasing values of K. Inset shows the maximum of the curves *vs* K.

with the other relevant energies. For such a purpose, in this section we study the role of the magnetic anisotropy on both the SPM properties and MCE for a system of magnetic nanoparticles of fixed size and saturation magnetization, while varying the anisotropy.

2.3.1 SPM properties

For the study of the role played by the anisotropy of the particles on the magnetic and magnetocaloric properties of a fine magnetic particle system we follow the same procedure as used for the field-dependent study: we simulate ZFC processes, now for different values of the anisotropy of the particles (keeping fixed its size, shape, and magnetization), and for the MCE characterization we have focused on the reversible region of the ZFC curves. We start our study with the simplest case of a non-interacting nanoparticle assembly, simulating the ZFC curves for a wide range of anisotropy values. To have an estimation of the results in real units, the study is based in the characteristics of maghemite-like nanoparticles [31] ($d = 3.5nm$, $M_S = 203.4emu/cm^3$, $K = 6 * 10^6 erg/cm^3$), and we have varied the anisotropy constant in one order of magnitude. We have chosen maghemite particles because their characteristics can be approximated to be constant in the temperature range considered for the simulation procedure (see Ref. [51] for computational details). All results presented in this work were simulated with a magnetic field $H = 500Oe$. For the non-interacting case ($c \to 0.00\%$) the results of the ZFC curves are plotted in FIGURE 2.6.

In FIGURE 2.6 is observed that the maximum of the ZFC curves shifts to higher temperatures for larger anisotropies. This behaviour reflects the SPM characteristics of the system as determined by the magnetic anisotropy: the larger is K the deeper is the energy barrier that the moment of the particles must overcome to reach the SPM state, and therefore a higher thermal energy is necessary to promote the jumping of the particles over the anisotropy barrier. The specific dependence $T_B(K)$ is shown in the inset.

The shape of the ZFC curves plotted in FIGURE 2.6 exhibits two other features calling our attention, which are the flatness at low temperatures and their overlapping at high temperatures. The overlapping of the curves at high temperatures reflects the SPM character of the system: for thermal energies larger than the anisotropy barrier, the total moment of the particles follows a paramagnetic-like decay with temperature, dependent only on the total magnetic moment of the particles and on the applied magnetic field. Since the magnetic field is low in comparison with the anisotropy field of the particles (always $H < 0.1H_A$), and the magnetic moment of the particles is always the same, it would be expected the overlapping of the curves at high enough temperature, as observed.

The flat range observed at low temperatures is wider for larger values of K, and our interpretation is that occurs only in the ideal non-interacting case. Since the effect of the external magnetic field is to align the magnetic moments of the particles, and its effect is smaller the greater is E_A, we can therefore expect that as long as the thermal energy is unable to make the particle moments to overcome the anisotropy barrier, the average total magnetization of the system remains the same. And consequently, this flat range enlarges with growing anisotropy. To obtain a more realistic physical picture and check our arguments about the non-interaction at the origin of the observed flat ranges, we have simulated the same processes but taking into account interparticle dipolar interactions, for the sample concentration values $c = 4.8\%, 14.8\%, 29.5\%$. The results are shown in FIGURE 2.7.

In FIGURE 2.7 we observe how increasing sample concentration (directly proportional to the dipolar interaction strength) results in an overall decrease of the magnetization and in a displacement of the maximum of the curves to higher temperatures, as expected [13]. With respect to the low-temperature features discussed after FIGURE 2.6, it is now observed that the flat data of the non-interacting case disappears as the coupling between the moments of the particles is stronger. With respect to the superparamagnetic range temperature, the shape of the curves coincides with the expected behaviour and apparently follows the same tendency of the non-interacting case of FIGURE 2.6.

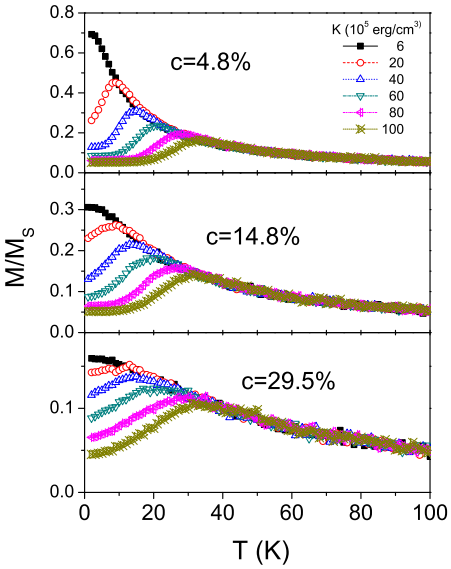

Figure 2.7:
ZFC processes for the same K-values of FIGURE 2.6, for different sample concentrations.

We analyze now the evolution of T_B with K for the different conditions considered. As introduced in SECTION 1.2, T_B is strongly dependent on the value of K, as described by Eq.(2.3). In fact, the dependence on K is more emphasized if using $H_A = 2K/M_S$ (with $\alpha = 1.5$):

$$T_B(H) = \frac{KV}{k_B \ln\left(\frac{\tau_m}{\tau_0}\right)} \left[1 - \left(\frac{HM_S}{2K}\right)\right]^{\frac{3}{2}} \tag{2.5}$$

This expression does not take into account interparticle dipolar interactions, and its suitability to account for interacting and non-interacting data can be seen in FIGURE 2.8, where the values of T_B for the different conditions of FIGURE 2.7 are plotted (figures) and fitted to Eq.(2.5) (lines).

There are two main features in FIGURE 2.8 that call our attention. Firstly, the fitting of the points to Eq.(2.5) is poor, specially for low values of the anisotropy constant and high interacting conditions. Secondly, the plotted data seems to follow a different trend at low and at high values of the magnetic anisotropy. At low values of K, T_B clearly increases with increasing sample concentration, in agreement with usual behavior reported in the literature [13, 46, 52]. However, at high values of K the tendency seems to follow the opposite trend, in agreement with other works [53]. These results are particularly interesting, since a long discussion has been kept in the literature above the dependency of T_B as a function of the interparticle dipolar

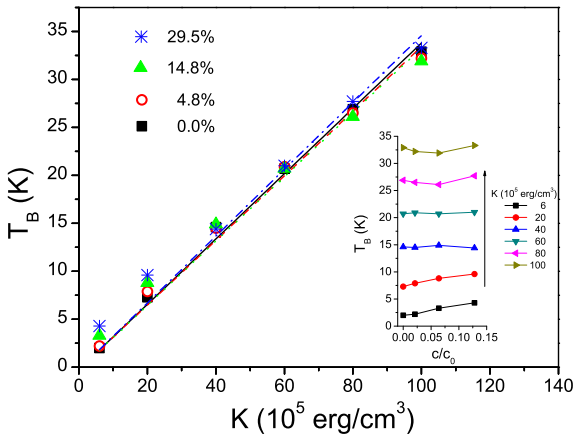

Figure 2.8: T_B *vs* K for the different sample concentrations considered.

interactions. More attention to this topic, in order to corroborate the apparently different tendencies will be discussed in CHAPTER 3.

The failing of Eq.(2.5) in describing well the data of FIGURE 2.8 is due to the fact that it is valid only for non-interacting cases. For taking into account the interactions between the particles, a modification of the random anisotropy model [1] (RAM) was proposed by W. C. Nunes et al. [54], who introduced the magnetic interparticle coupling on the field dependence of the superparamagnetic relaxation time. In this model the concentration and size of the particles are taken into account, as well as the field dependence of the correlation length. As it provides a generalization of Eq.(2.5), we have applied it to fit the data in FIGURE 2.8. However, the results obtained from this model provide also a rather poor fit, not very different from the one obtained with Eq.(2.5). The usual application objective of both models is the description of the field dependence of T_B on the strength of the applied magnetic field; perhaps the attempt to describe the theoretical dependence on the anisotropy deserves a deeper modification in order to include the results of FIGURE 2.5, were the obtained trends are in agreement with different tendencies reported in the literature. We will further treat this problem in CHAPTER 3.

2.3.2 MCE

Once the SPM characteristics of our simulated samples have been examined, we continue now with the study of the magnetocaloric properties. As in the previous section we examine the MCE for refrigeration purposes, dealing only with the reversible part of the magnetization curve, i.e. in the SPM range. For the $500Oe$ magnetic field change used for the simulations of the ZFC processes, the results of

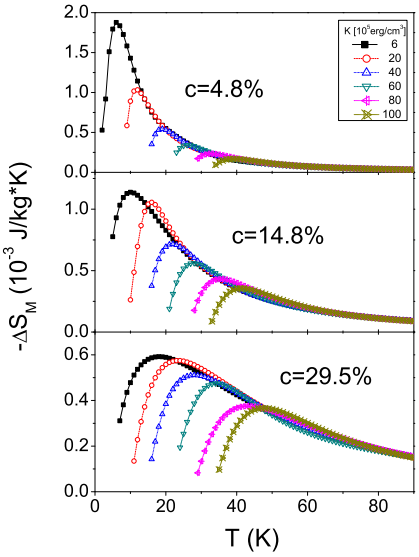

Figure 2.9:
$-\Delta S_M$ *vs* T curves for the different anisotropies and concentrations considered.

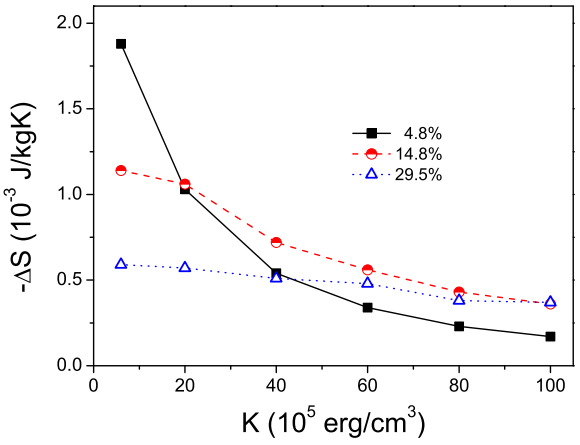

Figure 2.10:
Maximum values of the entropy change, $-\Delta S_M^{max}$, *vs* K for the sample concentrations c = 4.8%, 14.8%, and 29.5%.

the entropy change for the samples considered are plotted in FIGURE 2.9 (the ideal non-interacting case is not included).

At a first sight, we observe in FIGURE 2.9 that $-\Delta S_M$ always decreases with larger values K, although the diminishing rate is smaller the stronger is the dipolar interaction coupling. It is also observed that the concentration at which the maximum entropy change ($-\Delta S_M^{max}$) occurs varies as a function of K: for low values of K, $-\Delta S_M^{max}$ takes always place at diluted conditions; however, for higher values of K, $-\Delta S_M^{max}$ occurs successively at higher concentrations. We show $-\Delta S_M^{max}$ *vs* K in FIGURE 2.10, for the three concentrations considered.

In FIGURE 2.10, we observe how $-\Delta S_M^{max}$ occurs at different concentrations depending on the value of K. The higher values of the entropy enhancement are greater the smaller the anisotropy of the particles, what in principle points diluted conditions as the more adequate for MCE implementations. However, the more separate are the particles the higher would be the size of the system in order to get the same amount of heat transfer, inadequate for nanoscale MCE implementations. For particles with larger anisotropy the entropy change diminishes in a monotonic fashion for all concentrations. However, since its decay is rather small for large concentrations, the use of a more concentrate sample allows reducing the size of the system, what is more interesting for nanotechnological applications. Another noticeable feature observed in FIGURE 2.10 is the existence of a particular value of the concentration (for a fixed value of the anisotropy) for which the entropy change is maximized, as predicted by Ref. [55], where it is shown that for a magnetic nanoparticle system it is possible to fit the sample concentration able to produce a higher MCE.

We discuss now the MCE in these nanoparticle assemblies as compared to bulk materials. For our simulated samples the entropy change is of the order of $10^{-3} J/kgK$, much smaller than the values of the order of $1 J/kgK$ obtained for bulk materials. However, it is important to remark the different magnitude of the magnetic field (of the order of $10kOe$ for the bulk, whereas only $0.5kOe$ for the nanoparticle system), what represents a large difference in energy cost. For a more adequate comparison with respect to the bulk we use the ratio *entropy change/applied field* ($\Delta S/\Delta H$), which takes into account the magnetic field necessary to reach the correspondent entropy change. For a typical bulk material, the entropy change attained under a magnetic field of $10kOe$ is of the order of $1 J/kgK$, what results in a value $\Delta S/\Delta H \approx 0.1$. For our nanoparticle system we obtain $\Delta S/\Delta H \approx 0.02$, barely one order of magnitude smaller. This value is of the same order of magnitude than the reported for real nanoparticle systems [39]. The ability of ferrite nanoparticles to form magnetic fluids and its low-cost production favours the use of these systems in commercial magnetic refrigeration, despite the lower entropy change attained with respect to the bulk. It is necessary to remark, finally, that the intention of this work was not to find a good nanoparticle system for a real MCE implementation, but to study its magnetocaloric properties as a function of the anisotropy of the particles, along with its response under different strength of the dipolar interaction. A systematic search for the optimizing MCE-magnetic properties (size, shape, anisotropy, magnetic field, spatial arrangement, etc) will

undoubtedly give much better magnetocaloric properties, constituting to carry out such search a fundamental task for nanosized magnetic refrigeration.

Conclusions We have found that for a fixed sample concentration the magnitude of the entropy change diminishes for increasing anisotropy, and that the maximum values occur at higher temperatures for larger anisotropies. When comparing the entropies for different sample concentrations, we observe that *for a given value of the anisotropy it is possible to fit a particular sample concentration for which the negative change of the entropy is bigger, and that this particular concentration grows with larger values of the anisotropy.* Along with the study of the magnetocaloric properties of the system we have discussed its SPM features, focusing on the evolution of T_B with K at different concentrations. We have obtained a general increase of T_B with increasing K, as expected due to the enhancement of the energy barriers. We have tried also to fit our results in the basis of SPM theories, finding that the classical description given by Eq.(2.5) does not fit the results when the particles interact with each other. We have also fitted the results with the modification of the RAM proposed by W.C. Nunes et al. [54] that includes the sample concentration, but the results did not improve significantly the ones obtained by the non-interacting description, indicating that further work is necessary to be done in order to control interparticle interactions as referred to SPM theory.

2.4 Influence of interparticle dipolar interactions

Understanding the role played by magnetic dipolar interactions in the behavior of nanoparticle systems is fundamental for nanotechnological applications. For example, to increase the data recording capacity of hard drives it is necessary to control the interaction between neighbouring magnetic units, and for hyperthermia purposes, it is essential to know how the relative interparticle interactions determine the temperature rising of the system under a magnetic field variation. From the point of view of basic theoretical research, the study o such interactions as interpreted by the influence on T_B, has been the subject of intense attention for several years because of the controversial results reported in the literature, with very different tendencies reported in the evolution of T_B with increasing interactions strength. Hence it points out that to shed light into such matter is of great importance both theoretically and for application purposes.

We do not intend, however, to provide here a deep insight into the basic-properties research, which will be the subject of Chapter 3. Instead, the intention

of this section is solely to introduce the effect of the dipolar energy E_D in the context of its interplay with the other main energy sources of the system, namely Zeeman (E_Z) and anisotropy (E_A). For such a purpose, we follow in the present section the same procedure as in the previous ones, introducing first the SPM properties of the system as influenced by dipolar interactions, and later briefly complement its magnetocaloric properties in the line already introduced in the previous section. Additionally and because of its great relevance for magnetic recording technologies and biomedical applications, in this section we study too the influence of dipolar interactions in the SPM properties by means of $M(H)$ isotherms, and relate them to hyperthemia purposes. Finally, in the last part of the present section we discuss the role played by magnetic dipolar interactions on the macroscopic characteristics of a nanoparticle system in the context of spin glasses.

2.4.1 SPM properties

Following the same procedure used in the previous sections, to study the SPM properties of the system we have simulated ZFC processes, now at different sample concentrations accounting for different interparticle coupling strength (see Ref. [56] for computational details). The simulated sample concentrations are $c/c_0 = 0.064$, 0.128, 0.192, and 0.256, and the values of the reduced field vary between 0.05 and 1.20 for each value of c/c_0. We have simulated also the non-interacting limit case $c/c_0 = 0.000$ to compare with the interacting cases corresponding to the above concentrations. In FIGURE 2.11(a) are represented the ZFC curves for the increasing values of reduced field for the $c/c_0 = 0.064$ case.

In FIGURE 2.11(a) it is observed the expected trend for the magnetic nanoparticle assembly: overall increase of the magnetization for increasing values of the reduced applied field, together with the shift of the maxima to lower temperatures. We show also in FIGURE 2.11(b) the ZFC curves corresponding to different interacting conditions under the same applied field. It is observed the overall shift of the (reduced) blocking temperature (t_B) to higher values as the concentration increases [13]. From the maximum of the curves of FIGURE 2.11(a) we obtain t_B as a function of h, and analogously for the different interacting conditions of FIGURE 2.11(b). The results are shown in FIGURE 2.12.

The overall shape of the curves in FIGURE 2.12 shows that at low fields the value of t_B is quite close for the different interacting conditions, and gradually separates for increasing fields. This situation reflects the higher importance of E_A at low fields, and that low E_Z does not affect much the SPM behaviour. With regards to the influence of E_D at these low fields we cannot infer a clear tendency, since more

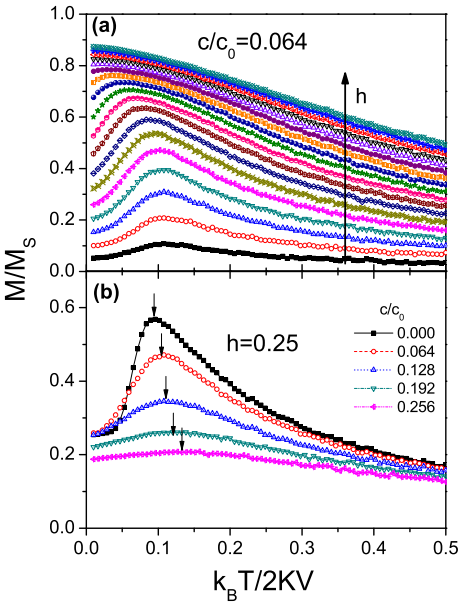

Figure 2.11:
(a) ZFC curves for increasing fields at $c/c_0 = 0.064$. The arrow signals the direction of increasing fields. (b) ZFC curves for increasing interacting conditions at a fixed reduced field $h = 0.25$. The arrows indicate the corresponding maxima of the curves.

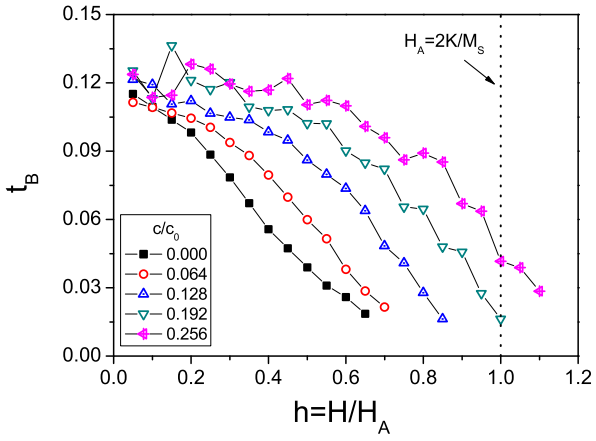

Figure 2.12:
t_B *vs* h for different interacting conditions. The dotted line stands for the reduced anisotropy field of the particles, $h = H/H_A \equiv 1.0$.

detailed calculus should be done in this aim[2]. For increasing fields the curves progressively separate, rapidly decaying to lower temperatures for diluted conditions, while this tendency is attenuated and shows a plateau-like shape for increasing concentrations. This behaviour is easily understood: for larger concentrations the dipoles are more tighten and therefore the same field produces a less noticeable

[2]Experimental works in 2D systems report negligible effect of the magnetic field on T_B at low concentrations [57], and so it remains as an interesting task the comparison between the 2D and the 3D arrangements. However, our purpose for this section is not to study this low-field scenario but instead the whole-field spectra, in particular the values around the anisotropy field of the particles, and for such objective the calculations are precise enough.

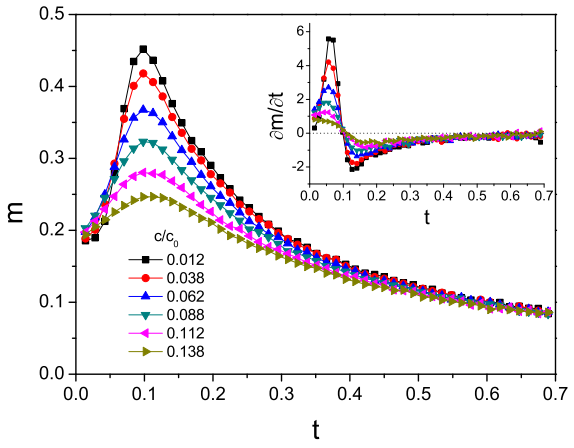

Figure 2.13: ZFC processes for increasing sample concentration, uner a magnetic field $h = 0.25$. Inset shows the first derivative of the curves.

effect. This is the reason why, though at low sample concentrations t_B disappears for fields quite below H_A, for large concentrations t_B exists even for fields $H > H_A$. This result, which contradicts the equation usually assumed to describe this dependence describing T_B as proportional to $(1 - H/H_A)^{3/2}$ (Eq.(2.3)), agrees with the results reported in the previous SECTION 2.3. As mentioned above, these and other aspects will be intensively treated in CHAPTER 3.

2.4.2 MCE

Once the SPM characteristics of our simulated samples have been examined, we continue now with the study of the magnetocaloric properties. We consider a systematic variation of the sample concentration, and simulate ZFC processes for the same field $h = 0.25$. The results are plotted in FIGURE 2.13

In FIGURE 2.13 we see that the curves flatten with increasing interactions, as expected. Regarding magnetocaloric considerations, the slope of the curves diminishes with increasing interparticle coupling (see inset), what indicates a smaller entropy variation. However, for MCE-related applications it is important to know the entropy variation *per unit volume*, and hence the fraction of the system must be taken into account when giving MCE results. The ΔS_M *vs* t curves for the different interacting conditions considered are shown In FIGURE 2.14.

We observe in FIGURE 2.14 that Δs_m experiences a maximum as a function of the sample concentration, both for the $t < t_B$ and $t > t_B$ cases, larger for the $t < t_B$ case as expected from the slope of the ZFC curves. This result is specially interesting for MCE-related applications, both for cooling (refrigeration) and heating

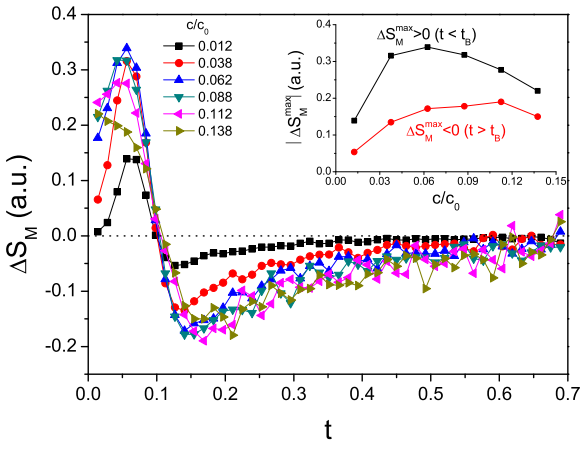

Figure 2.14: $-\Delta s_m$ *vs* t curves for the different c/c_0 values. Inset shows the maxima of the curves, both for the $t < t_B$ (squares) and $t > t_B$ (circles) cases.

(hyperthermia) purposes, indicating the existence of optimizing sample concentration conditions. This is an important result that must be further analyzed, seeking for the most adequate *magnetic field/anisotropy/sample concentration* conditions leading for an optimized MCE.

2.4.3 Hyperthermia applications

Magnetic nanoparticles find a very promising application in the field of biomedicine as hyperthermia agents for cancer treatment, as alternative/complementary to usual radio- and chemotherapy treatments [34]. The motivation to use magnetic nanoparticles to kill the malignant cells is based on their small size, which allows them to be attached into the tumoral nodes (either by direct injection or by diffusion throughout blood vessels) and to heat them under AC magnetic fields at radio frequencies. The higher sensitivity of the malignant cells to heat rise makes possible to selectively kill them while preserving the neighbouring healthy ones. In vivo experiments have documented the feasibility of this treatment in animal models of melanoma [58], breast tumors [59], and prostate cancer [60]; and depending on the experimental conditions and the type of particle this treatment either results in direct tumor cell killing or makes the cells more susceptible to concomitant radio- or chemotherapy.

The heating power of magnetic nanoparticles is usually associated to two origins, namely Néel relaxation (fluctuation of the particle' magnetic moment over the anisotropy barrier) and Brownian one (viscous losses due to particle reorientation) [61]. For clinical purposes in which the particles are inmobilized the Brownian contribution is negligible [44], and so in this work we focus on hysteretic Néel losses. The losses due to magnetization reorientation in ferromagnetic particles depend

on the type of remagnetizing process, which is determined in complicated ways by the particle moment, anisotropy, spatial distribution, interparticle interactions, etc. Modeling of the performance of magnetic nanoparticles has been previously reported [62, 63], although it has not been clarified yet if an increase in the sample concentration leads to an increase in the heating capacity, or to a decrease as recently suggested [64]. Due to the complex magnetic scenario constituted by magnetic nanoparticle systems as driven by dipolar interactions, it turns out that the use of a MC technique could be of valuable help to analyze such dipolar interactions-performance for hyperthermia purposes.

The heating efficiency is quantified by the specific absorption rate (SAR), actually by measuring the initial slope of the temperature rise before the effect of heat conduction becomes important [65], and this heating effect is usually interpreted as coming from the hysteresis losses during the reversal mechanism under the alternating magnetic field. Because of that reason we can associate the SAR with the hysteresis losses typical of SQUID measurements, by taking into account the proportionality of power with frequency [66]. Usual SAR measurements are made as a function of the maximum applied magnetic field, H_{max}, and for different sample concentrations. The usual shape of the experimental curves is a regular increase of SAR with H_{max} for fields comparable to the H_A of the particles and a tendency to saturate at large fields, whereas increasing concentration reduce the the SAR values (see for example Refs. [34, 64]). However, the origin of such decrease remains still unclear, being conjectured to be also attributable to size polydispersity and/or cubic anisotropy [34]. Thus, with the purpose of studying the role of magnetic dipolar interactions on the hyperthermia properties of the nanoparticle system, we performed MC simulations to treat the influence of particle concentration and field dependence on the SAR. The use of a MC method allows us to focus on the specific features of interest by modeling the physical system with ideal characteristics that avoid uncontrolled deviations found in real experiments as differences in composition (resulting in magnetization/anisotropy particle-particle variations) or size polydispersity.

We simulate $M(H)$ curves at different sample concentrations and for different values of H_{max}, considering the same physical model as in the previous sections (monodisperse system, uniaxial anisotropy, etc), and use parameter values corresponding to Fe nanoparticles with a MgO coating for biocompatibility [44] ($d = 75nm$, $K = 4.5 \times 10^5 erg/cm^3$, $M_S = 1700 emu/cm^3$). The process to simulate a $M(H)$ curve starts by first thermalizing the system at zero field from a very high temperature to the desired chosen temperature. Next, the magnetic field is applied

and increased in small intervals until a certain H_{max} value is reached; then, the field is decreased down to $-H_{max}$, and increased again up to H_{max} so that the cycle is complete. We have considered a system of $N = 1000$ particles and magnetization results are obtained from averaging the magnetization of all particles in the system over 5 different configurations. For all simulations the field variation ratio was kept constant as $\Delta H = 10Oe$ every 400 MC steps (see Ref. [44] for computational details). This ratio was chosen so that both the remanence (M_R) and coercive field (H_c), reproduce the expected values $M_R \approx 0.50M_S$ and $H_c \approx 0.48H_A$ in the ideal non-interacting case at very low temperatures [12], as illustrated in FIGURE 2.15(a). We have already emphasized in previous sections the primary importance of the H_A value in determining the magnetic properties of particle systems, since it weights the relative importance of the Zeeman energy [48]. Therefore, in our simulations we emphasize the value of the external field in relation with H_A.

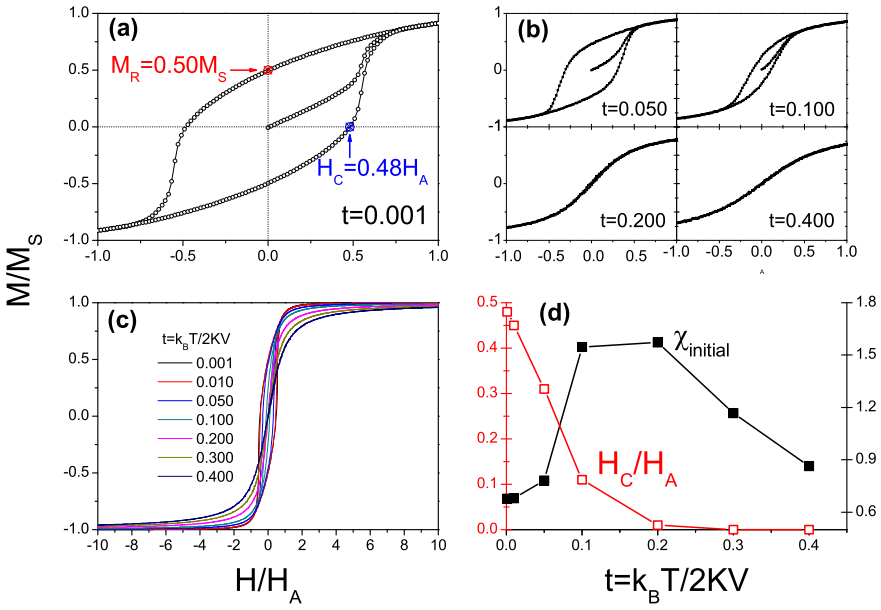

Figure 2.15:
(a) M *vs* H curve in the ideal very diluted limit at low temperatures, used as control for setting the amount of MC steps reproducing the StonerWohlfarth conditions, as indicated by the arrows. (b) $M(H)$ curves at increasing (reduced) temperatures illustrating the decrease of the hysteresis and H_c with temperature. (c) $M(H)$ curves at different temperatures showing the saturation behavior at field well above H_A. (d) temperature dependence of the initial susceptibility $\chi_{initial}$ (upper curve, full squares), and of H_c, in units of H_A (lower curve, empty squares).

Some $M(H)$ curves at higher temperatures (in the reduced temperature units $t = k_BT/2KV$) are plotted in FIGURE 2.15(b) showing the reduction of the hysteresis area with larger temperatures, as expected: higher thermal energy promotes larger fluctuations in the orientation of the magnetic moments, until at high enough temperatures the anisotropy energy wells of the particles are completely overcome and the particles reach the SPM state. The data shown in FIGURE 2.15(c) illustrates the occurrence of saturation of the $M(H)$ curves at the different temperatures, fields $H \gg H_A$.

The characteristic anhysteretic behaviour of the SPM state is analyzed in more detail in FIGURE 2.15(d), where it is plotted the temperature dependence of the initial susceptibility $\chi_{initial}$ and H_c in H_A units. The initial susceptibility first grows until a maximum is reached, and decays afterwards. This behavior agrees with the tendency observed in ZFC processes, in agreement with what we could expect since the process starts after thermalization in zero field. In fact, paramagnetic-like decay of $\chi_{initial}$ appears in the high-temperature regime, as corresponds to the SPM behavior. This reasoning is also supported by the trend followed by H_c/H_A *vs* temperature, for H_c decreases with growing temperature until it disappears when reaching the SPM temperature range.

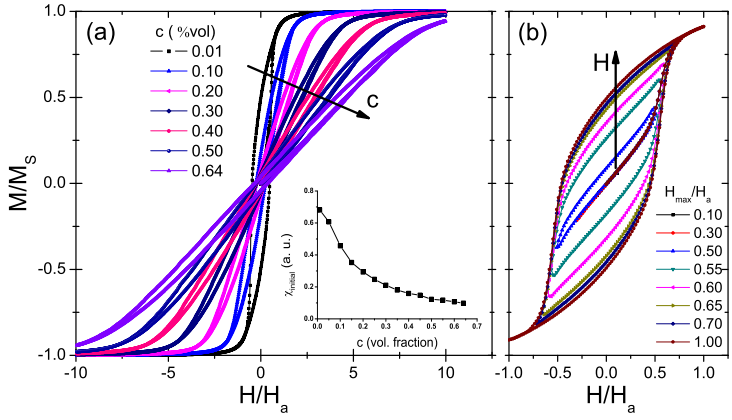

Figure 2.16:
(a) $M(H)$ curves for increasing sample concentration; inset shows $\chi_{initial}$ *vs* c. (b) $M(H)$ curves as a function of H_{max}, for a selected sample concentration $c = 0.007$. In both cases arrow indicates magnitude increasing direction.

In FIGURE 2.16(a), simulated $M(H)$ curves are shown as a function of the sample concentration. A decrease in $\chi_{initial}$ with increasing c is observed, so that the stronger the interaction between particles the lower the hyperthermia response. Our results partially agree with those published by Wang et al. [67] but run contrary

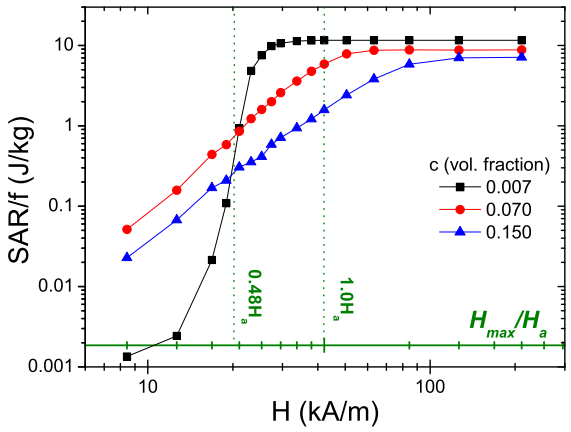

Figure 2.17: $-\Delta s_m$ *vs* t curves for the different c/c_0 values. Inset shows the maxima of the curves, both for the $t < t_B$ (squares) and $t > t_B$ (circles) cases.

to the findings in polydisperse ferrofluids reported by Jeun et al. [68], although we think that the different system analyzed in the latter (sample concentration is described as related to the size distribution, whereas in our case a monodisperse system is assumed) may be responsible for such discrepancy. FIGURE 2.16(b) shows $M(H)$ curves as a function of H for $c = 0.007$ for different values of H_{max}, where the relative importance of H_{max} with respect to H_A is underlined: for $H_{max} \prec H_c$, almost no noticeable effect in the area of the cycle is observed; whereas for $H_c \prec H_{max} \prec H_A$, large increases are observed. No noticeable variations are found for $H \succ H_A$. This dependence is analyzed in detail in FIGURE 2.17, along with results for different conditions $c = 0.070$ and $c = 0.150$.

The results displayed in FIGURE 2.17 show a well defined linear dependence on H_{max} for the concentrated samples ($c = 0.070$, $c = 0.150$), and a more complex behavior for the more diluted one ($c = 0.007$). The SAR diminishes with increasing concentration, and for all cases saturates at high fields, the saturation taking place at larger values for larger concentrations. These results reproduce and extend similar tendencies reported experimentally [34, 44], and therefore we unequivocally demonstrate that its characteristic shape, also reported in other works, is originated by the magnetic dipolar interactions among particles and not by size polydispersity of other anisotropy effects as had been hypothesized [34]. Our results also emphasize the importance of taking into account the characteristic value H_A to set our hyperthermia experimental conditions: it seems that H_A (larger the higher the concentration) gives an estimation of the upper limit of the field amplitude for larger SAR.

In summary, we observe that dipolar interactions significantly affect the magnetic susceptibility and hysteresis losses of magnetic nanoparticle systems, thus

implying a considerable reduction in specific heating power for hyperthermia applications.

2.4.4 Macroscopic state

From a macroscopic point of view, an aspect intensively discussed in the literature concerning the magnetic state of SPM nanoparticle systems is the possible existence of a spin-glass (SG) phase below the blocking temperature for highly interacting conditions [13, 69]. While some experiments present indications of a SG phase below T_B [24, 70], others favor the existence of a random anisotropy system [13, 30]. The usual signatures of a SG, frustration and disorder, are frequently found on frozen ferrofluids, induced by the randomness in the particle positions and anisotropy axis distributions. Frustration is introduced via dipole-dipole coupling, with competing ferromagnetic (FM) and antiferromagnetic (AFM) interactions, and randomness is found on the random location of the particles. This situation makes that for the same system both signatures of SG and SPM behavior can coexist [69].

The most common approach to study the physics of nanoparticle systems is based on observations of the dynamical behavior [24]. A phenomenological criterion usually employed is based on the magnitude of the FC magnetization memory effect, significantly larger for SG systems than for SPM behavior [69]. We have chosen a different method. With the purpose of understanding the influence of the dipolar interaction on the behavior of a fine magnetic particle system we have simulated its behavior by means of the Arrott plots [71], which have proved to be a useful tool for the study of phase transitions on magnetic materials [72]. We have simulated the evolution of the Arrott plots of a fine magnetic particle system for different sample concentration, ranging from the dilute limit at which SPM behavior is expected, to very concentrated samples at which the strength of the dipolar couplings is expected to introduce a collective relaxation behavior. We have focused our study on the temperature range around the blocking temperature.

The simulations are based on the same energy model described in Section 2.1, with the difference that in the present case the nanoparticle saturation magnetization M_S follows a Bloch-like temperature dependence

$$M_S(T) = M_S(0)\left[1 - AT^b\right] \tag{2.6}$$

Parameter values $A = 0.0005$ and $b = 1.5$ were chosen of the order of the experimental values of Zhang et al. [73] for iron nanoparticles of $5nm$ diameter. To simulate the evolution of the magnetization with the applied field we have at first relaxed the system in zero field in order to reach an equilibrium thermodynamic state

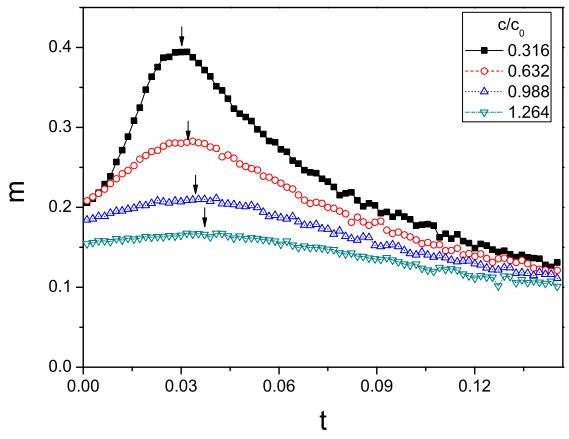

Figure 2.18:
ZFC curves for the different concentrations considered. Vertical arrows stand for the corresponding t_B.

for all temperatures considered. Then, the magnetic field was gradually increased resembling the experimental procedure (see Ref. [74] for computational details).

We have studied the Arrott representation around T_B for different interacting conditions. T_B was obtained in the usual way, approximated as the maximum of the ZFC curves. As shown in FIGURE 2.18, it is observed a general displacement of t_B to higher values as the concentration increases, in agreement with reported works [13]. We have chosen a wide range of temperatures around t_B to simulate the Arrott plots, above and below t_B. The simulations were done at high sample concentration conditions since that it is the scenario at which indications of a SG behaviour has been reported [24].

In FIGURE 2.19, we show the m *vs* h isotherms around t_B for different sample concentrations, being observed an overall decrease of the magnetization with increasing temperature for all ranges of dipolar interaction strength. At low concentration conditions, m tends to saturate for all temperatures, more easily the less concentrated the sample. However, for higher interacting conditions the curves do not show tendency to saturate at any temperature. This behavior is an indication of the presence of strong competing FM and AFM interactions on the system, and hence corroborating the presence of magnetic frustration that may account for the existence of a glassy phase [69].

In order to gain insight into the nature of the magnetic state at low temperatures for high dipole-dipole interacting conditions we have examined the m^2 *vs* h/m Arrott plots for the sample concentrations of FIGURE 2.19. Such representation, shown in FIGURE 2.20, exhibits two rather different features at high and low sample concentrations. At low concentrations the isotherms have a similar shape, keeping the same overall tendency for all temperatures. At high concentrations, however, a

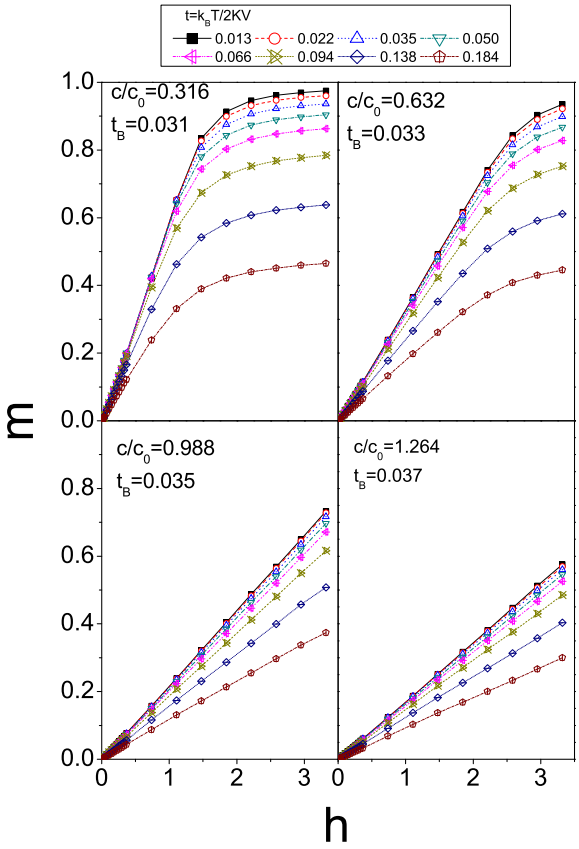

Figure 2.19: Magnetization isotherms versus applied field for different sample concentrations.

change of curvature occurs, the slope evolving from almost straight lines at low temperatures to a concave shape at high temperatures. Inset in FIGURE 2.19 shows the evolution of the isotherms with increasing higher fields, with the expected tendency to reach a maximum m^2 value correspondent to saturation. For high sample concentration where the inversion is observed, the extrapolation of the tangent of the high magnetic field data does not intercept the m^2 axis at any temperature, what is interpreted as an absence of spontaneous magnetization. This result indicates the absence of a FM long-range order between the magnetic moments, in a similar way as it is found in spin-glasses at low temperatures [75]. For the $m^2 \to 0$ limit, the curves progressively shift to higher temperatures for larger concentration. This situation is very similar to the effect of a random field on the magnetic phase transition of a conventional ferromagnet [72]. In fact, the evolution of the Arrott plots shown in FIGURE 2.19 is indicative of a crossover from a random anisotropy case (non-interacting particles) to a random field case, as dipolar interactions increase,

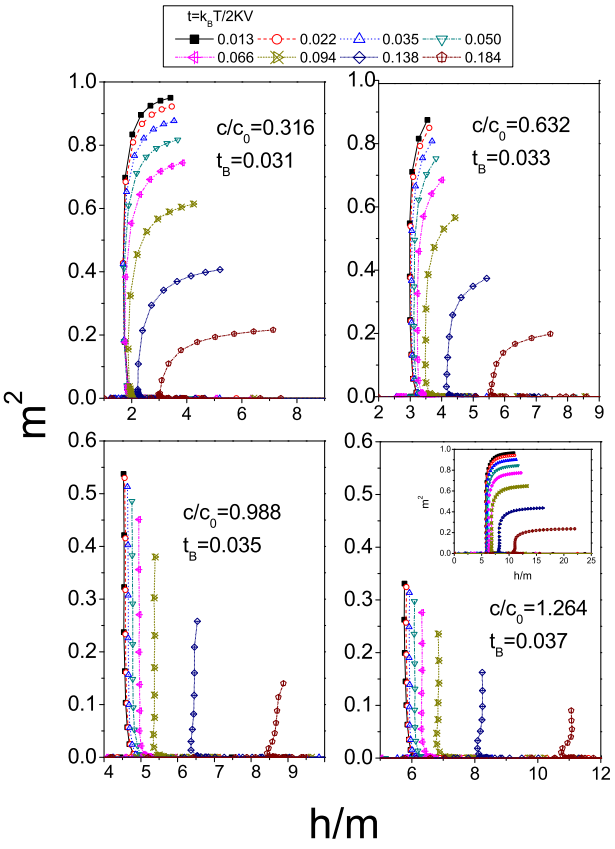

Figure 2.20: Arrott plots corresponding to the sample concentrations $c/c_0 = 0.316, 0.632, 0.988, 1.264$, for the isotherms of FIGURE 2.19. Inset shows the overall tendency to saturate at high fields.

in spite of not being in front of a conventional magnetic phase transition.

On the other hand, the change in curvature on the Arrott plots strongly reminds us the S-shape usually found around the critical temperature for first order magnetic transitions [73, 76]; however, the non-intercept of the m^2 axis for any temperature indicates the non-existence of a magnetic order temperature. The absence of a magnetic ordering temperature that would account for a phase transition is not observed also in the magnetization curves, where non-change in the low field data around the inversion temperature is found. However, for high interacting conditions of the same kind of systems, the existence of spin-glass behavior has been reported [24], what together with the inversion found on our simulations indicates the existence of a different interacting range.

Conclusions We have found that the effect of interparticle interactions on the SPM properties and MCE of nanoparticle systems exhibits a rich behavior. From

the theoretical point of view, interparticle interactions strongly affect the field-dependent SPM properties, demonstrating that the theoretical models usually employed in the literature are unable to describe the interacting conditions. Therefore, further work must be done in order to understand and account for the interacting systems. From the applied MCE-related point of view, a rich experimental frame arises due to the interparticle dipolar coupling that opens the door to optimized magnetocaloric properties, and so it is fundamental to extent this work in order to obtain a complete field-, anisotropy-, and dipolar interaction-dependent characterization of the MCE in assemblies of magnetic nanoparticles. Regarding hyperthermia applications, we have found that the decrease of the heating capacity with increasing interactions reported experimentally is ascribed to the dipolar interparticle coupling, and not other effects as polydispersity and/or anisotropy effects.

Concerning the macroscopic state of nanoparticle systems as determined by interparticle dipolar interactions, we have analyzed the two main features of a SG system, frustration and disorder, that can be found on frozen random anisotropy systems. From the disordered orientation of the magnetic moments a non-saturating state is found at high interacting conditions that reflects the frustrated character of the system. On the Arrott plots at high interacting conditions it is found an inversion on the curvature that reminds the shape of a first order transition. The inversion is found at sample concentrations of the same order of the sample concentrations at which some type of glassy phase at low temperatures has been reported. The general behavior of the isotherms with increasing concentration is to shift to larger temperatures, what accounts for the transition from random anisotropy scenario to a random field case [72].

2.5 Analytical fitting of the ZFC curves

As discussed in Section 1.2 (and seen in the previous sections), ZFC and FC thermomagnetization measurements constitute an advantageous tool for studying the magnetic properties of nanoparticle systems, in view of the valuable information contained in their shapes. It is a cheap and easy to develop technique and as a result many reports are based on using this protocol of magnetic characterization. It calls therefore the attention of both experimentalists and theoreticians the evident requirement of an analytical description, able to account for the detailed shape of these curves, which would constitute a powerful tool for experimental assessment and consequent design of specific applications.

In this regard, low-field susceptibility ZFC/FC curves can be fitted by using a very successful model based on the distribution of particle sizes [77]. The temperature dependence of the magnetization curves is described as the contribution of two susceptibility terms (χ^{SPM} and χ^{BL}), corresponding to the superparamagnetic (SPM) and blocked (BL) state of the nanoparticles. The relative importance of both terms is weighted by the amount of particles in each state with temperature, given as a function of the particle size distribution. This model has been widely used in the literature to fit experimental data with great success [78–81].

In order to improve the accuracy of this model as a tool for inferring information about the magnetic properties of nanoparticle systems, we have revised its meaning and tested it for the simplest case of an ideal monodisperse system. Surprisingly, the model is found to be unable to describe it, what indicates that the information inferred from its fitting must be carefully handled, despite its success to fit experimental data. Does this mean that the model functions worse the more monodisperse the system is? How is it possible however that the fitting works usually so well to fit experimental data?

With the purpose of clarifying the apparent inconsistency, we went through the physical meaning of its mathematical expression in order to figure out how it could be translated to the simple monodisperse case. Along this process we reviewed some basic concepts of the nanoparticles and arrived to the key-point of the fitting equation, the log-normal distribution of particle sizes. The natural size distribution associated to experimental samples can be properly attained from the nanoparticles' characteristic relaxation time, what constitutes an alternative approach to reproduce the typical experimental curves. Thus, this important aspect pretends to highlight the shape of the ZFC curve not arising from the particle size distribution, but from an intrinsic characteristic property of the magnetic nanoparticles such as the relaxation time[3].

Herein we emphasize therefore some details that most common models lack of and can be used to fit ZFC/FC magnetization processes. Outlining an explanation in fitting successfully the experiment will help to improve a more rigorous approach and will call the readers' attention to some aspects frequently forgotten that can lead to incorrect results.

[3]This analysis focuses on the ZFC curve since it gives the most relevant information about the system but analogous reasoning applies to the FC curve.

2.5.1 Polydisperse case and usual approach

The model usually assumed when studying systems of magnetic nanoparticles considers:

- Single-domain particles.
- Coherent rotation of the inner atomic magnetic moments.
- Uniform magnetization proportional to the particle volume, v , so that the magnetic moment per i-particle is given by $|\vec{\mu_i}| = M_S v_i$.
- Effective uniaxial magnetic anisotropy proportional to the particle volume, $\left|\vec{K_i}\right| = K_a v_i$, with K_a the uniaxial anisotropy constant.
- Random orientation of the anisotropy easy axes.
- Temperature-dependent anisotropy and saturation magnetization, $K_a = K_a(T)$ and $M_S = M_S(T)$.
- Log-normal size distribution:

$$f(v) = \frac{1}{\sqrt{2\pi}\sigma v} e^{\frac{-\ln^2\left(\frac{v}{v_0}\right)}{2\sigma^2}} \tag{2.7}$$

  where $v_0 = \int_0^\infty v f(v) dv$ is the average particle volume and σ is the standard deviation.

During a ZFC process the system is first cooled in zero field down to a very low temperature and afterwards the magnetization is measured while heating up the sample under a low magnetic field. As introduced in Section 1.2, the shape of the ZFC curves is on the whole characterized by an initial increase with temperature until the magnetization reaches a maximum and a paramagnetic-like decay immediately afterward. The maximum roughly defines the T_B, which stands for the transition between the SPM state in which the magnetic moments of the particles fluctuate freely with temperature, and the BL state in which the magnetic moments remain "blocked" along a favourable magnetic anisotropy direction.

In order to accurately consider the brought up temperature dependence of the low-field ZFC susceptibility, for systems of particles under the model above described, we can consider the following fitting equation [78]

$$\chi_{ZFC}(T) = \frac{\mu_0 M_S^2(T)}{3\left[k_B T + \frac{\epsilon_D(T)}{v_0} v_0\right]} \int_0^{v_m(T)} v^2 f(v) dv + \frac{\mu_0 M_S^2(T)}{3\left[K_a(T) + \frac{\epsilon_D(T)}{v_0} v_0\right]} \int_{v_m(T)}^{\infty} v f(v) dv \tag{2.8}$$

where the first and second terms account for the SPM and BL contributions, respectively. The term $\epsilon_D(T)$ stands for the effective dipolar interaction energy. The integral limit $v_m(T)$ is the frontier volume between the particles in the SPM state ($v < v_m(T)$) and in the BL one ($v > v_m(T)$) with temperature. This limiting volume is given by

$$v_m(T) = \frac{\ln\left(\frac{t_m}{\tau_0}\right) k_B T}{\left[K_a(T) + \frac{\epsilon_D(T)}{v_0}\right]} \tag{2.9}$$

with t_m the measuring time and τ_0 the characteristic value of the particles. For SQUID measurements both terms are tipically related as

$$\ln\left(\frac{t_m}{\tau_0}\right) \approx 25 \tag{2.10}$$

The fitting equation Eq.(2.8) covers the whole range of temperatures of the ZFC curve by means of the volume distribution $f(v)$ (or particle size distribution), which permits to weight the relative importance of each susceptibility term. The suitability of this equation to fit experimental data was already reported using experimental measurements reproduced in FIGURE 2.21, which shows the exceptional overlapping between the fitting curve (solid line) and the experimental data (open or solid triangles and circles, respectively). This good agreement with the experiment provides, in principle, good proof of its worth as a research tool, prompting us to extract information about the magnetic properties of the system directly from the fit.

However, prior to doing so we shall analyze next how the fitting works when applied to the simple case of a perfectly monodisperse system. There are two main reasons justifying this analysis: on the one hand, checking any analytical expression when applied to simple scenarios is a good way to understand its meaning, properties and limits. On the other hand, although at present experimental techniques do not allow yet the synthesis of entirely controlled sizes of nanoparticle systems and some dispersion degree is always expected, the rapid improvement of the synthesis methods that is taking place in recent years provides steadily improved narrower

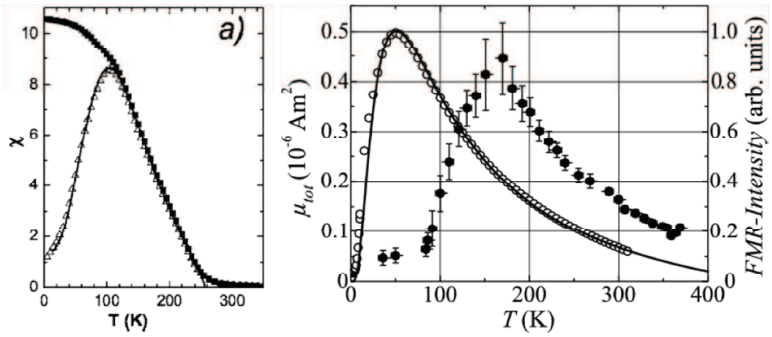

Figure 2.21:
Experimental results fitted using Eq.(2.8) (solid lines). Left panel: temperature dependence of the ZFC and FC susceptibilities of $FePt_3$ nanocubes [78]. Right panel: ZFC measurements of the total magnetic moment of $Fe_{70}Pt30$ nanoparticles (open circles) [79].

size-distributed systems. In view of this it is very feasible to imagine the approach to the ideal monodisperse system in the immediate future, and thereby the worth of analyzing this particular case. The further improvement then relies heavily on how Eq.(2.8) works when applied to the simple monodisperse sample, in order to elucidate and plump for the kind of information that can be obtained from the fitting of the ZFC curves.

2.5.2 Ideal monodisperse case

Aiming to focus in the analysis of the size-dispersion degree, we assume some additional simplifications in order to eliminate dependencies other than the size distribution. To shorten Eq.(2.8) we can consider a much more diluted sample so that interparticle interactions become negligible, i.e. $\epsilon_D(T) \to 0$. In addition we may also consider $T_B << T_C$ and assume that no surface-freezing effects occur, so that K_a and M_S are virtually temperature independent. In this case, Eq.(2.8) simplifies as

$$\chi_{ZFC}(T) = \frac{\mu_0 M_S^2}{3k_B T}\frac{1}{v_0}\int_0^{v_m(T)} v^2 f(v)dv + \frac{\mu_0 M_S^2}{3K_a}\frac{1}{v_0}\int_{v_m(T)}^{\infty} v f(v)dv \qquad (2.11)$$

Eq.(2.11) can also fit an entirely monodisperse system and in such case, there is no coexistence (in temperature) of both susceptibility contributions and instead, the temperature dependence splits into two different susceptibility ranges given by:

$$\chi_{ZFC}(T) = \begin{cases} \frac{\mu_0 M_S^2}{3K_a} & \text{if } T \prec T_B \\ \\ \frac{\mu_0 M_S^2 v_0}{3k_B T} & \text{if } T \geq T_B \end{cases} \tag{2.12}$$

Eq.(2.12) summarizes the simplest description of a SPM system with a low-temperature range where the particle's magnetic moment remain blocked ($T \prec T_B$, temperature-independent BL susceptibility), and a high-temperature range where the particle's magnetic moments behave freely with temperature ($T \geq T_B$, SPM temperature-dependent susceptibility). The relative importance of both susceptibility contributions at $T = T_B$ can be obtained from the well-known relationship

$$T_B = \frac{KV}{k_B} \ln\left(\frac{t_m}{\tau_0}\right) \tag{2.13}$$

and since for typical SQUID measurements $\ln(t_m/\tau_0) \approx 25$ at $T = T_B$, then $\chi_{ZFC}^{spm} \approx 25\chi_{ZFC}^{bl}$ at $T = T_B$.

The related question implies Eq.(2.12) to fit the ZFC curve corresponding to the perfectly monodisperse non-interacting system introduced. In order to obtain such an ideal curve, we have used a Monte Carlo method[4] that allowed us to construct a perfectly controlled system that suits the above mentioned characteristics. The result is shown in FIGURE 2.22.

FIGURE 2.22 reflects the exceptional correspondence between the model described by Eqs.(2.8,2.12) at temperatures well above and well below T_B. However, the theoretical fit is unable to match the ZFC curve, exhibiting a large deviation in the intermediate temperature range (around T_B). One can consequently conclude that Eq.(2.8) is unable to account for the simplest monodisperse-size case.

Taking into account the results included in FIGURE 2.22 and underlining the fact that the fitting equation Eq.(2.8) works only for polydisperse systems, the shape of the ZFC curve that comes from the distribution of particle sizes (log-normal type) would be equivalent in this picture to a continuous distribution of theoretical curves like the one corresponding to Eq.(2.12), but with different transition temperatures.

[4]Simulations were carried out in the same way as in Ref. [13], but considering a larger system of 1000 non-interacting particles. In order to use the simplest possible model, the particles were placed in this case in a simple cubic lattice with their anisotropy easy axes parallel to each other and aligned along the magnetic field direction, in order to avoid distribution of anisotropy energy barriers. One computational improvement included in the present simulations in comparison with those reported in Ref. [13] is that the trial angle $\delta\theta$ is now temperature-dependent, in the way proposed by U. Nowak et al. [15]. The temperature-dependence is given by $\delta\theta = (0.05k_BT/2KV)^{0.5}$ in the usual reduced units, and reproduces the 0.075 value of Ref. [13] approximately at $t = 0.11$. The purpose of including this modification was to set more realistic physical characteristics, reproducing the decrease of thermal fluctuations in the orientation of the magnetic moments with smaller temperatures.

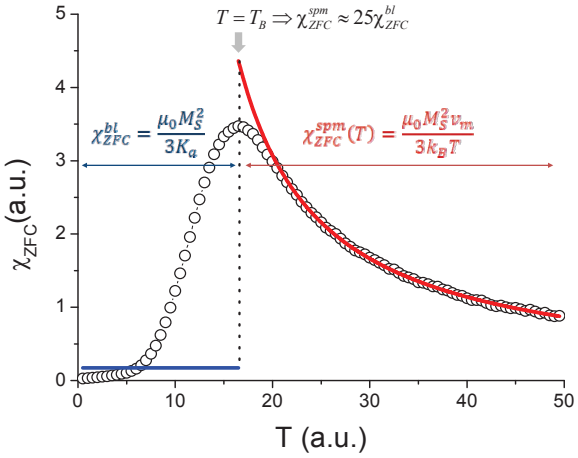

Figure 2.22: Fit (solid lines) obtained using Eq.(2.12) of a typical ZFC curve for a non-interacting monodisperse system (open symbols). Vertical grey arrow (and dotted line) indicates the transition temperature T_B at which $\chi_{ZFC}^{spm} \approx 25\chi_{ZFC}^{bl}$.

However, this reasoning is misleading since the shape of the ZFC curve does not arise from the size distribution, but from a temperature-dependent probability of the particles to reverse the magnetization direction. This probability originates its characteristic shape, which can be *altered* (but not generated) as well by means of a distribution of physical parameters like anisotropy or size. FIGURE 2.22 illustrates in fact our arguments on the magnetization reversal probability as the origin of the characteristic shape of ZFC curve: the physical model assumed for the Monte Carlo data is not only non-interacting and monodisperse but also the particles are totally equivalent to each other (all of them have parallel easy axes along the field direction). Outstandingly, its shape reproduces typical ZFC curves attributes found experimentally, supporting therefore our arguments about the shape of the curves not arising from any distribution of the particles' physical characteristics. Considering the above reasoning, it seems feasible to fit that shape without any nanoparticles size distribution as used in Eq.(2.8). However, we cannot ignore that Eq.(2.8) works very well for fitting experimental results (see FIGURE 2.21), what in fact indicates that its mathematical expression is certainly very good.

In order to shed light about why Eq.(2.8) fits so well the experimental results, we can rewrite it using the same mathematical expression but with a different interpretation of the theoretical terms used. In this sense we shall review its physical meaning and some basic properties of particles, in an effort to understand this paradigmatic situation. It is important at this point, however, to emphasize the main purpose of the present work as achieved, in terms of the discussion about fitting the perfectly monodisperse case and the limits regarding the use of Eq.(2.8). One step further attempts to understand the brought up system in order to figure out an explanation of the nice agreement between model and experiment.

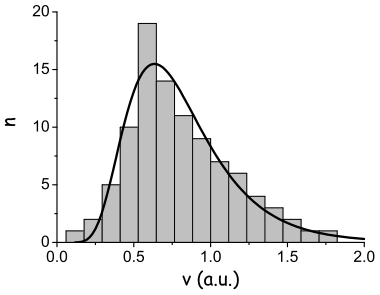

Figure 2.23:
Example of a log-normal particle size distribution.

2.5.3 Alternative approach

There are key-points subjacent to Eq.(2.8) in terms of; i) there is a direct relationship between size and temperature, and ii) the relative importance of each susceptibility term as a function of temperature, correctly introduced by means of a log-normal size distribution. Temperature is introduced by means of the limiting volume $v_m(T)$, and the size distribution weights the relative importance of each susceptibility term, SPM or BL, by summing up the amount of particles in each state. An example of a log-normal distribution is shown in FIGURE 2.23.

FIGURE 2.23 illustrates the behaviour of a ZFC process as a function of temperature, as discussed above, but in terms of the volume of the particles: at low temperatures the limiting volume is small and so only a few particles are in the SPM state, while most of them remain blocked; with increasing temperature -equivalent in the model to larger volume- the fraction of particles entering the SPM state grows, and the SPM term becomes the dominant susceptibility contribution in the high temperature range. In order to simulate this behavior the objective comprises a log-normal distribution for the fraction of particles that enters the SPM state with temperature, $f(T)$, but without the need of having any distribution of particle sizes.

This $f(T)$ can be directly described from the basic properties of the particles. Thus, following the SPM model, the period of time one particle needs to reverse its magnetization around the energy minima is given by $\tau = \tau_0 \exp(E_B/k_B T)$, with E_B the anisotropy energy barrier. Thus, the probability of the particle to reverse its magnetization direction as a function of the temperature is given by

$$p(T) = \tau^{-1} = \tau_0^{-1} e^{\left(\frac{-E_B}{k_B T}\right)} \tag{2.14}$$

For a system of identical particles without any interaction, this probability is the same for all particles and therefore, the slope of this curve contains information about the fraction of particles that reverses its magnetization with temperature.

This picture is illustrated in the left panel of FIGURE 2.24: at very low temperatures there is almost no variation in the slope, indicating that most of the particles remain blocked; with increasing T this slope rapidly grows, what is equivalent to a higher amount of particles reaching the SPM state; and finally, at very high T the slope tends to a very small value, indicating that most of the particles are already in the SPM state. Following the previous arguments, we may interpret the distribution of particles that reverse its magnetization at a certain temperature *T-reversal*, T_r, as a function of the variation rate of the reversal probability as

$$f(T_r) = \frac{dp(T)}{dT} \equiv \frac{T_B}{T_r^2} e^{\frac{-T_B}{T_r}} \tag{2.15}$$

where $T_B = \langle T_r \rangle$. Eq.(2.15) is hence equivalent to the distribution function of reversal mechanisms with temperature. To evaluate its suitability as a distribution function alternative to $f(v)$ we fit it to a log-normal function. The results are shown in FIGURE 2.24.

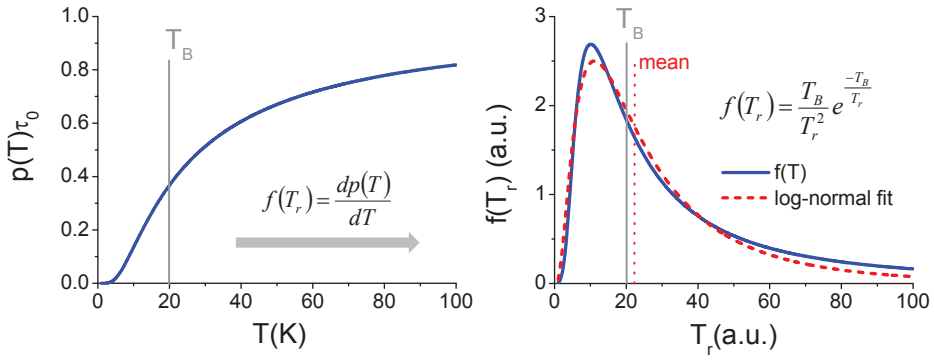

Figure 2.24:
Left panel: magnetization reversal probability (times τ_0); vertical line indicates T_B. Right panel: solid (blue) curve is the distribution function of particles reaching the SPM state with temperature (T_B is indicated by the vertical solid line). Dashed (red) curve is the corresponding log-normal fit, with the dotted vertical line indicating the mean value.

As we observe from FIGURE 2.24, the characteristic log-normal shape found in Eq.(2.8) can be closely obtained directly from the basic properties of the particles. Although this result does not provide an immediate alternative to equation Eq.(2.8) and further work has to be undertaken, it may become very helpful for understanding its success to reproduce the typical ZFC shape. From FIGURE 2.24 we interpret the ZFC process for a non-interacting monodisperse system as a chain of successive events (particles reaching the SPM state with increasing temperature), being those distributed in a log-normal fashion. This result may explain why the usual

log-normal distribution function considered in Eq.(2.8) works so well for fitting experimental results, since it agrees nicely with the basic properties of the particle system. Following the above arguments, describing a fitting equation as an alternative to the monodisperse case of Eq.(2.11) directly comes up, as it would be given by

$$\chi_{ZFC}(T) = C\left[\int_0^T T_r^2 f(T_r)dT_r + \int_T^\infty T_r f(T_r)dT_r\right], \tag{2.16}$$

with $C = \mu_0 M_S^2/3k_BT$. We hope that these results and reasoning may provide a useful insight for understanding the behaviour of such nanoparticle systems, and may contribute to the the design of a more general analytical model accounting for the shape of the ZFC/FC curves.

Conclusions The use of analytical models based on size-polydispersity distribution functions to deal with magnetic nanoparticle systems must be carefully handled, for such expressions have difficulties to described well dispersed systems and therefore, might lead to incorrect information about the systems. Such models, however, show an extraordinary potentiality to fit experimental data, what indicates its mathematical suitability. In an effort to understand their effectiveness, which key is based on the log-normal size polydispersity distribution function, and trying to search for the reason for their good functioning, we have revised the basic properties of single-domain SPM nanoparticles. Interestingly, we observe that a rough one-well anisotropy model provides a distribution function very close to a log-normal, what provides an interesting research line to develop more formal analytical models.

However, this alternative approach, in which the log-normal size distribution is substituted by a distribution function arisen from the SPM decaying-rate, remains still to be developed and other alternatives might be more useful. For example, a promising research line to obtain $f(T_r)$ can be based on the method proposed by M. Knobel et al. [9], who obtain information about the energy barrier distribution from the $d(M_{FC} - M_{ZFC})/dT$ *vs* T curve. We interpret, however, the $f(T_r) = d(M_{FC} - M_{ZFC})/dT$ function in a different way than in Ref. [9], where they consider a size-distributed sample. Our interpretation considers that *the* $f(T_r)$ *curve provides an inmediate description of the amount of particles entering the SPM state with temperature*. In FIGURE 2.25 it is shown the $f(T_r) = d(M_{FC} - M_{ZFC})/dT$ curve for the ideally-monodisperse system.

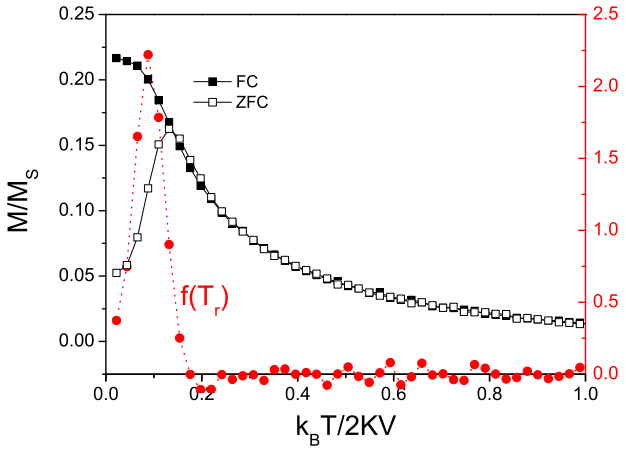

Figure 2.25: Typical ZFC/FC curves and $f(T_r)$ obtained as $f(T_r) = d(M_{FC} - M_{ZFC})/dT$.

In FIGURE 2.25 we observe the direct correlation between the information contained in the shape of the ZFC curves and that directly provided by $f(T_r)$: starting at very low temperatures, the amount of particles reaching the SPM state rapidly grows with temperature, the largest fraction occurring below T_B; after that peak, the amount of still blocked particles is low and therefore the jumping to the SPM state decreases, and practically all particles are SPM slightly above T_B.

3

A general scaling parameter for the magnetic dipolar interaction

This chapter focuses on the role played by the magnetic dipolar interactions of a SPM nanoparticle system in its magnetic response. The main idea stems from the fact that the influence of the dipolar interactions, given by sample concentration, can be better described if normalized by the related parameter $c_0 = \frac{2K}{M_S^2}$. The influence of the dipolar interactions as normalized by c_0 works so analogously to the influence of the applied magnetic field H as normalized by H_A. Thus, this chapter will focus on establishing a ***general scaling law for the magnetic dipolar interactions***.

The study of the role played by magnetic dipolar interaction on T_B has been the subject of intense investigation for several years due to its importance for technological applications, but despite the big effort devoted there is still lack of a theory able to give a general description of the different (often contradictory) behaviors reported. Usually, theoretical models consider a monotonic evolution of T_B as a function of the concentration, interpreting such evolution from the variation of the single-particle anisotropy barrier as modified by interparticle interactions; however, such models cannot account for the different experimental trends observed.

Let us try to gain a new perspective into the problem. For such a purpose, our first step is to check the experimentally reported non-monotonic behaviour, what would confirm the need to develop models able to account for non-monotonic tendencies. To do so, we have analyzed the evolution of T_B as a function of c for a system of magnetic nanoparticles (maghemite-like) for which a non-monotonic behavior had been reported. In order to focus on the role of dipolar interactions and neglect other effects as aggregation or polydispersity, we have used Monte Carlo simulations that provided us a well-controlled system. We confirmed the existence of a non-monotonic $T_B(c)$ behavior.

With this in mind and taking into account other results reported in the literature, our next step was to figure out how is it possible that $T_B(c)$ follows completely different trends for *a priori* very similar samples (considering the particles as governed mainly by the same energies: E_A, E_Z, and E_D). Interestingly, working with the energetic description we have found that it is possible to rewrite the total energy of the system in reduced units such that the strength of the magnetic dipolar interactions is directly proportional to c/c_0 in the same way as the influence of the magnetic field is normalized as H/H_A. This is to say, *we predict the existence of a general $T_B(c/c_0)$ curve for interacting systems analogous to the $T_B(H/H_A)$ curve of non-interacting ones.* In order to check this prediction we performed MC simulations for various types of particles accounting for different $T_B(c)$ trends reported in the literature. Our results, which reproduce the different experimental trends, collapse to the same curve if normalizing c by c_0, demonstrating the success of the c_0 value as a normalizing parameter for the magnetic dipolar interaction. The suitability of the c_0 parameter to described the influence of dipolar interactions was also analyzed by means of hysteresis properties, which also collapse in the same curve if normalizing the concentration by c_0

Once we have confirmed the good functioning of c_0 as a normalizing parameter for the dipolar interactions, we have next analyzed the specific shape of the $T_B(c/c_0)$ curve, finding the existence of three different interacting regimes: a low-concentrations non-interacting (or even decreasing) one, followed by a monotonically growing intermediate-concentrations range, to finally end by a tendency to saturate at high concentrations. To understand the existence of such regimes we have analyzed the system from a microscopic perspective, and arrived to the idea that such different regimes might arise from the different ratios between applied field H and dipolar field H_D, and by the amount of particles being parallel or antiparallel to H as influenced by the neighbour particles, which try to align them antiparallel. To confirm such hypothesis, we propose a simple fitting equation based on the amount of particles being parallel and antiparallel to H and the different energy barrier of each population. We have found that such approach becomes in contradiction with theoretical properties of the nanoparticle system, despite the remarkable good agreement of the fitting equation and the $t_B(c)$ data.

This result can therefore be interpreted as supporting our arguments about the magnetic properties of the system as described by the two different populations, despite the simple model we figure out is not correct. In order to confirm this interpretation, our next step was to perform a detailed analysis of the dipolar field histograms, finding that the population splits in rather well differentiated peaks at

low temperatures, and that such peaks occur at larger fields for larger interacting conditions. The population of each peak is quite similar, confirming our arguments on the necessity of taking into account the parallel and antiparallel populations of the sample in order to design a general theory for the influence of the dipolar interactions on the magnetic properties of the system. Unfortunately, due to time constraints we could not extend further this analysis, which undoubtedly constitutes the core of a promising future work.

Finally, we report the study about the suitability of the c_0 parameter for other purposes than purely theoretical ones, focusing on MCE-related purposes. Our results indicate that the c_0 parameter is very useful for the design of the most appropriate magnetic material for magnetocaloric-related applications.

3.1 Non-monotonic behaviour

Here we describe the effect of the magnetic dipolar interaction in the evolution of the ZFC-FC curves and T_B of a monodisperse system of maghemite-like SPM nanoparticles. The anisotropy energy (responsible for the existence of T_B) is for these particles rather low, and so the system is very sensitive to variations of the dipolar energy. The purpose of this work is to confirm the non-monotonic $T_B = T_B(c)$ dependence found experimentally to be of dipolar interaction origin.

3.1.1 Critical concentration c^*

We have studied the influence of the magnetic dipolar interaction on the SPM properties of the system by analyzing its influence on T_B, roughly evaluated as the temperature at which the ZFC curve exhibits a maximum. The strength of the dipolar interaction is introduced as proportional to the sample concentration c. For a monodisperse particle assembly the equation relating the dipolar energy E_D (see Eq.(2.1)) and c can be rewritten as

$$E_D^{(i,j)} = \frac{1}{2}\sum_{j\neq i}^{N}\left(\frac{\vec{\mu}_i\cdot\vec{\mu}_j}{r_{ij}^3} - 3\frac{(\vec{\mu}_i\cdot\vec{r}_{ij})(\vec{\mu}_j\cdot\vec{r}_{ij})}{r_{ij}^5}\right) \tag{3.1}$$

where $g = \frac{c}{c_0}\frac{KV}{N}$ characterizes the strength of the dipolar interaction. As introduced in Section 1.2, the unitless sample concentration c is the ratio between the total volume occupied by the particles and the volume of the sample, and $c_0 = \frac{2K}{M_S^2}$ is a dimensionless constant that characterizes the material [82]. The unit vector $\hat{e}_{\mu_i}$ stands for the direction of the magnetic moment $\vec{\mu}_i$ of the particle i, and the reduced distance $\vec{a}_{ij}$ is defined as $\vec{a}_{ij} = \vec{r}_{ij}/L$, the distance between the particles i

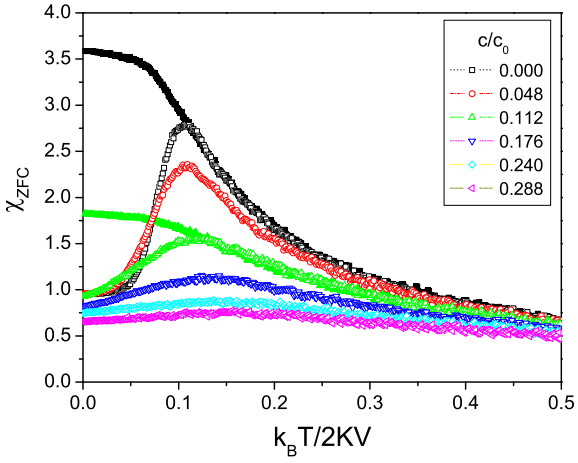

Figure 3.1: ZFC curves (empty symbols) of some representative samples. Two FC curves (full symbols) are shown, corresponding to the non-interacting case ($c/c_0 = 0.000$) and to $c/c_0 = 0.112$.

and j divided by the size of the cubic box that contains the sample. The results obtained from our simulations are presented in reduced units directly related to the real ones, i.e. the same that the reduced temperature is given in $t = k_BT/2KV$ units (normalized by KV), also the reduced sample concentration is given by c/c_0 units.

We studied the influence of the dipolar interaction on T_B by simulating ZFC processes at different sample concentrations, ranging from the non-interacting diluted limit $c/c_0 = 0.000$, to very dense samples $c/c_0 \leq 0.320$ (see Ref. [83] for computational details). The reduced susceptibility is defined as $\chi = m/h$. To vary the interactions strength, we systematically vary c (for a constant c_0 value[1]) to evaluate t_B as a function of the dipolar interaction energy. Some representative ZFC susceptibility curves of the dispersions of magnetic nanoparticles at different sample concentrations are shown in FIGURE 3.1, where also the FC curves of two different interacting conditions ($c/c_0 = 0.000$ and $c/c_0 = 0.112$) are included to illustrate the reliability of the code. The applied magnetic field was $h = H/H_A = 0.1$. This small value of the magnetic field was selected to not disturbing the intrinsic SPM behavior of the system as influenced by interparticle interactions. Large fields could mask this effect (as seen in Section2.4).

The numerical simulations of the ZFC/FC processes displayed in FIGURE 3.1

[1]To give an estimation in real units, for example for the $7nm$ diameter maghemite nanoparticles reported by Jonsson et al. [Phys. Rev. Lett. 75, 4138 (1995)], the characteristic values are $K = 1.9 * 105erg/cm3$ and $Ms = 420emu/cm3$, what for our simulations results to be an effective magnetic field $H \approx 90Oe$, a temperature variation ratio of $0.3K$ every 200 MC steps, and the critical concentration to be $c^* = 0.10$.

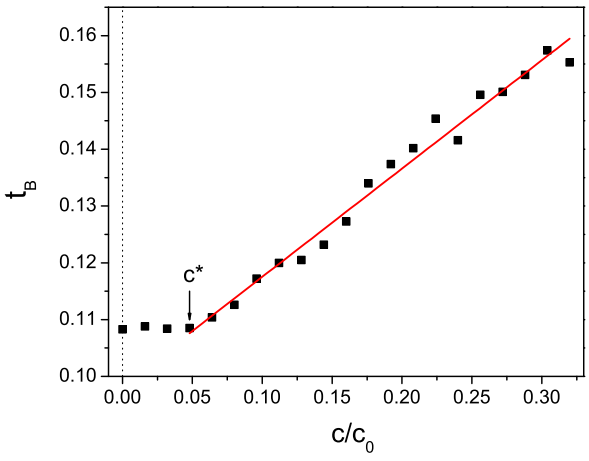

Figure 3.2: Detailed t_B *vs* c/c_0 curve. The solid line is a fitting to the modified single particle approach (see section3.1.5). The arrow stands for c^*.

show a good agreement with the general trend of experimental results on SPM particles [46, 54]. The ZFC curves exhibit a maximum at t_B that marks the transition to the SPM regime. Above t_B it is observed the superposition of the FC with the ZFC curves that stands for the reversible character of the SPM behavior. Below t_B, in the irreversible temperature range, the FC curve separates from the ZFC. We also see in FIGURE 3.1 an increase of t_B as the concentration increases, in agreement with the results reported in experimental [46] and theoretical works [13]. We systematically varied c to obtain t_B as a function of the dipolar interactions strengh; the detailed t_B *vs* c/c_0 dependence extracted from a complete set of measurements is summarized in FIGURE 3.2.

From FIGURE 3.2, we observe a non-monotonic dependence of t_B on sample concentration: there is a clear change of the slope from an independent t_B at low concentrations to a rapid increase at high concentrations. These different features suggest the presence of two different physical behaviors, an essentially non-interacting regime at low concentrations and an interacting regime at high values of c/c_0. The crossover between both regimes is marked by a particular concentration, estimated to be $c^*/c_0 \approx 0.05$. In the next sections, we show some tests we have done to analyze the characteristics of the observed two-regime feature.

3.1.2 Time dependence

As the SPM t_B is highly time-dependent [84], we have simulated the processes used to obtain the data shown in FIGURE 3.2, at different time intervals (different MC steps) in order to rule out the existence of the two regimes to be a time-dependent effect. We maintained the same cooling/heating temperature steps, and varied the

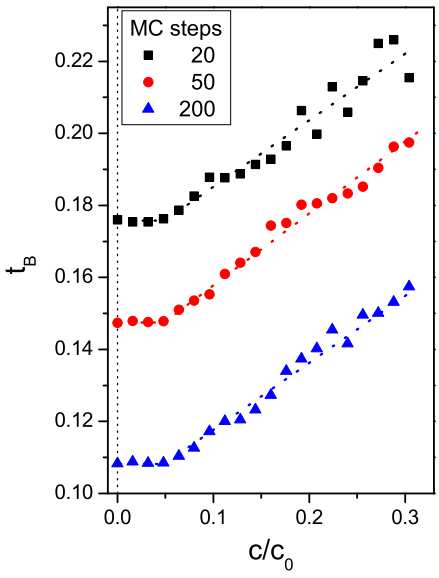

Figure 3.3:
t_B *vs* c/c_0 for different simulation times (MC steps). The dotted lines are guides to the eye.

simulated MC intervals as 20 and 50 MC steps. The results are shown in FIGURE 3.3, together with the 200 MC steps case of FIGURE 3.2 for the comparison.

Seemingly, the overall tendency is the same for the different measuring times: at low concentrations t_B remains basically constant, suggesting the particles to behave independently of each other as a non-interacting system; at higher concentrations t_B increases continuously with the concentration. Hence, we have confirmed that the evolution of t_B with c/c_0 is robust for different time intervals.

3.1.3 Maxima at t_B

To test the existence of the two different regimes we have also analyzed the relative values of the susceptibility at the maximum of the ZFC curves, $\chi(t_B)$, as a function of concentration. This study constitutes a more precise approach than the analysis of t_B based on the higher accuracy found on its determination (see FIGURE 3.1). As the overall observed trend results equal for the different MC step intervals we have focused our study on the 200 MC step case because the simulated ZFC processes show a better definition after more MC relaxation steps. The obtained results are shown in FIGURE 3.4.

The $\chi(t_B)$ *vs* c/c_0 curve exhibits an inflexion at low concentrations, as observed in its first derivative (see inset of FIGURE 3.4): an unambiguous minimum appears in $\chi'(t_B) = \partial\chi/\partial(c/c_0)$ at the same reduced sample concentration value $c^*/c_0 \approx 0.05$ observed in FIGURE 3.2. This inflexion in the $\chi(t_B)$ *vs* c/c_0 curve is related to a

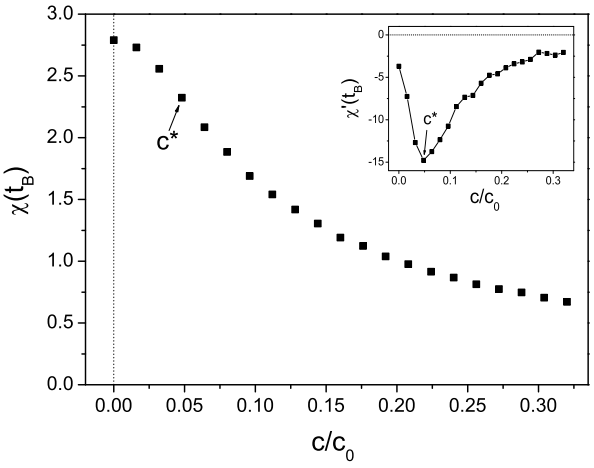

Figure 3.4:
Reduced susceptibility at the maximum of the ZFC curves, $\chi(t_B)$, for the different interacting conditions considered. Inset shows the first derivative at the maximum of the ZFC curves, $\chi'(t_B) = \partial\chi/\partial(c/c_0)$, as a function of c/c_0.

change in the magnetic behavior, and supports the existence of two intrinsic regimes of different magnetic behavior in a system of SPM nanoparticles being influenced by the dipolar interaction.

3.1.4 Comparison with the experiment

We report now experimental results extracted from the literature for similar systems but different particle sizes in order to analyze the size-dependence of the trend reported. A similar low-concentration behavior as that shown in FIGURE 3.2 has been observed for highly diluted samples of a frozen ferrofluid of maghemite NPs of $7nm$ diameter [85]. The existence of a defined interparticle spacing separating two different regimes on the evolution of T_B has been reported for iron oxide nanoparticles of $5.4nm$ diameter [86]. With the purpose of probing the generality of the observed behavior, we reproduce in FIGURE 3.5 our results [31] on the evolution of T_B with the sample concentration for a system of magnetic nanoparticles of smaller diameter ($3.5nm$) than those reported in Refs. [85] and [86].

In FIGURE 3.5, we show two cases of different aggregation level of the same system: a well dispersed sample (full circles, left bottom TEM micrograph), and a highly aggregated one (empty squares, left top TEM micrograph) (see Ref. [31] for further details). The presence of a non-interacting regime at low concentrations can be observed in these systems only in the well-dispersed sample (full circles). Presence of clustering (empty squares) clearly affects the shape of the curve and hampers the observation of this regime [31]. These results show that the existence of two different interacting regimes is an intrinsic property of maghemite-like nanoparticles without aggregation, and that is independent of the particle size.

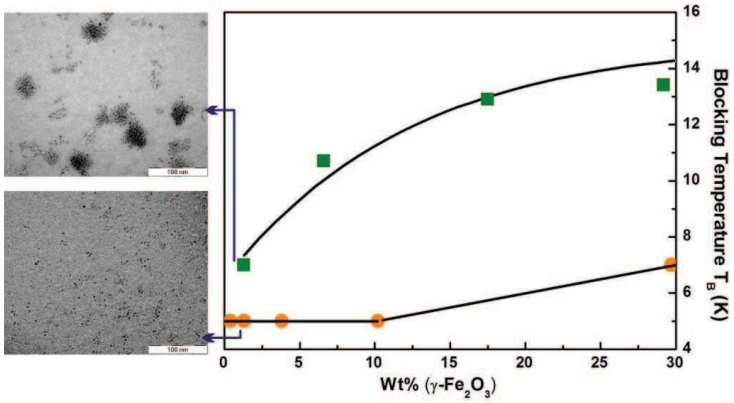

Figure 3.5:
T_B *vs* sample concentration for $\gamma - Fe_2O_3$ nanoparticles with different aggregation level: a well dispersed sample (open squares) and a highly aggregated one (full circles). The lines serve only to guide the eye. TEM micrographs show the dispersion of the particles for the well dispersed sample (bottom) and for the aggregated one (top) for the same concentration of particles, $1.3wt\%$ of $\gamma - Fe_2O_3$. Particle synthesis and experimental measurements were made by Prof. C.E. Hoppe (University of Mar del Plata and National Research Council, Argentina).

3.1.5 Fitting to classical models

Different models have been developed with the purpose to take into account the effect of interparticle interactions on the behavior of the magnetic nanoparticle assemblies. The first attempts were based on modifications of the SPM single-particle's model by Néel [10]. In such treatment the interactions among the particles are introduced as changes of the height of the energy barrier, where the different energetic terms add to the anisotropy one. It results in an increment of the thermal activation energy necessary to reach the superparamagnetic state [4]. Recently, Nunes et al. [54] have proposed a modification of the Random Anisotropy Model (RAM) that takes into account the concentration and size of the nanoparticles, as well as the field dependence of the correlation length. We have used both models to fit our results, with the purpose of having one more test to check our arguments. The fitting to both approaches is shown in FIGURE 3.6.

In FIGURE 3.6(A) the fitting of the whole-range data (the two regimes) is included, while in FIGURE 3.6(B) only the interacting regime ($c \geq c^*$) data is fitted. The (green) dashed lines correspond to the modified single particle approach, and the (red) dotted lines correspond to the modification of the RAM. The square of the correlation coefficient (R^2) is shown in the two fittings for both models. It is clearly

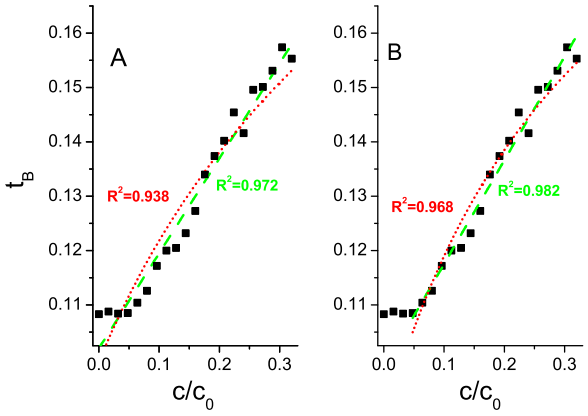

Figure 3.6: Fitting of the t_B *vs* c/c_0 curve to the modified single particle approach (dashed green lines) and the modified RAM approach (red dotted lines). In FIGURE 3.6(A) the whole range of values is fitted, while in FIGURE 3.6(B) only the data corresponding to the interacting regime is included in the fitting.

observed that the fitting gives very satisfactory results in the interacting range and deviates completely from the expectations at low concentration, since it improves the R^2 value for both approaches. This result in fact gives an additional support to our arguments of the existence of two different regimes of behavior of the blocking temperature as a function of the dipolar interaction.

3.1.6 Additional MC simulations

In order to assure the independency of the reported results on the system size, we have simulated the evolution of t_B *vs* c/c_0 by using a much larger system, of 1000 particles. Due to computational constraints with this large system size, the temperature variation ratio had to be enlarged and the results averaged over smaller configurations (see Ref. [83] for details). We have concentrated on the values around c^*, aiming to focus on the two-regime threshold feature. The values of t_B, $\chi(t_B)$, and $\chi^{'}(t_B)$ were evaluated, and the results are shown in FIGURE 3.7.

The results plotted in FIGURE 3.7 indicate that the existence of the two-regime feature discussed in the previous subsections is also observed with the 1000 particles' system and the different temperature interval variation. This demonstrates that the two-regime feature discussed on the previous subsections is independent of the system size used for the simulation. The number of particles considered initially ($N = 125$) is hence appropriate to study the influence of dipolar interaction on such nanoparticles samples.

Conclusions Our results demonstrate the existence of a critical concentration c^* that marks the transition between two different regimes in the evolution of T_B with interparticle interactions. At low concentrations ($c < c^*$), the particles behave

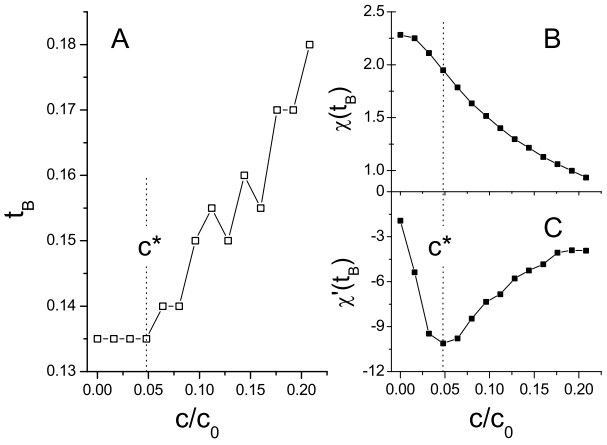

Figure 3.7:
t_B *vs* c/c_0 for the $N = 1000$ sample is shown in FIGURE 3.7(A), and the corresponding $\chi(t_B)$ and $\chi^{'}(t_B)$ values are plotted in FIGURE 3.7(B) and FIGURE 3.7(C), respectively. Vertical dotted lines indicates the concentration c* extracted from FIGURE 3.2 and FIGURE 3.4.

as an ideal non-interacting system with a constant T_B. At concentrations $c > c^*$, the dipolar energy enhances the anisotropic energy barrier and T_B increases with increasing c so that a larger temperature is required to reach the SPM state. The fitting of our results with classical particle models and experiments supports the existence of two differentiated regimes, which cannot be interpreted nor predicted by usual SPM theories. Therefore, it is necessary to further improve the theoretical approaches in order to account for non-monotonic behavior of the nanoparticle system as influenced by magnetic dipolar interactions.

3.2 Normalizing parameter $c_0 = \frac{2K}{M_S^2}$

Theoretical approaches aiming to take into account dipolar interparticle interactions are mainly based on modifications of the Neel theory (dipolar energy treated as an additional term in the energy barrier [52]) or on the random anisotropy model of amorphous ferromagnets [54]. Such approaches, however providing good results for many results in which an increase of T_B with c is reported [46, 87], predict monotonic dependencies of $T_B(c)$ and therefore cannot give a general description of experimental data, which often reports completely different tendencies (for example the non-monotonic dependence reported in the previous section, but also a completely opposite decreasing tendency [88]). Such discrepancy points out the necessity to have a different and more general approach to the underlying theoretical problem.

To tackle the problem from a wider point of view it is necessary to identify which are key parameters ruling the behaviour of the nanoparticles, in order to find

a relationship between the characteristics of the system and the behaviour observed. In general, there are three main different tendencies reported in the literature for the evolution of T_B with dipolar interaction strenght: i) practically constant range at low concentrations [86, 89], ii) regularly increasing at intermediate ranges [90], and tendency to saturate at higher concentrations [91]. So, the open question corresponds to what determines the different shapes of $T_B = T_B(c)$ observed. Other questions that can come up are the following; how is it possible that T_B exhibits a non-monotonic behaviour for constant variations of the sample concentration, which we would expect to have a progressive (and monotonic) influence? What originates those changes in the tendency?

Keeping these questions in mind, and with the purpose to have a general approach to the problem, we have revised the energetic frame of such nanoparticles assemblies, seeking for some clues giving a general scenario of the possible magnetic behaviours (it is clear, for example, that for low anisotropy conditions the dipolar interaction will be more relevant, and opposite for very high anisotropy). We have found that if appropriately rewriting the energy terms, it is possible to associate the dipolar coupling strength with c/c_0 (Section 3.2.1), what provides a scaling factor for the influence of interparticle interactions. In order to check our reasonings, we have simulated several ZFC processes accounting for different c_0 values and analyzed $t_B = t_B(c)$, obtaining that all curves collapse to the same one if normalized by c_0 (Section 3.2.2), and additional confirmation of our arguments was obtained when plotting $m(t_B)$ *vs* c/c_0, with also all curves overlapping in the same general one (Section 3.2.3). Complementary, we have also tested the suitability of the c_0 parameter to normalize interparticle dipolar interactions by means of an alternative approach (different from that based on the maxima of the ZFC curves), based on the analysis of the area of the $M(H)$ curves as a function of the dipolar interactions. The results show also an overlapping of the *area vs* c/c_0 curves, reinforce the general character of the c_0 parameter as a scaling factor (Section 3.2.4).

3.2.1 Energetic approach: c/c_0 scaling

[2]In a first approach, SPM nanoparticles are well described by their magnetic moment and anisotropy (which we consider uniaxial for simplicity). Both parameters determine their properties, being more relevant their relative importance than their absolute values. This is very well appointed in the evolution of T_B as a function of the external magnetic field H. If we consider that the only energies governing the

[2]In this section we will repeat, for making the comprehension of the writing more easier to follow, some equations already discussed in previous sections.

magnetic response of the system are Zeeman and anisotropy, then the energy per particle is

$$E_i = -KV_i \left(\frac{\vec{\mu}_i \cdot \hat{n}_i}{|\vec{\mu}_i|} \right)^2 - \vec{\mu}_i \cdot \vec{H} \tag{3.2}$$

For the ideal case in which the magnetic field is applied parallel to the anisotropy easy axis, we have for typical SQUID measurements [48]

$$T_B(H) = \frac{KV}{25k_B} \left[1 - \left(\frac{H}{H_A} \right) \right]^{\frac{3}{2}} \tag{3.2}$$

Eq.(3.2.1) illustrates how the influence of the magnetic field H on the particle system does not depend only on the absolute H-value, but instead on the ratio H/H_A. Thus, particles with different values of K and M_S may exhibit the same $T_B(H)$ behaviour depending on the relative value H_A. As seen in SECTION 1.2, this result is a direct consequence of rewriting the energy of a non-interacting system in terms of (H/H_A); analogously, the same procedure and reasoning can now be applied to study the dipolar interaction energy. Adding the dipolar energy term to Eq.(3.2), the expression of the total energy for a system of N-particles becomes:

$$\begin{aligned} E_T = \sum_{i=1}^{N} E_i = \sum_{i=1}^{N} \Bigg[& -KV \left(\frac{\vec{\mu}_i \cdot \hat{n}_i}{|\vec{\mu}_i|} \right)^2 - \vec{\mu}_i \cdot \vec{H} \\ & + \frac{1}{2} \sum_{j \neq i}^{N} \left(\frac{\vec{\mu}_i \cdot \vec{\mu}_j}{r_{ij}^3} - 3 \frac{(\vec{\mu}_i \cdot \vec{r}_{ij})(\vec{\mu}_j \cdot \vec{r}_{ij})}{r_{ij}^5} \right) \Bigg] \end{aligned} \tag{3.2}$$

To simplify Eq.(3.3) we can take into account the assumed monodispersity condition and that the magnetization of the particles is proportional to their volume, $\vec{\mu}_i = M_S V \hat{e}_{\mu_i}$, with $\hat{e}_{\mu_i}$ the unitary vector along the magnetic moment direction of particle i. Then, relating the interparticle distances $\vec{r}_{ij}$ with the (volume) sample concentration as $\vec{a}_{ij} = \vec{r}_{ij}/L$ (defining L as the side of the cubic box containing all particles), we can rewrite Eq.(3.3) so that the energy per particle E_i is now given by:

$$\begin{aligned} E_i = \quad & -KV \cos^2 \varphi - M_S V H \cos\theta \\ & + \tfrac{1}{2} \tfrac{M_S^2 V^2}{L^3} \textstyle\sum_{j \neq i}^{N} \left(\frac{\hat{e}_{\mu_i} \cdot \hat{e}_{\mu_j}}{a_{ij}^3} - 3 \quad \frac{(\hat{e}_{\mu_i} \cdot \hat{a}_{ij})(\hat{e}_{\mu_j} \cdot \hat{a}_{ij})}{a_{ij}^5} \right) \end{aligned} \tag{3.2}$$

where φ is the angle between magnetic moment and easy anisotropy axis of the i-particle. Dividing Eq.(3.3) by 2KV permits to simplify it to obtain the reduced energy per particle $e_i = E_i/2KV$ (analogous to the reduced temperature units $t = k_BT/2KV$). Also, using $H_A = 2K/M_S$ Eq.(3.3) can be rewritten as a function of the parameter H/H_A, which, in the form underlined in Eq.(3.2.1), is the one that accounts for the field dependence of T_B:

$$\begin{aligned} e_i = \quad & -\tfrac{1}{2}\cos^2\varphi - \tfrac{H}{H_A}\cos\theta \\ & +\tfrac{1}{2}\tfrac{M_S^2 V}{2KL^3}\sum_{j\neq i}^{N}\left(\frac{\hat{e}_{\mu_i}\cdot\hat{e}_{\mu_j}}{a_{ij}^3} \quad -3\frac{(\hat{e}_{\mu_i}\cdot\hat{a}_{ij})(\hat{e}_{\mu_j}\cdot\hat{a}_{ij})}{a_{ij}^5}\right) \end{aligned} \tag{3.2}$$

We can rewrite the above Eq.(3.3) in terms of the volume sample concentration, c, defined as the fraction between the volume of the particles and the box containing them, i.e. $c = \sum_i V_i/L^3$. Since we assumed a monodisperse system we have $c = NV/L^3$, and so Eq.(3.3) reads now

$$\begin{aligned} e_i = \quad & -\tfrac{1}{2}\cos^2\varphi - \tfrac{H}{H_A}\cos\theta \\ & +\tfrac{1}{2}\tfrac{M_S^2 c}{2KN}\sum_{j\neq i}^{N}\left(\frac{\hat{e}_{\mu_i}\cdot\hat{e}_{\mu_j}}{a_{ij}^3} \quad -3\frac{(\hat{e}_{\mu_i}\cdot\hat{a}_{ij})(\hat{e}_{\mu_j}\cdot\hat{a}_{ij})}{a_{ij}^5}\right) \end{aligned} \tag{3.2}$$

From Eq.(3.3) we can define the unitless parameter $c_0 = \frac{2K}{M_S^2}$, and so we have:

$$\begin{aligned} e_i = \quad & -\tfrac{1}{2}\cos^2\varphi - \tfrac{H}{H_A}\cos\theta \\ & +\tfrac{1}{2N}\tfrac{c}{c_0}\sum_{j\neq i}^{N}\left(\frac{\hat{e}_{\mu_i}\cdot\hat{e}_{\mu_j}}{a_{ij}^3} \quad -3\frac{(\hat{e}_{\mu_i}\cdot\hat{a}_{ij})(\hat{e}_{\mu_j}\cdot\hat{a}_{ij})}{a_{ij}^5}\right) \end{aligned} \tag{3.2}$$

Thus, same that H/H_A provides a general behaviour for the evolution of the system as a function of the magnetic field, independently of the characteristics of the particles K and M_S, there will also be a general behaviour for the dipolar interaction independently of the characteristics of the particles. In this case, the general behaviour is introduced by the normalizing c_0-parameter, demonstrating the existence of an inner scale of energies in the thermomagnetic properties of those nanostructured systems. We can expect therefore a general relationship $T_B(c/c_0)$ for different types of particles (as described by means of its characteristic c_0-value), so that different values will be distributed along different ranges of the general curve.

In order to illustrate the relative importance of the energetic terms during the ZFC processes, in FIGURE 3.8 the temperature evolution of the different energy terms is shown for some selected interacting conditions of the data of Section3.1.

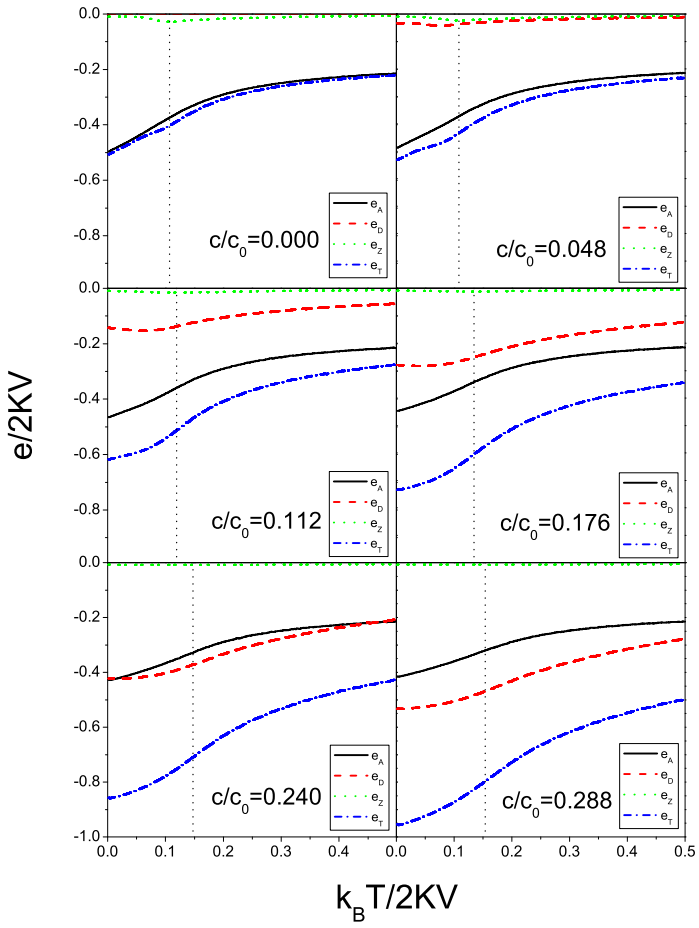

Figure 3.8:
Energy data (e_A, e_D, e_Z, and e_T) along ZFC processes, corresponding to different interacting conditions of the results presented in Section3.1. Vertical arrows stand for the corresponding t_B of each case.

The (reduced) energy contributions displayed in FIGURE 3.8 exhibit the expected behavior: increasing sample concentration leads to an increase of e_D, and the influence of the Zeeman energy is smaller the higher the concentration, while a slight decrease in e_A is also observed. In general, higher temperature leads to smaller energy, particularly e_A and e_D. It is interesting to point out at this point

that a detailed analysis of the different energy terms and their relative interplay did not provide us a correct interpretation of the c^* feature reported in Section3.1. We interpret this result in the following way: the results displayed in FIGURE 3.8 correspond to the total system, independently of the characteristics of the particles regarding their orientation with respect to the applied field of neighbouring particles, what gives support to the need of considering such particular features to understand the magnetic response of the system.

3.2.2 General t_B *vs* c/c_0 curve

Our intention now is to check the above assertion on c_0 as a scaling factor for the influence of magnetic dipolar interactions (as directly proportional to sample concentration). For this purpose, we need to compare the T_B *vs* c data for different types of particles, represented those by their correponding c_0-values. Since experimental data is usually subjected to uncontrolled secondary effects (polidispersity [67], aggregation [31], etc) that mask the real influence of dipolar interactions, we have used MC simulations to perfectly control the characteristics of the sample and hence to be sure about the nature of the different $t_B(c/c_0)$ trends to study.

ZFC processes for a systematic sample concentration variation were simulated for different types of particles, being those represented by the corresponding c_0-value. To vary c_0 we decided to vary M_S while keeping the same K value, because by doing so we can expect that in the non-interacting limit case the blocking temperature for the different systems considered will be the same, and so we may observe in detail how T_B evolves with increasing dipolar interaction starting from this common non-interacting case. It is worth to note that although this is an ideal assumption, it is in fact possible (however complicated) to design different materials so that they have a common (or very similar) K value but different M_S. Also, for computational purposes it is easier to keep the same value of K (included in the reduced temperature definition) and vary only M_S.

The physical meaning of c_0 can be interpreted as a measure of the relative importance between the anisotropy and dipolar energies [82], since they are respectively proportional to both terms of c_0, i.e. $E_A \propto K$ and $E_D \propto M_S^2$. In this sense c_0 provides an estimation of the relative importance of both energies[3]:

[3]The usefulness of the c_0 parameter to describe the relative influence of the magnetic dipolar energy in comparison with the anisotropy one had already been pointed out in the literature (see for example Refs. [13, 92, 93]); the novelty in our work is the interpretation of its meaning and the application to the unsolved problem of how interparticle dipolar interactions influence T_B.

$$c_0 = \frac{2K}{M_S^2} \propto \frac{E_A}{E_D} \tag{3.2}$$

Following this reasoning, we can expect a small influence of the dipolar energy for large values of c_0 ($c_0 >> 1 \Leftrightarrow E_A >> E_D$) so that T_B will not vary much with c. However, for small c_0 values ($c_0 << 1 \Leftrightarrow E_A << E_D$) the same variation of the concentration will have a more significant effect on T_B. Therefore, we have to test out whether the evolution of T_B with the sample concentration, when we plot it *vs* c/c_0, has a similar behaviour independently of the kind of particle (defined by K and M_S). To check this, we choose different c_0 values to systematically simulate ZFC processes (to estimate T_B as the maximum of the curves) at different concentrations. The values of c_0 that we have chosen are:

$$c_0 = \begin{cases} 4.00 \\ 3.00 \\ 2.00 \\ 1.00 \\ 0.50 \\ 0.33 \\ 0.25 \end{cases} \tag{3.2}$$

These values tailor the importance of one energy with respect to the other, with the ratio between E_A and E_D varying between 4 and 1/4 (we consider for the moment the Zeeman energy to be small enough to play a minor role in the magnetic behaviour of the system, although we will see later its great importance to determine the shape of the $T_B(c/c_0)$ curve). As mentioned above, to vary c_0 we have chosen to keep K constant and change the M_S values, so that the corresponding H_A and c_0 parameters vary accordingly. In Table 3.1 it is shown the complete set of M_S values used and the corresponding H_A and c_0 parameters. Also, the equivalent (in reduced units) field $H = 200Oe$ it is shown for each case.

Table 3.1: Values of M_S accounting for the different c_0 cases, together with the corresponding H_A values and the $h(H = 200Oe)$ case.

M_S	c_0	H_A	$h(200Oe)$
274	4.00	1095	0.18
316	3.00	949	0.21
387	2.00	775	0.25
548	1.00	548	0.36
775	0.50	387	0.52
949	0.33	316	0.63
1095	0.25	274	0.73

To investigate the role of the H_A and c_0 parameters as normalizing factors for the influence of the the Zeeman and dipolar energies,

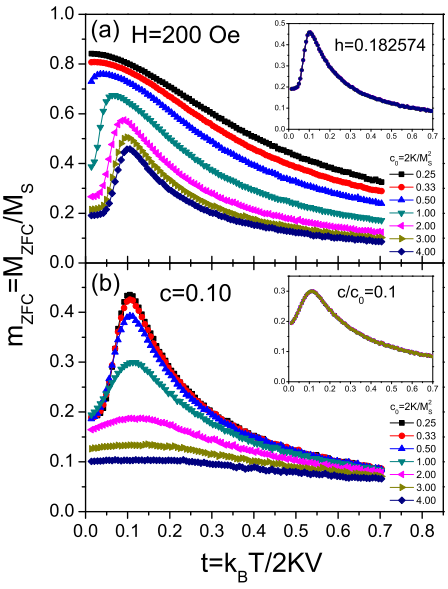

Figure 3.9:
ZFC curves for different (reduced) fields (a) and interacting conditions (b). In FIGURE 3.9(a), ZFC curves for different kind of particles (different c_0) are simulated for the same field $H = 200Oe$; inset shows the same processes for the same value $h = H/H_A = 0.18$. In FIGURE 3.9(b), analogous situation is shown but in this case considering the dipolar interaction (for $h = 0.18$), for the same concentration (main panel, $c = 0.10$) and same reduced concentration (inset, $c/c_0 = 0.1$).

we have simulated some ZFC processes at selected conditions: to emphasize the importance of the H/H_A term, we have simulated ZFC curves for the non-interacting case corresponding to Eq.(3.2.1), for both a fixed applied magnetic field $H = 200Oe$ and for the same reduced field $h = 0.18$, for the different c_0 values of Table 3.1. Analogously, to investigate the role of c_0 as a normalizing parameter for the sample concentration we have simulated ZFC processes for the same c_0 values, both for the same c value and for the same c/c_0 case (for a same reduced field). The results are shown in FIGURE 3.9.

In FIGURE 3.9(a), we observe that the ZFC curves peak at smaller temperatures for smaller c_0 values and that their overall magnetization is bigger, as expected due to higher influence of the magnetic field (see Table 3.1) and in agreement with Eq.(3.2.1): the smaller is c_0 the smaller is H_A, and so greater the influence of the magnetic field on the system, reaching a higher orientation of the magnetic moments of the particles. The inset shows the same processes if simulated at the same H/H_A value, case in which all curves overlap, as expected. In FIGURE 3.9(a), we observe analogous case for the influence of the magnetic dipolar interaction: the shape of the ZFC curves is different for the same sample concentration $c = 0.10$, but all curves collapse to the same one when the reduced sample concentration is the same, $c/c_0 = 0.1$ (see inset). These results confirm that the c_0 parameter works as a normalizing factor for the dipolar interaction analogously to the anisotropy field for the Zeeman energy.

In addition, we have also used the same procedure as used with the magnetization in FIGURE 3.9, applied to the energy of the system, in order to check our arguments described on the previous subsection 3.2.1 regarding the existence of an inner scale of energies as defined by h and c/c_0. To do so, we have recorded the evolution of the total energy (as given by $e_T/2KV$) for some selected conditions of applied magnetic field, sample concentration, and c_0. The results are shown in FIGURE 3.10.

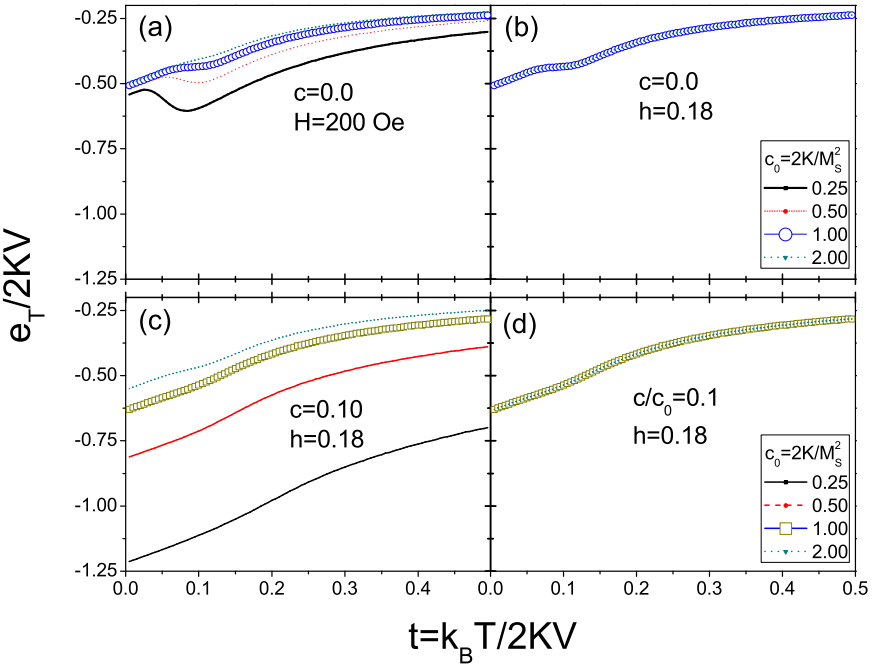

Figure 3.10:
Reduced total energy $e_T/2KV$ for some selected field and interacting conditions, for the cases $c_0 = 0.25, 0.50, 1.00, 2.00$ of Table (a). In FIGURE 3.10(a), data corresponds to processes of non-interacting systems under the same field $H = 200Oe$; in FIGURE 3.10(b), data corresponds to the same processes when using the same reduced field $h = H/H_A = 0.18$. In FIGURE 3.10(c), a similar case as in FIGURE 3.10(b) is shown, but in this case considering an interacting system with $c = 0.10$ (under a reduced field $h = 0.18$); and in FIGURE 3.10(d), the plotted data corresponds to the same processes, if having the same $c/c_0 = 0.1$ concentration and under the same field $h = 0.18$. The data corresponding to $c_0 = 1.00$ is shown with symbols because it is the case for which $H = 200Oe \Leftrightarrow h = 0.18$.

FIGURE 3.10 illustrates our arguments on the existence of an inner scale of energies defined by the parameters h and c/c_0. For non-interacting systems, the energy of the system differs for different types of particles under the same magnetic

field H (FIGURE 3.10(a)), but result in the same one under the same reduced field h (FIGURE 3.10(b)). And, analogously, the splitting of the energy for the interacting system (under the same field h) observed in FIGURE 3.10(c), overlap in one single same curve when using the c/c_0 value. Therefore, these results confirm the general character of the c/c_0 parameter, together with $h = H/H_A$, to provide a general description of the properties of the system.

Our next step is to investigate the usefulness of the c_0 parameter to provide a general $T_B(c/c_0)$ tendency. To carry out such study, we have simulated ZFC processes for a systematic variation of the sample concentration, between the diluted limit (0.0%) to high concentration samples up to 40.0% (with a 2.5% variation rate step). In FIGURE 3.11 we show the ZFC curves corresponding to three different c_0 cases, obtained under the same magnetic field $H = 200Oe$ from the systematic dipolar interaction strength variation.

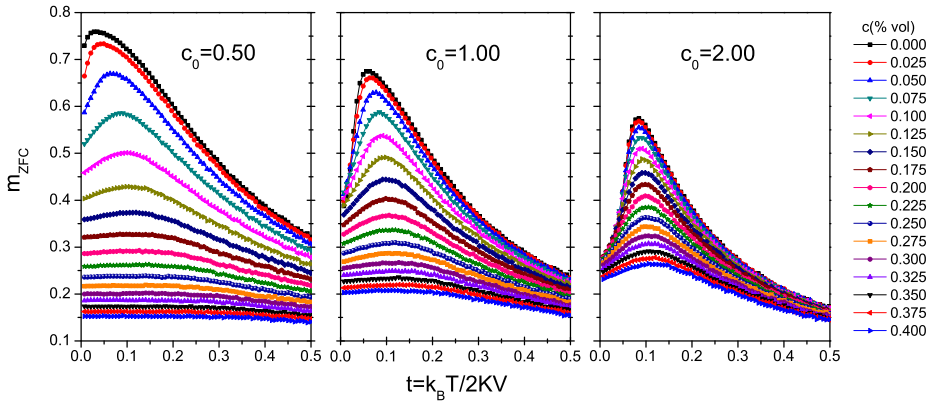

Figure 3.11:
ZFC curves corresponding to a systematic variation of c for a field $H = 200Oe$, for three different cases $c_0 = 0.50, 1.00, 2.00$.

The shape of the curves displayed in FIGURE 3.11 confirms what we expected: for increasing c_0 the importance of the anisotropy energy becomes more important, rendering more difficult to align the magnetic moments along the field direction (smaller the relative importance of the magnetic field, as shown in the table above). Hence, the maximum position becomes less sensible to variations of the dipolar interaction strength. From these curves (and the other c_0 values indicated in Table 3.1) we determine the t_B *vs* c dependence. The results are shown in FIGURE 3.12.

The first feature we have to mention regarding FIGURE 3.12 is the absence of data in the high-concentrations regime, extending this lack over a wider range of

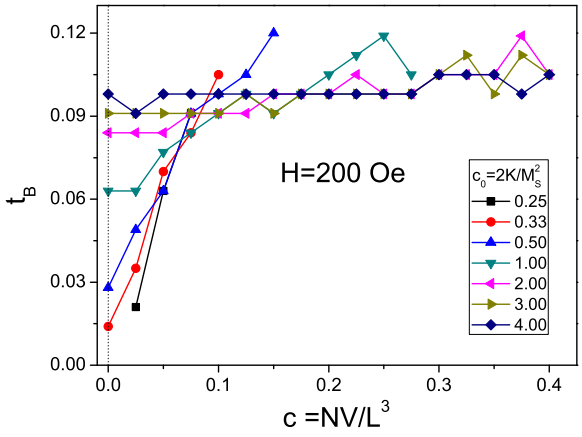

Figure 3.12:
t_B *vs* c curves for the different c_0 values considered, for a field $H = 200Oe$.

concentrations the smaller the c_0 values. The reason why this happens is found in the flattening of the curves under high-interacting conditions (as seen in FIGURE 3.11), which makes very complicated to determine the maxima of the curves. Apart from that technical constraint, the more important characteristic observed in FIGURE 3.12 is that for the larger c_0 values the dipolar interaction does not influence much the position of the maximum, as expected. On the contrary, for low c_0 values the influence of the dipolar interaction is much more relevant, experiencing T_B a rapid increase as c grows. It is worth to mention the rich variety of tendencies observed depending on the c_0 value, reproducing different trends reported from the experiment: a rapid increase at low concentrations (very low c_0), a regular increase at intermediate concentrations (intermediate c_0 values, and even a initial decrease for the larger c_0 value[4]. In order to get further insight into the properties of c_0 as a scaling parameter, we represent now the values of FIGURE 3.12, but normalizing the concentrations as c/c_0. The results are shown in FIGURE 3.13.

In this representation it calls our attention that the evolution of t_B *vs* c/c_0 is not as different as it seemed in the FIGURE 3.12. However, the curves appear far apart from each other so that no overlapping of the different curves on a general one is observed. This is reasonable, however, as the H/H_A ratio was different for each type of particle. Hence for, to rigorously check our hypothesis about c_0 as a scaling parameter we need to have normalized as well the effect of the magnetic field. To do so, we have repeated the ZFC processes for a fixed reduced field $h = 0.18$ and

[4]It is important to emphasize here the following: the precision on determining t_B diminishes with high concentration, but is very good in the low concentrated range. Regarding the initial decrease of t_B with c observed for the $c_0 = 4.00$ case, this tendency is undoubtedly observed in relation to the measuring precision.

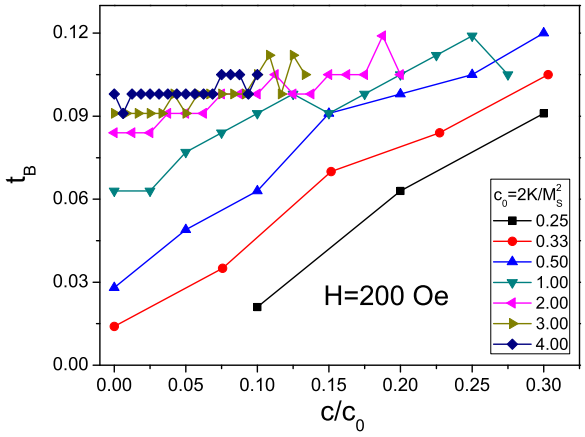

Figure 3.13:
t_B *vs* c/c_0 curves for the different c_0 values considered, for a field $H = 200Oe$.

analyzed the same data as in FIGURE 3.13. This reduced field value was chosen so that it is large to record the magnetization with precision enough, but not so large that it could mask the effect of the dipolar interaction on the value of t_B. The equivalence of $h = 0.18$ in real units is shown in Table 3.1 for the different types of particles considered.

In FIGURE 3.14 we show the new results, representing together t_B *vs* c (open black squares) and t_B *vs* c/c_0 (full red squares) in the same panel for the comparison.

Every panel stands for a different c_0 value, with the black (empty squares) data corresponding to $t_B(c)$ and the red (full circles) data displaying the $t_B(c/c_0)$ case. Despite the low precision of these results[5], it can be clearly observed that different experimental tendencies in the evolution of t_B with c are reproduced: the curves corresponding to low c_0 values (i.e. low anisotropy, and so the effect of the dipolar interaction is more relevant) grow rapidly with increasing c, the intermediate ones grow at a lower rate, and the curves for large c_0 values grow at a very low rate. A very important conclusion, therefore, is that the different experimental data obtained experimentally can be properly explained in terms of the characteristic c_0 value of the particles.

A remarkable feature observed in FIGURE 3.14 is that the red data shows a similar tendency for the different cases considered. For $c_0 < 1.00$ the unnormalized black data is above the red one, whereas for $c_0 > 1.00$ it is below the red data. The

[5]It is evident from the amount of data shown, that a large number of simulations were carried out to analyze the $t_B(c)$-dependence and, since the objective was to analyze the maxima of the curves, the simulations required powerful resources in order to be precise enough. However, despite the big effort devoted to the present study, achieving precision enough to precisely determine the maxima of the curves in the high-interacting regime is very complex and could not be done with the computational resources available during the simulation process.

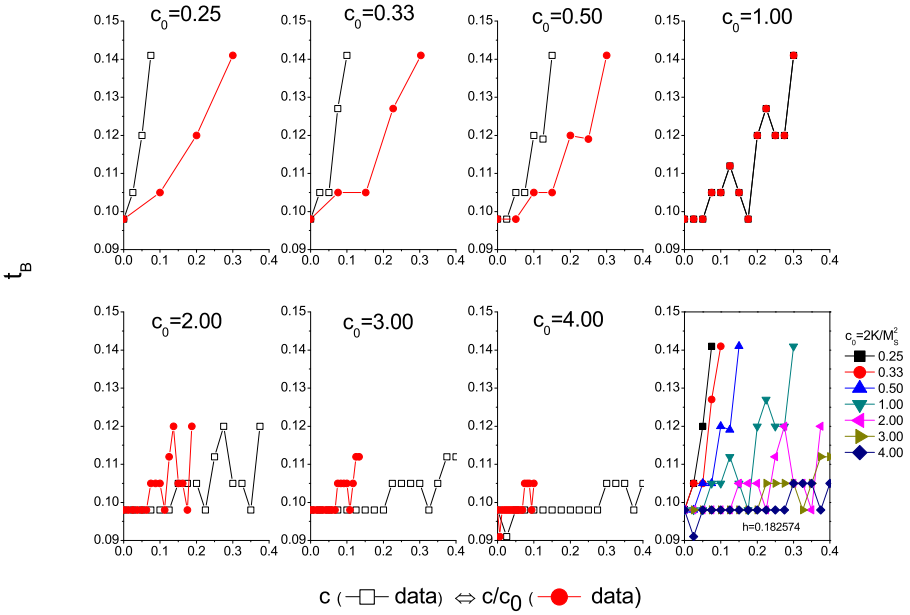

Figure 3.14:
t_B data for the different c_0 values, obtained under a reduced field $h = 0.18$. In each panel it is shown both the unnormalized t_B *vs* c data (open black squares) and the normalized t_B *vs* c/c_0 one (full red squares).

whole dataset t_B *vs* c is shown in the right bottom panel. Let us remark here the fact that these values were determined as the maximum of the ZFC curves, and so for small c_0 values and large concentrations the fluctuations might be more evident in the general trend of the curve, what is reflected in the smaller precision. We show next those values plotted as a function of c/c_0, i.e. the red data all together:

In FIGURE 3.15 we observe that all curves exhibit a rather similar tendency, being the apparently different shapes observed in FIGURE 3.14 only specific parts of this general curve, i.e. we can associate the same role to c_0 as scaling parameter to the sample concentration, as the anisotropy field for the applied field, being also possible to define a general curve as shown in FIGURE 3.15. Even that such general curve is not very precise, some behaviors can be identified and associated to different trends observed in FIGURE 3.15: the non-interacting regime observed in some highly anisotropy systems, stands for the low-concentration regime of the general curve of FIGURE 3.15 (if also M_S is low), being possible even to identify a

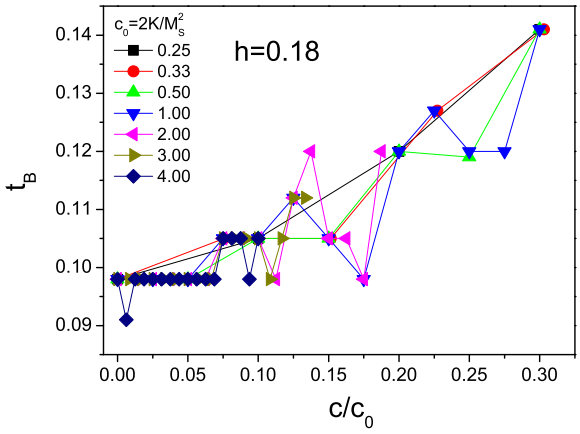

Figure 3.15: t_B *vs* c/c_0 curve for the different c_0 values considered.

decreasing tendency. For higher lower anisotropy systems, for which dipolar interactions are more relevant, we have the increase of t_B with sample concentration[6]. Therefore, this figure clearly remarks (with the restrictions of precision) the envisioned tendency as all the curves look pretty similar, supporting the argument about the dipolar interaction influence described in a general manner if normalizing the sample concentration as c/c_0.

3.2.3 General $m(t_B)$ *vs* c/c_0 curve

The general $t_B(c/c_0)$ tendency reported in the previous section, together with the arguments obtained from the energetic description of the system, gives support to our hypothesis on c_0 being the scaling parameter for the influence of the magnetic dipolar interaction. However, it is also conceivable that the fare precision of the data displayed in FIGURE 3.15, might arise some doubts about the actual goodness of the c_0 parameter. In order to erase any possible doubt and since the $t_B(c/c_0)$ curve is not very precise, we have also analyzed the maximum of the curves, $m(t_B)$, following the same procedure we used to evaluate t_B as a function of the dipolar interaction. This is to say, we have analyzed $m(t_B)$ as a function of the sample concentration for the same c_0 values of the previous section, under a fixed absolute value of the magnetic field $H = 200Oe$, *vs* c (a) and *vs* c/c_0 (b); under the same reduced

[6] It is worth to mention that in FIGURE 3.14 no tendency to saturate is observed, although we might expect it if assuming the c_0 parameter to be able to account for any experimental situation. We interpret that such tendency is not observed due to the special conditions of our system, with not precision enough to obtain the maxima of the curves in the high-interacting regime for the low c_0 cases (see FIGURE 3.11(a)).

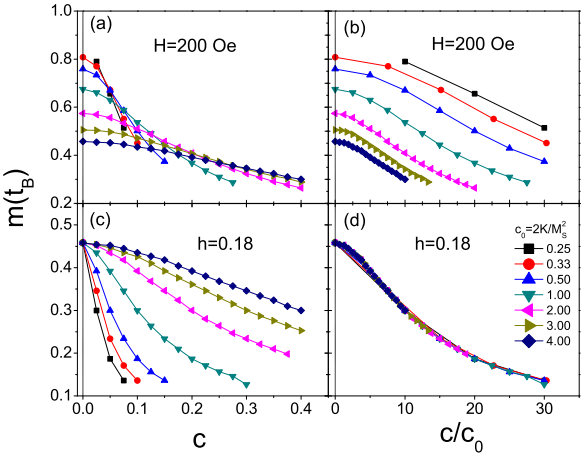

Figure 3.16: $m(t_B)$ data corresponding to the results shown in SECTION 3.2.2, under a fixed absolute value of the magnetic field $H = 200Oe$, *vs* c (FIGURE 3.16(a)) and *vs* c/c_0 (FIGURE 3.16(b)); under the same reduced magnetic field $h = 0.18$, *vs* c (FIGURE 3.16(c)) and *vs* c/c_0 (FIGURE 3.16(d)).

magnetic field $h = 0.18$, *vs* c (c) and *vs* c/c_0 (d). The results are summarized in FIGURE 3.16

In FIGURE 3.16, we observe a clear confirmation of c_0 acting as the scaling parameter for the influence of the dipolar interaction introduced as proportional to the sample concentration. The apparently unconnected curves displayed in FIGURE 3.16(a), show however a very similar tendency when plotted as a function of c/c_0. And, if in addition we the same reduced field $h = 0.18$ is used, we obtain that in such case all curves start at the same point for the non-interacting case (FIGURE 3.16). Finally, if the data is plotted taking into account to have the same $h = H/H_A$ value and to plot it *vs* c/c_0, we obtain that all curves overlap and collapse over the same one.

3.2.4 Hysteresis area *vs* c/c_0

It turns out that testing the suitability of the c_0 parameter to normalize interparticle dipolar interactions by means of an alternative approach (different than the usual one based on the ZFC/FC curves) would reinforce its general character as a scaling factor. This probe can be achieved for example by evaluating hysteresis properties as extracted from $M(H)$ cycles as those analyzed in SECTION 2.4.3. With this aim, in the present section we will briefly introduce some of our most recent studies, still currently in progress.

To check the use of c_0 as a normalizing parameter for the dipolar interaction throughout hysteresis properties, the quantity we decided to evaluate is the area of the curves following the same procedure as in SECTION 2.4.3 based on its interest for hyperthermia applications, i.e. simulating $M(H)$ cycles at different sample

concentrations and evaluating the area. To have a general approach to the problem we have considered different types of particles accounting for different c_0 values, and two different volumes were considered so that thermal effects can be noticeable (in order to emphasize the effect of temperature). For the sake of the comparison with the experiment, real temperature units are used. The characteristics of the different particles considered are summarized in Table 3.2.

Table 3.2:
Characteristics of the particle types considered in the present section.

$d(nm)$	$M_S(emu/cm^3$	$K(10^4erg/cm^3)$	c_0
20	420	5.46	0.62
20	420	3.64	0.41
20	420	1.82	0.21
40	480	2.55	0.22
40	480	1.70	0.15
40	480	0.85	0.07

A systematic variation of the sample concentration was performed for each of the different particles summarized in Table 3.2, in order to evaluate the area of the cycle *vs* concentration. The computational procedure followed was the same as in SECTION 2.4.3, and as since we focused on the effect of dipolar interactions, only one magnetic field case was considered of value $h_{max} = 10$. The results of *area vs c* for the different particle types described in Table 3.2, are plotted in FIGURE 3.17.

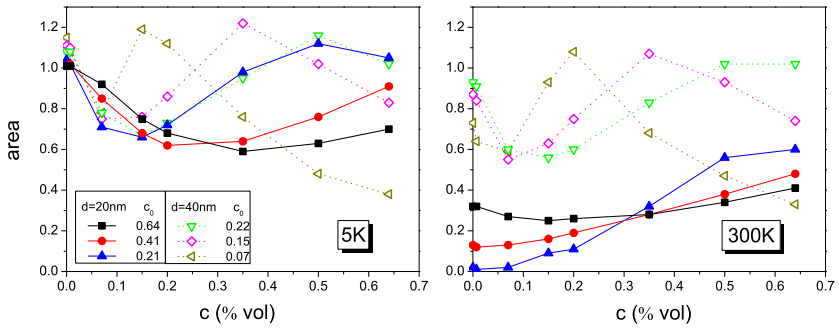

Figure 3.17:
area vs c for the different particles of Table 3.2, at $T = 5K$ (left panel) and $T = 300K$ (right panel).

The curves shown in FIGURE 3.17 exhibit a rich behaviour, depending both on the diameter of the particles and the c_0 value. At first sight, it is observed that the

different *area vs c* curves[7] have a very similar initial value in the low-temperature case, with the initial values of all curves (for the non-interacting case) very close to $area = 1$, but that such feature is not observed in the high-temperature one. This different arises because of the higher influence of thermal fluctuations on the smaller particles. This influence is also observed in the evolution of the correspondingly c_0 curves, which share a common shape at low temperatures: initial decrease, followed by a peak, and then again a decreasing tendency. Such feature, which is smoother the higher the c_0 value, is not maintained for the small particles at $T = 300K$, where the initial decrease practically disappears.

It is important to remind here that the intention of the present section is not related with the analysis of the specific trends of the data displayed in FIGURE 3.17, but it is solely to give additional probe on the role of the c_0 parameter as a scaling factor for the influence of dipolar interactions. Therefore, we will only mention that the results reproduce the usual decrease of the *area* with increasing interactions reported experimentally for large c_0 values, and that small c_0 values exhibit a richer behavior that brings out a promising research scenario (actually, the core of a currently ongoing work [94][8]). Therefore, we analyze again the data displayed in FIGURE 3.17, but plotted now *vs* c/c_0. The results are shown in FIGURE 3.18.

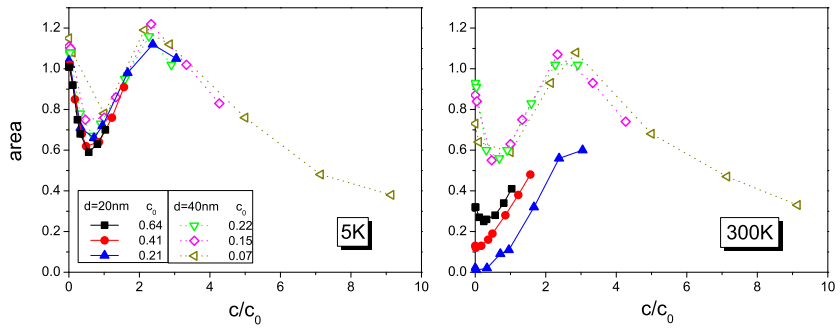

Figure 3.18:
area vs c/c_0 for the different particles of Table 3.2, at $T = 5K$ (left panel) and $T = 300K$ (right panel).

In FIGURE 3.18, we observe that effectively all curves share a common shape if plotted *vs* c/c_0: initial decrease, followed by a consequently increase until a

[7] It is worthy to note that our simulations indicate a very similar tendency both for the *area* and the coercive field H_c of the curves, what gives a wider dimension to our study if interpreting the evolution of the *area vs c* curves as analogous in the H_c *vs* (c) ones.

[8] This is also the reason why we have focused in low values of c_0, since those are the ones corresponding to the experimental particles we are dealing with [94].

maximum is reached, and finally a further decrease. The different data displayed in FIGURE 3.17 fits into different or partial ranges of this general curve, what gives the additional proof we were seeking about the role of c_0 as a general scaling parameter for the magnetic dipolar interaction.

There are other interesting features on the curves displayed which call our attention. The first one is the strong influence of the temperature, which for the high-temperature case hampers the observation of the initial decrease for the smaller particles, which serves as an explanation for different experimental behaviours. However, the most remarkable feature is the existence of a peak in the *area vs* c/c_0, which has extraordinary importance for nanotechnological applications: on the most immediate side as related to hyperthermia properties, such peak stands for the concentration at which heating rise is enhanced. Also, keeping in mind that the shape in the *area vs c* curves is pretty much the same followed by the H_c *vs c* data, such peak may be used to define, for a given type of particle (as represented by the corresponding c_0 value), of the sample concentration leading to the larger H_c value, which is strongly important for magnetic recording technologies. From the theoretical point of view, the different trends observed in FIGURE 3.18 provide a new perspective to understand the contradictory results reported experimentally on the $H_c(c)$ dependence, which vary from a decreasing H_c with increasing concentration [95], to a completely opposite increasing tendency [96].

Conclusions We have found that the influence of magnetic dipolar interactions on the SPM properties of nanoparticle systems can be described in a general way, being possible to define a scaling parameter that normalizes its influence (if associating dipolar interaction with sample concentration). By analyzing the energy frame of nanoparticle systems, we have obtained that it is possible to define a unitless parameter, $c_0 = 2K/M_S^2$, which works as a scaling factor for the dipolar energy as related to the sample concentration as c/c_0. In order to prove this hypothesis, we have simulated ZFC processes for different types of particles (identified by their corresponding c_0-characteristic parameter), and found that different experimental $t_B(c)$ trends reported experimentally can be reproduced and that such different tendencies overlap in a general t_B *vs* c/c_0 curve. The different experimental trends correspond to different parts of the general curve in the c/c_0 scale. Since the precision of the t_B data is rather poor in the high-interacting conditions, we have also analyzed the maxima of the curves, $m(t_B)$, which are much more precise to determine that their temperature position. Remarkably, these results perfectly overlap in the same general curve if normalized by c/c_0, what gives additional support to

our arguments and results about c_0 as being the scaling factor for the influence of dipolar interactions as proportional to the sample concentration. Finally, in order to test the suitability of c_0 as a scaling parameter in a different scenario than the corresponding to the ZFC/FC curves, we have also simulated $M(H)$ cycles at different interacting conditions and for different types of particles (as corresponding to different c_0 values). We have found that the *area vs c* curves overlap in the same one if plotting c/c_0, giving additional support to our arguments about the suitability of c_0 as a normalizing factor for the magnetic dipolar interaction.

3.3 Microscopic analysis of the dipolar interaction

Our results in the previous section confirm c_0 as a general scaling factor for the influence of the dipolar interactions. Therefore, the next question that we have to consider is, which is the specific shape of the $t_B(c/c_0)$ curve?

From our computational results we do not have precision enough yet as to define its overall shape for the whole range of dipolar interaction strength (unable to account for the high-interacting regime). However, both from previous computational results and from experimental data, it seems quite clear the existence of three different ranges of behavior in the evolution of t_B with sample concentrations, being those i) an essentially constant regime at low concentrations, ii) a regular increasing behaviour in the intermediate concentration range, and iii) a tendency to saturate at high concentrations. Our results seem to indicate that such different parts of behaviors are in fact parts of the same general curve. This is to say, we figure out the shape of the general $t_B(c/c_0)$ curve as constituted by i) a low-concentration constant (even decreasing) regime, ii) a regularly increasing intermediate concentration range, and ii) a saturation regime at high concentrations. The objective of the present section is to investigate the physical origin of such features.

Aiming such a purpose, we have revised the basic features of the system as influenced by growing interparticle interactions, and we have envisioned that for interacting conditions the properties of the system could be more accurately described if taking into account the different dipolar fields acting on the particles as a function of their relative orientation with respect to the application of the magnetic field, i.e. their orientation parallel of antiparallel to the applied field. With this idea in mind, we propose a simple alternative description of the evolution of t_B *vs* c as a result of the different contributions of the parallel and antiparallel populations, and simulate ZFC processes of a well controlled system as a function of the dipolar interaction strength. The agreement between the simulated data and the proposed

fitting is very good, what provides support to our arguments on the need to take into account the different orientation of the particles with respect to the applied magnetic field. However, there are theoretical inconsistencies between the interpretation of the proposed fitting and the theoretical background that indicate that although to consider the different fields acting each particle is a promising approach to the problem, to split the sample into parallel and antiparallel populations is not the good one. In order to save this inconsistency and to check our ideas regarding the distribution of dipolar fields, we have simulated ZFC processes and analyzed dipolar field histograms. The results indicate a complex scenario, in which the dipolar fields of the particles change from a bell-like peak at high temperatures, to well differentiated peaks at low temperatures, and the magnetic field influencing in a different fashion the shape of those peaks depending on the interaction strength and temperature.

3.3.1 Two different contributions

If we consider the system as a function of the relative orientation of the magnetic moments of the particles with respect to the applied magnetic field, in the non-interacting limit case the particles orientation is only determined by the magnetic field and thermal disorder. As the concentration increases and the particles approach each other, there is an increased influence onto the nanoparticles to align parallel or antiparallel (along the applied field $\vec{H}$ direction[9]). It is this relative orientation among the particles, and therefore its contribution to align parallel or antiparallel to the external field H, what we want to analyze in detail to approach the general shape of the $t_B(c/c_0)$-curve.

In the ideal non-interacting case in which the particles are away from each other and do not interact, the energetic description is given by the thermal energy over the anisotropy energy barrier as influenced by the Zeeman energy (see SECTION 1.2). This situation is resembled in FIGURE 3.19, where the anisotropy energy wells of a non-interacting system are shown under the influence of a magnetic field H parallel to the easy axis.

When the magnetic moment of the particles is oriented parallel ($\uparrow\uparrow$) to the field the energy well becomes deeper, while for the antiparallel ($\uparrow\downarrow$) ones the barrier diminishes. Since the transition from the deep well over $E_B^{\uparrow\uparrow}$ is much less probable than the transition over $E_B^{\uparrow\downarrow}$, the usual approach describing the $T_B(H)$ dependence is given by

[9] We consider hereafter H as the component of $\vec{H}$ along the anisotropy easy axis, as usual.

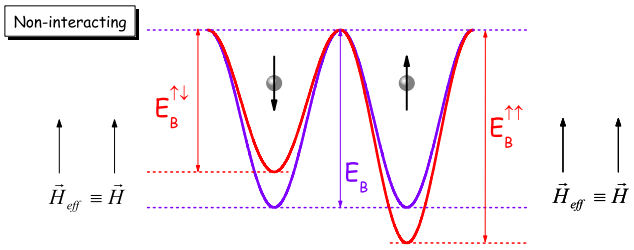

Figure 3.19: Uniaxial anisotropy energy wells for non-interacting systems, under a magnetic field H.

$$T_B = \frac{KV}{25k_B}\left(1 - \frac{H}{H_A}\right)^{\frac{3}{2}} \tag{3.2}$$

where the reversal transition over $\uparrow\uparrow$ is usually neglected because of being much less probable.

However, the situation is different when interparticle interactions become relevant and its influence may be even greater than the influence of the Zeeman energy. In such case, each particle is subjected not only to the tendency of the external field to align them along the field direction: now, each particle may be subjected either to a larger tendency to align along the field, or to an anti-alignment tendency (depending on the strength of the interparticle dipolar interaction, which in turns depends on the orientation of the neighbouring particles). The magnetic dipolar interaction can be described as the coupling of one particle magnetic moment with the neighbouring particles, and its resultant is zero if the system is randomly distributed (with zero net magnetization). However, when an external magnetic field is applied and tries to align the particles along its direction, a net resultant along the field direction appears as a consequence of the net magnetization. Such resultant can be defined as a *dipolar field* in a similar way as applied magnetic field, i.e. $E_D[i] = -\vec{\mu}_i \cdot \vec{H}_D[i]$. Even that such field is different for each particle, since it is given by

$$\vec{H}_D[i] = \sum_{j \neq i}^{N} \left(3\frac{(\vec{\mu}_j \cdot \vec{r}_{ij})\,\vec{r}_{ij}}{r_{ij}^5} - \frac{\vec{\mu}_j}{r_{ij}^3} \right) \tag{3.2}$$

in a rough approximation we can consider that it has the same average value $\vec{H}_D$ for all particles but different sign depending on their relative orientation with respect to the applied field H, i.e. if they point parallel or antiparallel to the system. Therefore, the whole system of particles can be classified into two subgroups, named hereafter as parallel ($n^{\uparrow\uparrow}$) and antiparallel ($n^{\downarrow\uparrow}$), and the effective magnetic field

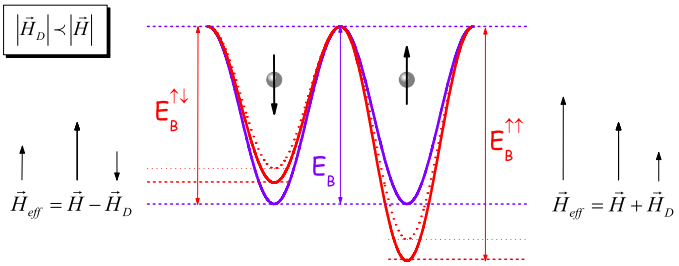

Figure 3.20: Uniaxial anisotropy energy wells for interacting systems, under the condition $H_D < H$.

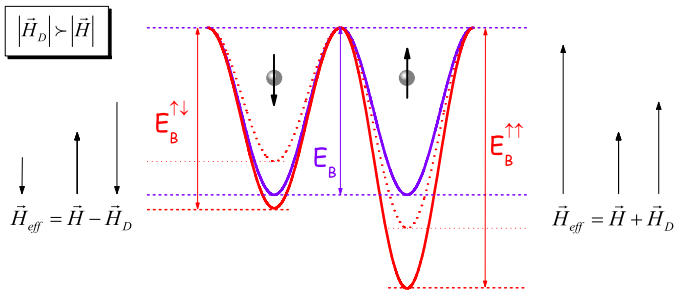

Figure 3.21: Uniaxial anisotropy energy wells for interacting systems, under the condition $H_D \succ H$.

(H_{eff}) experimented by each one is $H_{eff}^{\uparrow\uparrow} = H + H_D$ and $H_{eff}^{\downarrow\uparrow} = H - H_D$, respectively. FIGURE 3.20 illustrates the effect of H_D on each subgroup[10].

In FIGURE 3.20, we observe that the effect of the dipolar interaction is always to enlarge the size of the anisotropy wells, i.e. a higher thermal energy is necessary to promote the jumping from one well to the other. Following this picture, one could therefore expect a regular increment of T_B with increasing interparticle interaction. However, to justify the existence of a non-monotonic behaviour as previously demonstrated it is clear that some thresholds have to exist able to generate the different trends observed in the $t_B(c/c_0)$ curve. In this respect, if analyzing in detail the diagram depicted in FIGURE 3.20 we can also foresee a special effect at $H_D \equiv H$: for higher interacting conditions the particles aligned antiparallel to the field, no longer would tend to align along the field, since in that case $H_{eff}^{\downarrow\uparrow}$ has negative sign (i.e. tends to keep the particles antiparallel aligned with respecto the the external field). Can this threshold stand for one of the different regimes observed in the $t_B(c/c_0)$ curve? This $H_D \geq H$ case is shown in FIGURE 3.21 to illustrate the effect of strong interacting conditions on the energy barrier diagram.

Despite the $H_D \geq H$ feature displayed in FIGURE 3.21 does not explain *per se*

[10] Again, we consider only the projection along the field direction.

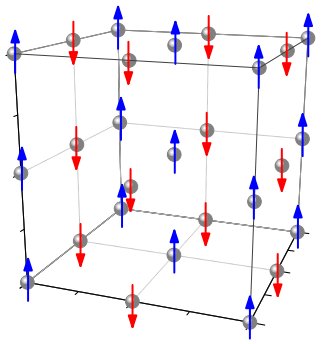

Figure 3.22:
Schematic drawing of the effective fields (represented by the arrows) experienced by the magnetic particles, under the conditions $H_i \equiv H_D \forall i$ and $n^{\uparrow\uparrow} = n^{\downarrow\uparrow}$, and with the particles regularly distributed in a simple cubic cell.

the non-monotonic dependencies reported for the $T_B(c)$ curve, it provides nevertheless an alternative approach to the problem, i.e. to analyze both the different effect of the interparticle interactions on the sample as a function of the relative orientation of the particles with respect to the applied field. If assuming the magnetic field applied parallel to the easy anisotropy azis, the respective T_B value of the antiparallel and parallel populations is given, respectively, by

$$T_B^{\downarrow\uparrow} = \frac{KV}{25k_B}\left(1 - \frac{H_{eff}}{H_A}\right)^2 = \frac{KV}{25k_B}\left(1 - \frac{H}{H_A} + \frac{H_D}{H_A}\right)^2 \tag{3.2}$$

and

$$T_B^{\uparrow\uparrow} = \frac{KV}{25k_B}\left(1 + \frac{H_{eff}}{H_A}\right)^2 = \frac{KV}{25k_B}\left(1 + \frac{H}{H_A} + \frac{H_D}{H_A}\right)^2 \tag{3.2}$$

It is clear, however, that the above scenario constitutes a very naive approximation to the problem: it is based on the rough assumptions that all particles experience the same dipolar field strength, $H_i \equiv H_D \forall i$, and that $n^{\uparrow\uparrow} = n^{\downarrow\uparrow}$, i.e. it is only valid in case that the amount of particles aligned parallel and antiparallel to the applied field is equal and regularly distributed, so that each particle is surrounded by a similar environment of neighbouring particles, as illustrated in FIGURE 3.22 for the particles distributed in a simple cubic cell with parallel easy axis aligned along the magnetic field.

It is evident that such $H_i \equiv H_D \forall i$, and $n^{\uparrow\uparrow} = n^{\downarrow\uparrow}$ assumptions do not correspond to the features of a ZFC curve[11], since $n^{\uparrow\uparrow}$ and $n^{\downarrow\uparrow}$ are very different along the ZFC processes. Furthermore, their larger difference if found at the maximum of the curves. Also, increasing interparticle interactions decrease the magnetization

[11] Although the $n^{\uparrow\uparrow} = n^{\downarrow\uparrow}$ condition is close to the system while cooling in zero field, in fact only in the ideal case $T = 0$ such situation would be possible because thermal oscillations would promote an irregular distribution of the preferred orientation of the particles.

attained by the systems, what implies a smaller difference $(n^{\uparrow\uparrow} - n^{\downarrow\uparrow})$. This $(n^{\uparrow\uparrow} - n^{\downarrow\uparrow})$ difference will also be reflected in the values of H_D over each particle, since the $(n^{\uparrow\uparrow} - n^{\downarrow\uparrow}) \neq 0$ case implies that there will differences in the value of $H_D[i]$ (even if belonging to the same $n^{\uparrow\uparrow}$ of $n^{\downarrow\uparrow}$ population), due to the different environment of each particle.

In resume, our interpretation on the non-monotonic shape of the $t_B(c)$ curve is that the different dipolar fields acting on the particles as a function of the dipolar interaction strength have to be taken into account, together with the amount of particles belonging to each scenario. A first approach to undertake such a purpose can be based on the rough approximation of considering the system as composed by two subsystems, $n^{\downarrow\uparrow}$ and $n^{\uparrow\uparrow}$, with their respective blocking temperatures $t_B^{\downarrow\uparrow}$ and $t_B^{\uparrow\uparrow}$, so that the estimated blocking temperature t_B^{est} is given by

$$t_B^{est} = \frac{t_B^{\downarrow\uparrow} \cdot n^{\downarrow\uparrow} + t_B^{\uparrow\uparrow} \cdot n^{\uparrow\uparrow}}{n^{\downarrow\uparrow} + n^{\uparrow\uparrow}} \tag{3.2}$$

To check our hypothesis, in the next subsection we will analyze the influence of dipolar interactions on a well controlled nanoparticle system.

3.3.2 Simple cubic cell with aligned easy axes

In the previous section we proposed to consider the dipolar fields acting on the particles, together with the relative orientation of their magnetic moments and amount of particles in each situation, to explain the non-monotonic $t_B(c)$ results reported both experimentally and by MC simulations. To check our arguments, we have simulated the influence of dipolar interactions on a very simple scenario: the particles are distributed in a simple cubic cell, so that interparticle distances are well controlled, and the anisotropy uniaxial easy axis are parallel along the field direction so the main components of H and H_D are easily comparable. In FIGURE 3.23 it is shown a scheme of the simulated system.

The motivation to use a MC approach in this study is not only its suitability to provide us the the $t_B(c)$ data from the maxima of the ZFC curves, as usual, but also because with the MC technique we can control the inner properties of the system in order to check Eq.(3.3.1), namely, $t_B^{\downarrow\uparrow}$, $n^{\downarrow\uparrow}$, $t_B^{\uparrow\uparrow}$, and $n^{\uparrow\uparrow}$. To do so, we had to record the evolution of the magnetization of the both the $n^{\downarrow\uparrow}$ and $n^{\uparrow\uparrow}$ populations in each ZFC process separately, so that we can later analyze $t_B^{\downarrow\uparrow}$ and $t_B^{\uparrow\uparrow}$, respectively. The ZFC curves obtained for a systematic 2.5% volume fraction (up to 40%) are shown in FIGURE 3.24, under a magnetic field $h = 0.25$ applied parallel to the easy axes.

FIGURE 3.24 shows slightly different features in comparison with disordered systems: the maxima of the curves progressively shifts to higher values with increasing

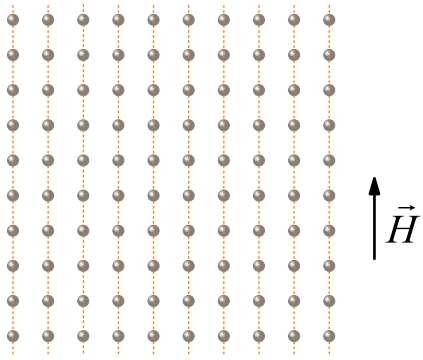

Figure 3.23:
XZ snapshot of the simulated system: 1000 particles distributed in a simple cubic cell, with the uniaxial easy anisotropy axes (dashed lines) parallel aligned along the magnetic field direction.

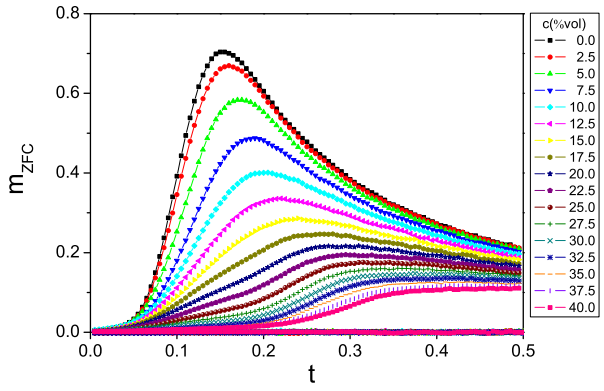

Figure 3.24:
ZFC curves as a function of the sample concentration, for a field $h = 0.25$ applied parallel to the easy axes.

interaction and the total magnetization reached is smaller, as expected[12], but what calls more our attention is the change in the shape of the curves at about the $c = 0.20$ value. For concentrations $c \prec 0.20$ the shape of the curves is the usual one, with a monotonic growing until the maximum and a paramagnetic-like decay above it. However, for concentrations $c \geq 0.20$, the curves exhibit a practically flat shape at low temperatures, until a change in slope occurs after which the curves reach the maximum. Two features characterize these high-interacting curves: the flat range broadens with interaction, and the maximum is very wide and difficult to determine. For the sake of simplicity we shall therefore concentrate in the $c \prec 0.20$ range.

To determine $t_B^{\downarrow\uparrow}$, $t_B^{\uparrow\uparrow}$, and the respective $n^{\downarrow\uparrow}$ and $n^{\uparrow\uparrow}$ at the maxima of the curves, we have to separately analyze the two components of the magnetization curves, i.e. $m^{\downarrow\uparrow}$ and $m^{\uparrow\uparrow}$ so that $m_{total} = m^{\downarrow\uparrow} + m^{\uparrow\uparrow}$. In FIGURE 3.25 it is shown

[12]It is worth to note that in this case no constant regime at low concentrations is observed. This can be due either to the special arrangement of the easy axes and/or also due to the larger magnetic field value, which may mask the non-interacting range effect.

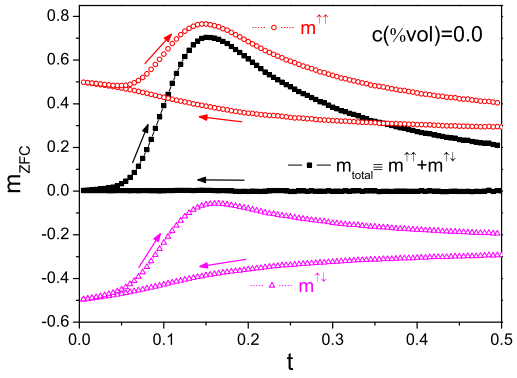

Figure 3.25: $m^{\downarrow\uparrow}$ and $m^{\uparrow\uparrow}$ curves corresponding to a typical ZFC process, recoded while cooling without field and while heating up under $h = 0.25$, for the non-interacting case ($c = 0.0$). The arrows indicate the temperature variation direction.

a typical ZFC curve, with the two components recorded. The magnetization is also recorded while cooling in zero field in order to check the characteristics of the system both with and without applied magnetic field.

The shape of the $m^{\downarrow\uparrow}$ and $m^{\uparrow\uparrow}$ curves shown in FIGURE 3.25 provides information about the ZFC process in the particular system of our study. While cooling in zero field $\left|m^{\downarrow\uparrow}\right| \equiv \left|m^{\uparrow\uparrow}\right|$, and the curves progressively separate from each other with decreasing temperature[13]. This behavior is a direct result of the special arrangement of the easy axes: with smaller thermal oscillations, the anisotropy energy becomes more relevant and tends to align the magnetic moments along the easy axes. Since those are parallel, all particle moments align along the same direction, splitting the population in two subsystems of equal magnitude and opposite sign, as observed. In the very low temperature limit, $m^{\downarrow\uparrow} \to -0.5$ and $m^{\uparrow\uparrow} \to 0.5$ so that $m_{total} \to 1$.

From the $m^{\downarrow\uparrow}$ and $m^{\uparrow\uparrow}$ curves we can now obtain $t_B^{\downarrow\uparrow}$ and $t_B^{\uparrow\uparrow}$ values, approximated as usual as the maximum of the curves (minimum for the $m^{\downarrow\uparrow} \to -0.5$ data). In FIGURE 3.26 we show the $m^{\downarrow\uparrow}$ and $m^{\uparrow\uparrow}$ curves corresponding to the ZFC curves displayed in FIGURE 3.24.

The curves shown in FIGURE 3.26 exhibit special characteristics, which arise some doubts about the adequacy of using Eq.(3.3.1) to describe the $t_B(c)$ data. On the one hand, the maximum (or minimum) disappears for concentrations $c \geq 0.20$; on the other hand, the extremal values of the $m^{\downarrow\uparrow}$ data is above the $m^{\uparrow\uparrow}$ data, contrary to the expected after the arguments presented in SECTION 3.3.1. Despite this difficulties, we have still completed our study on the properties of the system

[13] In a randomly distributed particle system the $m^{\downarrow\uparrow}$ and $m^{\uparrow\uparrow}$ curves follow a completely different trend on cooling under zero field, keeping constant values $\left|m^{\downarrow\uparrow}\right| = \left|m^{\uparrow\uparrow}\right| = 0.25$ for all temperatures. This different behavior arises from the random distribution of easy axes, which result in the same average value independently of the temperature.

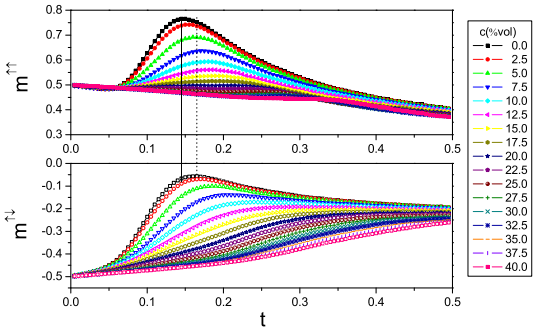

Figure 3.26:
$m^{\downarrow\uparrow}$ and $m^{\uparrow\uparrow}$ curves corresponding to the processes displayed in FIGURE 3.24 (only the heating-up branches are shown). Vertical lines stand for the maxima of the non-interacting $c = 0.0$ processes, i.e. $t_B^{\uparrow\uparrow}$ (solid line) and $t_B^{\downarrow\uparrow}$ (dotted line).

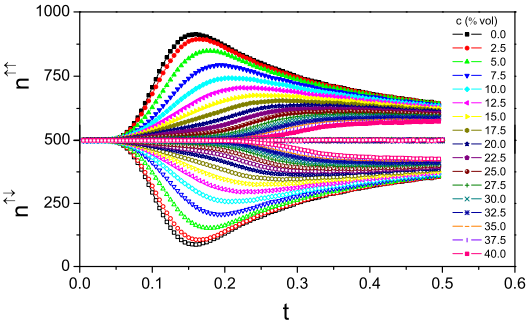

Figure 3.27:
$n^{\downarrow\uparrow}$ and $n^{\uparrow\uparrow}$ data corresponding to the processes displayed in FIGURE 3.24 (system of N=1000 particles).

as a function of the two populations. To do so, we have also analyzed the $n^{\downarrow\uparrow}$ and $n^{\uparrow\uparrow}$ data corresponding to the results plotted in FIGURE 3.26, which is presented in FIGURE 3.27.

The data displayed in FIGURE 3.27 shows the expected behavior: the amount of particles particles oriented parallel and antiparallel is complementary with respect to $N = 500$ (i.e. half of the total system), and their value at the maxima diminishes with increasing interaction strength. Hence, to check Eq.(3.3.1) we have now to analyze the $t_B^{\downarrow\uparrow}$ and $t_B^{\uparrow\uparrow}$ data, and the corresponding $n^{\downarrow\uparrow}$, and $n^{\uparrow\uparrow}$ at the maxima (minima) of the curves. The results are shown in FIGURE 3.28, together with the $t_B(c)$ data obtained directly from the ZFC curves.

The results shown in FIGURE 3.28(a), in which $t_B^{\downarrow\uparrow} \succ t_B^{\uparrow\uparrow} \forall c$, corroborate our guess after FIGURE 3.26 that computing the parallel and antiparallel populations is not a good approach to tackle the problem of the influence of interparticle dipolar interactions on t_B, for it lead to an inconsistency regarding the anisotropy wells as displayed in Figs.3.20,3.21. Besides that, the results displayed in FIGURE 3.28(b) follow the expected trends: with higher interaction strength, the particles are more tightened bounded to each other so that a tendency to keep similar values in the parallel and antiparallel populations is reinforced. In FIGURE 3.29 it is shown the

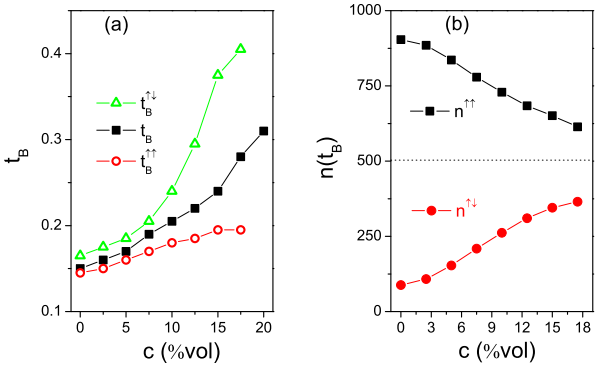

Figure 3.28:
(a) $t_B^{\downarrow\uparrow}$ (green triangles) and $t_B^{\uparrow\uparrow}$ (red circles), together with t_B (black squares) obtained directly from the ZFC curves. (b) $n^{\downarrow\uparrow}$ (red circles) and $n^{\uparrow\uparrow}$ (black squares) at the maxima and minima of the curves.

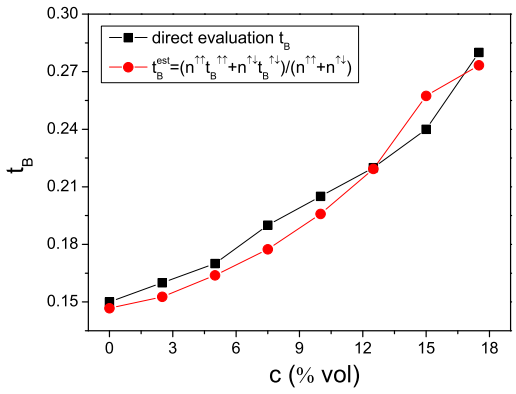

Figure 3.29:
t_B^{est} data obtained by using Eq.(3.3.1) with the data shown in FIGURE 3.28, together with the t_B data directly obtained from the maxima of the ZFC curves of FIGURE 3.24.

blocking temperature as estimated from Eq.(3.3.1), t_B^{est} in comparison with the t_B data directly obtained from FIGURE 3.24.

Eq.(3.3.1) provides a good fit to the influence of dipolar interactions on t_B, as evidenced in FIGURE 3.29. However, it is important to keep in mind the contradictions between the height of the energy wells and the relative values of the $t_B^{\downarrow\uparrow}$ and $t_B^{\downarrow\uparrow}$, which do not correspond to the expected theoretical case. Therefore, our interpretation of the results obtained in the present section are:

- the *parallel* and *antiparallel* approach is not a good one from the theoretical point of view
- even so, its good working to fit the $t_B(c)$ dependence gives in fact support to our arguments on the need of taking into account the dipolar fields acting on the particles as a function of the relative orientation of their magnetic moments with respect to the applied magnetic field.

It is worth to note here that the $t_B(c)$ curve displayed in FIGURE 3.29 does not exhibit the different interacting regimes envisaged. This result was also not

expected: the three different ranges in the $t_B(c)$ curve are associated to randomly distributed nanoparticle systems, whereas the present one constitutes a very specific arrangement. In fact, it might be even more complicated to understand this very symmetric system that the usual randomly distributed, but it was chosen because of being more desirable for the microscopic analysis of the energies involved, with much less energy barrier distribution.

3.3.3 Dipolar field histograms

Our next step in order to study the dipolar fields acting on the particles is to directly estimate them. To gain such objective, we have recorded the dipolar fields of all particles at selected temperatures in order to build up histograms describing the amount of particles under each dipolar field. In order to have well defined histograms we have used a much larger system size than usual, of $N = 8000$ particles. An example of the histograms obtained is shown in FIGURE 3.30, where the dipolar field H_D is given in normalized $h_D = H_D/H_A$ units.

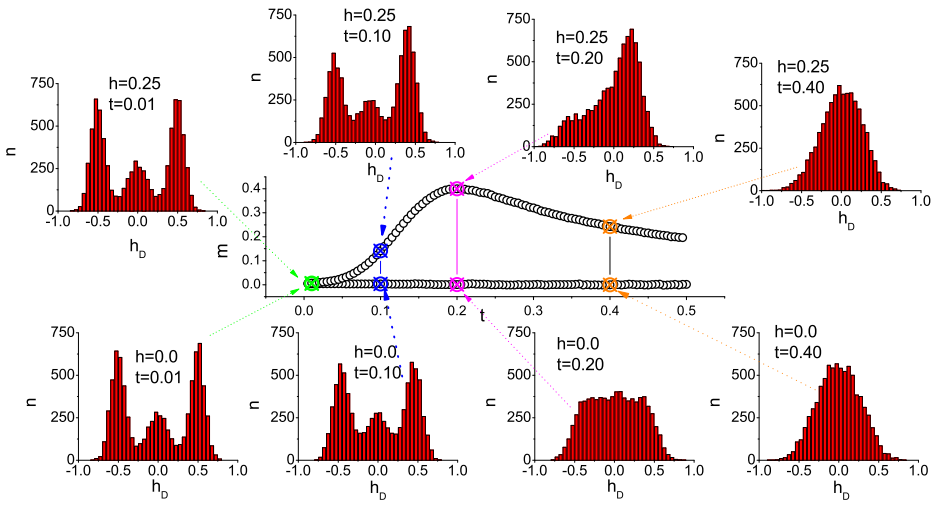

Figure 3.30:
Some dipolar field-histograms corresponding to selected conditions of the $c = 0.10$ ZFC curve.

In FIGURE 3.30 it is shown the ZFC curve corresponding to the $c = 0.10$ case of FIGURE 3.24, together with the dipolar field histograms corresponding to different different selected temperatures, both while cooling the sample in zero field, and while heating it up under $h = 0.25$. The overall trend of the histogram is the change from a bell-like shape at high temperatures, to a multiple-peak shape at low

temperatures. The high-temperature peak (above t_B) is centered at $h_D = 0$ when no field is applied, and bends towards positive values when the field is applied. The multiple-peak low-temperature feature consists on two high peaks at non-zero h_D values, and a smaller one around $h_D = 0$. The non-zero peaks occur at symmetric $h_D \neq 0$ when no field is applied, and the symmetry breaks when $h \neq 0$.

The histograms displayed in FIGURE 3.30 support our arguments on the need of considering the different signs of the dipolar field acting on the particles. Furthermore, their shapes also indicate that the rough approximation of $H_D[i] \equiv H_D \forall i$ is not valid, as expected after FIGURE 3.26. In general, the interpretation of FIGURE 3.30 is that interparticle dipolar interactions favour the grouping of the particles with similar $H_D[i]$ values at low temperatures when no field is applied, and that such scenario disappears when a magnetic field is applied, since it bends the histogram towards the more favoured anisotropy well. High temperatures break such features (both for the $H = 0$ and $H \neq 0$ cases), and the histogram acquires a bell-like shape centered about $h_D = 0$.

In order to analyze how the interaction strength influences the shape of the histograms, we have also recorded the dipolar fields for different sample concentrations, corresponding to higher ($c = 0.20$) and smaller ($c = 0.05$) interacting conditions. The results are shown in FIGURE 3.31.

In FIGURE 3.31, we observe that the main features discussed after FIGURE 3.30 (i.e. single-peak at high temperatures, and multiple peaks at low temperatures) occur independently of the dipolar interaction strength. However, there are some characteristics that differ depending on such interacting: at low temperatures increasing interaction conditions result in farther separation between the peaks, accompanied such separation by an decrease of their height. Particularly, the central one (around $h_D = 0$ tends to disappear. With increasing temperatures the peaks initially drop tehir height, and as the temperature keeps rising one of the wells is favoured (the positive one) while accompanied by a rise on its size. With increasing temperature the peak centered at negative h_D values disappears, as observed in FIGURE 3.30, and the h_D value around which peak decreases. At very high temperatures the shape of the histogram is bell-like around $h_D = 0$. The influence of the temperature is stronger the smaller the interacting conditions.

The results displayed in Figs.3.30,3.31 indicate that there are large differences between the effective field experimented by the particles depending on the interaction strength and temperature. In fact, for very high interacting conditions and low temperatures, the approximation of the particles splitting in two subsystems of similar H_D value and opposite sign fits very well the histograms, although such

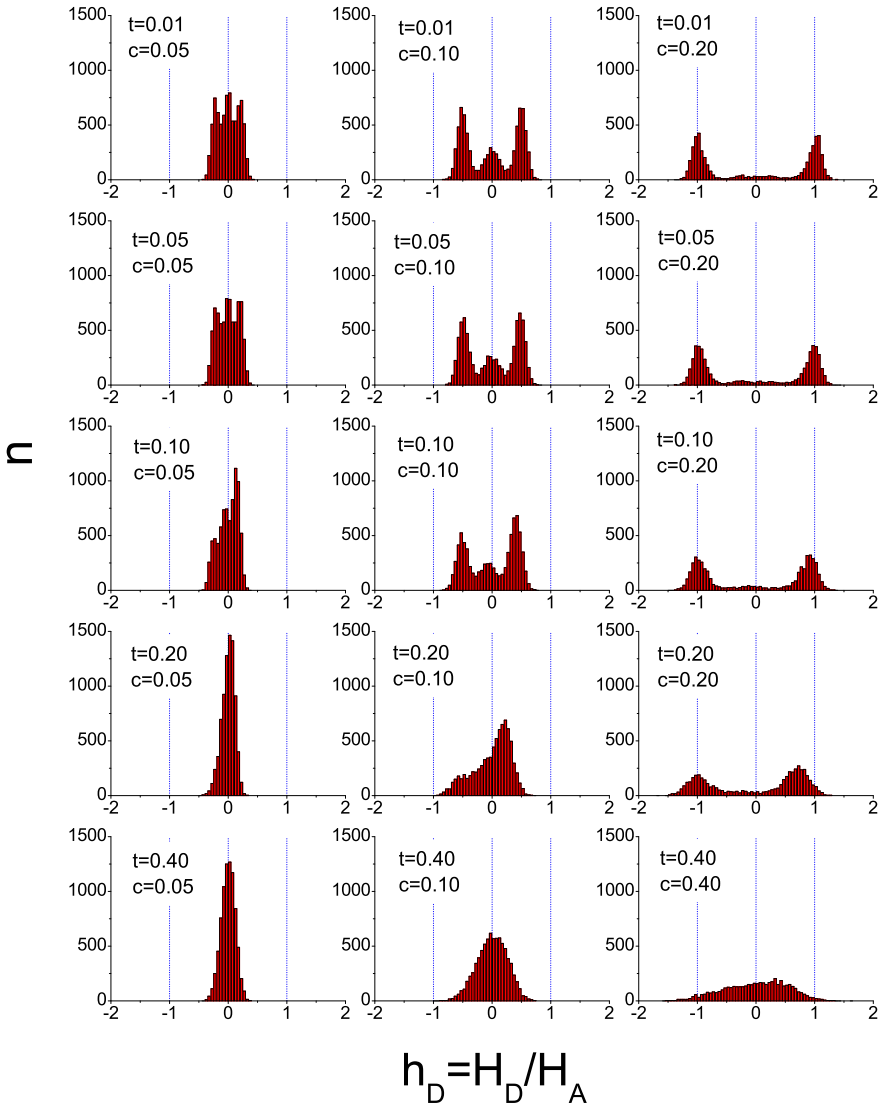

Figure 3.31:
Dipolar field-histograms corresponding to different interacting strength conditions ($c = 0.05, 0.10, 0.20$) at some selected temperatures $t = 0.01, 0.05, 0.10, 0.20, 0.40$.

agreement disappears with increasing temperature. Therefore, such results support our arguments about the need of considering the different situation of the particles in relation to the applied field to account for the influence of dipolar interactions, but suggest a very complex scenario in which temperature plays a fundamental role.

Conclusions The microscopic analysis of the influence of magnetic dipolar interactions on the magnetic properties of nanoparticles ensembles, and in particular on the t_B *vs* c evolution, suggest that the single-particle energy barrier models are not valid, and that the different characteristics of the particles as a function of their relative orientation with respect to the applied magnetic field and effective dipolar field have to be taken into account. In order to check our hypothesis, we proposed to account for the $t_B(c)$ curve a very simple model based on the idea that the particles can be classified into two subsystems, as parallel or antiparallel to the magnetic field, and that each subsystem could be related to its own blocking temperature. The detailed analysis of this naive approximation underlines its controversies with the theoretical background, what makes it not suitable to tackle that general problem. However, its good agreement for fitting the $t_B(c)$ curve gives support to our arguments on the need to consider the different dipolar fields acting on each particle and their relative orientation with respect to the applied field. In order to check this hypothesis, we have analyzed the dipolar field histograms of the system under different interacting conditions and temperature. The results show a complex and scenario in which our arguments are confirmed, but opens also the door to a systematic study on the properties of nanoparticle systems as influenced by dipolar interactions.

3.4 Use of c_0 as a magnetocaloric parameter

In previous sections we discussed the role of the c_0 parameter as a scaling factor for the influence of magnetic dipolar interactions. In the present one, we analyze its use for practical purposes, in particular its suitability as a magnetocaloric parameter. For such a purpose, we use the Monte Carlo method to study the entropy change and refrigerant capacity of an assembly of fine magnetic particles as a function of their anisotropy and magnetization, key-parameters of the magnetic behavior of the system. We focus our attention on the *anisotropy energy/dipolar energy* ratio by means of the related parameter $c_0 = 2K/M_S^2$ as representative of the magnetic properties of the system. Making to vary the value of c_0 parameter by choosing different $K-M_S$ combinations, allows us to discuss how the magnetocaloric response of an assembly of magnetic nanoparticles may be tuned by an appropriate choice of the magnetic material composition. We have obtained that the MCE strongly depends on the $K - M_S$ combination, and that the c_0 factor may be a useful parameter to choose the characteristics of the particles more adequate for a MCE-based implementation.

3.4.1 How to choose the best magnetic material?

As discussed in previous sections, the magnetic properties of fine magnetic particle systems are strongly dependent on external parameters as the magnetic field or the interparticle distances, what is useful for obtaining a specific desired MCE response. However, the MCE measured experimentally in nanoparticle systems [39, 97, 98] is lower than the one reported for bulk materials [99]. This makes necessary to determine the conditions under which this effect is enhanced. We have previously shown that for a system of magnetic nanoparticles it is possible to determine the sample concentration and magnetic field values for which the MCE is optimized [50, 55], and also how to choose particles with specific magnetic anisotropy for a desired magnetocaloric response [51]. The objective of the present section is to further determine the more adequate conditions for magnetic refrigeration using magnetic nanoparticles, starting from the more fundamental point: how to choose the magnetic material composition for a nanoparticle-based refrigerant implementation based on the MCE?

To investigate this, we have analyzed the magnetocaloric response of a wide variety of materials to fabricate the nanoparticles. The different types of particles were identified to the more representative parameters characterizing them, namely magnetic anisotropy K and saturation magnetization M_S, as related by the $c_0 = 2K/M_S^2$ parameter. This procedure allows us to evaluate the MCE as a function of this c_0 parameter by means of a systematic variation of K and M_S, which we can perfectly controlled by using a Monte Carlo technique (see Ref. [82] for computational details). The interparticle distances and applied magnetic field were kept constant in order to focus on the c_0-dependence, which was obtained from the systematic variation of K and M_S as shown in the diagram of FIGURE 3.32.

The different values of c_0 shown in the diagram of FIGURE 3.32 allow us to consider a wide range of different particles characteristics. Since c_0 provides and estimation of E_A/E_D (see Eq.(3.2.2)), the diagonal $c_0 \equiv 1.00$ represents comparable anisotropy and dipolar energies, i.e. $E_A \sim E_D$. The values in this diagonal allow us to know how the MCE in the nanoparticle system evolves for larger values of both magnitudes but keeping the same the ratio between them. For values $c_0 \succ 1.00$ (above the 1.00 diagonal) E_A dominates over E_D, i.e. $E_A \succ E_D$. The opposite scenario, in which dipolar dominates over the anisotropy one, i.e. $E_A \prec E_D$, occurs for values $c_0 \prec 1.00$ below the main diagonal.

In order to study how the magnetic response of the system varies through the different scenarios considered, we simulate the ZFC curves corresponding to all

$c_0 = \frac{2K}{M_S^2}$

$M_S^2 (10^5 emu^2/cm^6) \leftarrow$ \ $K(10^4 erg/cm^3) \rightarrow$	5	15	25	35	45	55
1	1.00	3.00	5.00	7.00	9.00	11.00
3	0.33	1.00	1.67	2.33	3.00	3.67
5	0.20	0.60	1.00	1.40	1.80	2.20
7	0.14	0.43	0.71	1.00	1.29	1.57
9	0.11	0.33	0.56	0.78	1.00	1.22
11	0.09	0.27	0.45	0.64	0.82	1.00

Figure 3.32:
Different $K - M_S$ combinations that cover a wide range of c_0-values. The diagonal $c_0 = 1.00$ represents the $K - M_S$ values for which $E_A \sim E_D$. The values above this diagonal ($c_0 \succ 1.00$) stand for $E_A \succ E_D$, and the values below the diagonal ($c_0 \prec 1.00$) stand for $E_A \prec E_D$.

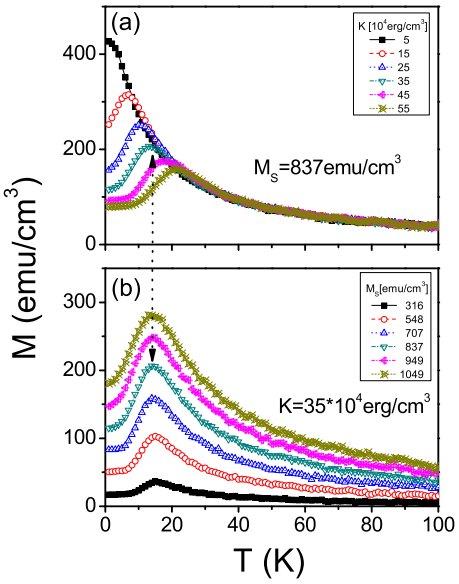

Figure 3.33:
ZFC curves for different $K - M_S$ combinations. FIGURE 3.33(a) shows how the K-dependence of the curve for the same M_S value. FIGURE 3.33(b) shows the complementary data: M_S-dependence for the same K value. The dotted double arrow signals the same K, M_S curve on both representations.

cases of FIGURE 3.32. Some representative curves to illustrate the different K,M_S-dependences are shown in FIGURE 3.33

In FIGURE 3.33(a), we show the ZFC curves corresponding to particles with the same magnetization but different anisotropy. The curves peak at larger temperatures and its magnitude diminishes for larger K values, accordingly to the results discussed in Ref. [51]. Meanwhile, FIGURE 3.33(b) shows the ZFC curves for particles with same anisotropy but different magnetization. The overall shape of the curves is very similar, with a peak corresponding to T_B that is nearly constant for

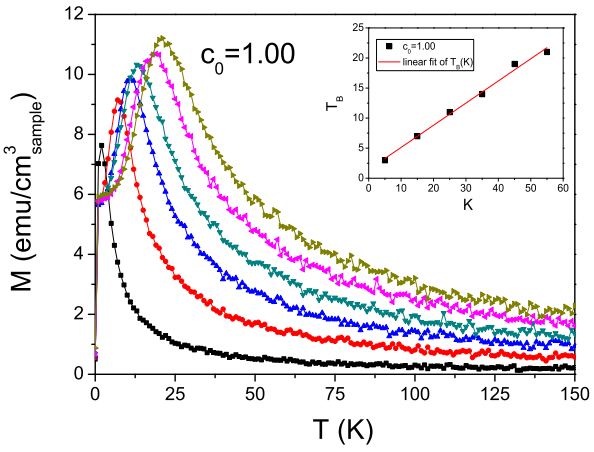

Figure 3.34:
ZFC curves for the different $K - M_S$ resulting in the $c_0 = 1.00$ diagonal of FIGURE 3.32. Inset shows the linear fit of T_B *vs* K.

different values of M_S, although a slight flatness is observed with larger M_S values (as expected since larger M_S values stand for higher interaction strength under the same K, c, and H conditions). However, it is different the magnitude of the magnetization at T_B, which increases with increasing M_S, also expected since the magnetic moment of the particles is bigger ($\mu \propto M_S$) and so the system can achieve a larger magnetization.

The results shown in FIGURE 3.33 have units of magnetization per volume of the particles. However, for an actual implementation of the MCE using magnetic nanoparticles, the results have to consider also the interparticle separation. Because of this, we shall give the results from now on with respect to the volume occupied by the sample. An example is shown in FIGURE 3.34, where the ZFC curves of the magnetic particles for the same $c_0 = 1.00$ value (main diagonal in FIGURE 3.32). The purpose of showing these curves is to illustrate the magnetic response of particles with the same characteristic c_0 value.

The ZFC magnetization curves displayed in FIGURE 3.34 exhibit a maximum that shifts to larger temperatures with increasing K, together with an enhancement of the magnetization at the maximum. Both tendencies are in agreement with the results plotted in FIGURE 3.33. Inset in FIGURE 3.34 shows the linear fitting of T_B *vs* K (see Ref. [51]). Regarding magnetocaloric properties, the slope of the curves plotted in FIGURE 3.34 diminishes with increasing M_S, what is equivalent to smaller entropy change. These MCE-related aspects are analyzed in detail in the next section.

3.4.2 Magnetocaloric properties in terms of c_0

We have computed the magnetic entropy change in the reversible part of the ZFC curves where the process is reversible, i.e. $T \succ T_B$, as usual. The ΔS_M data for the different cases considered in FIGURE 3.32 is plotted in FIGURE 3.35.

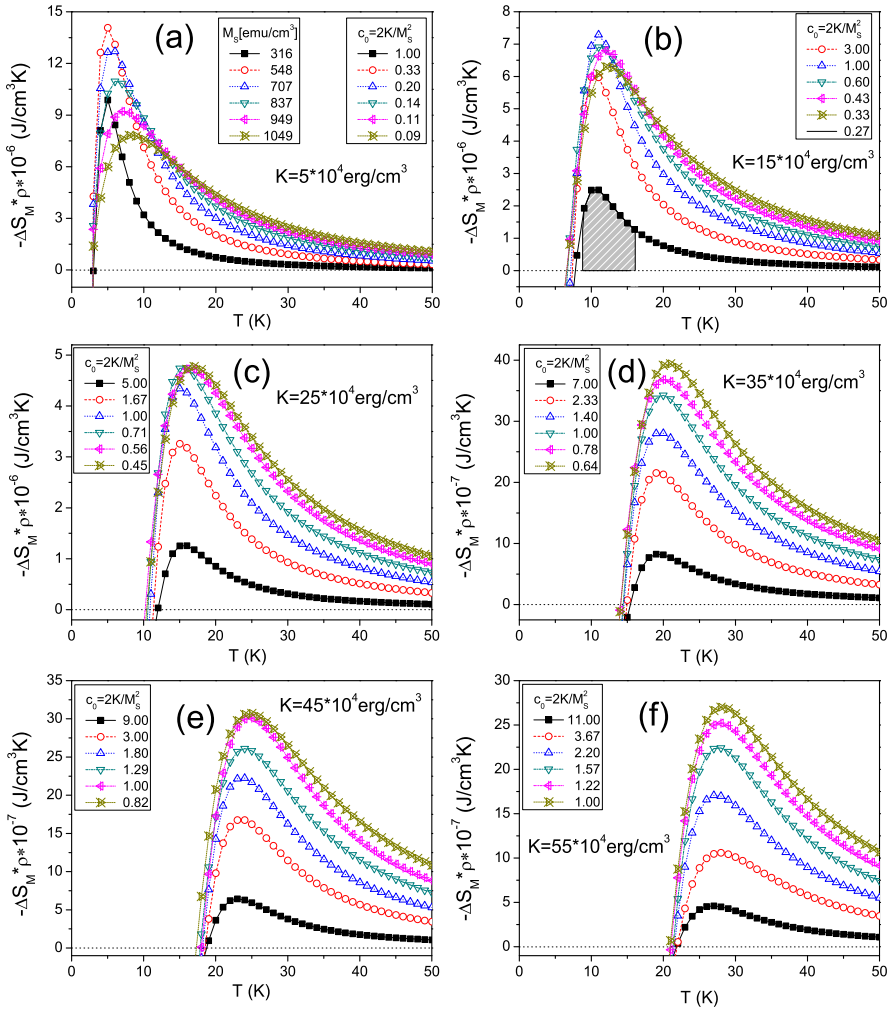

Figure 3.35:
$-\Delta S_M$ *vs* T curves for the different $K-M_S$ combinations shown in FIGURE 3.32. In every single graph, the $-\Delta S_M$ values for a different K-value are represented for the same values of the M_S, and also the correspondent c_0 value is shown. In FIGURE 3.35(a) appears listed the M_S values common to all curves displayed in FIGURE 3.35.

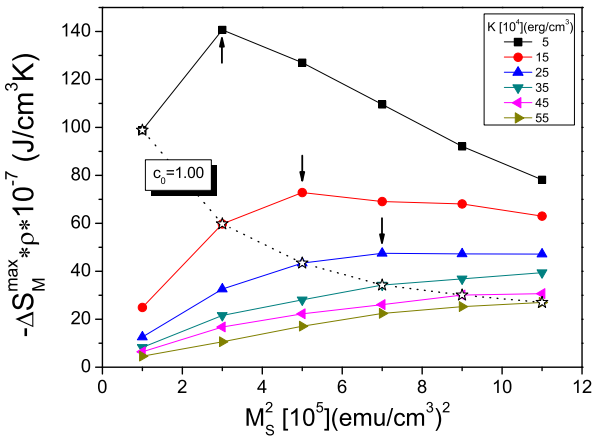

Figure 3.36: $-\Delta S_M^{max}$ values attained for a field change of $100Oe$, for the cases accounted in FIGURE 3.32. The dotted line links the $c_0 \equiv 1.00$ values. The arrows signal the absolute maximum for the low-anisotropy curves.

The general tendency observed in FIGURE 3.35 is that the $-\Delta S_M$ curves broaden with increasing K, and that the magnitude of the peak diminishes while its position shifts to higher temperatures, in agreement with Ref. [51]. However, when we examine in detail the behavior of the entropy curves in each graph, we discover that the tendency followed by the entropy curves is completely different at low K-values than at high. For the high-anisotropy cases the peak of the $-\Delta S$ curves continuously decrease with increasing M_S values, while for the low-anisotropy cases the peak initially grows, and later decreases in the general fashion. The maximum values of the magnetic entropy variation, $-\Delta S_M^{max}$, for all the cases represented in FIGURE 3.35 are plotted in FIGURE 3.36 for the comparison.

From FIGURE 3.36, we observe that the overall value of $-\Delta S_M^{max}$ attained diminishes for increasing values of K. The shape of the low anisotropy curves exhibits a peak (vertical arrows in FIGURE 3.36 which stands for a particular $K - M_S$ combination optimizing ΔS_M. This absolute maximum rapidly decreases and shifts to higher temperatures with increasing K (arrows in FIGURE 3.36). This feature results especially useful for choosing the characteristics of the particles that lead to an enhancement of ΔS_M for the MCE. In FIGURE 3.36 it appears remarked the ΔS_M data corresponding to the $c_0 \equiv 1.00$ values of the diagonal of FIGURE 3.32 (dotted line) with the purpose to understand how the maxima $-\Delta S_M^{max}$ values are placed onto the c_0 distribution. They show that the maximum entropy change for the same *anisotropy energy/dipolar energy* ratio diminishes for higher anisotropies, and that the special $K - M_S$ combinations leading to larger ΔS_M values are right above the $c_0 = 1.00$ curves. This characteristic signals the $c_0 = 1.00$ values as a key-point for choosing the more adequate $K - M_S$-materials. The distribution of the $-\Delta S_M^{max}$ values attained for the $K - M_S$ combinations of FIGURE 3.32 and

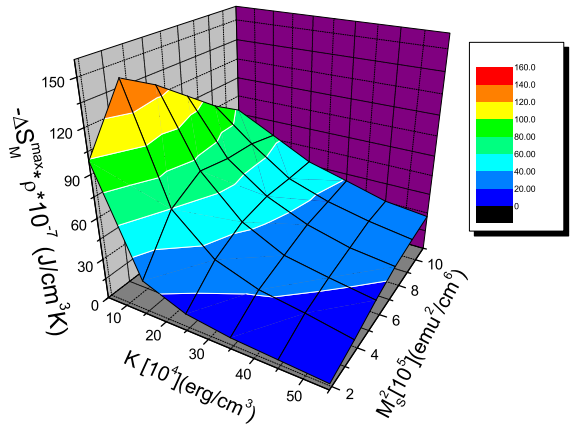

Figure 3.37: Negative magnetic entropy change for all the c0 values accounted in Table I (every c0 value given by the K-MS combination). This representation qualitatively describes the importance of the c0 value for the MCE.

displayed in FIGURE 3.36, it is also shown in a 3D-representation to have a more qualitative description of the overall scenario, as shown in FIGURE 3.37.

FIGURE 3.37 is a qualitative example illustrating how strongly the magnetocaloric properties of a magnetic nanoparticle system are driven by the particles' characteristics, i.e. the c_0 parameter. The variation of a factor of 5 in the anisotropy constant results in a variation of two orders of magnitude in ΔS_M, while different values of M_S as a function of K may result in an optimal enhancement of the entropy variation, as it was previously discussed after FIGURE 3.36.

From the results shown in Figs.3.36.3.37 it could be inferred that the most appropriated conditions for magnetic refrigerants based on the MCE are those of low K and the particular M_S value at which $-\Delta S_M$ is maximized. However, as explained in SECTION 1.4, to appropriately choose a magnetic material for magnetic refrigeration not only the ΔS_M value must be considered, but also the RC (i.e. the amount of heat that can be transferred in one thermodynamic cycle) should be taken into account. The shaded area in FIGURE 3.35(b) represents an example of the RC.

So, depending on the magnetic refrigerating process we are interested on, not only the maximum magnetic entropy attained is important, but also how the temperature working range must be considered in the shape of the entropy curve (the shape of the curves broadens with increasing K and M_S, widening the working temperature range). The RC values and the respective working temperature range $T_{hot} - T_{cold}$ (defined as usual as the temperaratures at half maximum peak of the entropy curve) are shown in FIGURE 3.38 for the $K - M_S$ combinations of FIGURE 3.32.

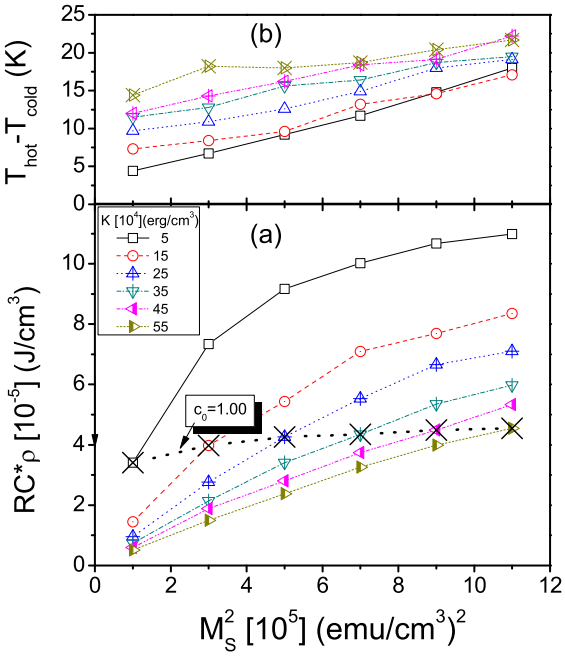

Figure 3.38: (a) RC for the different c_0 values considered in FIGURE 3.32. Every curve stands for a different K-value. The dotted line stands for the $c_0 = 1.00$ values. (b) Working temperature range ($T_{hot} - T_{cold}$) for the same $K - M_S$ combinations.

From FIGURE 3.38(a) we observe that the RC is larger the smaller is K and the greater is M_S. This behavior is monotonic, not showing any special $K - M_S$ combinations leading for a larger RC. The RC values correspondent to the $c_0 = 1.00$ case remain basically constant, demonstrating that to obtain a particular RC any $K - M_S$ combination accounting for $c_0 = 1.00$ would transfer the same amount of heat. In FIGURE 3.38(b) the correspondent temperature working ranges are plot, being observed their increase with larger K and M_S. This feature is very important from the point of view of real MCE-based implementations, showing how to choose the K and M_S in order to fit a desired temperature working range with no loss of the transferable amount of heat. It remains as an interesting task for a future work to investigate this entropy variation through different $K - M_S$ combinations leading to different c_0 constant ratios.

Conclusions We have studied the MCE in a fine magnetic particle system from the point of view of the characteristics of the particles. We introduced the parameter $c_0 = 2K/M_S^2$ to characterize them, and systematically varied K and M_S in order to cover a wide range of c0 values. For a fixed sample concentration, under the same magnetic field change, we computed the MCE properties of the system evaluating ΔS_M and RC. We found that at low values of K it is possible to fit

the adequate $K - M_S$ combination leading to a larger $-\Delta S_M$ value. The overall $-\Delta S_M$ is higher the smaller the K, and diminishes with increasing M_S. For the constant $c_0 \equiv 1.00$ cases, $-\Delta S_M$ diminishes with increasing K and M_S. On the contrary, the RC values grow with increasing M_S, which become larger for smaller values of K. It calls our attention that for the $c_0 = 1.00$ cases the RC remains practically constant. This feature is especially remarkable from the point of view of practical implementations, showing that a correct choice of the c_0 parameter by means of the adequate $K - M_S$ combination may set a desired working range for magnetic refrigeration.

In summary, we have shown that the magnetocaloric properties of a fine magnetic particle system are strongly dependent on the material properties, which may be properly described by using the characteristic dimensionless material constant c_0.

4

Nanoparticle chains

Recently, much investigation has being focused on the synthesis and magnetic characterization of 1D-arrangements of magnetic nanoparticles [100–102]. This is motivated by their promising technological potential [103], particularly to increase the storage density data [104] and for digital processing [105]. In such 1D-nanostructured systems, the interplay between the magnetic anisotropy and the interparticle dipole-dipole interaction is the main key-point determining the magnetic properties of the system, for the relationship between both energy terms constitutes a complex problem that turns out to be non trivial. Although ferromagnetic (FM) order along the nanoparticle chain can be easily predicted from minimum energy arguments [106], however the opposite behaviour, that is antiferromagnetic (AFM) order along the chain has been experimentally observed [101]. Also, it has been theoretically calculated that in non-interacting particle systems, uniaxial magnetic anisotropy can be misinterpreted as FM or AFM coupling depending on the relative angle between the magnetic field and the anisotropy easy axes [107], what adds more factors to take into account in an already very complex system.

With respect to the applied viewpoint of magnetic refrigeration, the role played by the magnetic anisotropy is receiving a growing attention lately based on its importance for tailoring the magnetocaloric response of the system, as it has been recently reported for an ordered array of non-interacting oriented uniaxial magnetic objects under the effect of an external field H, perpendicularly applied respect to their easy-magnetization uniaxial anisotropy axes [27]. Hence, understanding the interplay between the magnetic anisotropy and dipolar interaction energies constitutes not only an interesting scientific problem, but also from the applied point of view due to its relevance for technological applications. On this basis, we have carried out a detailed analysis of both the magnetic and magnetocaloric properties of

a system of dipolar interacting magnetic nanoparticles collinearly arranged in 1D-nanoparticle chains. This system is very representative to compare not only with particle chains but also with highly-anisotropic systems as magnetic nanowires [28], and hence its relevance. By means of the usual MC technique we study the nature of its magnetic ordering resulting from the interplay between dipolar and anisotropy energies. The computational technique provides us two different data sources to study the system: a macroscopic approach (averaging the macroscopic parameters, magnetization vs. temperature), and a microscopic one (direct observation of the temperature evolution of the magnetic moment of each single nanoparticle). The information provided by both approaches is discussed and compared with other results previously reported in the literature. Next we study the magnetocaloric properties, obtaining coexistence of direct and inverse MCE both of reversible character. Having focused on the direct-MCE due to its much larger temperature range, we have found the existence of a particular field H^* that optimizes both ΔS_M and RC. This field is larger than the anisotropy of the particles, $H^* \approx 2.5 H_A$, and likely arises from the contribution of the enhanced dipolar coupling along the chains, which in fact acts like an extra anisotropy source. With the purpose to have a further insight into the physical origin of this optimizing field H^* we have analyzed the system from the $M(H)$ curves, and we have obtained that at that field the system exhibits typical features of a phase transition.

4.1 Magnetic ordering in 1D-chains

With the purpose to understand the physical nature of the magnetic interaction in the 1D-nanoparticle chain arrangement we have analyzed its temperature evolution from two different approaches: a macroscopic mean-field treatment on the averaged magnetization of the system, and a microscopic single-particle magnetic moment analysis. For the macroscopic study, we have simulated zero field cooling ZFC and FC magnetization curves for different values of the applied field analyzing the evolution of the macroscopic averaged magnetization value with temperature. For the microscopic one, we have recorded the evolution along temperature of the magnetic moment of each single particle in the same ZFC/FC processes, to directly study the magnetic evolution of the system *vs* temperature from its individual components. In the next subsections we present each approximation employed in each scenario and discuss the results obtained.

The simulated system consists of $N = 250$ nanoparticles distributed in a net of relative positions $(\Delta x, \Delta y, \Delta z) = (0.067, 0.200, 0.200)$. Each single chain consists of

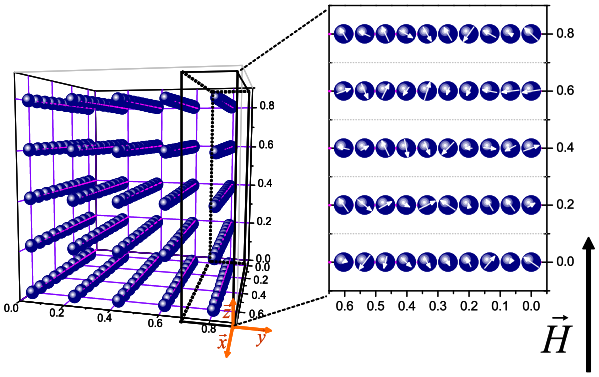

Figure 4.1:
Schematic representation of the simulated system. Left panel stands for the particle chains in the YZ-plane square distribution that extend along the X-direction. Right panel exemplifies a set of 5 chains in the XZ-plane view, showing a snapshot of the magnetic moments of the nanoparticles.

10 particles aligned along the x-direction, and so the system consists of 5×5 parallel chains of 10 particles in length in a square distribution on the YZ plane. Periodic boundary conditions are assumed (see Ref. [108] for computational details). An schematic drawing of the simulated system is shown in FIGURE 4.1

Ordered structures as those shown in FIGURE 4.1 result in an enhanced anisotropy along the chain, resulting from the preferential coupling of the magnetic moment along the structure. This preferred alignment direction constitutes an extra anisotropy source, and therefore it is important to understand the interplay between the magnetic anisotropy of the particles, defined by their easy axes, and the chain-direction. In order to study both contribution we have carried out a differentiated analysis, considering i) collinear easy axes along the chain, and ii) non-collinear easy axes along the chain, and for both situations a detailed analysis of the intra- and inter-chain magnetic arrangement has been carried out.

4.1.1 Collinear easy axes

In this section the uniaxial easy anisotropy axes of the particles are all collinear aligned along the particle chains. The perpendicular application of a magnetic field gives place to an interesting theoretical scenario in which the field does not favour one anisotropy well over the other, as in usual SPM random systems. The purpose of the next sections to characterize the ordering properties of such system, starting from the usual ZFC/FC macroscopic properties, and complemented by a insightfull microscopic analysis of the individual magnetic moments of the particles.

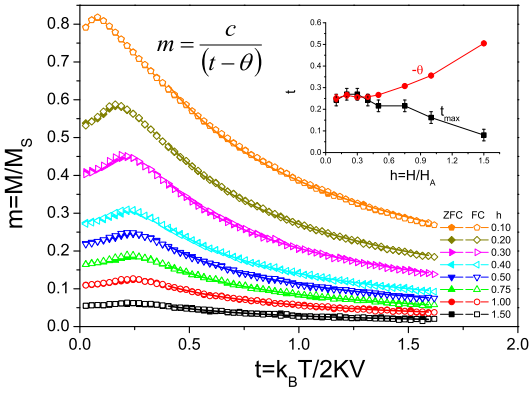

Figure 4.2:
ZFC (full symbols) and FC (empty symbols) curves for different values of the applied magnetic field. Inset shows the field dependence of the maxima of the curves (vertical arrows in the main panel) and the θ values obtained from a Curie-Weiss fitting.

4.1.1.1 Macroscopic approach

We simulated the magnetic response of the system under ZFC and FC conditions analyzing its field dependence. Such processes are commonly used to study the magnetic properties of magnetic nanoparticle systems due to the useful information they provide about the magnetic properties of the system. As described in SECTION 1.2, they are usually characterized by i) a PM-like dependence at high temperatures, where both ZFC and FC curves coincide, ii) a splitting between both curves with the decreasing of the temperature, with the ZFC one slightly diminishing its growing rate until it reaches a maximum, and iii) below this maximum the ZFC curve decreases with decreasing T, while the FC one keeps growing although at a lower rate. The maximum in the ZFC curve roughly corresponds to T_B [109, 110]. In the ideal non-interacting case T_B is expected to disappear at applied fields $H > H_A$ ($h > 1.0$ in reduced units), although other factors as the interparticle interactions may extend its existence to larger fields [56]. However, those characteristics of the ZFC and FC curves are not observed in a system of dipole-dipole interacting magnetic nanoparticles distributed into parallel 1D-chains with collinear anisotropy axis under a perpendicular magnetic field [28]. Although the PM-like dependence is observed at high temperatures and also the maximum in the ZFC curve, there are however eye-catching features different from the characteristics above described as the coincidence of both ZFC and FC curves at low temperatures, and the existence of the maximum even for fields $h > 1.0$. In FIGURE 4.2 we show the ZFC and FC m(t) curves for different field values perpendicularly applied to the easy axes of the particles (i.e. perpendicular to the nanoparticle chains).

The curves plotted in FIGURE 4.2 show two distinctive features. First, both ZFC and FC processes coincide for the whole temperature range, indicating reversibility. Second, the curves exhibit a maximum, t_{max}, above which the ZFC-FC curves follow

a paramagnetic-like behaviour that shifts towards smaller t values with h increasing. The coincidence of the ZFC and FC curves in the whole temperature range means that the particles are not "blocked" at low temperatures, indicating that t_{max} stands for a different feature than the usual one obtained for a SPM system below T_B (i. e., it does not indicate the transition between the blocked and the SPM states). In fact, as the magnetic field is perpendicularly applied to the anisotropy axes of the particles, none of the anisotropy directions is favored, and so the peak of the curves must have a different physical meaning than the jumping temperature of the magnetic moment between the two anisotropy wells. The general shape of the curves strongly reminds the one observed for AFM materials, which exhibits an initial magnetization increase until the ordering temperature (θ) is reached, followed by a PM-like dependence. To analyze the possibility of the peak to account for an ordering temperature (Ω), we have fitted the thermal dependence of magnetization in the range of temperatures well above t_{max} to Curie-Weiss law $m = c/(c - \theta)$. The results are shown in the inset of FIGURE 4.2 for the different values of applied field considered, together with the values of t_{max}. A negative θ value is obtained suggesting an AFM-type magnetic ordering. The coincidence between t_{max} and *theta* in the low-field regime reinforces the idea of magnetic ordering temperature. Simulations carried out at different computational times indicate that t_{max} and θ are time-independent, a fact that also supports an AFM-ordering temperature scenario. The error in the determination of t_{max} is given by the temperature variation step, whereas the error of θ is smaller than the symbol size. Moreover, it must be emphasized that the c-fitting parameter grows linearly with increasing field, as expected from Curie-Weiss dependence.

From the results above discussed, it seems to be clear the AFM character of the system, with the magnetic ordering temperature found as

$$lim_{h\to 0}\,[\theta] \equiv lim_{h\to 0}\,[t_{max}] \equiv \Omega \tag{4.0}$$

However, at this stage it is very important to make some observations about the adequacy of using a mean-field theory when dealing with assemblies of magnetic nanoparticles, and about the reliability of the conclusions attained. It has been theoretically demonstrated that a Curie-Weiss approach leads to AFM-type order in a non-interacting particle system when the direction of the applied magnetic field is perpendicular to the easy anisotropy axes of the particles [107]. With the aim to understand the role played by the magnetic anisotropy, the dipolar interaction, and its combined influenced on the shape of the ZFC and FC m(t) curves, we show in FIGURE 4.3 both processes for the same magnetic field value of $h = 0.1$ considering

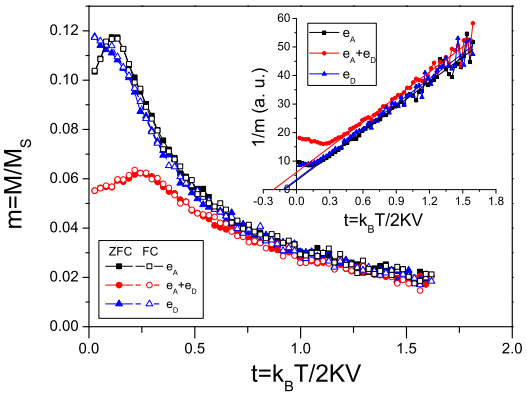

Figure 4.3:
ZFC (full symbols) and FC (empty symbols) magnetization as a function of temperature curves in reduced units m(t) considering different energetic contributions: (a) magnetic anisotropy and dipolar energies both together (circles); (b) dipolar energy only (triangles), and; (c) anisotropy energy only (squares). Inset shows the inverse of the ZFC magnetization curves vs. temperature.

the three following possibilities: interplay between anisotropy and dipolar energies (circles), dipolar energy only (triangles), and anisotropy energy only (squares).

The thermomagnetic curves shown in FIGURE 4.3 illustrate the peculiar features associated with the different energetic contributions. Both the ZFC and FC processes practically coincide for the three cases considered, and so from now on we shall refer to the different curves making no difference between both curves, just among the different considered energies. When solely the magnetic anisotropy is present in the system the curve exhibits a maximum, and the inverse of the susceptibility points to an AFM-like alignment in the Curie-Weiss mean field treatment (as the inset states). This result coincides with the described by Vargas et al. [107] that uniaxial magnetic anisotropy acts similarly to AFM coupling under a magnetic field applied perpendicular to the uniaxial easy anisotropy axes. When the magnetic anisotropy is not taken into account and the dipole-dipole interacting energy is the only internal contribution governing the magnetic behaviour of the system, the shape of the curve is quite different. At high temperatures (roughly above the maximum of the only-anisotropy curve) the dipolar interacting curve follows a paramagnetic-like dependence. However, at temperatures below the maximum the curve rapidly reduces its growing rate, showing something similar to a plateau. The inverse-susceptibility curve for this case (see inset) shows the same tendency of the anisotropy contribution, indicating an AFM-type coupling when extrapolating the curve from high-temperature values. Interestingly, the value of θ obtained is quite comparable to that of the only-anisotropy curve. When the combined influence of magnetic anisotropy and dipolar interaction is taken into account for the magnetic behaviour of the system, the curve exhibits the characteristics displayed and discussed in FIGURE 4.2.

In summary, our MC simulations agree with the previous results reported by Vargas et al. [107], establishing that the Curie-Weiss approximation is not an adequate scenario to study the magnetic ordering of magnetic nanoparticles since it leads to wrong interpretations when the magnetic field is applied perpendicular to the easy anisotropy axes. In view of this, we shall study the magnetic ordering of the system in a different manner, directly observing the thermal evolution of the individual magnetic moments.

4.1.1.2 Microscopic approach

We have recorded the temperature evolution of the magnetization of each particle while varying the temperature, and analyzed the snapshots of the magnetization of the whole system at different temperatures. We have focused this analysis in the magnetization behaviour when cooling with zero field in order to observe any spontaneous ordering in the magnetic configuration of the nanoparticles ensemble. In FIGURE 4.4, we display snapshots of the magnetic configuration of some selected nanoparticle chains (y = 0.8) on the XZ-plane.

In FIGURE 4.4, we show the snapshots of the magnetic configuration for the $y = 0.8$ chains projected in the XZ-plane at some selected temperatures respect to the maxima t_{max} of the $h = 0.1$ ZFC curve. Different external conditions for applied field are shown. In the first column left we show the $h = 0.0$ case, the one in which we are more interested in since it may show some spontaneous magnetic ordering effect. Center and right columns show the $h = 0.1$ and $h = 1.0$ cases, respectively, to give an idea of the effect of the external magnetic field on the orientation of the single magnetic moments of individual particles. Focusing on the $h = 0.0$ case, we clearly observe the transition from an overall disordered state at high temperatures, to a FM-like intra-chain ordering at low temperatures, where AFM-type inter-chain ordering is also observed. Similar behaviours are observed for the other chains of particles, although we only plot this case for sake of simplicity on its qualitative understanding. Interestingly we make note that some chains are broken into two different FM-like groups having opposite orientations. The origin of the broken intra-chain ordering might be found in the influence of the magnetic anisotropy, which hinders the intra-chain magnetization reversal process leading to the minimal-energy FM-like parallel array of the particles. We shall come back later to this point, when analyze the behaviour of the system without magnetic anisotropy. Let also mention here the absence of a regular AFM inter-chain ordering. The magnetic arrangement of the chains exhibits nor a perfectly nor a regular nearest-neighbour AFM-like alignment in the YZ-plane. This effect can be

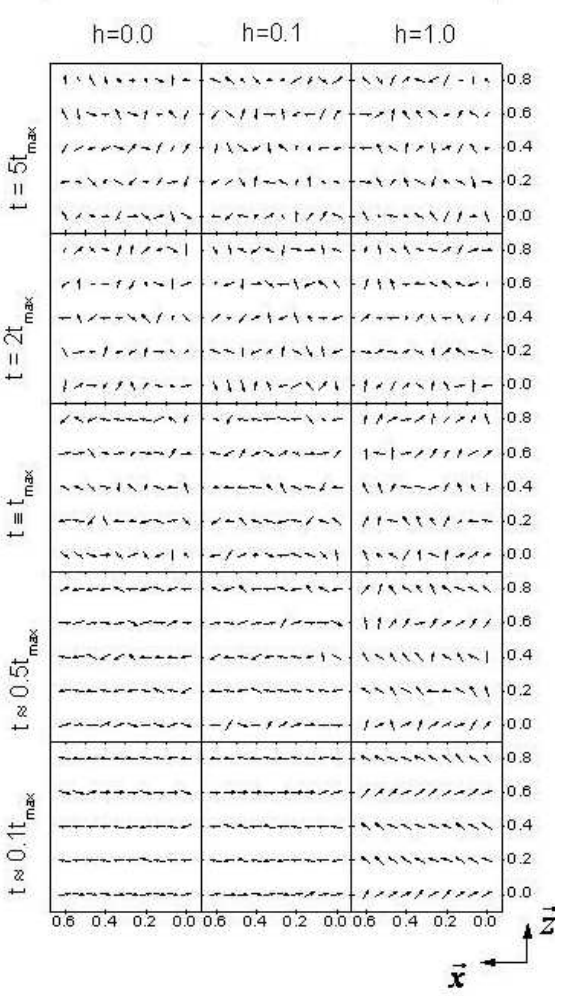

Figure 4.4:
XZ-snapshot of the magnetic moments for the particular set of chains located at $y = 0.8$, at some selected temperatures chosen above and below the maximum of the ZFC/FC curve and the applied magnetic field values, $h = 0.0$, 0.1, and 1.0..

explained by the large difference between the intra-chain dipolar field favouring the FM-type alignment and the inter-chain dipolar field that favours the inter-chain AFM-like arrangement. The latter is about 26 times smaller than the first one, and consequently it is unable to generate a complete chain-reversal magnetization process leading to a perfectly regular inter-chain AFM-like arrangement. The intra- and inter-chain reversal mechanisms are time-dependent (larger times, imply more chances to reverse the magnetization) and therefore we have simulated the evolution of the magnetization for much larger number of MC steps (until 140000 MC steps) in order to check the time-dependence of the inter-chain arrangement. No noticeable effects on the magnetic configuration were observed, suggesting that larger time-scales are required in order to reach magnetization reversal of entire chains [111].

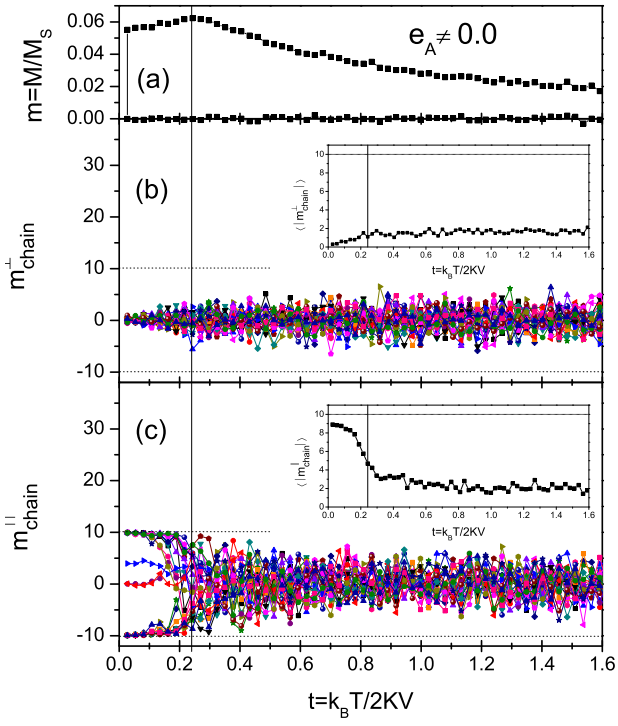

Figure 4.5: Magnetization projection *vs* temperature for h = 0.0, perpendicular (b) and along (c) the chains. (a) shows the ZFC curve for h = 0.1. The vertical solid line is a guide to indicate the position of tmax. Insets in (b) and (c) show the averaged absolute values of the magnetization along the chains.

The effect of the applied magnetic field ($h = 0.1$, $h = 1.0$) on the magnetic configuration is included to illustrate the influence of the external field on the magnetic state of the sample. It points out the practically negligible deviation from the easy axes at the small field value $h = 0.1$, what supports the use of this value in a low-field inverse susceptibility mean-field approximation. For the $h = 1.0$ case the magnetostatic dipolar interaction opposes to the alignment of the magnetic moments along the field direction. In the case of the magnetic moments are allowed to reach an angle larger than 45 from the easy anisotropy axes, its dipolar-field component in the external field would try to reverse the neighbouring particles' moments, and reciprocally.

From FIGURE 4.4, it is clear the existence of intra-chain FM-like ordering and inter-chain AFM-like one. With the purpose to study both aspects and going further into the magnetic behaviour study of the system, we select now each chain as a proper magnetic entity and analyze its temperature evolution. We show in FIGURE 4.5 the magnetization *vs* temperature data along and perpendicular to the 1D-chains axis, at zero applied field.

The total magnetization of every YZ-chain is defined as

$$\vec{m}_{yz} = \sum_{i=1}^{10} \vec{m}_i \tag{4.0}$$

and so the maximum possible value of magnetization for each 1D-chain is 10. The y, z-variation stands for every different particle chain that extends along the x-direction. In FIGURE 4.5, the temperature evolution of the magnetization of the nanoparticle chains is recorded along the chains axis ($m^{\parallel}_{chain}$) and perpendicular to them ($m^{\perp}_{chain}$), the respective averaged magnetization values, $\left\langle \left| m^{\parallel}_{chain} \right| \right\rangle$ and $\langle |m^{\perp}_{chain}| \rangle$, being introduced as the corresponding macroscopic order parameters. FIGURE 4.5(a) shows the temperature dependence of the magnetization along the field direction for $h = 0.1$, while cooling the system at zero field (i.e. $h = 0.0$, and so the average magnetization zero), and when heating the sample under the applied field. This process is shown to facilitate the comparison of the magnetization processes inside every chain with respect to the maxima observed in FIGURE 4.2. The vertical solid line signals the maximum of the ZFC curve that roughly corresponds to θ, as shown in the inset of FIGURE 4.2 and discussed in the text (see subsection *Macroscopic approach*). FIGURE 4.5(b) shows the situation with perpendicular magnetization for the whole array of 1D-chains. The horizontal dotted lines indicate the maximum magnetization possible for every chain (i.e. 10), which would stand for a parallel orientation of all the particles' moments inside one chain. It must be noted the overall non-zero moment at high temperatures due to the thermal disorder, and the disorder reduces when the temperature tends to zero. This is more visible in the inset of FIGURE 4.5(b), where is plotted $\langle |m^{\perp}_{chain}| \rangle$ as a function of temperature. Interestingly, this value approximately decreases with temperature for $t < t_{max}$ (t_{max} indicated by the vertical dotted line). FIGURE 4.5(c) shows the magnetization of the chains along their longitudinal direction, being observed two main features differing from the perpendicular case. First, the disorder observed at high temperatures is greater than the one observed in the perpendicular direction. Second, at low temperatures the magnetization of the chains starts to grow, reflecting an intra-chain FM-order at low temperatures. This FM-type internal ordering splits the chains into two subsystems of opposite sign, what indicates the occurrence of AFM-type ordering between them. Both components tend to saturation to the maximum possible value (i.e. 10), although some chains do not reach saturation and keep low magnetization values (around 0, 4) roughly constant with temperature. Inset in FIGURE 4.5(c) shows the averaged absolute values of these tendencies, $\left\langle \left| m^{\parallel}_{chain} \right| \right\rangle$. At high temperatures it is observed a larger average

magnetization value than for the perpendicular case as well as a tendency to increase at low temperatures, although the maximum value attained does not reach the maximum possible value. No clear correlation was observed with the ordering temperature Ω as discussed from FIGURE 4.2 (indicated by the vertical dotted line).

The simulations shown in FIGURE 4.5 demonstrate that in absence of an external field the magnetization of the system spontaneously orders at low temperatures, forming intra-chain FM-like entities with inter-chain AFM order. The existence of "broken" chains discussed after FIGURE 4.4 is reflected in the non-saturating magnetization value of some chains. At this point some open questions still arise veiled: what might be the origin of the broken magnetization inside some of the chains? Why the AFM-like disposition between the chains is irregular? It is clear that it must be the magnetostatic dipolar interaction, the only interparticle interaction present in the system, the responsible mechanism for the observed spontaneous orientation of the magnetic moments inside the chains. It is also noticeable the important role that the magnetic anisotropy plays in the magnetization reversal process of the magnetic moments along the chain (as it has been discussed from FIGURE 4.3). For a better understanding of the role played by the magnetic anisotropy onto the resulting magnetic ordering of the system and trying to answer the abovementioned questions, two next steps have been considered. Firstly, we have analyzed the same properties as in FIGURE 4.5, but considering only the magnetostatic dipolar interaction between the particles vs. temperature, to eliminate the influence of the magnetic-anisotropy as a preferential orientation for the magnetic moments inside the chains. Secondly, we also analyzed the magnetic behaviour of the system for a random distribution of the anisotropy easy axes. FIGURE 4.6 displays the similar scenario as shown in FIGURE 4.5, but considering the dipolar interaction as the only energy driving the magnetic behaviour of the system as a function of the temperature.

FIGURE 4.6(a) shows the ZFC m(t) curve, where no maximum should appear as discussed in FIGURE 4.3, and its inset shows the ordering temperature as a function of the applied magnetic field. FIGURE 4.6(b) shows that the perpendicular component of the magnetization, exhibits a similar behaviour to the case with magnetic anisotropy. But it is in FIGURE 4.6(c) where the difference between both cases is pointed out: all the magnetic chains reach the maximum possible magnetization value at low temperatures (see also the inset of FIGURE 4.6(c)). Therefore, it is demonstrated that in absence of magnetic anisotropy complete intra-chain FM order can be found.

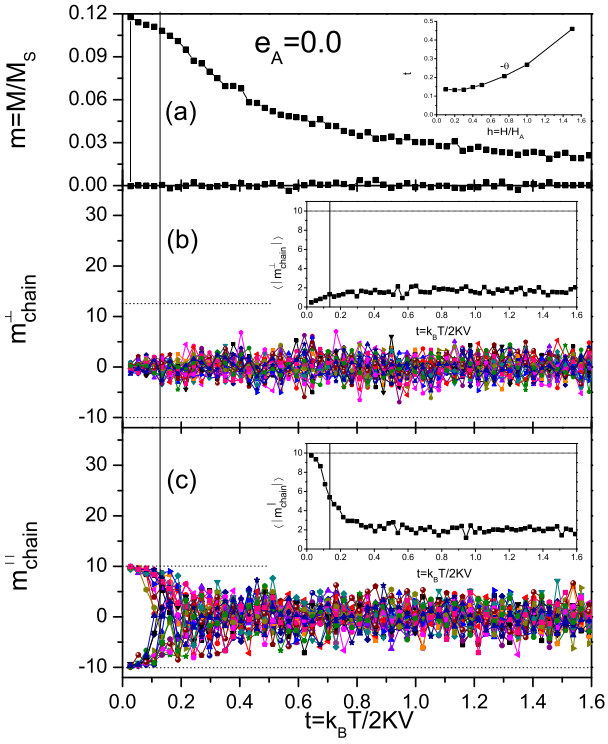

Figure 4.6: Magnetization projection vs. temperature for h = 0.0, perpendicular (b) and along (c) the chains axes, when the dipolar interaction is the only internal energy driving the magnetic behaviour of the system. (a) shows the ZFC h = 0.1 m(t) curve. The vertical solid line serves as a guide to illustrate $lim_{h\to 0}[\theta]$. Insets of (b) and (c) show the averaged absolute values of the magnetization along the chains axes.

However, the spontaneous FM-type order observed does not arise at a well-defined value, but extends over a wide temperature range as in the case with anisotropy (FIGURE 4.5. The lack of a well-defined change in the macroscopic order parameters, $\left\langle \left| m^{\parallel}_{chain} \right| \right\rangle$ and $\left\langle \left| m^{\perp}_{chain} \right| \right\rangle$, reflects the complexity of the system, where the magnetic order generated by the dipolar interactions is distorted by the dynamical effects arising from the anisotropy barrier, or, in the case analyzed in FIGURE 4.6, by the anisotropy induced by the dipolar interaction itself[1]. With regard to the YZ-plane, we observe that the AFM arrangement is still not perfectly regular. In this inter-chain scenario we reproduce similar results that with magnetic anisotropy, what indicates that larger time-scales are also required to reverse an entire chain even when no magnetic anisotropy is present [111].

[1]For more information about the interplay between the dynamical effects (associated with the blocking temperature) and phase transitions (associated with dipolar interactions) in nanoparticle systems see for example Refs. [112, 113].

4.1.2 Non-collinear easy axes

Until now, we have evidenced that magnetic nanoparticle chains exhibit intra-chain FM order together with AFM inter-chain one at low temperatures. The 1D-chains exhibit a "broken" FM order when the nanoparticles arrange their uniaxial magnetic anisotropy axes parallel aligned to the chains, while the AFM order it not fully regular regardless of existing or not magnetic anisotropy. However, our results indicate a different magnetic ordering than the one recently reported by Bliznyuk et al. [101] These authors experimentally found intra-chain AFM order in 1D chains of Ni nanoparticles. We believe that this different magnetic ordering is originated by a different orientation of the easy anisotropy axes, since the splitting between the field cooling and field heating magnetization curves indicates non-perpendicular orientation of the magnetic field with respect to the anisotropy axes. In fact, AFM coupling between nanomagnets arranged in linear chains remaining confined in a plane can be observed if the magnetic anisotropy axes lie transverse to the longitudinal chain direction [114]. In order to investigate the influence of non-collinear anisotropy axis distribution we treat the problem in the most general case, when considering randomly oriented anisotropy easy axes and analyzing the magnetic properties of the system in the same way as for the parallel-aligned case. Aimed with such a purpose, we have simulated the similar scenarios as those considered in FIGURE 4.2, but in this case of random easy-axes distribution. In this particular situation, the ZFC and FC magnetization curves resemble the usual superparamagnetic features, with the characteristic splitting between the ZFC and FC curves at low temperatures. In FIGURE 4.7, we show the most representative features of the magnetic behaviour of the system in order to compare with the collinear-anisotropy case.

The ZFC and FC curves for the $h = 0.1$ and $h = 0.2$ cases are shown in the top panel of FIGURE 4.7 to illustrate the difference with the parallel-aligned anisotropy case. The fitting of the inverse susceptibility to a Curie-Weiss-like dependence in the high-temperature regime (i.e. well above t_{max}) indicates AFM-like behaviour with negative θ-ordering parameter, being also observed the coincidence between t_{max} and $(-\theta)$ in the $h \to 0$ limit (as shown in the inset). Bottom panel in FIGURE 4.7 shows the XZ-snapshots of the magnetic configuration for three different representative temperature values for the magnetic properties of the system: $0.2t_{max}$, t_{max}, and $5t_{max}$. The snapshots clearly illustrate that the system does not attain any type of intra-chain FM-like order at any temperature, but instead of that shows some kind of irregular AFM-like intra-chain order. Therefore, this demonstrates that

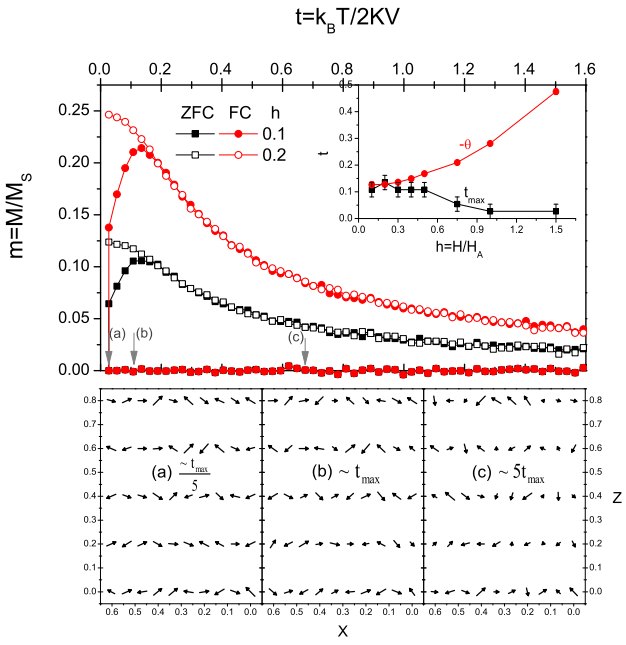

Figure 4.7:
Top panel: ZFC and FC magnetization curves m(t) for field values $h = 0.1$ and $h = 0.2$. Inset shows the field dependence of θ and t_{max}. Bottom panel: snapshots of the magnetic configuration at some representative temperatures, (a) $\approx t_{max}/5$, (b) $\approx t_{max}$, and (c) $\approx 5t_{max}$.

the spatial distribution of the easy anisotropy axes is the key-parameter responsible for the magnetic ordering in this kind of 1D-nanoparticle system assemblies: a collinear distribution leads to FM-like intra-chain order, whereas the random-easy-axes distribution leads to an AFM-like order. However, it still remains an open unsolved question with respect to the type of magnetic ordering in these kinds of 1D-structures, which is to determine the frontier between the FM-like and the AFM-like magnetic ordering. At this point of the research we recognize that the next issues we must face to characterize the resulting magnetic ordering in 1D-assemblies of magnetic nanoparticle systems is the effect of the relative orientation of the easy anisotropy axes with respect to the nanoparticle-chain longitudinal direction, together with the relative strength of the dipolar interaction related to the anisotropy energy.

Conclusions From the macroscopic point of view of fitting the magnetization to a Curie-Weiss mean-field approximation we have found that a mean-field treatment is not adequate to study the magnetic behaviour of nanoparticle chains with collinear easy axes, in agreement with Ref. [107], since incorrect interpretations regarding the magnetic properties of the system might be inferred. The microscopic analysis of the system shows the occurrence of spontaneous intra-chain FM ordering combined with an inter-chain AFM one while decreasing the temperature.

Both magnetic dispositions are not completely regular. In the intra-chain case some chains are divided in two sections having opposite FM alignment, while in the inter-chain side some neighbour chains are parallel aligned in a FM-type form. In order to better understand the role played by the magnetic anisotropy on the magnetic properties of the system and particularly in this case with non-completely regular magnetic ordering features, we simulated its magnetic evolution considering negligible the magnetic anisotropy of the nanoparticles. In this case a complete intra-chain FM-like order, although no noticeable changes in the irregular inter-chain AFM order, was appreciated. We believe that a complete AFM-like arrangement of the system would be achieved for a much longer time-scenario, for which a complete or collective single-chain magnetization reversal mechanism could take place.

Finally, aimed to understand the intra-chain AFM ordering experimentally observed by Bliznyuk et al. [101], we also performed the similar calculations as those carried out for the study of the collinear-axes and the negligible-anisotropy cases, but taking a random distribution of the anisotropy easy axes. In this case we obtained an intra-chain AFM-like ordering, both from a macroscopic Curie-Weiss type fitting and from microscopic analysis, what emphasizes the importance of the anisotropy easy axes on determining the magnetic properties of the system.

4.2 MCE in 1D-chains

Experimental studies in highly anisotropic materials report coexistence of both direct and inverse MCE under a magnetic field applied perpendicularly to the easy magnetization axes. Our results in SECTION 4.1 agree with the experimental findings [28], and hence with the purpose to further investigate the MCE in these highly-anisotropic 1D-nanoparticle chains we have carried out a complete set of simulation studies.

Simulations were carried out in the same way as in previous SECTION 4.1 (see Ref. [115] for computational details). Although for the computational procedure all variables have been treated in the usual normalized units $t = k_BT/2KV$ and $h = H/H_A$, in order to give the reader a more intuitive idea about the results, ΔS_M and RC values have been expressed in unnormalized units. The characteristics of the particles used are $d = 3.5nm$, $M_S = 541emu/cm^3$, and $K = 4.1 \cdot 10^5 erg/cm^3$ (similar to those of Ni nanoparticles) [116]. The sample concentration is 5.8%

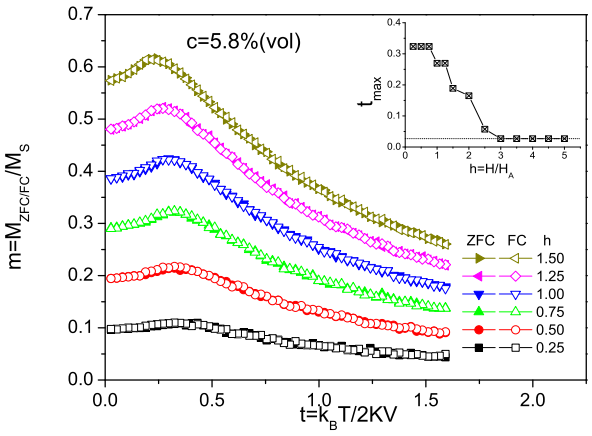

Figure 4.8:
ZFC (full symbols) and FC (open symbols) m(t) curves for different values of h. Inset shows t_{max} as a function of h.

volume fraction for this system. We show in FIGURE 4.8 some simulated ZFC/FC m(t) curves for normalized magnetic field values in the range $0.25 \leq h \leq 3.00$[2].

The general trend of the ZFC/FC curves shown in FIGURE 4.8 presents similarity with random anisotropy systems exhibiting superparamagnetism [110], with the overlapping of the ZFC/FC curves at high temperatures, and the existence of a maximum (t_{max}) that progressively shifts its position towards lower values with increasing h [47]. However, remarkable differences with respect to the usual SPM behavior are observed illustrating a different physical origin. The maximum of the curves takes place for fields much larger than H_A, contrary to the expected disappearance of the peak for fields larger than H_A when t_{max} stands for the SPM blocking temperature [48]. This behavior is similar to that observed in randomly distributed particle systems at strong interacting conditions [56], although we believe that in this particular case it might be related to other phenomena as a magnetic phase transition [108]. The ZFC/FC curves also coincide at low temperatures, contrary to the usual SPM behavior observed in random anisotropy systems in which the splitting between the ZFC and FC curves signals the blocked state of the particles. Meanwhile, the decrease of the FC curve below t_{max} with decreasing t instead of keeping growing as in SPM systems, points to an AFM-like arrangement of the system. These peculiar features arise from the particular orientation of the applied magnetic field with respect to the anisotropy axes of the nanoparticles. In usual SPM systems, the splitting between the ZFC and FC reflects the existence of local

[2]In SECTION 4.1 we were mainly interested in the low-field region, up to values comparable to H_A. For the MCE-stuy we extend this range to much larger fields, up to $5 \times H_A$

energy minima in the direction of the applied magnetic field. These minima originate by the magnetic anisotropy, and represent stable energy wells that stand for different shapes of the m(t) curves depending on the thermal history of the system. For particles with uniaxial anisotropy the most stable anisotropy well is the one that corresponds to parallel orientation of the magnetic moments with respect to the magnetic field, whereas the antiparallel case is less stable. It is this existence of the anisotropy wells what causes the irreversibility reflected in the divergence between the ZFC and FC curves: the different temperature trends followed in each process lead to different occupancies of the magnetic moments on the two energy wells, and so to different thermomagnetization curves (until the thermal energy is large enough to overcome the anisotropy energy barrier between the minima). However, in our particular choose of the magnetic field direction perpendicularly applied to the easy-magnetization axes of the particles, none of the anisotropy wells is favored. Therefore, no irreversibility is generated and this is reflected in the coincidence of both the ZFC and FC curves. The decrease of the FC curve with decreasing t below t_{max} is also originated by the particular situation of the magnetic field applied perpendicular to the anisotropy axes, and agrees quite well with the experimental behavior observed in systems having well-defined anisotropy easy axes under a perpendicularly applied magnetic field [27]. With the purpose to prove the above reasoning about the interplay between the orientation of the applied magnetic field with respect to the anisotropy easy axes as the origin of the features observed, we have simulated the same processes as in FIGURE 4.8, but instead of collinear anisotropy axes case, by considering a random distribution of the easy axes for the array of nanoparticles. The ZFC and FC curves for some selected values of the applied field ($h = 0.50$, 1.00, and 1.50, i.e. smaller, equal, and larger than the anisotropy field) are shown in FIGURE 4.9 for giving a representative example of the arguments discussed above.

The noticeable differences between the collinear-easy-axes and the random-easy-axes cases represented in FIGURE 4.9(a) and (b), respectively, clearly provide evidence supporting our arguments given above: the coincidence between the ZFC and FC curves corresponding to the collinear anisotropy case disappears when the uniaxial easy axes of nanoparticles are randomly distributed, in which case the usual features of SPM systems are recovered. For a detailed study of the subjacent physical phenomena and the meaning of the maxima of the curves in the collinear anisotropy case as related to a possible magnetic phase transition, see Ref. [108]. In connection with MCE, some features draw our attention. First, the coincidence

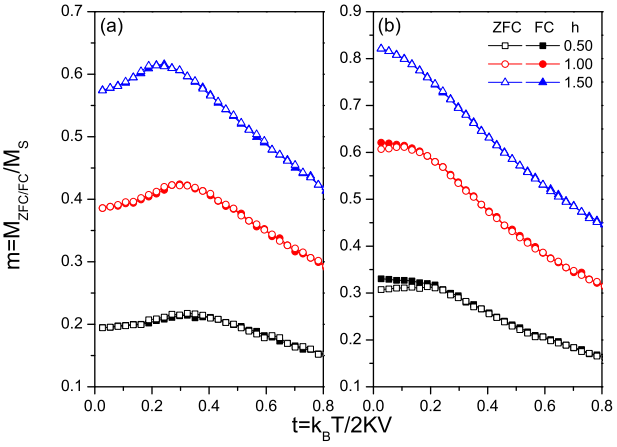

Figure 4.9:
ZFC (full symbols) and FC (open symbols) m(t) curves for the same values of h, both for the collinear-easy-axes case (a) and for the random-easy-axes case (b).

of the ZFC and FC m(t) curves in the whole temperature range, above and below t_{max}, proves the coexistence of both reversible normal (negative $\partial m/\partial t$ slope, above t_{max}) and inverse MCE (positive $\partial m/\partial t$ slope, below t_{max}). Therefore, we have demonstrated that the irreversible inverse MCE found in a randomly distributed interacting nanoparticle system at low temperatures6 may be tuned into reversible character by controlling the magnetic anisotropy of the system. As we argued above, it is this specific orientation of the magnetic field, being perpendicularly applied with respect to the anisotropy easy axes, what accounts for the existence of reversible inverse MCE. Second, the slope of the curves for $t > t_{max}$ seems to rise with increasing fields in the considered ranges, what would account for larger MCE higher than the H_A limit for the disordered case [50]. For a complete characterization of the reversibility range and magnetic field-dependence we have extended the simulations to fields up to $5.0H_A$. Inset in FIGURE 4.8 shows the evolution of t_{max} as a function of h. It is observed that it progressively diminishes with increasing h, until it disappears for $h > 2.5$, further than the H_A-limit for the SPM case [48]. The temperature range accounting for the inverse MCE is short and of smaller slope than the direct MCE range. So, from now on we will focus our attention on the normal MCE temperature range, in order to compare the results with those obtained in the random case. It remains as an interesting task for a future work about the study of how to extend the temperature operativeness of the inverse reversible MCE.

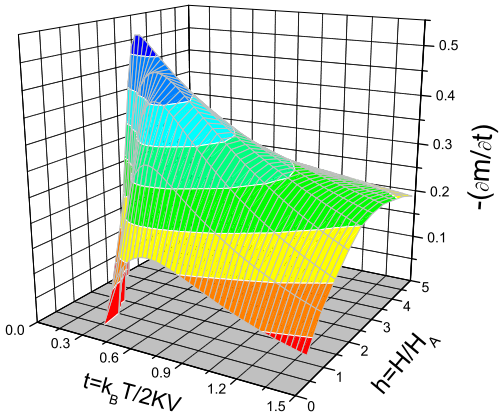

Figure 4.10:
$(-\partial m/\partial t)$ vs. h in the direct-MCE reversible temperature range.

4.2.1 Optimized ΔS_M and RC

In order to characterize the direct MCE in this peculiar system we have first analyzed by separate the value of $(\partial m/\partial t)$ as a function of h, with the purpose to check the possible existence of an optimizing magnetic field similar to that found in a randomly distributed particle system [47]. The results $(-\partial m/\partial t)$ vs. h in the $t > t_{max}$ range where the system is reversible (and therefore in equilibrium) are plotted in FIGURE 4.10.

It can be observed that the isofield curves exhibit a maximum, $(-\partial m/\partial t)$max, that progressively shifts to lower temperature values with increasing field, attaining an absolute maximum value at $t \to 0$ for $h* \approx 2.5$. For temperatures above the maximum the curves monotonically decrease, in a similar way as it was previously found in the random anisotropy case. However, although the general shape of the curves is similar to that observed in disordered systems the specific features completely differ. First, the value t$(-\partial m/\partial t)$max diminishes with increasing h, opposite to the disordered case [47]. Second, the absolute maximum takes place at an applied magnetic field value larger than the anisotropy field H_A of the particles, whereas for the disordered case it occurs at a field $h < 1$.

In FIGURE 4.11 we represent both, $(-\partial m/\partial t)_{max}$ and $t(-\partial m/\partial t)_{max}$ vs. h in detail. Two differentiated regimes are observed, the transition marked by the particular field $h* = 2.5$. The $(-\partial m/\partial t)_{max}$ value grows with increasing field until it attains an absolute maximum at the particular value of $h* = 2.5$, after which it decreases. This result is especially important for practical MCE implementation, since it evidences the existence of a magnetic field value that optimizes the energy costs. The existence of a particular value of the magnetic field separating two ranges of behavior in both magnitudes had already been previously reported

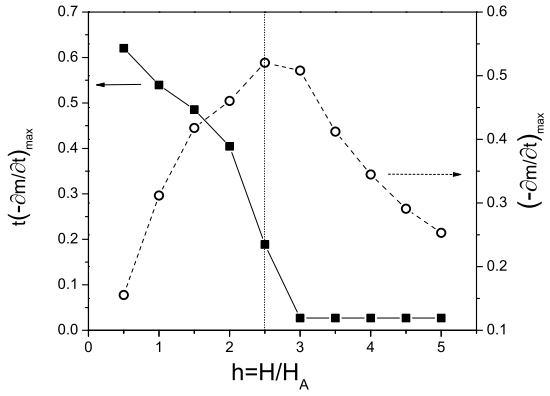

Figure 4.11:
Maximum $(-\partial m/\partial t)$ values and its temperature position, for the considered range of h values.

for disordered systems [47], although at a much smaller value, around $0.3H_A$. This different behavior is important from the applied point of view, since it allows setting the optimal magnetic field to larger fields. The temperature position of the maxima, t$(-\partial m/\partial t)$max, rapidly decreases with increasing applied magnetic field h, following the opposite trend that in the random anisotropy case, where it rises with h. For $h* > 2.5$, it remains constant at the minimum temperature considered in the simulations. Finally, it is important to mention that the overall $(-\partial m/\partial t)$ values are considerably reduced in comparison with the random case. In this system $(-\partial m/\partial t)_{max} \approx 0.5$, while in the random case $(-\partial m/\partial t)_{max} \approx 1.5$, what indicates a better a priori adequacy of the random case for MCE-based implementations. As the MCE in magnetic nanoparticle systems depends much on the particle characteristics [82], it constitutes the subject of a future work to evaluate the MCE in this spatial arrangement with other kinds of nanoparticles. As it was previously, although the results here presented are applicable to any particle system with the assumed characteristics we express the magnetocaloric parameters in unnormalized units to facilitate the interpretation to the reader. To translate the results obtained from the previous sections into unnormalized units, it must be only necessary take into account that $M = mM_S$, $H = hH_A$, and $T = t2KV/k_B$. FIGURE 4.12 shows the ΔS_M values for the same cases as illustrated in FIGURE 4.11, but using unnormalized magnitudes.

The overall shape of the ΔS_M hyperplane displayed in FIGURE 4.11 exhibits two different tendencies depending on the temperature range. For high temperatures, ΔS_M monotonically increases with H, although the growing ratio diminishes above intermediate fields (for intermediate fields we mean values of the order of the h* obtained in FIGURE 4.11). At low temperatures the curves exhibit a peak, as expected from the results discussed in Figs. 4.9, and 4.10. For a real MCE-based

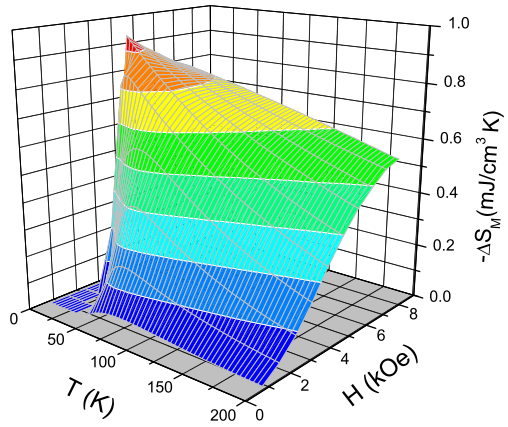

Figure 4.12:
$-\Delta S_M$ hyperplane in the direct-MCE reversible temperature range for different values of H.

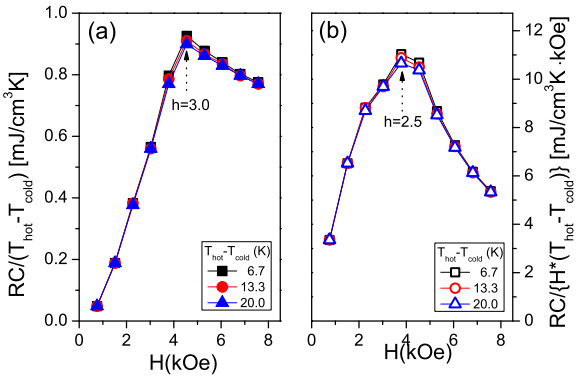

Figure 4.13:
RC as a function of h, normalized by the WTR (a) and by the $WTR \cdot h$ (b).

implementation, as much important as having high values of ΔS_M it matters the temperature range at which those values are attained. For a complete characterization of the MCE it is usually also computed the refrigerant capacity, RC. As introduced in SECTION 1.4, RC takes into account the shape of the ΔS_M curves, computing the amount of heat that the material is able to transfer in a thermodynamic cycle for a given field change ΔH between the working temperatures of cold and heat sinks, T_{cold} and T_{hot}, respectively, with T_{cold} and T_{hot} are usually evaluated as the temperatures at half maximum of the $\Delta S_M(T)$ curve. However, in our system the curves are very flat and would account for a wide temperature range not very representative of the obtained values. Therefore, instead of evaluating the RC for different working temperature ranges ($WTR = T_{hot} - T_{cold}$) we normalized it as RC/WTR, in order to evaluate its potentiality as a heat transfer. The results for $WTR = 6.7K, 13.3K, and 20.0K$ are displayed in FIGURE 4.13.

In FIGURE 4.13(a), it can be observed that RC remains practically unchanged for the different WTR considered values. The overall shape continuously increases

until $h = 3.0$, followed by a further decrease. For the nanoparticles here considered, this value stands for a magnetic field $H = 4.542kOe$. It is very important for real applications to optimize the energy necessary to implement a MR cycle, which is the energy necessary to generate the magnetic field. Therefore we have also analyzed the previous value normalized by the magnetic field, being plotted in FIGURE 4.13(b). It is obtained a maximum at the particular value of $h^* = 2.5$, the same value that maximizes $\partial m/\partial t$. For the particles we consider here, $H_A = 1.514kOe$, and therefore the field that optimizes RC is $H^* = 3.785kOe$.

Finally, we compare the present results with some MCE studies recently reported in other nanosized systems. Although the results obtained were expressed in volumetric units to give an useful estimation from the applied point of view [117], it is commonly found in the literature the use of mass units $Jkg^{-1}K^{-1}$, therefore we also express the results in these same units for comparison. To translate the values to this scale it is only necessary to know the volume density, and in our case we take the Ni bulk density, $\rho = 8.9g/cm^3$. The largest values obtained, in the low-temperature limit and for a field change of $3.8kOe$, correspond in mass units to $\Delta S_M = 0.105J/kgK$ and $RC = 2.0J/kg$. The maximum ΔS_M is about one order the magnitude larger than the ones found in ferrite nanoparticles [39], and only one order of magnitude smaller than the large cryogenic MCE recently reported in the low-temperature limit for magnetic nanocapsules if normalized by the magnetic field: in our system $\Delta S_M = 0.27J/kgKT$, while for magnetic nanocapsules as $TbAl_2$, graphite-coated Gd, and $GdAl_2$ (Refs. [118], [119], and [120], respectively), $\Delta S_M = 3.04J/kgKT$, $8.13J/kgKT$, and $2.90J/kgKT$. In general, both the ΔS_M and RC values are around two orders of magnitude smaller than the reported for the best bulk magnetocaloric materials [117] when normalizing with the magnetic field.

Good candidates to exhibit such novel phenomena described in this work, particularly the reversible character of the inverse MCE, are, in general, systems with a well-defined and collinear anisotropy easy axis. Those characteristics may be found in a wide variety of systems, ranging from the ferromagnetic nanowires reported in Ref. [27] to large arrays of nanostructured ferromagnets as those reported in Ref. [121]. Using magnetic nanoparticles, the most promising candidates at the moment are $FePt$ systems, which large anisotropy allows a quite good (although not complete yet) alignment of the anisotropy easy axes (see for example Refs. [122, 123]).

Conclusions We have found the coexistence of direct (above the maximum)

and inverse (below the maximum) MCE both of reversible character, although the inverse MCE-temperature range is small and must be extended to be of practical use, and so we focused our analysis in the direct MCE-temperature range. The detailed analysis of the $(-\partial m/\partial t)$ factor in this range reveals the existence of a maximizing field $H^* \approx 2.5H_A$, what optimizes ΔS_M and accounts so for an optimal MCE. We have also evaluated the RC and found that it is practically temperature independent for temperature ranges up to $20K$, and it is also optimized at the same field $H^* \approx 2.5H_A$, what reinforces the adequacy of using this particular field to optimize the MCE.

4.2.2 Origin of the optimized MCE

In previous Section 4.2.1, we reported the existence of a MCE-optimizing field h^* for nanoparticle chains with collinear aligned easy axes, when the field is perpendicularly applied. The objective of the present section is to investigate why the MCE is optimized at such field.

In general, the MCE in bulk systems is enlarged at phase transitions where ΔS_M exhibits a peak. However, as seen in previous chapters this is different in nanoparticle systems, where the MCE exhibits smaller ΔS_M peaks but displays however other interesting characteristics not observed in bulk ones. In bulk systems the temperature position of the ΔS_M peak has to be tuned either by varying the composition or by doping the sample [40], whereas in nanoparticle systems can be tuned by the different parameters determining the SPM properties, giving place to a much richer scenario. In this regards, a different situation than in usual randomly distributed particle systems is found when the particles form chains and the magnetic field is applied perpendicularly. This configuration results in very special characteristics originated by the fact that none of the anisotropy wells is favoured. Therefore, other magnetic properties different than superparamagnetism must be the responsible for the optimizing MCE properties. It is the purpose of the present Section to study the physical origin of such special MCE features, and in particular their relation to a possible field-induced phase transition.

The results reported in the previous Section 4.2.1 were based on a system of $N = 250$ particles distributed in 5×5 chains of 10 particles length, with the chains distributed in a square lattice, and periodic boundary conditions were applied. Aiming to eliminate possible system size-effects as the origin of the observed phenomena, we consider now a bigger system of $N = 1000$ particles with the relative intra-chain and inter-chain particle distribution being the same. Also, to eliminate the influence of periodic boundary conditions we consider now a finite system. The

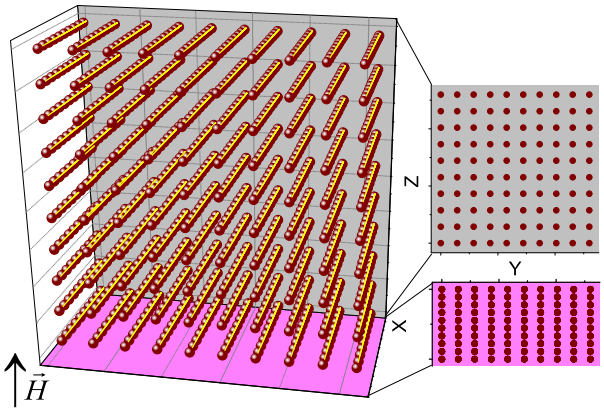

Figure 4.14:
Schematic drawing of the simulated system: $10 \times 10 \times 10$ chains of 10 particles length each, distributed in a square lattice and a magnetic field applied perpendicular to the chains.

simulation of the physical properties is done in the same way as in Ref. [115], with the only difference being that the trial jump $\delta\theta$ is now temperature-dependent[3] in the same way as done in Ref. [44]. An schematic drawing of the $N = 1000$ system is shown in FIGURE 4.14.

The first step is to simulate ZFC/FC processes in the same way as in previous SECTION 4.2.1, in order to confirm that the magnetic features are the same. Even though some differences may be expected since the system is not exactly the same, the general features should be resembled at least qualitatively accordingly to the results reported in SECTION 4.1, where it was demonstrated that the magnetic properties of the system were mainly determined by the intra-chain dipole-dipolar magnetic coupling. The ZFC/FC curves corresponding to the ones of FIGURE 4.8, are shown in FIGURE 4.15.

The ZFC/FC curves shown in FIGURE 4.15 share common characteristics with those of FIGURE 4.8, with the overlapping of the ZFC and FC curves in the whole temperature range, and a maximum that decreases with higher h. Therefore we can conclude that such characteristics do not originate in the periodic boundary conditions or size of the system, but only in the particular spatial arrangement of the particles aligned in parallel chains with the easy axes collinear along the chains. It is interesting to note that additional MC simulations considering the chains distributed in an hexagonal lattice, instead of a square one, display the same features as those in FIGURE 4.15; only tiny differences are found in the quantitative values. The next step is to analyze the $\partial m/\partial t$ *vs* h data, in order to check the

[3]This dependence is included even though the results are only slightly affected, because we consider it to have a more physical meaning than having a constant value with temperature (see SECTION 1.3).

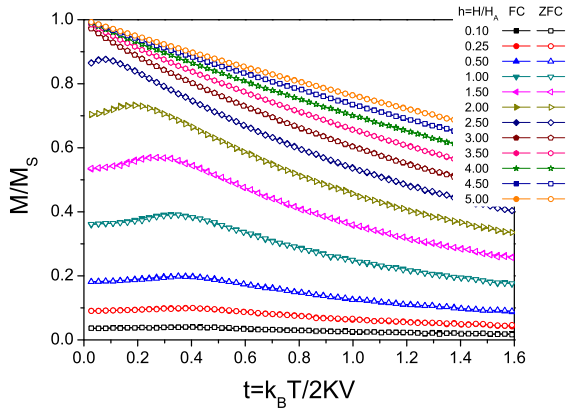

Figure 4.15:
ZFC (full symbols) and FC (open symbols) $m(t)$ curves for different values of applied field, with $0.1 \leq h \leq 5.0$.

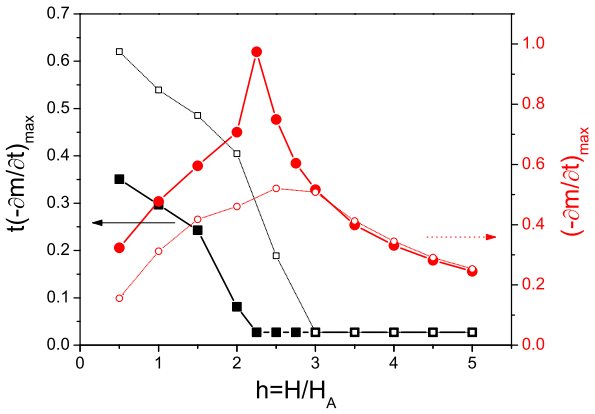

Figure 4.16:
Maximum $(-\partial m/\partial t)_{max}$ values and its temperature position $t(-\partial m/\partial t)_{max}$, for the considered range of h-values (full symbols, solid lines), together with the results of FIGURE 4.11 (empty small symbols, dotted lines).

existence of a magnetic field optimizing the $\partial m/\partial t$ ratio as found in SECTION 4.2.1. The results are shown in FIGURE 4.16, together with the $N = 250$ data.

The results plotted in FIGURE 4.16 reproduce the same features observed in FIGURE 4.11, i.e. the $(-\partial m/\partial t)_{max}$ data exhibits an absolute maximum, whereas its temperature position $t(-\partial m/\partial t)_{max}$ shifts to smaller temperatures with increasing h until the minimum temperature considered is reached. Noteworthy, the position of the maximum, $h^* = 2.25$, is very close to that corresponding to SECTION 4.2.1 (in fact, coincides if using the same precision in h), whereas their temperature position is smaller. A new feature exhibited by the new results is the exponential decay of $(-\partial m/\partial t)_{max}$ for fields $h \geq h^*$. Also, it calls our attention the seemingly two different tendencies in the values of $(-\partial m/\partial t)_{max}$, which increase for $h \prec h^*$ (while higher than the $N = 250$ data) and decrease exponentially for $h \geq h^*$ (overlapping now with the $N = 250$ data). In a general approach we can conclude, therefore,

that the optimizing-MCE phenomena is still observed and so it is independent of the system size or boundary conditions.

In SECTION 4.1, we observed that the magnetic ordering in the system was mainly governed by the intra-chain dipolar coupling over the inter-chain one. In this respect, with the purpose of testing the optimizing conditions and also in order to analyze the influence of the finite length of the chains, we carry out the same simulations but focused now on a single very large chain. The characteristics of the particles in this chain are the same as in the multi-chain case, the only difference being its individuality and length, now of $N = 1000$ (in order to minimize effects of the broken conditions at the ends of the chain). A schematic drawing of the $N = 1000$ single chain is shown in FIGURE 4.17.

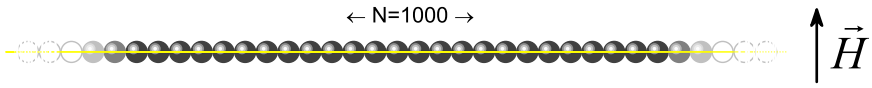

Figure 4.17:
Schematic drawing of the $N = 1000$-single chain system, under the perpendicular application of a magnetic field. Yellow horizontal line stands for the easy anisotropy axes, collinear along the chain.

The ZFC/FC magnetization results for the $N = 1000$-single chain are very similar to the previous ones, both in the shape of the ZFC/FC curves which also overlap, as in the evolution of the $(-\partial m/\partial t)_{max}$ data[4]. Such high similarity in the magnetic properties between the single-chain system and the multiple-chain one, without a doubt indicates that the observed phenomena is uniquely originated by the intra-chain dipole-dipole interaction. Factors as chain length or boundary conditions influence only the quantitative results, but not the qualitative phenomenon of a particular magnetic field that optimizes the MCE.

With the aim of having a further insight into the physical origin of this optimizing field, as for example as related to a phase transition [112, 113], we analyze the properties of the system by means of $M(H)$ curves. This analysis will be focused on one single chain of $N = 1000$ particles, in order to neglect influences from the borders (both the periodic boundary conditions of the $N = 250$ particle, as the finiteness of the $N = 1000$ distributed in 100 chains of 10 particles length). Since we are interested on the optimizing-MCE properties of the previous section, we

[4]These new results are not shown since no relevant new information is contained in the curves; for practical reasons for the sake of comparison, the new results can be associated to the previous case

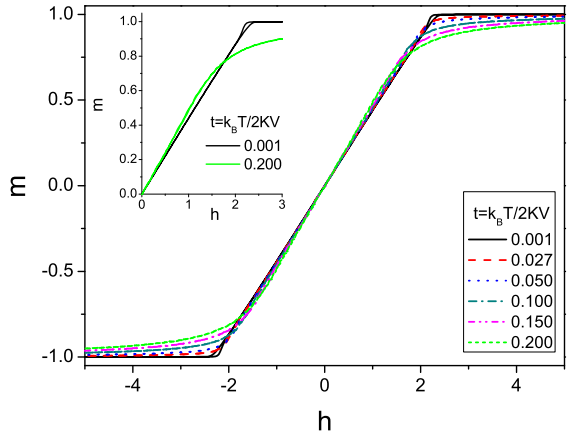

Figure 4.18:
$m(h)$ curves at different temperatures, for a system of one chain of $N = 1000$ particles under a perpendicular magnetic field. Inset shows the cases $t = 0.001$ and $t = 0.200$ in the initial part of the $m(h)$ cycles.

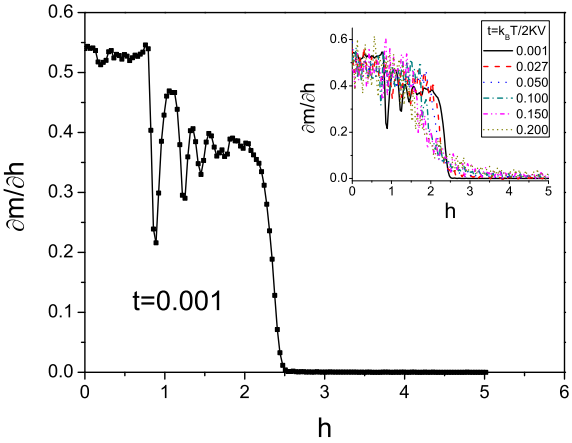

Figure 4.19:
$\partial m/\partial h$ data corresponding to the initial part of the $m(h)$ curve at $t = 0.001$. Inset shows the complete set of $\partial m/\partial h$ curves of the data shown in FIGURE 4.19.

have focused the $M(H)$ analysis also on the perpendicular-field scenario. As usual, we prefer to employ reduced units; some $m(h)$ cycles at different temperatures are shown in FIGURE 4.18.

In FIGURE 4.18 we observe the expected non-hysteretic behaviour of the $m(h)$ curves, with $H_c = 0$. The influence of the temperature is noticeable in the slope of the curves, smoother the higher t (see inset), and in the saturation, which decreases with larger t. To check the possible existence of a phase transition we analyze the $\partial m/\partial h$ data, focusing on the initial part of the magnetization curves starting from $m_{(h=0)} = 0$ and in the low-temperature regime, as illustrated in FIGURE 4.19

In FIGURE 4.19, an abrupt change of $\partial m/\partial h$ is observed at $h^* = 2.5$. This feature is typically characteristic of phase transitions, in this case considering the magnetic field h as the intensive parameter (instead of the more common temperature

dependence). As a result, we can conclude that the system exhibits phase-transition features in the dependence of $\partial m/\partial h$ *vs* h and, precisely, the abrupt change occurs at the field value at which the MCE is optimized, i.e. $h^* = 2.5$. Other remarkable feature displayed in FIGURE 4.19 is the oscillatory behavior observed from values slightly smaller than $h = 1.0$, which diminishes its intensity with larger fields. We are unsure about the origin of this behavior. We hypothesize it might be either due to a critical rotating at the transition when the external field is comparable in strength to the effective anisotropy field arising from the anisotropy plus dipolar coupling effects; or due to some sort of macro-spin waves resulting form the coupling between the magnetic moments of the particles. Studies are in progress to analyze such behavior. For smaller fiels, $\partial m/\partial h$ remains essentially constant, what can be simply interpreted as the competition between the anisotropy and applied field. Inset in FIGURE 4.19 shows the $\partial m/\partial h$ data corresponding to the different temperatures in FIGURE 4.18, where we can observed that the change at $h^* = 2.5$ is smoother with increasing temperature.

The next step is to check that effectively the system exhibits phase-transition features around $h^* = 2.5$, and that the oscillatory behaviour observed at smaller fields is of metastable character. With this aim we carried out simulations of the same processes but considering different MC steps, which is equivalent to different *computational time intervals*, in order to perform a time-dependence analysis. This study was focused on the $t = 0.001$ case, where the abrupt change is more accentuated. The results are shown in FIGURE 4.20.

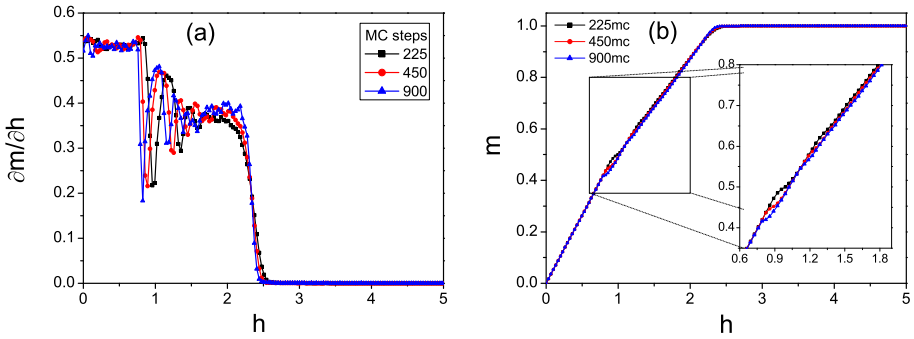

Figure 4.20:
(a) $\partial m/\partial h$ data at $t = 0.001$, for different *computational time* MC steps, and (b) detailed view of the corresponding $m(h)$ curves around the range where the oscillatory behaviour begins. Inset shows a detailed view of the oscillatory range.

In FIGURE 4.20(a) it is clearly observed that the abrupt change at $h^* = 2.5$ results more accentuated the higher the *computational time*, being this behaviour in accordance with phase-transition features. On the contrary, the oscillations below $h^* = 2.5$ occur at different fields depending on the amount of MC steps (as also seen in the detailed view of FIGURE 4.20(b)), confirming its metastable origin.

We have therefore corroborated that the the magnetic field that optimizes the MCE when perpendicularly applied is a critical field that exhibits phase transition features. It is clear that this transition must be of dipolar origin, the only interaction considered in the system. Then, which is the physical explanation of this phenomena? In the basis of the dipolar interaction, we can interpret such behaviour in the reorientation of the magnetic moments of the particles from the maximum stability configuration ($h = 0$, parallel aligned along the chains), towards the one in which in which the magnetic moments in each chain are oriented perpendicular to the chain longitudinal axis. In such field-induced configuration the minimal energy configuration would prefer the antiparallel orientation of the magnetic moments, situation broken by the magnetic field. This argument is illustrated in FIGURE 4.21, where the different previous configurations are illustrated (this scheme is developed over various chains in order to give a wider description of the system; it is evident that the same one applies to the single-chain case).

If our arguments are correct and the magnetic dipolar interaction is the responsible for the observed phenomena, then it must be possible to stablish a direct relationship between M_S^2 (which measures the strength of the interparticle coupling) and the field responsible for the phase-transition features. To check this, we have simulated the same processes for different values of M_S. The results are shown in FIGURE 4.22

In FIGURE 4.22 it is observed that the critical field inducing the transition depends on M_S, increasing the field with increasing M_S. More precisely, the critical field exhibits a linear dependence on M_S^2, what demonstrates the direct relationship between dipolar interaction strength and h^*. This dependence is shown in the inset of FIGURE 4.22, together with the non-anisotropic case. Both curves exhibit a linear behaviour and keep parallel to each other; the existence of h^* in the non-anisotropy systems proves that the observed phenomena is purely of dipolar origin. Note that in the $M_S^2 \to 0$ limit case the curves deviate from the linearity; this feature is of unknown origin to us, although we conjecture it could be related to the difference between the parallel and perpendicular components of the dipolar field. The two different situations shown in the inset stand for the possible physical scenarios: other anisotropy values would result in the same curve, since simulations

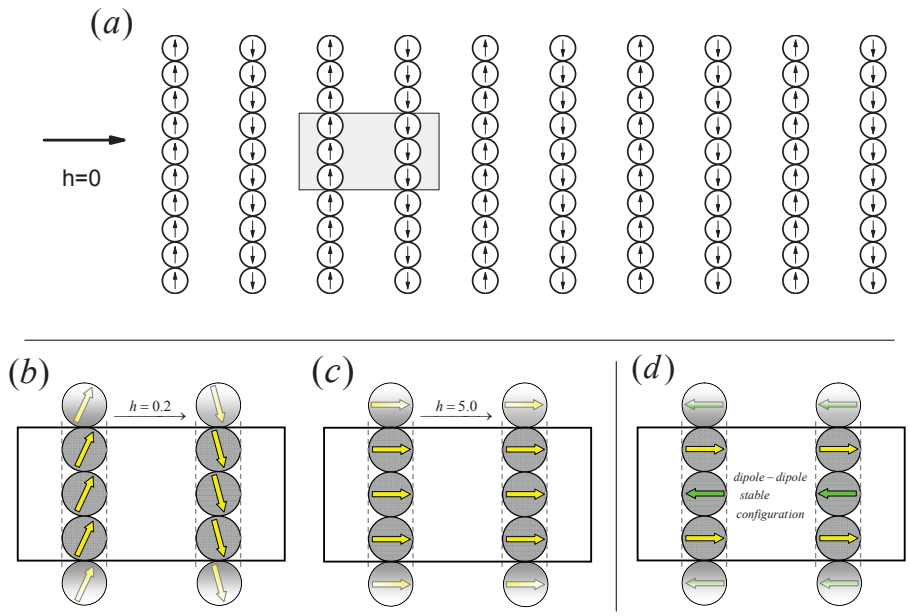

Figure 4.21:
(a) Schematic drawing of the $10 \times 10 \times 10$ chains system, each of them of 10 particles, under the influence of a perpendicular field h. In this case $h = 0$, so that the magnetic moments in the system spontaneously arrange parallel intra-chain and antiparallel inter-chain. In (b) it is shown the visualization of a fraction of the system in (a), under the influence of a small field $h = 0.2$; in (c), the same particles are shown for a large field $h = 5.0$, whereas (d) illustrates the minimal-energy stable configuration for particles perpendicularly arranged with respect to the longitudinal chain axis.

were carried out in reduced field units. This can be interpreted in the sense that the magnetic anisotropy adds an extra component (equivalent to the anisotropy field of the particles) to the field which induces the transition, which is of purely dipolar origin. This characteristic may result very useful for the design of applications based on this phase transition, since the value of h^* van be adjusted not only by varying M_S, but also K.

Accordingly to the above arguments, a change from an stable configuration to an unstable one should be observed in the dipolar energy near h^*, which should change form a negative sign (stable configuration) to a positive one (unstable configuration). This argument was also investigated by recording the different energy contributions during the magnetizing process; the results corresponding to the case of one single-chain of $N = 1000$ particles at $t = 0.001$, are shown in FIGURE 4.23.

Figs.4.23(a),(b) provide a general interpretation of the magnetic behaviour of the system as a function of their energy terms. Starting at $h = 0$, increasing h diminishes

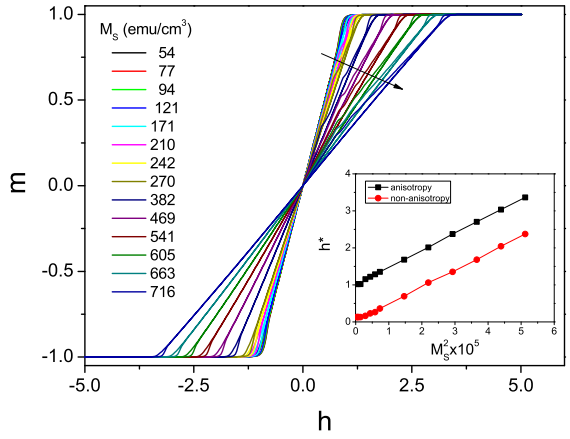

Figure 4.22:
$m(h)$ curves for different M_S values. Inset shows the dependence of the critical field on M_S^2.

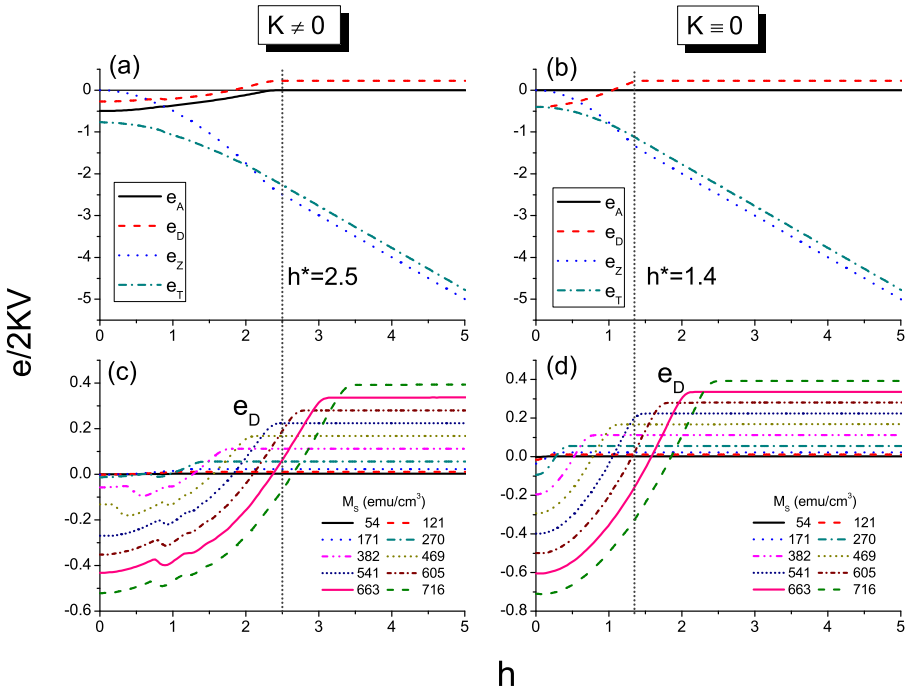

Figure 4.23:
Energy curves for the single-chain $N = 1000$ system. The different energy components during the magnetizing process are shown both for the cases with- (a) and without-anisotropy (b) cases. In (c) and (d), the e_D curves for different M_S values are shown. Vertical dotted lines stand for the respective h^* value of the upper panel curves.

both e_A and e_D (in absolute values) until eventually the sign of e_D changes from negative (stable configuration) to positive (unstable configuration), as hypothesized above (and illustrated in FIGURE 4.21). On the other side, e_A keeps also diminishing until it reaches $e_A = 0$. Interestingly, in relation to the h^* we cannot identify a well defined point in the energetic frame[5]. Because, although for the $K \neq 0$ case h^* apparently is given by the field at which $e_A = 0$, as seen in FIGURE 4.23(a), this result is however misleading as it lacks generality: in FIGURE 4.23(b) it is seen that even when $K \equiv 0$ the h^* value still matches the inflexion of e_D in the range $e_D \succ 0$, hence pointing to purely dipolar origin the existence of h^*. Our hypothesis is that such feature might be related to the different weight of the two components of the dipolar energy; to undertake such possibility by means of dipolar field histograms is the core of an ongoing project.

Regarding the general shape of the e_D curves for the different M_S values, in FIGURE 4.23 we observe the same overall features for all cases, with a sign change with increasing field that evolves from an stable to an unstable configuration, hence supporting our interpretation about the physical problem as displayed in FIGURE 4.21. Other remarkable features observed in FIGURE 4.23 are the oscillations exhibited by the e_D curves of the $K \neq 0$ case (FIGURE 4.23(c)), which are not observed however for $K \equiv 0$ (FIGURE 4.23(d)). This result indicates that the oscillations observed in FIGURE 4.19 arise from the combined influence of dipolar and anisotropy energies, and not from the dipolar one alone.

Conclusions We have obtained features of a phase transition for the magnetic field that optimizes the MCE when applied perpendicularly to nanoparticle chains. Such features are found in the evolution of $\partial m/\partial h$, exhibiting an abrupt change at exactly the optimizing field of h^* of SECTION 4.2.1. This phase-transition feature is robust under time-dependence analysis, independent on the system size or boundary conditions, and exhibits a well defined linear dependence on the dipolar energy factor M_S^2. Noteworthy, recent experimental results conducted on single-domains magnetic nanowires in the group of Prof. B. Hernando (Universidad de Oviedo, Spain), corroborate the computational behavior and give support to our arguments explaining the optimized MCE as generated by a phase transition.

[5] Of course, it is evident that h^* occurs at the point at which e_D (in the positive range) exhibits an inflexion, but, which is the origin of such feature?

5 MCE in NiMn-based Heusler alloy ribbons

5.1 Martensitic transformations

As introduced in Section 1.4, the adiabatic entropy change ΔS_M responsible for the MCE is usually found to exhibit large values around first-order phase transitions, where the abrupt change in the magnetization results in a large ΔS_M-variation. We report in this chapter some MCE studies developed in NiMn-based Heusler alloy ribbons undergoing a first order transition called *martensitic transformation* that results in large inverse MCE. The experimental preparation of the ribbons and the magnetic measurements were carried out in the group of Prof. Blanca Hernando (Universidad de Oviedo, Spain).

The study of the magnetocaloric properties of non-stoichiometric NiMn-based alloys has been the center of intense research over the last years based on the large inverse MCE values reported [124–132]. NiMn-based Heusler alloys are ferromagnetic alloys that exhibit a large shape memory effect under the application of an external magnetic field or by means of temperature variation. The memory effect occurs at the so-called martensitic transformation, the structural transition from the high-temperature *austenite* (AST) phase to the low-temperature *martensite* (MST) phase. The austenite phase has $L1_0$ high crystallographic cubic structure whereas the austenite phase has a structure of lower symmetry (orthorhombic, tetragonal, monoclinic or a modulated variation). The transition between both phases spreads over a range of temperature that depends on the transformation direction. Thereby, if starting from the AST phase, the transformation to the MST phase starts at M_s and finishes at M_f, whereas if starting from the MST phase, the transformation starts at A_s and finishes at A_f. These characteristic temperatures are called starting and finish temperatures for MST and AST phase transformation, respectively.

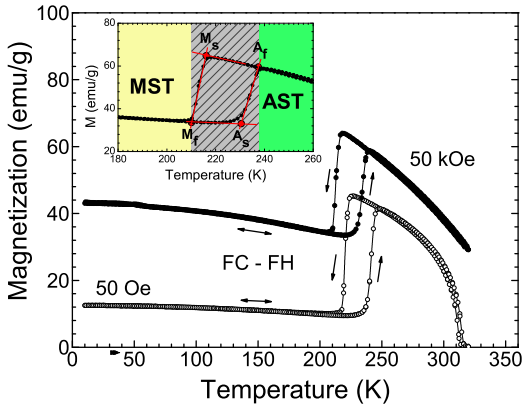

Figure 5.1: Thermomagnetization FC and FH curves for 50 Oe and 50 kOe applied field values. Inset illustrates the meaning of A_s, A_f, M_s, and M_f values. The light yellow area stands for the MST phase temperature range, the light green stands for the AST-phase one, and the light gray stands for MST-AST coexistence temperature range.

In FIGURE 5.1, typical FC-FH thermomagnetization curves are shown to illustrate the martensitic transformation and the characteristic temperatures A_s, A_f, M_s, and M_f corresponding to $Ni_{50}Mn_{35}Sn_{14}$ ribbons [133].

FIGURE 5.1 serves to illustrate the characteristics of these NiMn-based alloy systems as considered for magnetic refrigeration, with the occurrence of the first-order martensitic phase transition leading to large inverse MCE[1], followed by the conventional direct MCE associated to the second-order PM to FM transition at higher temperature (in the AST phase). Both the characteristic transition temperatures and the respective Curie temperature of MST and AST phases are very sensitive to small variations in the valence electron concentration per atom e/a and consequently to chemical composition. Therefore, their properties can be tuned by slightly changing the elemental composition composition [134], and so by adequately tuning the composition the martensitic transformation range can be adjusted to a desired temperature. They also depend on the applied magnetic field (see the above FIGURE 5.1 for two different applied magnetic fields, $50Oe$ and $50kOe$), thermomagnetic history [129], or hydrostatic pressure [132].

Our work focuses on the non-stoichiometric Heusler $Ni-Mn-Sn/In$ alloys with ribbon shape, specifically $Ni_{50.3}Mn_{35.5}Sn_{14.4}$, $Mn_{49.5}Ni_{40.4}In_{10.1}$, and $Ni_{50.4}Mn_{34.9}In_{14.7}$. The non-stoichiometric compositions were chosen in order to have the martensitic transformation around room temperature. Both MST and AST phases are FM at the structural transition, and so the large inverse MCE obtained is originated in the different FM exchange interactions between both phases. Ribbon shape was obtained by rapid quenching by melt-spinning, a large-mass production

[1]The inverse MCE has been proposed, rather than for cooling *per se*, as complementary to the conventional MCE [124]

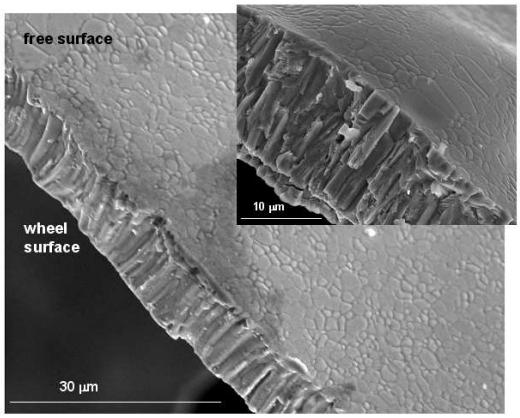

Figure 5.2:
SEM micrograph showing the fractured cross section and free surface of $Ni_{50}Mn_{35}Sn_{14}$ ribbons. Inset: higher magnification micrograph.

technique that offers two potential advantages for the fabrication of these magnetic shape memory alloys: the avoiding, or reduction, of the annealing to reach a homogeneous single phase alloy, and the synthesis of highly textured polycrystalline ribbons. In addition, ribbon shape can be also more appropriate for use in practical devices. Ribbons are single phase and grain oriented with an ordered columnarlike microctructure perpendicular to ribbon plane, as can be observed in FIGURE 5.2, where a typical SEM micrograph of the synthesized ribbons ($Ni_{50}Mn_{35}Sn_{14}$, see Ref. [133]) is shown.

In the next subsections we study the MCE in $Ni_{50}Mn_{35}Sn_{14}$ [135], $Mn_{50}Ni_{40}In_{10}$ [136], and $Ni_{50}Mn_{35}In_{15}$ [137] Heusler alloy ribbons. The overall analysis will be the same for all cases, starting with a description of the sample, thermomagnetization curves, magnetization isotherms, and the evaluation of the magnetic entropy change and refrigerant capacity. It is worth to note that the first-order character of the martensitic transition has associated large hysteresis losses that have to be considered when computing the RC of the sample.

5.1.1 $Ni_{50}Mn_{35}Sn_{14}$ ribbons

We study here the magnetic entropy change and refrigerant capacity of $Ni_{50}Mn_{35}Sn_{14}$ Heusler alloy ribbons. Experimental details of the ribbons fabrication procedure can be found elsewhere [133]. Magnetization isotherms were measured up to 30 kOe applying the magnetic field along the ribbon axis (i.e. rolling direction) by means of a Quantum Design SQUID magnetometer. Before recording each curve sample was cooled-down at zero field from the measuring temperature to 200 K (a temperature where martensite is the existing phase) to maintain the thermomagnetic history.

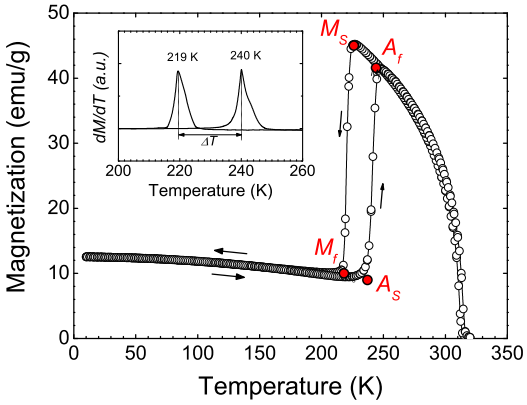

Figure 5.3: Low-field magnetization curves measured on heating and cooling at H = 50 Oe for $Ni_{50.3}Mn_{35.3}Sn_{14.4}$ ribbons. Inset: dM/dT curve in the structural transformation region. The horizontal double arrow indicates the thermal hysteresis of the structural transformation.

From the FC and field-heating (FH) thermomagnetic curves recorded at 2 K/min under a field of 50 Oe (FIGURE 5.3), we determined the starting and finish temperatures for martensite and austenite phase transformation (i.e. M_S, M_f, A_S, and A_f, respectively). The abrupt change in M(T) in the range 220-250 K points out the occurrence of martensitc transformation from a single phase $L2_1$ bcc austenite phase to a 7M orthorhombic martensite [133], with transformation temperatures $M_S = 226K$, $M_f = 218K$, $A_S = 237K$, and $A_f = 244K$. As indicated by the horizontal doubled arrow of the inset the transformation shows a thermal hysteresis of $\Delta T = 21K$. In the martensitic region M(T) shows a small negative slope suggesting that the Curie point of martensite is well above A_S. The further decay in magnetization with inflection point at 313 K reflects the FM to PM transition of austenite.

FIGURES 5.4(a) and (b) show the M(H,T) curves measured around the structural and magnetic transition. For a better clearness in FIGURE 5.4(a) we only plot some isotherms measured at selected temperatures to show the noticeable hysteresis owing to the magnetic field-induced reverse transformation denoted by the stripped area. The computing of hysteretic losses in this temperature range is a key-point for a proper evaluation of the magnetocaloric properties around the structural transition because they are a counterbalance to the magnetic entropy change decreasing magnetic refrigeration efficiency. The hysteretic losses as a function of the temperature are shown in FIGURE 5.5.

The magnetic entropy change for different field values up to $20kOe$ as a function of temperature has been calculated by means of the usual Maxwell relationship 1.4, and the results are plotted in FIGURE 5.6. The different character of both transitions is reflected by the height and width of their respective $\Delta S_M(T)$. While for the structural transition the peak is sharp and higher over a narrow temperature

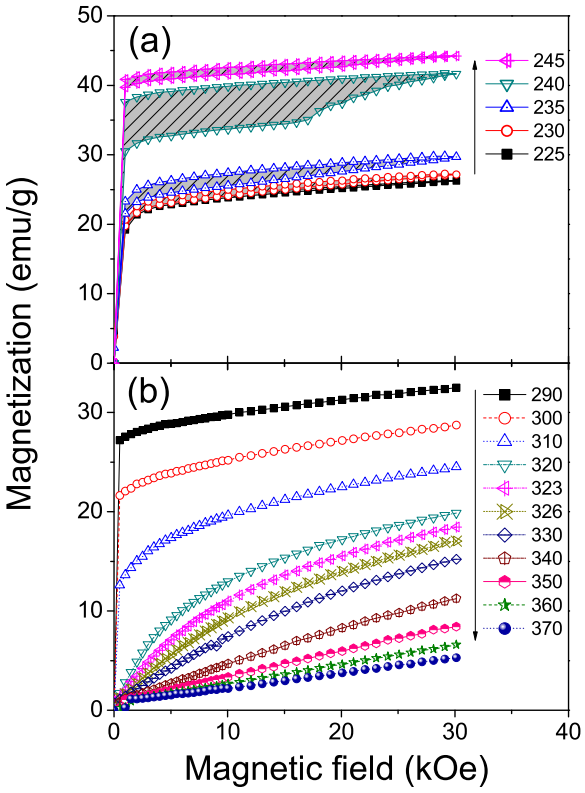

Figure 5.4:
Magnetization isotherms measured around the structural (a), and magnetic (b), transitions for $Ni_{50.3}Mn_{35.5}Sn_{14.4}$ ribbons. The stripped area in (a) denotes the large hysteretic losses due to the effect of the magnetic field on the reverse martensitic transformation.

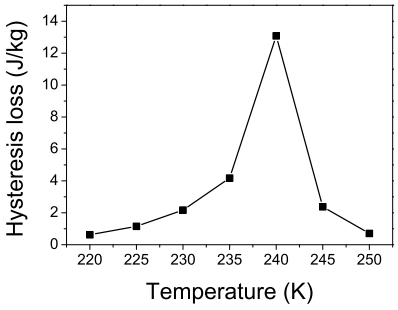

Figure 5.5:
Hysteresis losses as a function of temperature around the martensite-austenite phase transformation for $Ni_{50.3}Mn_{35.5}Sn_{14.4}$ ribbons.

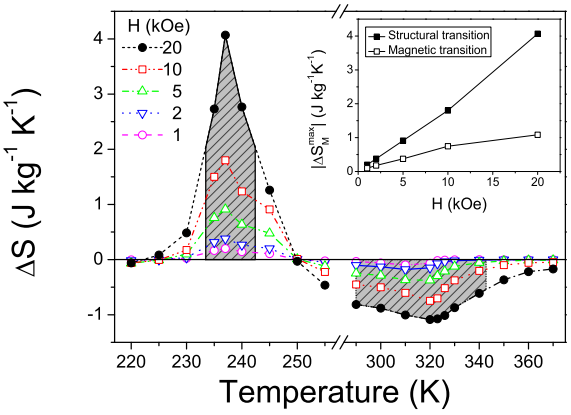

Figure 5.6: Temperature dependence of ΔS around the structural and magnetic transitions for $Ni_{50.3}Mn_{35.5}Sn_{14.4}$ ribbons at different values of the applied magnetic field. The peaks appear at $237K$ and $320K$, respectively. The shaded areas indicate the RC at $20kOe$. Inset shows the field dependence of $|\Delta S_M^{max}|$ in both temperature intervals.

interval, for the magnetic transition the peak is much lower and wider over a broader temperature range. For the structural transition ΔS_M^{max} is about $4.1 Jkg^{-1}K^{-1}$. This is a 25% lower than the one reported for bulk $Ni_{50}Mn_{50-x}Sn_x$ alloys with $x = 15$ [124], but larger than the reported in other recent works for $x = 16$ [138]. For the magnetic transition, where no hysteresis occurs [FIGURE 5.4(b)], ΔS_M^{max} is $-1.1 Jkg^{-1}K^{-1}$, in agreement with reported values for bulk alloys [124, 138].

The refrigerant capacity RC, which takes into account both the width and the height of the ΔS_M vs. T, properly quantifies the amount of heat that can be transfer in one thermodynamic cycle. It is usually evaluated as the integral of the shaded area below the $\Delta S_M(T)$ curve at half maximum width as displayed in FIGURE 5.6. The inset shows the field dependence of absolute value of maximum magnetic entropy change in both temperature intervals. For the structural and magnetic transitions RC is around $26 Jkg^{-1}$ and $46 Jkg^{-1}$, respectively. Hence, despite the lower height of the entropy curve a larger value of RC is reached for the magnetic transition region. From the RC value for the structural transition the average hysteretic loss, roughly evaluated as $6 Jkg^{-1}$, must be subtracted in that temperature range. Therefore, in this alloy ribbons the temperature range at the magnetic transition is more adequate for magnetic refrigeration than at the structural transition.

To summarize, we evaluated the MCE of rapidly quenched $Ni_{50.3}Mn_{35.5}Sn_{14.4}$ alloy ribbons along the rolling direction at 20 kOe. Although, the maximum entropy change was obtained around the structural transition, the large hysteretic losses induced by the magnetic field on the structural transition diminish refrigeration capacity making the magnetic transition range of a higher refrigeration efficiency for a refrigerant cycle.

5.1.2 $Mn_{50}Ni_{40}In_{10}$ ribbons

As-quenched melt spun ribbons of the Mn-rich Heusler alloy $Mn_{50}Ni_{40}In_{10}$ (with average chemical elemental composition $Mn_{49.5}Ni_{40.4}In_{10.1}$ and e/a=7.8.1) crystallize in a $L2_1$-type cubic austenite, which transforms into a fourteen-layered modulated (14M) monoclinic martensite with the temperature decreasing being both phases in dominant ferromagnetic state [139]. FIGURE 5.7 and its inset show the field cooling (FC) and field heating (FH) M(T) curves at 50 Oe and the FH dM/dT vs. T dependence, respectively (the curves were recorded with a temperature heating or cooling rate of 1.5 K/min). They illustrate the occurrence of the FOMT followed by the transition of austenite from the ferromagnetic to paramagnetic state with the temperature increasing. The characteristic martensitic and austenitic start and finish transition temperatures and Curie point of austenite T_C^A, were $M_S = 213K$, $M_f = 173K$, $A_S = 222K$, $A_f = 243K$, and $T_C^A = 311K$. T_C^M is well above A_S. Ribbons exhibited a textured microcrystalline microstructure with crystal directions [400] and [040] of austenite and martensite, respectively, preferentially oriented perpendicular to the ribbon plane. In the present study we evaluate magnetic entropy change and refrigerant capacity (RC) for a maximum field change $\Delta H = 30kOe$, around both structural and magnetic transitions. The field H has been applied along two characteristic directions of the ribbon: its length (rolling direction) and the perpendicular to the ribbon plane (hereafter the magnetic field shall be referred to as $H_{\parallel}$ or $H_{\perp}$, respectively). The latter will provide useful technical information on how the crystallographic texture may affect magnetocaloric properties in these Heusler alloy ribbons since the magnetic field will be applied either parallel or perpendicular to the preferential crystalline growth direction of columnar grains [139].

Details of the experimental procedure employed to produce samples can be found elsewhere [139]. Magnetization isotherms were measured up to $H_{max} = 30kOe$ using a Quantum Design vibrating sample magnetometer in the temperature intervals of the structural ($180K \leq T \leq 270K$) and magnetic ($280K \leq T \leq 350K$) transitions. In the former one, the thermal protocol to record each isotherm was as follows: the sample was first zero-field heated to 350 K (a temperature where austenite is the existing phase in paramagnetic state), cooled down to 100 K (where martensite is the existing phase), and then heated to the measuring temperature. A simpler protocol was followed to record the isotherms around the magnetic transition: the field was first set in zero, the sample was heated up to 350 K, and then cooled down to the lowest measuring temperature. After each M(H) curve is measured the temperature is increased to the next consecutive value. M(H) measurements

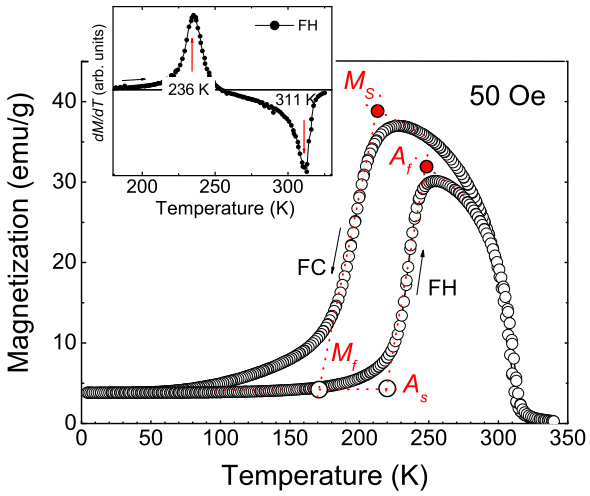

Figure 5.7:
FH and FC M(T) curves measured under an applied field $H_{\parallel} = 50Oe$ for $Mn_{50}Ni_{40}In_{10}$ ribbons. Inset: field heating dM/dT *vs* T curve.

for H were corrected due to the demagnetizing field effect[NOTA: pensar se fago un apendice describindo como se fixo isto...].

In Figs. 5.8(a), 5.8(c), and 5.8(b), 5.8(d), respectively, we show the M(H,T) curves obtained for $H_{\parallel}$ and $H_{\perp}$ around both transitions. For sake of clarity in each graph we only include some of the isotherms measured in order to exemplify their behaviour. The shaded areas in Figs. 5.8(a) and (b) illustrate the noticeable hysteretic losses of the material due to the occurrence of the first order field-induced metamagnetic martensite to austenite transition. The qualitative comparison of Figs. 5.8(a) and (b), so as (c) and (d), respectively, suggests that ribbons show a lower magnetocrystalline anisotropy along the rolling direction. Note the higher initial magnetic susceptibility and the faster approach to saturation at lower fields exhibited by field-up M(H) curves recorded for $H_{\parallel}$. The effect of the higher anisotropy observed for $H_{\perp}$ is also unveiled by the shearing effect exhibited by the magnetization isotherms (that is also present in the field-down curves around the structural transition). The main contribution to $\Delta S_M(T)$ arises from the area enclosed between consecutive isotherms for fields values within the range of approach to saturation and not by the low-field region below.

$\Delta S_M(T)$ curves for $H_{\parallel}$ and $H_{\perp}$ at different field values are shown in FIGURE 5.9. The overall shape of the curves for both cases is rather similar: a large positive peak (inverse MCE) centred around 230 K followed by a negative smaller and broader one at 312 K (direct MCE). The curves corresponding to $H_{\perp}$ are systematically somewhat below. At 30 kOe for $H_{\parallel}$, ΔS_M^{max} values were $3.6 Jkg^{-1}K^{-1}$ and $-1.3 Jkg^{-1}K^{-1}$, whilst for $H_{\perp}$, ΔS_M^{max} values were $3.5 Jkg^{-1}K^{-1}$ and $-1.3 Jkg^{-1}K^{-1}$

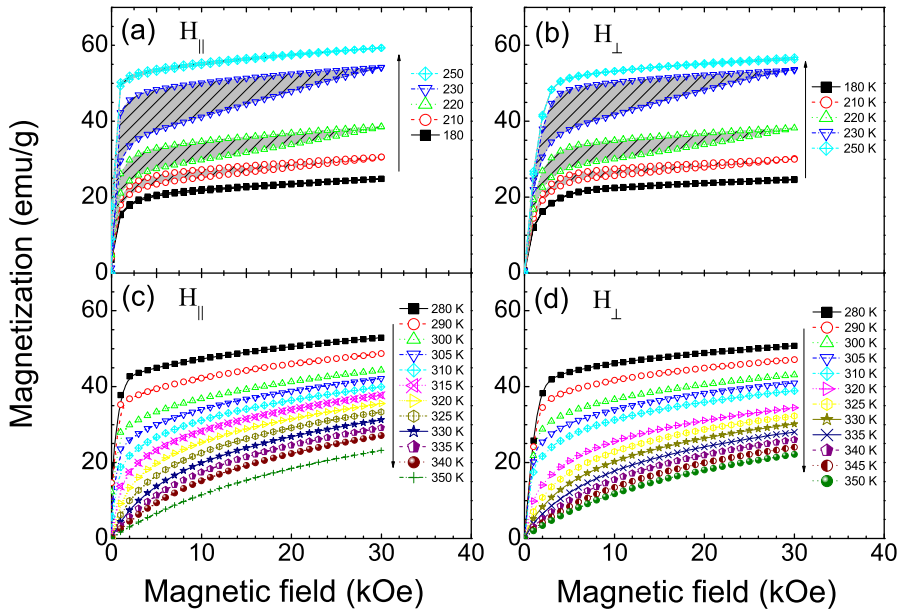

Figure 5.8:
Magnetization isotherms for $H_{\parallel}$ (field applied parallel to the ribbon length) and $H_{\perp}$ (perpendicular to the ribbon plane) measured around the structural [(a) and (b)] and magnetic [(c) and (d)] transitions for $Mn_{50}Ni_{40}In_{10}$ ribbons. The shaded areas in (a) and (b) stand for the hysteretic losses.

for the structural and magnetic transition, respectively. In the inset of FIGURE 5.9, the field dependence of the absolute ΔS_M^{max} values is plotted. In both directions we observe the same rough-linear growing tendency, with a slight slowing down at large fields. Via the Clausius-Clapeyron equation we estimated the upper limit for the field-induced entropy change at the structural transition [140]. For our system we have a change in magnetization between MST and AST phases at the structural transition of $\Delta M = 45 emu/g$ and a shift of the transition temperature with the magnetic field of $-0.4 K/kOe$, what results in a maximum absolute entropy change reachable value of $11 Jkg^{-1}K^{-1}$.

Finally, we compute the refrigerant capacity RC of the sample. For $\Delta H_{max} = 30 kOe$ and $H_{\parallel}$, the RC values obtained for the structural and magnetic transition regions were $RC^{struct} = 71 Jkg^{-1}$ and $RC^{magn} = 89 Jkg^{-1}$, while for $H_{\perp}$, $RC^{struct} = 71 Jkg^{-1}$ and $RC^{magn} = 86 Jkg^{-1}$. Taking into account the large hysteresis losses at the field-induced martensitic transition (shown in FIGURE 5.10 for

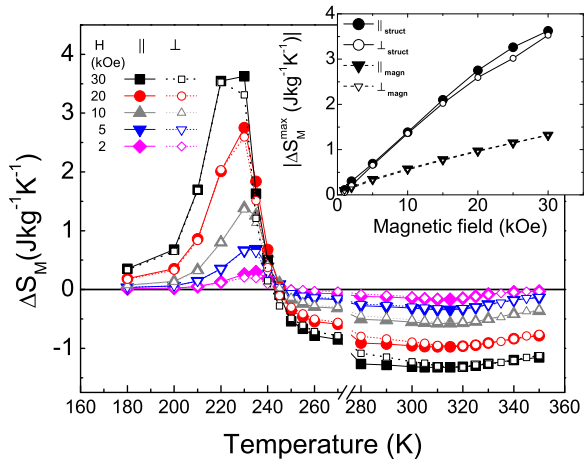

Figure 5.9:
ΔS_M *vs* T for $H_{\parallel}$ (full symbols) and $H_{\perp}$ (empty symbols) measured around the structural and magnetic transitions for $Mn_{50}Ni_{40}In_{10}$ ribbons. $\Delta S_M(T)$ is plotted for several field values between 2 and 30 kOe. Inset: field dependence of $|\Delta S_M^{max}|$.

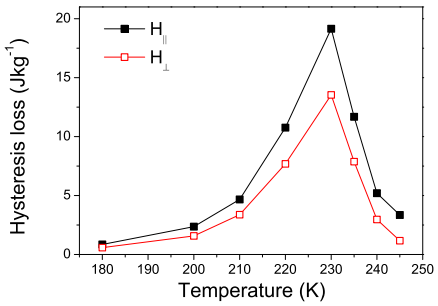

Figure 5.10:
Hysteretic losses as a function of temperature for a field change of $\Delta H = 30kOe$ owing to the field-induced reverse martensitic transformation: $H_{\parallel}$ (full circles) and $H_{\perp}$ (empty circles).

the 30 kOe applied field), the effective refrigerant capacity at the structural transition is $RC_{eff}^{struct}(H_{\parallel}) = 59Jkg^{-1}$ and $RC_{eff}^{struct}(H_{\perp}) = 60Jkg^{-1}$, for the parallel and perpendicular applied fields, respectively. It must be pointed out that despite the smaller magnetic entropy change value achieved around the magnetic transition RC^{magn} values were around twice of those of RC_{eff}^{struct} for both applied field directions.

In summary, direct and inverse magnetocaloric effect properties of melt spun ribbons of the Heusler alloy $Mn_{50}Ni_{40}In_{10}$ were not significantly dependant on their crystallographic texture. This may be advantageous from the point of view of their practical utilization as magnetic refrigerants in magnetic refrigeration technology (directly used in ribbon shape or after compaction into a bulk pieces). This result arises from the relatively small difference in magnetic anisotropy along both ribbon directions. The large average hysteretic losses together with the narrower working temperature interval at the structural transition strongly reduce the refrigeration

capacity leading to a higher cooling power and efficiency around the magnetic transition. Taking into account that Mn-Ni-In Heusler alloys can be fabricated as single phase materials using a single-step, large mass and continuous production method like melt spinning, the efforts for improving their cooling power in the temperature range where FOMT occurs must mainly concentrated in reducing the large hysteretic losses originated in the field-induced reverse martensitic transformation. Research is in progress to understand the key parameters that may effectively reduce hysteresis losses around FOMT in MnNi-based Heusler alloys.

5.1.3 $Ni_{50}Mn_{35}In_{15}$ ribbons

As-quenched melt spun $Ni_{50.4}Mn_{34.9}In_{14.7}$ ribbons crystallize in a $L2_1$-type cubic AST crystal structure at room temperature, whilst transforms into a ten-layered structurally modulated (10M) monoclinic MST whilst decreasing the temperature [141].

Magnetic measurements were performed using a physical properties measuring system platform with the model P525 vibrating sample magnetometer module (Quantum Design). Measurements were done on a ribbon piece of approximately 4 mm in length and 1 mm in width. The magnetic field was applied along the ribbon length (i.e. rolling direction) to minimize demagnetizing field effect. Field cooling (FC) and field heating (FH) magnetization curves were recorded from 330 K to 10 K under a static magnetic field of 50 Oe at 1.5 K/min heating and cooling rate. Magnetization isotherms were measured each 4 K up to a maximum magnetic field of $H_{max} = 30kOe$ in the temperature intervals of the martensitic ($242K \leq T \leq 270K$) and magnetic ($274K \leq T \leq 338K$) transitions. In the former one, the thermal protocol to record each isotherm was as follows: the sample was first zero-field heated to 330 K (then AST is in paramagnetic state), cooled down to 150 K (where MST is the existing phase), and then heated to the measuring temperature. A simpler modus operandi was followed to record the isotherms around the magnetic transition: the field was first set in zero, the sample heated up to 330 K, and then cooled down to the lowest measuring temperature. After M(H) curve is measured the temperature is increased to the consecutive next measurement temperature value.

FIGURE 5.11 and its inset show the FC and FH M(T) curves at 50 Oe and their corresponding dM/dT vs. T dependence, respectively. As temperature increases we first observe a broad decrease in M(T) with an inflexion point roughly located at 192 K that we assign to the Curie temperature of MST, T_C^M. Around 270 K an abrupt and considerable increase in magnetization starts revealing the occurrence of MST-to-AST transformation. The characteristic martensitic and austenitic start

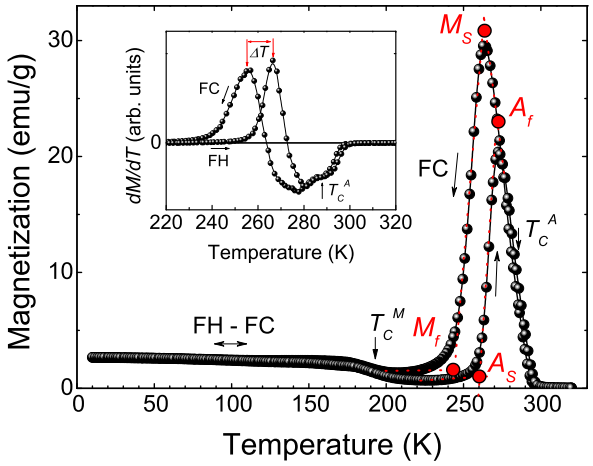

Figure 5.11:
FH and FC M(T) curves measured under $H = 50Oe$ for $Ni_{50.4}Mn_{34.9}In_{14.7}$ ribbons. Inset shows the FH and FC dM/dT *vs* T curves.

and finish transition temperatures are indicated in the figure. Their values were $M_S = 263K$, $M_f = 243K$, $A_S = 260K$, and $A_f = 272K$. The process is reversible with a thermal hysteresis of $\Delta T = 9K$ calculated as $(A_f - M_S)$, in good agreement with the value obtained from the difference between the peak of FC and FH dM/dT versus T curves (shown in the inset). As T_C^M is below A_S a significant large positive entropy change associated to the inverse MCE effect should be obtained. M(T) curve shows that the temperature interval where austenite is ferromagnetic is narrow. Moreover, the decay related to its magnetic transition is also broad and its Curie point was roughly estimated as $T_C^A = 288K$.

In Figs. 5.122(a) and 2(b), we show M(H,T) curves obtained around the structural and magnetic transitions, respectively. For sake of clarity in FIGURE 5.12(a) we only depict field-up and field-down isotherms at selected temperatures to illustrate the behaviour of the material. The temperature interval where MST transforms into AST is characterized by noticeable hysteretic losses as denoted by the stripped areas. They are originated in the field-induced metamagnetic reverse martensitic transition. In the low-field range (typically below 2.0-1.0 kOe), the field dependence of the magnetization M(H) behaves as expected for a ferromagnet but for higher field values the curves leaves this trend due to the magnetization increase produced by the growing austenite fraction. The hysteretic losses as a function of temperature are shown in FIGURE 5.13.

As it the previous sections, we calculated $\Delta S_M(T)$ from M(H,T) curves by numerical evaluation of the Maxwell relation. FIGURE 5.14 shows $\Delta S_M(T)$ curves at different field values. A narrow large positive peak located around 258 K, followed by a negative smaller and broader one located at around 286 K was obtained.

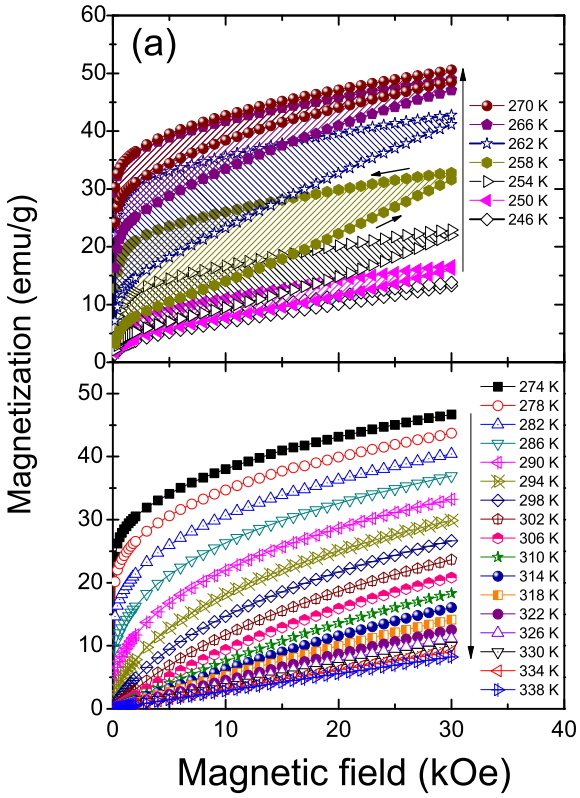

Figure 5.12:
Magnetization isotherms measured around the structural (a) and magnetic (b) transitions for $Ni_{50.4}Mn_{34.9}In_{14.7}$ ribbons. The stripped areas in (a) stand for the hysteretic losses due to the effect of magnetic field on reverse martensitic transformation.

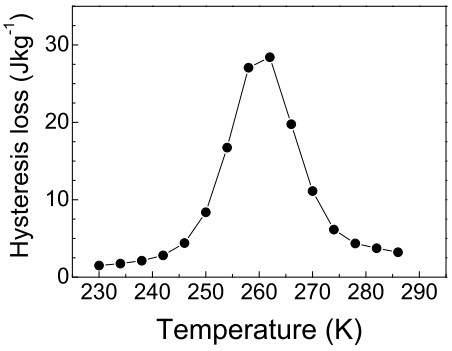

Figure 5.13:
Hysteretic losses as a function of temperature for a field change of $\Delta H = 30kOe$ owing to the field-induced reverse martensitic transformation for $Ni_{50.4}Mn_{34.9}In_{14.7}$ ribbons.

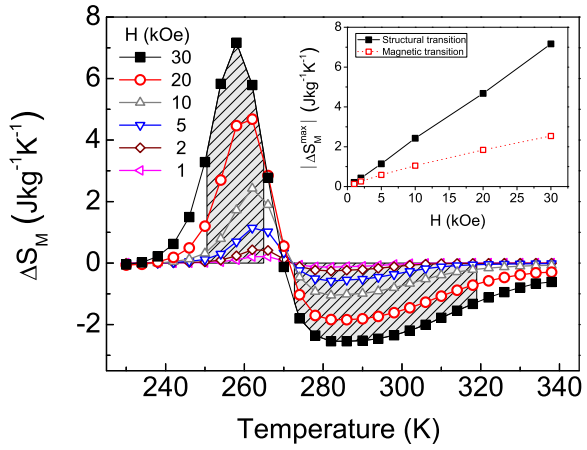

Figure 5.14: Temperature dependence of ΔS_M around the structural and magnetic transitions for $Ni_{50.4}Mn_{34.9}In_{14.7}$ ribbons at different field values. The shaded areas indicate working temperature interval at $30kOe$ whilst the inset shows the field dependence of ΔS_M^{max} in both temperature intervals.

ΔS_M^{max} values for the structural and magnetic transition were $7.2Jkg^{-1}K^{-1}$ and $-2.6Jkg^{-1}K^{-1}$, respectively. The inset of FIGURE 5.14 shows the field dependence of the absolute value of the maximum magnetic entropy change $\Delta S_M^{max}(H)$.

By integrating the shaded areas in FIGURE 5.14 we obtain now the RC, being for the structural and magnetic transition regions and for a field change of $\Delta H_{max} = 30kOe$, $RC^{struct} = 82Jkg^{-1}$ and $RC^{magn} = 99Jkg^{-1}$, respectively. If we substract now the average hysteresis losses at the martensitic transition to obtain the effective RC, we obtain $RC_{eff}^{struct} = 60Jkg^{-1}$. Therefore, despite the smaller magnetic entropy change value achieved around the magnetic transition, RC^{magn} was larger than RC_{eff}^{struct}, similarly to the results obtained for $Ni_{50.3}Mn_{35.5}Sn_{14.4}$ ribbons [135].

6 Anomalous deviation from Curie-Weiss behaviour

6.1 Influence of surface chemistry on the magnetic properties of FePt nanoparticles

The structural and magnetic properties of monodisperse Fe_xPt_{1-x} nanoparticles have been the subject of intense research activity over the last few years, due to their potential for usage in biomedical theranostic and magnetic data storage as well as magnetic sensor applications [92, 142]. The established methods of wet-chemistry synthesis of FePt nanoparticles yield highly controllable particle sizes, compositions and morphologies as well as narrow size distributions. These FePt particles are in the chemically disordered fcc structure which is characterized by a very small magnetic anisotropy energy density (MAE) and soft magnetic properties [143, 144]. Small modifications of crystallinity and composition are known to result in large changes of the MAE and the intrinsic magnetic correlations rendering these nanoparticulate systems attractive prototype models for understanding nanomagnetism [145]. Theoretical descriptions of the macroscopic magnetic response of nanoparticulate assemblies rely intrinsically upon the accurate knowledge of the effective magnetic anisotropy density K_{eff}, the volume and the magnetic dipolar interaction strengths of the particles. Acquisition of such values is, however, notoriously difficult. Additionally, surface effects (generally controlled by the molecular ligands attached) dominate their magnetic properties due to the increased surface-to-volume ratio of fine nanoparticles [91, 146]. The surface magnetism differs from volume properties due to the lower coordination of magnetic moments and the breaking of symmetry at the surface. This can result in site-specific, generally uniaxial, surface anisotropy and broken exchange bonds, which inevitably lead to surface spin disorder and frustration (most prominently in oxydic ferro-, antiferro-

and ferrimagnets) [147]. In terms of surface chemistry, FePt nanoparticles offer an excellent chemical stability that allows surfactant exchange and/or (bio)molecules attachment, permitting for example their transfer from non-polar solvents to aqueous solution [148]. This method opens the door, not only to biological applications [149], but also to the water-based colloidal chemistry of FePt nanostructures [150]. Moreover, the collective magnetic behaviour of a nanoparticle assembly is generally investigated using a nonmagnetic matrix or solvent [151]. Magnetic interactions between particles can be due to dipolar, direct or indirect exchange coupling. In some circumstances, interactions can dominate the magnetic behaviour, resulting in an ordered or disordered magnetic state of the nanoparticle ensemble, for example *spin-glass-like* ordering of magnetic moments [24, 74]. In this work, we investigated two types of ligand-stabilized $Fe_{60}Pt_{40}$ nanoparticles that promote different three-dimensional (3D) self-assemblies and distances in between. A detailed analysis and comparison of the magnetic properties of these FePt nanoparticles with identical size distribution but different surface chemistry is reported, proving experimentally the substantial discrepancies in the effective magnetic anisotropy. Our extensive analysis of the magnetic behaviour of the nanoparticulate system excludes a dominating role of inter-particle interactions or the different spatial distribution. Rather different individual particle characteristics are promoted by the different surface conditions. The preparation of the particles and experimental measurements were carried out in the group of Prof. M. Farle (Universität Duisburg-Essen, Germany).

6.1.1 Anomalous $\chi^{-1}(T)$ *vs* T behaviour

With the purpose of studying the influence of the surface ligands on the magnetic properties of $Fe_{60}Pt_{40}$ nanoparticles, we analyze the magnetic temperature evolution of two samples, H and W, in which the particles are covered by different surface chemical ligands (see Ref. [152] for details about the chemical characterization). The H-sample stands for hexane-based disolution, while the W-sample is water based. The main difference between both samples is the different size of the ligands and the oxidation of the surface atoms, what determines their spatial arrangement and the particles' characteristics, respectively. For the H-sample the spatial distribution is a FCC structure with interparticle distances $\approx 2.5nm$ ($\approx 15\%$ vol), and for the W-sample the particles are randomly distributed in space with an average interparticle distance $\approx 1.0nm$ ($\approx 30\%$ vol) (see Ref. [152] for details about the characterization). The oxidation of the surface atoms is much larger in the W sample.

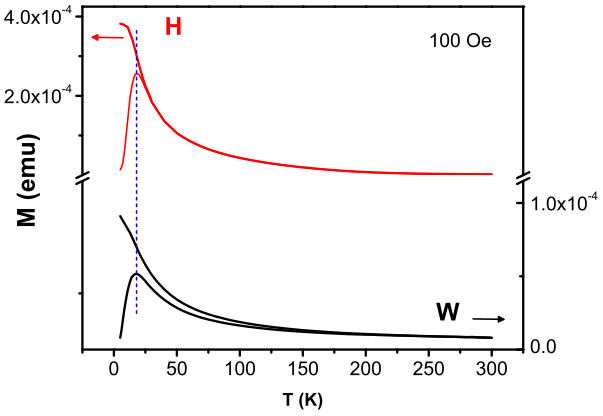

Figure 6.1:
ZFC-FC curves of the FePt nanoparticles from sample H (upper curves, red line) and from sample W (lower curves, black line).

With these main differences in mind, we characterize now the magnetic response of the system. We start by measuring the ZFC and FC processes, which provide much information about single-domain particle systems. FIGURE 6.1 shows zero-field cooled (ZFC) magnetization curves recorded after cooling the samples in zero field from room temperature to 5 K and field cooled (FC) curves recorded after cooling the samples in a small field (100 Oe). These ZFC-FC magnetization curves display the usual signatures observed in single-domain magnetic particle systems. For both samples, the curves coincide at high temperatures and exhibit a paramagnetic-like decay with increasing temperature reflecting the superparamagnetic response of the particles within the time window of the measurement technique. With decreasing temperature the curves split, the ZFC reaches a maximum at $T_m = 18$ K that roughly corresponds to the average blocking temperature T_B of the system and decreases after that while the FC one keeps increasing. The slope of the curves is less pronounced for the more densely packed sample W consistent with the existence of larger dipolar coupling and/or larger size/anisotropy dispersions: the maximum of the ZFC curve is proportional to the individual particles' anisotropy energy barriers E_B (proportional to the particle size K and volume V of the particles), in a first approximation and for typical SQUID measurements given by $T_B \approx E_B/25k_B$, with k_B the Boltzmann constant (see Eq.(6.1.1)). Therefore, dispersion in these K,V-parameters among the particle population result in dispersion of the corresponding E_B, and thereby in a less pronounced peak of the ZFC curve. The effect of this distribution in the particles' energy barriers can also be induced by interparticle dipole-dipole interactions, which modify the height of the energy barriers resulting therefore also in a distribution of effective E_B values.

As pointed above, T_m depends only on the average particle size if the magnetic

anisotropy energy density K is size independent. The temperature (23 K in the case of sample H, and around 150 K in sample W) at which the ZFC and FC curves separate corresponds to the T_B of the largest particles. This could imply that the average volume or K of the nanoparticles in sample W has increased when transferred to the aqueous solution. An increase in volume is not evident from the TEM measurements.

It is very important to remember that a distribution of blocking temperatures stems not only from a size distribution as has been suggested in several publications but more precisely from a distribution of energy barriers E_B, i.e. a distribution of particle sizes and/or magnetic anisotropy energy densities. The shape of the ZFC curve, with its initial increase until T_B is reached, is also observed in fully monodisperse samples. In fact, since the relaxation time for a single particle is given by

$$\tau = \tau_0 e^{\frac{E_B}{k_B T}} \tag{6.0}$$

every particle has a non-vanishing temperature dependent probability $p(T)$ for a reversal of its magnetization at any temperature,

$$p\left(T\right) = \tau^{-1}\left(T\right) = f_0 e^{\frac{-E_B}{k_B T}} \tag{6.0}$$

One has to distinguish the temperature T_0 of the energy barrier $E_B = k_B T_0$ from the temperature at which their magnetization reverses according to the thermal probability expressed by Eq.(6.1.1). Obtaining a precise picture of the distribution of switching rates is quite complicated due to the random spatial distribution of easy axes. Most of the single-particle properties are indeed hidden by the complex distribution function of the MAE due to different particle sizes, shapes and even compositions resulting. In sample W, this distribution stems from the partial and heterogeneous oxidation of the nanoparticles when transferred to the aqueous solution. The effect of oxidation induced changes that has been analyzed for example by Wiedwald et al. [153] for Co. Nogues et al. [154] also discuss the drawback of having antiferromagnetic (AFM) shells that usually grow highly disordered, making the control of its microstructure rather difficult. Under these conditions, particle surface and core effects are not easily distinguished and contribute to the magnetic behaviour of nanoparticles in a non-separatable way. The increase of T_S in sample W can be explained by a combination of increased interparticle interactions and a broader distribution of effective magnetic anisotropy constants (K_{eff}) compared to sample H. Both contributions are a direct consequence of the different chemical compounds surrounding the nanoparticles. Samples H and W have a differently dense

volume fraction, of 15.22% and 30.68% assuming a face centered cubic superstructure and a maximally random jammed state, respectively. The ligands also dictate the chemistry at the surface of the nanoparticles. A partial oxidation of Fe atoms is expected due to handling sample H under air atmosphere. A thicker irregular oxide shell in sample W forming a core-shell $FePt-(Fe_xO_y)Pt$ nanoparticle is likely, because of the hydroxide ions at the surface and the oxygen-rich environment using water as solvent. How these surface oxides of transition metal nanoparticles affect the magnetic properties has been a subject of intensive research. The oxides are usually AFM and can introduce extra sources of anisotropy due to uncompensated magnetic moments, grain size distribution, structural defects, interfacial roughness and variations in the chemical composition [153]. As can be directly understood in terms of Néel's pair model, the surface anisotropy is mainly due to local symmetry breaking at the surface and structural defects [155]. In the two systems under study (samples H and W) these contributions clearly differ. The increase of T_S to 150 K in the ZFC-FC curves of sample W is consequently not due to an increase in size but related to an increase of the effective MAE distribution [153]. The very thin, possibly incomplete AFM shell around the FM core varies from particle to particle 48 and results in a broader distribution of MAE, relaxation times and blocking processes. The later are strongly influenced by dipolar coupling effects as the temperature is lowered. From Eq.(6.1.1), $T_B = K_{eff}V_m/k_BTln(\tau_m/\tau_0)$, and considering that for typical SQUID measurements $ln(\tau_m/\tau_0) \approx 25$, the experimentally determined mean particle volume V_m and T_B, can be used to roughly estimate K_{eff} by:

$$K_{eff} = \frac{25k_BT_B}{V_m} \tag{6.0}$$

Unfortunately, an unambiguous determination by measuring the magnetization in a different time window of relaxation processes [79] was not possible [156]. For very fine particles, it is unlikely that their "magnetic" or "activation" mean volume V_m is the same as their geometric volume, as for sample W. As the surface layers may be quite thin and/even incomplete the irregular increase of the surface anisotropy and a decrease in the magnetocrystalline anisotropy energy due to the reduced core size become important. This model fits indeed, if most of the particles are modelled by an oxidized surface layer unable to form a crystalline AFM phase, and the atomic moments form a magnetically frustrated shell instead. The existence of an AFM phase for a very small fraction of particles only justifies the existence of large energy barriers reflected in the high-T_S. When interpreting the average T_m and the T_S one has to consider the competing influence of the effective magnetic anisotropy density K_{eff}, saturation magnetization M_S, and the volume V_m of every individual

particle, as well as the variation of interparticle interactions (mainly of dipolar type proportional to M_S^2) and average size distribution. As the particles in sample W are much closer packed, we would expect larger interparticle interactions and shift of T_m to higher temperatures which is not observed. This indicates that the dipolar interaction energy between the particles is rather small in comparison to the MAE, and its contribution to the blocking phenomena is negligible. Also, Monte Carlo simulations (not shown) considering the same concentration but different spatial arrangement, fcc or random, indicate that such different spatial arrangement would not affect noticeably the shape of the curves in the small dipolar coupling regime. Accordingly, we may conclude that the different behavior arises from the different physical and chemical characteristics of the particles in each sample due to the different ligands at the surface.

For systems of non-interacting nanoparticles, the susceptibility follows a simple Curie law above the blocking temperature, with a deviation from the linear slope at high temperatures due to the temperature dependence of the nanoparticles' magnetic moment [78]. FIGURE 6.2 shows the inverse of the susceptibility curves for both samples.

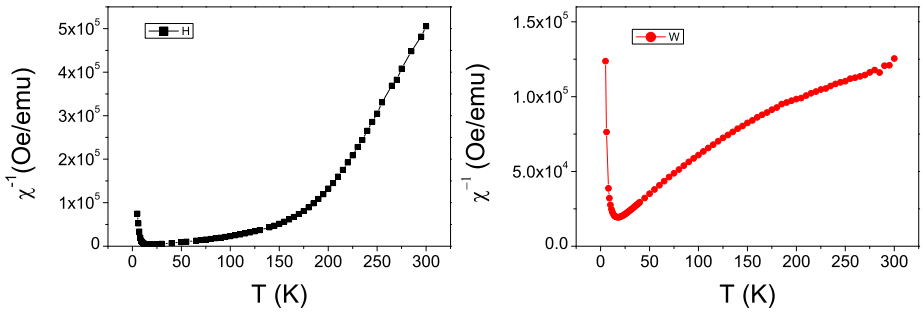

Figure 6.2:
Experimental curves of inverse susceptibility *vs* temperature for both samples H (left) and W (right) that deviate from the classical Curie law.

The inverse susceptibility shows different tendencies : a) for sample H, the slope of the $\chi_{-1}(T)$ curve increases up to 220 K and becomes constant, b) for the sample W the slope monotonically decreases before reaching a constant value near room temperature. In order to interpret the magnetic behavior above T_B we consider the characteristic superpara-/paramagnetic (SPM-PM) transition. In a first approximation, the initial susceptibility of a PM system is described by

$$\chi_{PM}(T) = \frac{\rho_{AT}\mu_{AT}^2}{3k_B(T - T_C)} \tag{6.0}$$

where ρ_{AT} is the number of atomic moments μ_{AT} per unit volume. The initial susceptibility χ_{SPM} of a SPM is given by

$$\chi_{SPM}(T) = \frac{\rho_p\mu_p^2}{3k_B(T + T_D)} \tag{6.0}$$

where μ_p is the total magnetic moment of the particle and ρ_p the number of magnetic particles per unit volume. T_D stands for the effective dipolar interaction energy [157].

Taking into account that each particle is composed to a large extent of different atomic magnetic moments (N) within the PM and the SPM regimes (paramagnetic *atomic moments* or exchange coupled moments forming coherently fluctuating *supermoments*), i.e. $\mu_p = N\mu_{AT}$, and so $\rho_p = \rho_{AT}/N$, in a first approximation the magnetic susceptibility for the SPM sample is about N-times larger than the PM one, since $\chi_{SPM} = N\chi_{PM}$. N is on the order of hundreds or thousands of atoms. Accordingly, the inverse susceptibility must be larger for the system in the PM state than in the SPM one. The curvature observed in the intermediate temperature range accounts for the thermal dependence of the magnetic moment of the nanoparticles, which well above the blocking temperature satisfactorily follows a mean-field dependence:

$$\mu_p(T) = \mu_p(0)\left(1 - \frac{T}{T_C}\right)^{1/2} \tag{6.0}$$

Based on these assumptions, we have carried out fittings of the inverse susceptibility vs temperature for both samples (see for example Ref. [78] and references therein for a detailed description of using such equations for treating the magnetic properties of a magnetic nanoparticle system). By using Eq.(6.1.1) to fit the PM-temperature range we have obtained $T_C = 172$ K, and by combining equations 6.1.1, 6.1.1 to fit the SPM-temperature range, obtaining in this case $T_C = 254K$ and a negligible T_D $(-2 \pm 3K)$. FIGURE 6.3 shows the fits for sample H in the SPM (left) and PM (right) regimes, respectively. Although these results are satisfactory and support the proposed SPM-PM transition (the $R^2 = 0.999$ value obtained in both cases corroborates the good agreement between the fits and the experimental data), one has to understand the large difference between the T_C values for the SPM-temperature range ($T_C = 254$ K) and the PM-range ($T_C = 172$ K). We ascribe this difference to the nanoparticles size distribution. For cores and particles

in the 1 to 3 nm range T_C is strongly reduced and consequently the different T_C values can be regarded as the lower and upper limits of the T_C-distribution.

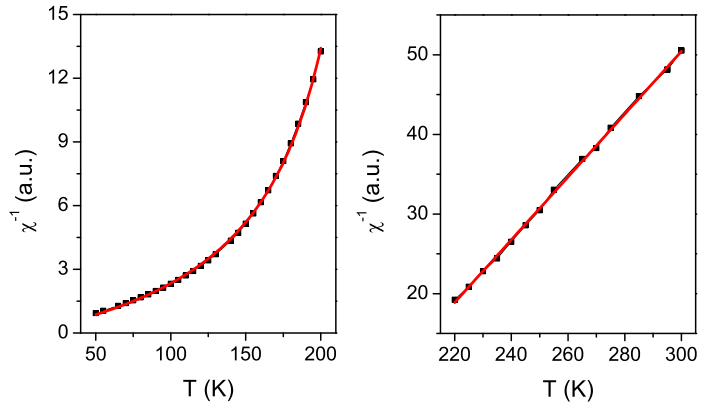

Figure 6.3:
Fits of the inverse susceptibility vs temperature for sample H according to equations 6.1.1,6.1.1 in the SPM regime (left) and according to Eq.(6.1.1) in the PM (right) regime.

6.1.2 Fitting model

The $\chi^{-1}(T)$ vs T curve of sample W shows a completely different tendency. To understand such discrepancy we propose two different physical pictures that would explain the decrease of the slope; a) the overall magnetization of the particle shows a step-like shape. b) There is an additional magnetic contribution that increases with T. Model a) would require the existence of two different magnetic materials at the surface and in the core. Incomplete spin compensations of the AFM state in the oxidized shell would have to be assumed resulting in a very small magnetization and causing an exchange-bias. Neither exchange bias nor the existence of two big enough distinct magnetic volumes have been observed in our characterizations. Since model a) cannot be experimentally confirmed we discuss the possible existence of an extra source of susceptibility that gradually increases with T. The origin of this extra contribution can be found in the frustrated spins at the surface of the magnetic particles. At low temperatures, the contribution of these spins to the particle magnetic moment is negligible, with no appreciable net moment along the field direction. However, with increasing T, these spins will eventually become unpinned and align in the direction of the external field. Although the contribution of these spins should be of the PM type and also very small, it can indeed

justify the slight increase of the magnetization of the ZFC curve that stands for the anomalous behavior of the inverse susceptibility curve. Another factor supporting this argument is that the saturation magnetization for sample W effectively exhibits a slowing down of the decreased ratio at high T as described below (see Ref. [152] for details). Although we cannot ascribe this effect to the effective M_S as resulting from two different magnetic phases, we can emphasize the contribution of these "defrozen" surface spins. Based on these results, we have developed a simple model. If we model the depinning probability of one surface spin according to:

$$p\left(T\right) = f_0 e^{\frac{-E_A}{k_B T}} \tag{6.0}$$

with k_B the Boltzmann constant, f_0 a normalizing factor and E_A as the activation energy necessary for the particle to become unpinned. We define this dependence in the same way as the probability of one particle to overcome the MAE barrier and switch the magnetization direction. The difference in this case is that; i) it deals with atomic moments instead of particles magnetic moments, and ii) there is only one energy well of depth E_A. These surface spins behave paramagnetically and their contribution to the total magnetic susceptibility is given by

$$\chi_{PM_{surf}}(T) = \frac{\rho_{AT}(T)\mu_{AT}^2}{3k_B T} \tag{6.0}$$

where $\rho_{AT}(T)$ is the fraction of surface spins per particle that becomes PM with increasing T. We can approximate that the fraction of magnetic atoms at the surface (dS) of a spherical nanoparticle is given by $dS = 4/3\sqrt{N}$, and so we may approximate the density of spins that can become unfrozen at a given T by:

$$\rho_{AT-surf}(T) = dSN\rho_p f_0 e^{\frac{-E_A}{k_B T}} \tag{6.0}$$

and their contribution to the total susceptibility is given by;

$$\chi_{PM-surf}(T) = \frac{dSN\rho_p f_0 e^{\frac{-E_A}{k_B T}} \mu_{AT}^2}{3k_B T} \tag{6.0}$$

The total susceptibility of the system is computed as the sum of the SPM contribution plus the surface-spins contribution, $\chi_{total}(T) = \chi_{SPM}(T) + \chi_{PM_{surf}}$, so that:

$$\chi_{total}(T) = \frac{\rho_p \mu_p^2}{3k_B\left(T + T_D\right)} + \frac{dSN\rho_p f_0 e^{\frac{-E_A}{k_B T}} \mu_{AT}^2}{3k_B T} \tag{6.0}$$

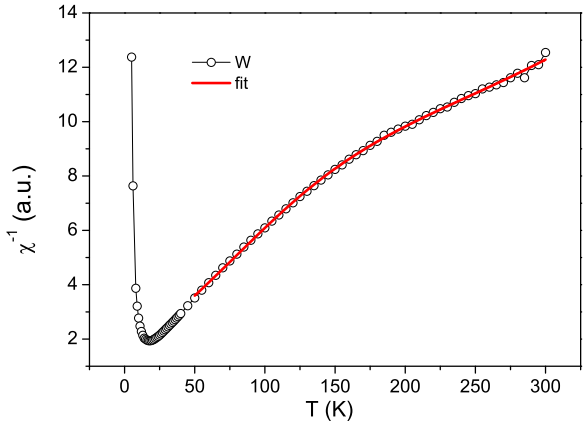

Figure 6.4:
Fits of the inverse susceptibility vs temperature according to Eq.(6.1.2) for sample W.

Using $\mu_{AT} = \mu_p/N$ and Eq.(6.1.1), the inverse total susceptibility is therefore given by

$$\chi^{-1}_{total}(T) = \frac{3k_B}{\rho_p \mu_p^2(0)\left(1-\frac{T}{T_C}\right)\left\{\frac{1}{(T+T_D)} + \frac{dSf_0 e^{\frac{-E_A}{k_B T}}}{NT}\right\}} \tag{6.0}$$

Eq.(6.1.2) provides a very good fit of the experimental data of sample W, as it is shown in FIGURE 6.4. Considering that the total amount of atoms per particle is $N_0 \approx 2500$, therefore the fraction of magnetic ones (Fe) is 60%, i.e. N = 1500, and $dS \approx 0.034$. Using these values and the above Eq.(6.1.2) we obtain the corrected values $T_D = 32.3$ K, $T_C = 806.0$ K, $E_a/k_B = 616.0$ K and the normalizing factor $f_0 = 6806$. $T_D = 32.3$ K indicates a small interaction energy, as evidenced above; the higher $T_C = 806.0$ K is a sign of higher thermal stability, in agreement with the assumption above and $E_A/k_B = 616.0$ K is interpreted as the average temperature for the surface atomic moments to become free and is smaller than T_C, again as expected. This supports our arguments for the existence of frustrated spins at the surface that progressively unpin with increasing temperature and contribute paramagnetically to the total magnetic susceptibility, accounting thereby for the anomalous behaviour of sample W.

7 Conclusions

In Chapter 2 we studied the magnetic properties and MCE of randomly distributed single-domain SPM nanoparticle systems as governed by the magnetic field, magnetic anisotropy, and dipolar interactions. To undertake such complex problem we have used a computational technique that allowed us to eliminate uncontrolled dispersion aspects. Our results indicate that:

- Increasing H lowers the anisotropy barrier and hence results in an increase of T_B, as expected. Regarding the MCE, we have demonstrated the existence of a particular field value H^* at which the magnetocaloric properties are optimized, which indicates the more efficient field for MCE implementations.

- Increasing K results in an overall increase of T_B, in agreement with SPM properties. Noteworthy, different K values account for different evolutions on the $T_B(c)$ dependence, pointing out an explanation to some contradictory reports reported in the literature. Regarding the MCE, we have found an overall decrease of ΔS_M with increasing K. When comparing different sample concentrations, we have found that for a given K it is possible to fit a particular concentration for which ΔS_M is maximized, and that this particular concentration grows with larger K values.

- From the theoretical point of view, interparticle interactions strongly influence the field-dependent SPM properties, demonstrating that the theoretical models usually employed in the literature are unable to describe the interacting conditions. From the applied MCE-related point of view, we have found the existence of a particular concentration c^* at which the MCE is optimized, complementing the field-dependent optimizing properties. Regarding hyperthermia applications, we have found that the decrease of the heating capacity with increasing interactions reported experimentally is ascribed to the dipolar interparticle coupling, and not other effects as polydispersity and/or anisotropy effects. Concerning the macroscopic state of nanoparticle systems

as determined by interparticle dipolar interactions, we have found that increasing interactions change the shape of the Arrott plots resembling a typical first-order phase transition.

- We have reviewed a common analytical approach to fit the ZFC/FC curves, finding that such approaches fail in describing good monodisperse systems. Therefore, much care must be taken when extracting information about the system from the fitting. The origin of such failure and a simple alternative approach are discussed.

In Chapter 3, we studied the role played by the dipolar interaction on the SPM properties of nanoparticle systems as given by the evolution of T_B *vs* c. The scenario we want to understand is, how is it possible to obtain completely different trends in the $T_B(c)$ for *a priori* similar samples? Our MC simulations indicate that:

- The existence of different trends in the $T_B(c)$ curves can be reproduced by taking into account only dipolar interactions; other sources as anisotropy- or size- distribution may alter this effect, but the dipolar interactions *per se* are enough to account for completely different trends (even non-monotonic).

- We have found that it is possible to rewrite the total energy of the system in reduced units such that the strength of the magnetic dipolar interactions is directly proportional to c/c_0 in the same way as the influence of the magnetic field is normalized as H/H_A. This is to say, we predict the existence of a general $T_B(c/c_0)$ curve for interacting systems analogous to the $T_B(H/H_A)$ curve of non-interacting ones. This result is confirmed by MC simulations. Also, the suitability of c_0 as a normalizing parameter for the dipolar interaction is evaluated throughout hysteretic properties from the simulation of $M(H)$ curves, which also confirm the normalizing character of c_0.

- To explain the three different regimes observed in the shape of the general $T_B(H/H_A; c/c_0)$ curve (constant at low concentrations, regularly increasing intermediate range, and tendency to saturate at high concentrations), we figured out an explanation based on the parallel and antiparallel populations of the sample and their different features. Our hypothesis, despite fitting very well the $T_B(c)$ data, seems incorrect due to some contradictions with theoretical properties.

- The analysis of the dipolar-field histograms shows well differentiated peaks at similar field values of opposite signs. This result gives support to our argument on the need of taking into account the different features of the system in relation to the applied field in order to explain the T_B shape, despite the proposed model is incorrect.

- The c_0 parameter can be very useful for designing specific MCE and recording applications.

In Chapter 4 we have carried out a detailed analysis of both the magnetic and magnetocaloric properties of a system of dipolar interacting magnetic nanoparticles collinearly arranged in 1D-nanoparticle chains. Our results indicate that:

- A mean-field treatment is not adequate to study the magnetic behaviour of nanoparticle chains with collinear easy axes, since incorrect interpretations regarding the magnetic properties of the system might be inferred.
- The ZFC and FC curves overlap in the whole temperature range when the field is applied perpendicular to the chains (if the easy axes are collinear aligned along the chains). Both curves exhibit a maximum and decay in a SPM fashion at higher temperatures; however, this maximum cannot be associated to the SPM T_B, because none of the anisotropy wells is favoured by the field and so it must have a different origin.
- FM-type intra-chain ordering and AFM-type inter-chain one are found when the anisotropy axes are collinear aligned along the chains, and also when no anisotropy is taken into account. However, if the easy anisotropy axes are distributed at random an AFM-like intra-chain magnetic ordering is observed.
- We have found coexistence of direct and inverse MCE both of reversible character when the magnetic field is applied perpendicular to the chains and the easy axes are collinear aligned along the chain. Having focused on the direct-MCE, we have found the existence of a particular field $H^* = 2.5H_A$ that optimizes the MCE.
- A detailed analysis of the H^* feature at different simulation conditions indicates that it is independent of the computational characteristics (size of the system of boundary conditions). By simulating $M(H)$ processes for the same conditions, from the $\partial M/\partial H$ analysis we have found typical phase transition at exactly H^*. This phase-transition feature is robust under time-dependence analysis, independent on the system size or boundary conditions, and exhibits a well defined linear dependence on the dipolar-energy factor M_S^2.

In Chapter 5, the MCE is studied in NiMn-based Heusler alloys in ribbon shape around the martensitic first-order structural phase transition. The ribbons exhibit a columnar-like structure perpendicular to the rolling direction. For the $Ni_{50.3}Mn_{35.5}Sn_{14.4}$ composition under a $20kOe$ field along the rolling direction, the large hysteresis losses around the structural transition make the magnetic transition range more desirable for being used in a refrigeration cycle. A similar result was obtained for the $Ni_{50.4}Mn_{34.9}In_{14.7}$ and $Mn_{50}Ni_{40}In_{10}$ compositions, being also observed that the MCE in this latter composition does not show a significant dependency on the crystallographic structure.

In Chapter 6 it is studied the influence of the surface chemistry on the magnetic properties of $FePt$ nanoparticles. By covering the particles with two different ligands, it is found that in one case the $\chi^{-1}(T)$ curve follows the expected deviation

from the Curie-Weiss-like dependence (above the linear curve), but that in the other case it deviates in the opposite direction, below the linear tendency. This anomalous behaviour is explained as due to the contribution from the frustrated surface spins, which progressively unpin with increasing temperature and add an extra paramagnetic contribution to the total magnetic susceptibility. To test this assumption we proposed a simple fitting model; the good agreement to the experimental data supports our arguments.

8

Summary in Galician / Resume en galego

A redución do tamaño de materiais magnéticos ordinarios á escala nanométrica, resulta a miúdo na aparición de propiedades magnéticas radicalmente diferentes e/ou aumentadas respecto das correspondentes ó estado masivo. Estas propiedades dan lugar a un amplo espectro de aplicacións con grandes implicacións nas actividades e calidade de vida humana, que van dende os sistemas de gravación magnética ata aplicacións biomédicas [1]. A orixe destas propiedades especiais atópase na reducida dimensionalidade [2]: cando o tamaño do material alcanza a orde de nanómetros, a influenza dos átomos da superficie resulta totalmente comparable (ou incluso maior) á da contribución da parte masiva, os defectos debidos á rotura de simetría poden ter unha importancia significativa, e outros efectos físicos poden tamén chegar a ser moi relevantes cando o tamaño alcanza a orde das escalas características do material (como por exemplo o tamaño de dominio magnético). As propiedades que ocorren en tales dimensións reducidas son extraordinariamente sensibles a pequenas variacións de tamaño, forma, composición, etc; e estas diferencias fan que diferentes estruturas magnéticas (nanopartículas, nanofíos, capas delgadas, etc) formen campos específicos de investigación con características propias diferenciadas [3]. O obxectivo desta tese é investiga-las propiedades termomagnéticas en sistemas nanoestructurados, motivado polas inusuais propiedades que aparecen en tales dimensións.

Unha das características máis chamativas que teñen lugar nestas dimensións reducidas é o chamado *superparamagnetismo*. O fenómeno superparamagnético consiste na dependencia tipo paramagnético que ten lugar en entidades magnéticas monodominio por riba dunha temperatura característica chamada *temperatura de bloqueo*, T_B. As propiedades superparamagnéticas veñen determinadas por unha complexa interrelación entre os parámetros magnéticos do sistema (campo aplicado, momento, anisotropía, etc), e entender estas propiedades SPM en función dos diferente parámetros é moi importante tanto polo coñecemento teórico [4] como para aplicacións específicas (como por exemplo o aumento da capacidade de información

de discos duros e a súa estabilidade [5], ou o desenrolo de aplicacións biomédicas ben controladas [6]). Como resultado disto, durante as últimas décadas estase a levar a cabo un tremendo esforzo co obxectivo de entender os mecanismos físicos do fenómeno SPM

Nembargantes, a investigación das propiedades SPM é unha tarefa complexa debido á súa forte dependencia en parámetros non controlados, os cales enmascaran a orixe física e fan polo tanto moi complicada unha caracterización precisa. Así, a alta diversidade de parámetros que se acha en sistemas reais, orixinada na ampla variación das propiedades físicas (dispersión de tamaños, anisotropías, etc), así como en interaccións non controladas, resulta nun complexo problema físico non soluble mediante técnicas analíticas. Neste senso, o forte desenrolo da capacidade computacional que está a ter lugar na actualidade permite un control preciso das características non controlables do sistema cunha cada vez maior semellanza coa realidade, o que convirte o uso de técnicas computacionais en ferramentes moi potentes para o estudo de complexos escenarios físicos como o descrito anteriormente.

Nesta tese usamos un método de Monte Carlo baseado no algoritmo de Metropolis para estudar tales nanoestruturas magnéticas: por unha beira, co método de MC podemos controlar perfectamente as características do sistema e, pola outra beira, podemos estudar problemas para os que non existe solución analítica, como por exemplo a interacción magnética dipolo-dipolo. Este é o principal obxectivo da tese: estudo de diferentes sistemas magnéticos nanoestruturados mediante o uso dunha técnica de MC, como sistemas de partículas distribuídas ó azar ou conxuntos de partículas formando cadeas, e investigar cómo os diferentes parámetros característicos (anisotropía, tamaño, forma, interaccións, etc) governan o seu comportamento.

En paralelo ó estudo das propiedades magnéticas básicas de tales sistemas nanoestructurados, levamos tamén a cabo unha análise detallada dunha característica magnetotérmica moi especial, o chamado *efecto magnetocalórico* (EMC), i.e. a variación da temperatura dun material magnético debido á variación dun campo magnético externo. O EMC é moi importante para aplicacións tecnolóxicas como a refrixeración magnética (diminución da temperatura mediante o uso do MCE a través de ciclos adiabáticos/isotérmicos) ou tratamentos de hipertermia (destrucción das células tumorais malignas mediante un aumento selectivo da dúa temperatura). O EMC, coma calquera outro efecto magnético no mundo *nano*, está suxeito a novas e incontroladas propiedades que xorden das especiais características propias da baixa dimensionalidade. Co obxectivo de acadar un maior coñecemento destas propiedades, levamos a cabo un estudo sistemático das propiedades magnetocalóricas dos sistemas nanoestructurados de xeito complementario ó de caracterización das propiedades magnéticas.

A tese organízase do seguinte xeito. Os tres aspectos anteriores, i.e. *superparamagnetismo*, *método de MC* e *MCE*, constitúen as liñas de guía do noso traballo e

polo tanto as súas propiedades xerais son primeiramente analizadas, para despois pasar á descrición dos nosos resultados de investigación.

Superparamagnetismo: ó fenómeno magnético observado en sistemas de entidades magnéticas monodominio con moitas similaridades ó paramagnetismo atómico. Basicamente, a idea é que entidades magnéticas monodominio poden ser caracterizadas polo seu *supermomento* magnético total, o cal ten un decaemento tipo paramagnético por riba de T_B. Esta temperatura característica, a diferencia da temperatura de Curie, depende fortemente no tempo de medida e dá lugar a un complexo escenario con características especiais [4, 7–9].

Método de MC: son simulacións numéricas baseadas en xerar números aleatorios [17] para resolver problemas con moitos graos de liberdade. A técnica de MC consiste en representar as características dun sistema particular mediante probabilidades, para xerar unha grande cantidade de números ó azar e contar a fracción deles que obedezan certas condicións. O xeito de contar e as condicións impostas definen o algoritmo numérico. Nesta tese usámo-lo algoritmo de Metropolis, escolla realizada en base ás súas adecuadas caracterísicas para simula-las propiedades magnéticas de sistemas nanoestructurados [20].

EMC: variación de temperatura experimentada por un material magnético (ΔT_{ad}) cando se somete a unha variación adiabática dun campo magnético externo. A magnitude e signo de ΔT_{ad} dependen fortemente tanto nas características do sistema (forma, anisotropía, etc) como nas condicións experimentais (temperatura, campo magnético, tempo, presión, historia térmica, etc), dando lugar a un rico escenario para aplicacións tecnolóxicas. A magnitude usualmente empregada para medi-lo EMC é a variación de entropía magnética ΔS_M, directamente relacionada con ΔT_{ad} [32].

A continuación descríbense brevemente os nosos resultados acerca do SPM e EMC en diferentes sistemas naneostructurados. Comezaremos coa presentación dos referidos a sistemas de nanopartículas magnéticas distribuídas ó azar, analizando o comportamento dos mesmos en función das principais enerxías que regulan o seu comportamento. Despois, centrámonos na análise da influencia da interacción dipolar magnética neste tipo de sistemas, tratando de comprende-la disparidade atopada entre diferentes medidas experimentais e propondo unha lei de escala xeral capaz de describi-los diferentes comportamentos. A continuación, estudámo-las propiedades magnéticas e EMC nun sistema de partículas que forman estructuras unidimensionais, tipo cadeas, onde encontramos que a orientación dos eixos de anisotropía é un parámetro fundamental á hora de determina-las propiedades do sistema. Ademáis, encontramos a existencia dun campo magnético que optimiza o EMC, o cal ten características de transición de fase.

Ó longo deste periodo de tese, tamén, non analizamos somentes sistemas monodominio mediante simulacións de MC, senón que, de xeito complementario, mantivemos unha estreita colaboración con grupos experimentais que nos deu a oportunidade de extende-la nosa investigación a outros escenarios. Neste senso, cabe

destacar a similaridade entre o comportamento das cadeas de partículas unidimensionais e o de nanofíos magnéticos. Tamén estudamos o EMC en aleacións tipo Heusler baseades en NiMn con forma de cintas; así como desenrolamos un simple modelo teórico para tratar de comprende-la desviación anómala respecto do comportamento tipo Curie-Weiss usual que se obtén experimentalmente en partículas de FePt dependendo da química de superficie das mesmas.

Sistemas de nanopartículas magnéticas distribuídas ó azar

Neste capítulo estudámolas propiedades magnéticas e o EMC en nanopartículas magnéticas distribuídas ó azar en función dos principais parámetros que governan o seu comportamento: campo magnético H, interaccións dipolares entre as partículas, e anisotropía magnética (asumimos de tipo uniaxial, dada por K). Tamén realizamos algunhas consideracións teóricas acerca da importancia das medidas *zero field cooling* (ZFC) en *field cooling* (FC) para o estudo de sistemas de nanopartículas, e discutímo-la importancia de ter unha descrición analítica. Obtivemos os seguintes resultados:

- *Influencia do campo aplicado*: a variación de entropía magnética ΔS_M sempre aumenta con valores crecentes de campo [50]) e, ademáis, demostramos que existe un valor de campo magnético $H < H^*$ que optimiza o EMC. Este campo particular delimita tamén dúas tendencias diferentes no comportamento de ΔS_M: para campos $H < H^*$ a curva da entropía é estreita, medra rapidamente con valores crecentes de campo e a súa posición na temperatura permanece esencialmente constante. Pola outra beira, para campos $H > H^*$ a curva de entropía faise máis ampla conforme aumenta o campo mentres vai ocorrendo a maiores temperaturas, medrando nembargantes a un ritmo menor co campo. O campo $H < H^*$ indica as condicións máis eficientes para a implementación do EMC, esenciais para reduci-lo consumo de enerxía.

- *Papel da anisotropía magnética*: para unha concentración fixa ΔS_M diminúa conforme aumenta a anisotropía, mentres que os máximos ocorren a maiores temperaturas. Cando comparámo-los valores de ΔS_M a diferentes concentracións, observamos que para un valor da anisotropía é posible definir un valor particular da concentración para o que ΔS_M é maior, e que esta concentración aumenta con valores crecentes da anisotropía. En paralelo ó estudo do EMC no sistema, analizamos tamén as súas propiedades SPM, centrándonos na evolución de T_B con K para a diferentes concentracións. Obtemos en xeral un incremento de T_B con K, o que corresponde cun aumento das barreiras de enerxía. Topamos tamén que os resultados non son ben descritos polos modelos clásicos, o que indica a necesidade dun maior esforzo teórico para poder ter en conta as interaccións dipolares magnéticas en relación coa teoría SPM.

- *Influenza das interaccións dipolares* As interaccións dipolares en sistemas de nanopartículas distribuídas ó azar da lugar a un amplo escenario, tanto respecto ás propiedades SPM como ó EMC. Dende o punto de vista teórico, as interaccións entre as partículas infúen fortemente na dependencia no campo das propiedades SPM, demostrando que os modelos teóricos usualmente empregados na literatura son incapaces de describi-las interaccións. Acerca do EMC, o rico escenario que xorde das interaccións dipolares abre a porta a propiedades magnetocalóricas optimizadas, xa que é posible definir unha concentración que leva a un maior EMC. É entón evidende a necesidade de extender este traballo para opter unha completa caracterización da dependencia no campo, anisotropía e concentración en sistemas de nanopartículas que dea conta dun EMC óptimo. Acerca de aplicacións de hipertermia, achamos que a diminución da capacidade de quecemento co aumento de concentración que se atopa experimentalmente se debe ó acoplo dipolar, e non a outros efectos como polidispersión e/ou efectos de anisotropía. Analizando o estado macroscópico do sistema en función da interacción entre as partículas, encontramos que as dúas características principais dos vidros de espín, frustración e desorde, poden ser achados en sistemas conxeados de partículas distribuídas ó azar. Nos diagramas de Arrott, a altas concentracións obsérvase unha inversión na curvatura que nos recorda a forma dunha transición de fase de primeira order. Esta transición áchase na mesma order de concentracións á cal se observou comportamento de vidro de espín [24]. O comportamento xeral das isotermas coa concentración é o desprazamento cara maiores temperaturas, o que concorda coa transición dende un escenario tipo anisotropía ó azar ata a un escenario tipo campo ó azar.

- *Axuste analítico das curvas ZFC* Revisando unha aproximación analítica para axusta-las curvas ZFC e FC topamos que falla para describir sistemas monodispersos, o que nos indica que hai que ter moito coidado coa información do sistema que pretendamos obter do axuste. Nembargantes, o axuste é matemáticamente moi bo, o que nos indica que quizais unha reinterpretación dos seus termos, mantendo a estructura matemática, poida indicarnos unha correcta descrición tamén do caso ideal monodisperso. Con este obxectivo, propomos unha simple alternativa baseada nas propiedades SPM das partículas.

Unha lei de escala para a influenza da interacción dipolar magnética

Neste capítulo estudámolo papel desenrolado pola interacción dipolar magnética nas propiedades dun sistema de partículas superparamagnéticas. O estudo da interacción dipolar, analizado a través da súa influenza en T_B, foi o obxecto dunha intensa investigación durante moitos anos debido á súa importancia para aplicacións tecnolóxicas, pero a pesares do grande esforzo realizado non se chegou a desenrolar

unha teoría capaz de describi-los diferentes (a miúdo contradictorios) comportamentos experimentais descritos na literature. En xeral, modelos teóricos consideran unha evolución monotónica de T_B en función da concentración (que dá conta da intensidade da interacción dipolar), e interpretan os resultados basándose na idea de que a interacción modifica a barreira de enerxía de anisotropía dunha única partícula equivalente. Nembargantes, ese tipo de modelos non describen as diferentes dependencias obtidas experimentalmente, sendo somentes exitosos nalgúns casos particulares.

O noso obxectivo é tratar de acercarnos ó problema dende unha perspectiva diferente. Para iso, o primeiro paso foi o de comprobar que comportamentos non-monotónicos descritos experimentalmente e que os modelos clásicos non poden describir, son efectivamente de orixe puramente dipolar e non doutro tipo. Despois, a nosa maneira de aborda-lo problema é a tratar de responder á seguinte pregunta: cómo é posible que se obteñan curvas $T_B(c)$ tan diferentes para *a priori* sistemas moi semellantes? (considerando os sistemas como governados polas mesmas enerxía principais, é dicir, Zeeman, anisotropía, e dipolar). Os nosos resultados indican que:

- Existe unha concentración crítica c^* que marca a transición entre dous réximes diferentes na evolución de T_B coas interaccións entre partículas (representadas a través da concentración). A baixas concentracións ($c < c^*$), as partículas compórtanse como un sistema ideal non-interactuante cun valor constante de T_B. A concentracións $c > c^*$, nembargantes, a interacción dipolar aumenta a barreira de enerxía (T_B aumenta con c), de tal xeito que unha maior temperatura é necesaria para alcanza-lo estado SPM. O axuste dos nosos resultados con modelos clásicos e medidas experimentais apoian a existencia de dous réximes diferenciados, os cales non poden ser interpretados nin preditos polas teorías SPM usuais. Estes resultados confirman a necesidade de mellora-los modelos teóricos.

- Topamos que a influencia da interacción dipolar pode ser descrita dun xeito xeral, sendo posible definir un parámetro de escala que normaliza a súa influenza. Esto obtense de analiza-la marco enerxético dos sistemas de partículas, de onde é posible definir un parámetro adimensional, $c_0 = 2K/M_S^2$, que funciona como un factor de escala para a interacción dipolar dada a través da concentración, tal que c/c_0. Para demostrar isto realizamos simulacións de procesos ZFC para diferentes tipos de partículas (identificadas polo seu parámetro correspondente c_0), e achamos que as diferentes tendencias $T_B(c)$ obtidas experimentalmente se poden reproducir con diferentes valores de c_0, e que corresponden a diferentes partes dunha curva xeral $T_B(c/c_0)$. Este resultado confírmase tamén con outro tipo de medidas como propiedades de histérese e valores relativos da magnetización, o que confirma o carácter de c_0 como un factor de escala xeral para a influenza da interacción dipolar magnética.

- A análise microscópica da influenza da interacción dipolar na evolución de T_B *vs* c suxire que os modelos baseados na barreira de enerxía dunha partícula non son válidos, e que as diferentes características das partículas en función da súa orientación relativa e respecto do campo teñen que ser tidas en conta. Para probar este razoamenteo, propomos un modelo para describi-la curva $T_B(c)$ baseado na idea de que as partículas poden ser clasificadas segundo dous subsistemas, como paralelas e antiparalelas ó campo, e que cada subsistema se poida asociar á súa propia temperatura de bloqueo. O resultado é contradictorio: por unha beira, resulta nun moi bo axuste dos datos experimentais pero, pola outra, entra en contradicción con propiedades teóricas das partículas, o que o invalida. Para comprobar entón a nos hipótese acerca das dúas subpoboacións de partículas, analizámo-los histogramas dos campos dipolares do sistema a través dos procesos típicos ZFC, tanto durante o enfriamento sen campo, como no seguinte quecemento con campo. Os resultados mostran un escenario complexo, pero que confirma plenamente os nosos argumentos acerca da necesidade de ter en conta as relativas orientacións das partículas respecto do campo aplicado para poder describi-lo efecto da interacción dipolar.

- Estudamos tamén o uso do parámetro c_0 dende o punto de vista de aplicación, tanto para o EMC como para aplicacións baseadas nas propiedades de histérese, e achamos que pode ser moi útil para o deseño de valores optimizantes an ambos casos.

Cadeas de nanopartículas magnéticas

Neste capítulo levamos a cabo unha análise detallada das propiedades magnéticas e EMC nun sistema de partículas distribuídas en cadeas unidimensionais, considerando a interacción dipolar entre elas. Este tipo de sistema ten moita interese polas súas prometedoras aplicacións tecnolóxicas [103], en particular para incrementa-la capacidade de almaceamento magnética [104] e para procesado dixital [105]. Nestes sistemas, a interrelación entre a anisotropía magnética a a interacción dipolo-dipolo constitúe a clave que determina as propiedades magnéticas do sistema, xa que a relación entre ambos termos enerxéticos constitúe un complexo problema. Os nosos resultados indican que:

- Dende o punto de vista macroscópico, o axuste da magnetización a unha dependencia campo medio tipo Curie-Weiss non é adecuada para estudalas propiedades magnéticas do sistema cando os eixos das partículas están aliñados ó longo das mesmas e o campo se aplica en dirección perpendicular. Este resultado coincide co indicado por Vargas et al. [107], demostrando que de tal axuste se podería inferir información incorrecta acerca do ordeamento do sistema. A análise microscópica do problema mostra a aparición

de ordeamento FM entre cadeas combinado con AFM dentro das mesmas conforme diminúe a temperatura. Ambas disposicións magnéticas non son totalmente regulares. Co obxecto de comprender mellor o papel desenrolado pola anisotropía magnética, simulamos tamén a evolución do sistema considerándoo sen anisotropía. Neste caso obsérvase ordeamento tipo FM ben definido entre as cadeas, inda que non se observan cambios apreciables na irregular orde AFM dentro das cadeas. Cremos que un arranxo total AFM sería alcanzado para tempos moito maiores, de tal xeito que poida ter lugar unha inversión colectiva da magnetización de toda unha cadea. Finalmente, para comprende-la orde AFM observada por Bliznyuk et al. [101], simulámolos mesmos casos pero considerando agora unha distribución aleatoria dos eixos de anisotropía. Neste caso obtivemos ordeamento AFM entre as cadeas tanto da aproximación macroscópica tipo Curie-Weiss como da análise microscópica, o que resalta a importancia da orientación dos eixos de anisotropía para determina-las propiedades magnéticas do sistema.

- Con respecto ó EMC neste sistema, achamos coexistencia de EMC directo e inverso ambos de carácter reversible, inda que o rango inverso é bastante pequeno e polo tanto debe ser extendido para usos prácticos. Polo tanto, centramos a nosa análise no rango de EMC directo, obtendo que a dependencia no campo aplicado do factor $(-\partial m/\partial t)$ revela a existencia dun campo optimizante $H^* \approx 2.5H_A$ para o EMC. Analizando tamén a capacidade refrixerante (RC), obtivemos que é practicamente independente da temperatura para intervalos ata de $20K$ ó redor do máximo de ΔS_M, e que resulta tamén optimizada para o mesmo campo $H^* \approx 2.5H_A$, polo tanto reforzando a idoneidade deste valor de campo para optimiza-lo EMC.

- Co obxectivo de comprende-la orixe deste campo optimizante, realizamos un estudo sistemático das súas características a través das curvas $M(H)$, obtendo que presenta características típicas de transición de fase. Estas características son independentes do tempo, tamaño do sistema e condicións de contorno, tendo unha dependencia liñal no factor proporcional á enerxía dipolar M_S^2. Cabe destacar que resultados experimentais levados a cabo no grupo da Prof. B. Hernando (Universidad de Oviedo, Spain), corroboran os nosos resultados experimentais.

Estes son os resultados obtidos en relación ó superparamagnetismo e baseados no método de MC. En paralelo a este estudo, ó longo desta tese analizamos outro tipo de sistemas en colaboración con grupos experimentais. En particular cabe destacar os seguintes.

EMC en materiais tipo Heusler con forma de cinta

Estudámo-lo EMC en aleacións basadas en NiMn tipo Heusler con forma de cinta con transición de fase estructural martensítica. A síntese das cintas e a súa caracterización experimental foi levada a cabo polo grupo da Prof. B. Hernando (Universidad de Oviedo, Spain). As cintas teñen unha estrutura tipo columnar en dirección perpendicular ó plano. Estudamos tres composicións, $Ni_{50.3}Mn_{35.5}Sn_{14.4}$, $Ni_{50.4}Mn_{34.9}In_{14.7}$, e $Mn_{50}Ni_{40}In_{10}$, obtendo para os tres casos un elevado EMC na transicón estructural, pero acompañado de grandes perdas por histérese, o que fai máis atractiva para o EMC a transicón magnética. Para as tres composicións obsérvase unha influenza desprezable da estrutura cristalográfica sobre o EMC.

Desviación anómala respecto do comportamento tipo Curie-Weiss

Estudámo-la influenza da química de superficie nas propiedades magnéticas de nanopartículas de $FePt$. A síntese das partículas e a súa caracterización experimental foi levada a cabo polo grupo do Prof. M. Farle (Universität Duisburg-Essen, Germany). Cubrindo as partículas por dous ligandos diferentes, tópase que nun caso a inversa da susceptibilidade, $\chi^{-1}(T)$, segue a desviación agardada respecto da dependencia tipo Curie-Weiss (por riba do comportamento liñal), mentres que no outro caso se desvía na dirección oposta, é dicir por baixo do comportamento liñal. Este comportamento anómalo explícase pola contribución dos espíns frustrados na superficie, os cales van progresivamente soltándose co aumento da temperatura e engaden unha contribución PM extra á susceptibilidade magnética total. Para comprobar esta suposición propomos un simple modelo analítico; a boa concordancia cos datos experimentais apoia os nosos argumentos.

Bibliography

[1] G. Herzer, J. Magn. Magn. Mater. **294**, 99 (2005).

[2] A. P. Guimarâes, *Principles of Nanomagnetism* (Springer, 2009).

[3] R. Skomsky, J. Phys.: Condens. Matter **15**, R841 (2003).

[4] J. Dormann, D. Fiorani, and E. Tronc, Adv. Chem. Phys. **98**, 283 (1997).

[5] V. Skumryev, S. Stoyanov, Y. Zhang, G. Hadjipanayis, D. Givord, and J. Nogués, Nature **423**, 850 (2003).

[6] P. Tartaj, M. Puerto-Morales, S. Veintemillas-Verdaguer, T. González-Carreño, and C. Serna, J. Phys. D: Appl. Phys. **36**, R182 (2003).

[7] K. Sattler, ed., *Handbook of Nanophysics: Nanoparticles and Quantum Dots* (Taylor&Francis, Honolulu, 2010), vol. 3.

[8] O. Petracic, Superlattices and Microstructures **47**, 569 (2010).

[9] M. Knobel, W. Nunes, L. Socolovsky, E. D. Biasi, J. Vargas, and J. Denardin, J. Nanoscience and Nanotechnology **8**, 2836 (2008).

[10] L. Néel, Ann. Geophys. **5**, 99 (1949).

[11] P. Jönsson, Adv. Chem. Phys. **128**, 191 (2004).

[12] E. Stoner and E. Wohlfarth, Proc. R. Soc. London A **240**, 599 (1948).

[13] J. García-Otero, M. Porto, J. Rivas, and A. Bunde, Phys. Rev. Lett. **84**, 167 (2000).

[14] K. Usadel, Phys. Rev. B **73**, 212405 (2006).

[15] U. Nowak, R. Chantrell, and E. Kennedy, Phys. Rev. Lett. **84**, 163 (2000).

[16] X. Cheng, M. Jalil, H. Lee, and Y. Okabe, Phys. Rev. Lett. **96**, 067208 (2006).

[17] K. Binder and D. Heermann, *Monte Carlo Simulations in statistical physics: an introduction* (Springer, 2002).

[18] O. Iglesias, Doctoral Thesis (2005).

[19] N. Metropolis, Los Alamos Science **Special Issue**, 125 (1987).

[20] J. P. Nunes, M. Bahiana, and C. Bastos, Phys. Rev. E **69**, 056703 (2004).

[21] D. Hinzke and U. Nowak, Comput. Phys. Commun. **121**, 334 (1999).

[22] J. García-Otero, M. Porto, J. Rivas, and A. Bunde, J. Magn. Magn. Mater. **203**, 268 (1999).

[23] J. García-Otero, M. Porto, J. Rivas, and A. Bunde, J. Appl. Phys. **855**, 2287 (1999).

[24] M. Ulrich, J. García-Otero, J. Rivas, and A. Bunde, Phys. Rev. B **67**, 024416 (2003).

[25] R. Lavin, J. Denardin, A. Espejo, A. Cortés, and H. Gómez, J. Appl. Phys. **107**, 09B504 (2010).

[26] J.-H. Lim, W.-S. Chae, H.-O. Lee, L. Malkinski, S.-G. Min, J. Wiley, J.-H. Jun, S.-H. Lee, and J.-S. Jung, J. Appl. Phys. **107**, 09A334 (2010).

[27] V. Franco, K. Pirota, V. Prida, A. Neto, A. Conde, M. Knobel, B. Hernando, and M. Vazquez, Phys. Rev. B **77**, 104434 (2008).

[28] V. Prida, V. Vega, D. Serantes, D. Baldomir, M. Ilyn, A. Zhukov, J. González, and B. Hernando, Phys. Status Solidi A **206**, 2234 (2009).

[29] D. Serantes, V. Prida, M. Pereiro, B. Hernando, and D. Baldomir, manuscript in preparation (????).

[30] W. Luo, S. Nagel, T. Rosenbaum, and R. Rosensweig, Phys. Rev. Lett. **67**, 2721 (1991).

[31] C. Hoppe, F. Rivadulla, M. López-Quintela, M. Buján, J. Rivas, D. Serantes, and D. Baldomir, J. Phys. Chem. C **112**, 13099 (2008).

[32] V. Pecharsky and K. Gshneidner, J. Magn. Magn. Mater. **200**, 44 (1999).

[33] K. Gshneidner and V. Pecharsky, Int. J. Refrig. **31**, 945 (2008).

[34] R. Hergt, S. Dutz, R. Müller, and M. Zeisberger, J. Phys.: Condens. Matter. **18**, S2919 (2006).

[35] R. Bjørk, C. Bahl, A. Smith, and N. Pryds, Int. J. Refrig. **33**, 427 (2010).

[36] L.-M. Lacroix, R. B. Malaki, J. Carrey, S. Lachaize, M. Respaud, G. Goya, and B. Chaudret, J. Appl. Phys. **105**, 023911 (2009).

[37] N. de Oliveira and P. von Ranke, Phys. Rep **489**, 89 (2010).

[38] K. Gshneidner, V. Pecharsky, and A. Tsokol, Rep. Prog. Phys. **68**, 1479 (2005).

[39] P. Poddar, J. Gass, D. Rebar, S. Srinath, H. Srikanth, S. Morrison, and E. Carpenter, J. Magn. Magn. Mater. **307**, 227 (2006).

[40] A. Tishin and Y. Spichkin, *The Magnetocaloric Effect and its Applications* (Institute of Physics Publishing, Bristol, 2003).

[41] B. Yu, Q. Gao, B. Zhang, X. Meng, and Z. Chen, Int. J. Refrig. **26**, 622 (2003).

[42] J. Amaral and V. Amaral, J. Magn. Magn. Mater. **322**, 1552 (2010).

[43] H. Callen, *Thermodynamics* (Institute of Physics Publishing, Bristol, 2003).

[44] D. Serantes, D. Baldomir, C. Martinez-Boubeta, K. Simeonidis, M. Angelakeris, E. Natividad, M. Castro, A. Mediano, D.-X. Chen, A. Sanchez, et al., J. Appl. Phys. **108**, 073918 (2010).

[45] J. Sun, B. Shen, and F. Hu, eds., *Nanoscale Magnetic Materials and Applications* (Springer Science+Business Media, 2009).

[46] J. Vargas, W. Nunes, L. Socolovsky, M. Knobel, and D. Zanchet, Phys. Rev. B **72**, 184428 (2005).

[47] D. Serantes, D. Baldomir, M. Pereiro, J. Rivas, C. Vázquez-Vázquez, M. Buján-Núñez, and J. Arias, Phys. Status Solidi A **205**, 1349 (2008).

[48] R. Victora, Phys. Rev. Lett. **63**, 457 (1989).

[49] M. Azeggagh and H. Kachkachi, Phys. Rev. B **75**, 174410 (2007).

[50] D. Baldomir, J. Rivas, D. Serantes, M. Pereiro, J. Arias, M. Buján-Núñez, and C. Vázquez-Vázquez, J. Non-Cryst. Solids **353**, 793 (2007).

[51] D. Baldomir, D. Serantes, M. Pereiro, J. Rivas, C. Vázquez-Vázquez, M. Buján-Núñez, and J. Arias, Phys. Status Solidi A **205**, 1343 (2008).

[52] J. Dormann, L. Bésais, and D. Fiorani, J. Phys. C **21**, 2015 (1988).

[53] S. Mørup and E. Tronc, Phys. Rev. Lett. **72**, 3278 (1994).

[54] W. Nunes, L. Socolovsky, J. Denardin, F. Cebollada, A. Brandl, and M. Knobel, Phys. Rev. B **72**, 212413 (2005).

[55] D. Baldomir, J. Rivas, D. Serantes, M. Pereiro, J. Arias, M. Buján-Núñez, and C. Vázquez-Vázquez, J. Non-Cryst. Solids **353**, 790 (2007).

[56] D. Serantes, D. Baldomir, M. Pereiro, J. Arias, C. Mateo-Mateo, M. Buján-Núñez, C. Vázquez-Vázquez, and J. Rivas, J. Non-Cryst. Solids **354**, 5224 (2008).

[57] G. Kakazei, Y. Pogorelov, J. Santos, J. Sousa, P. Freitas, S. Cardoso, N. Lesnik, and P. Wigen, J. Magn. Magn. Mater. **266**, 57 (2003).

[58] A. Ito, K. Tanaka, M. Kondo, M. Shinkai, H. Honda, K. Matsumoto, T. Saida, and T. Kobayashi, Cancer Sci. **94**, 308 (2003).

[59] I. Hilger, R. Hiergeist, R. Hergt, K. Winnefeld, H. Schubert, and W. A. Kaiser, Invest. Radiol. **37**, 580 (2002).

[60] M. Johannsen, U. Gneveckow, L. Eckelt, A. Feussner, N. Waldöfner, R. Scholz, S. Deger, P. Wust, S. Loening, and A. Jordan, Int. J. Hyperthermia **21**, 637 (2005).

[61] S. Barry, Int. J. Hyperthermia **24**, 451 (2008).

[62] R. Rosensweig, J. Magn. Magn. Mater. **252**, 370 (2002).

[63] S. Purushotham and R. Ramanujan, J. Appl. Phys. **107**, 114701 (2010).

[64] A. Urtizberea, E. Natividad, A. Arizaga, M. Castro, and A. Mediano, J. Phys. Chem. C **114**, 4916 (2010).

[65] T. Samaras, P. Regli, and N. Kusterl, Phys. Med. Biol. **45**, 2233 (2000).

[66] R. Hergt, W. Andrä, C. d'Ambly, I. Hilger, W. Kaiser, U. Richter, and H.-G. Schmidt, IEEE Trans. Mag. **34**, 3745 (1998).

[67] A. Wang, J. Li, and R. Gao, Appl. Phys. Lett. **94**, 212501 (2009).

[68] M. Jeun, S. Bae, A. Tomitaka, Y. Takemura, K. Park, S. Paek, and K.-W. Chung, Appl. Phys. Lett. **95**, 082501 (2009).

[69] M. Bandyopadhyay and S. Dattaguptal, Phys. Rev. B **74**, 214410 (2006).

[70] P. Jönsson, M. Hansen, and P. Norblad, Phys. Rev. B **61**, 1261 (2000).

[71] A. Arrott, Phys. Rev. **108**, 1394 (1957).

[72] A. Aharony and E. Pytte, Phys. Rev. Lett. **45**, 1583 (1980).

[73] D. Zhang, K. Klabunde, C. Sorensen, and G. Hadjipanayis, Phys. Rev. B **58**, 14167 (1998).

[74] D. Baldomir, D. Serantes, M. Pereiro, J. Botana, J. Arias, S. Masunaga, and J. Rivas, J. Nanoscience and Nanotechnology **10**, 2717 (2010).

[75] T. Nath and A. Majumdar, J. Appl. Phys. **70**, 5828 (1991).

[76] Z. Zhan, Z. Hua, D. Wuang, C. Zhang, B. Gu, and Y. Du, J. Magn. Magn. Mater. **302**, 109 (2006).

[77] M. Respaud, J. Broto, H. Rakoto, A. Fert, L. Thomas, B. Barbara, M. Verelst, E. Snoeck, P. Lacante, A. Mosset, et al., Phys. Rev. B **57**, 2925 (1998).

[78] O. Margeat, M. Tran, M. Spasova, and M. Farle, Phys. Rev. B **75**, 134410 (2007).

[79] C. Antoniak, J. Lindner, and M. Farle, Europhys. Lett. **70**, 250 (2005).

[80] C. Antoniak, J. Lindner, V. Salgueiriño-Maceira, and M. Farle, Phys. Status Solidi A **203**, 2968 (2006).

[81] A. Trunova, J. Lindner, R. Meckenstock, M. Spasova, M. Farle, D. Ciuculescu, C. Amiens, B. Chaudret, and M. Respaud, J. Magn. Magn. Mater. **321**, 3502 (2009).

[82] D. Serantes, D. Baldomir, M. Pereiro, J. Botana, V. Prida, B. Hernando, J. Arias, and J. Rivas, J. Nanoscience and Nanotechnology **10**, 2512 (2010).

[83] D. Serantes, D. Baldomir, M. Pereiro, C. Hoppe, F. Rivadulla, and J. Rivas, Phys. Rev. B **82**, 134433 (2010).

[84] M. Hansen, C. Koch, and S. Mørup, Phys. Rev. B **62**, 1124 (2000).

[85] T. Jonsson, J. Mattsson, C. Djurberg, F. Khan, P. Norblad, and P. Svendlindh, Phys. Rev. Lett. **75**, 4138 (1995).

[86] B. Frankamp, A. Boal, M. Tuominen, and V. Rotello, J. Am. Chem. Soc. **127**, 9731 (2005).

[87] G. Papaefthymiou, E. Devlin, A. Simopoulos, D. Yi, S. Riduan, S. Lee, and J. Ying, Phys. Rev. B **80**, 024406 (2009).

[88] M. Hansen and S. Mørup, J. Magn. Magn. Mater. **184**, 262 (1998).

[89] H. Yang, D. Hasegawa, M. Takahashi, and T. Ogawa, Appl. Phys. Lett. **94**, 013103 (2009).

[90] S. Tomita, P. Jönsson, K. Akamatsu, H. Nawafune, and H. Takayama, Phys. Rev. B **76**, 174432 (2007).

[91] C. Vestal and Z. Zhang, J. Am. Chem. Soc. **125**, 9828 (2003).

[92] D. Weller, A. Moser, L. Folks, M. Best, W. Lee, M. Toney, M. Schwickert, J.-U. Thiele, and M. Doerner, IEEE Trans. Mag. **36**, 10 (2000).

[93] D. Berkov, N. Gorn, and P. Görnert, J. Magn. Magn. Mater. **226**, 1936 (2001).

[94] C. Martinez-Boubeta, D. Serantes, D. Baldomir, and et al., manuscript in preparation (????).

[95] D. Kechrakos and K. Trohidou, Phys. Rev. B **58**, 12169 (1998).

[96] W. Nunes, F. Cebollada, and M. Knobe, J. Appl. Phys. **99**, 08N705 (2006).

[97] C. Vázquez-Vázquez, M. Lovelle, C. Mateo-Mateo, M. López-Quintela, M. Buján-Núñez, D. Serantes, D. Baldomir, and J. Arias, Phys. Status Solidi A **205**, 1358 (2008).

[98] T. Yamamoto, M. Tanaka, Y. Misaka, T. Nakagawa, T. Nakatama, K. Niihara, and T. Numazawa, Scripta Mater. **46**, 89 (2002).

[99] F. Tegus, E. Brück, K. Buschow, and F. de Boer, Nature **415**, 622 (2002).

[100] Z. Zhou, G. Liu, and D. Han, ACS Nano **3**, 165 (2009).

[101] V. Bliznyuk, S. Singamaneni, S. Sahoo, S. Polisetty, X. He, and C. Binek, Nanotechnology **20**, 105606 (2009).

[102] H. Wang, Q.-W. Chen, L.-X. Sun, H.-P. Qi, X. Yang, S. Zhou, and J. Xiong, Langmuir **25**, 7135 (2009).

[103] D. Forrester, K. Kürten, and F. Kusmartsev, Phys. Rev. B **75**, 014416 (2007).

[104] I. McDayen, E. Fullerton, and M. Carey, MRS Bull. **31**, 379 (2006).

[105] R. Cowburn and M. Welland, Science **287**, 1466 (2000).

[106] J. Martín, J. Nogués, K. Liu, J. Vicent, and I. Schuller, J. Magn. Magn. Mater. **256**, 449 (2003).

[107] P. Vargas, D. Altbir, M. Knobel, and D. Laroze, Europhys. Lett. **58**, 603 (2002).

[108] D. Serantes, D. Baldomir, M. Pereiro, B. Hernando, V. Prida, J. Sánchez-Llamazares, A. Zhukov, M. Ilyin, and J. González, J. Phys. D: Appl. Phys. **42**, 215003 (2009).

[109] O. Iglesias, A. Labarta, and X. Batlle, J. Nanoscience and Nanotechnology **8**, 2761 (2008).

[110] S. Bedanta and W. Kleemann, J. Phys. D: Appl. Phys. **42**, 013001 (2009).

[111] S. Russ and A. Bunde, Phys. Rev. B **74**, 064426 (2006).

[112] W. Figueiredo and W. Schwarzacher, J. Phys.: Condens. Matter **19**, 276203 (2007).

[113] D. Stariolo and O. Billoni, J. Phys. D: Appl. Phys. **41**, 205010 (2008).

[114] R. Cowburn, Phys. Rev. B **65**, 092409 (2006).

[115] D. Serantes, D. Baldomir, M. Pereiro, B. Hernando, V. Prida, J. Sánchez-Llamazares, A. Zhukov, M. Ilyin, and J. González, Phys. Rev. B **80**, 134421 (2009).

[116] D. Gozzia, A. Latinia, G. Capannelliba, F. Canepac, M. Napoletano, M. Cimberled, and M. Tropeano, J. Alloys Compd. **419**, 32 (2006).

[117] K. Gshneidner, V. Pecharsky, and A. Tsokol, Rep. Prog. Phys. **68**, 1479 (2005).

[118] X. Liu, D. Geng, J. Du, S. Ma, B. Li, P. Shang, and Z. Zhang, Scr. Mater. **59**, 340 (2008).

[119] X. Liu, D. Geng, Q. Zhang, J. Jiang, W. Liu, and Z. Zhang, Appl. Phys. Lett. **94**, 2009 (2009).

[120] S. Ma, D. Geng, W. Zhang, W. Liu, X. Ma, and Z. Zhang, Nanotechnology **17**, 5406 (2006).

[121] C. Teichert, J. Barthel, H. Oepen, and J. Kirschner, Appl. Phys. Lett. **74**, 588 (1999).

[122] S. Kang, Z. Jia, S. Shi, D. Nikles, and J. Harrell, Appl. Phys. Lett. **86**, 062503 (2005).

[123] Z. Jia, S. Kang, S. Shi, D. Nikles, and J. Harrell, J. Appl. Phys. **99**, 08E904 (2006).

[124] T. Krenke, E. Duman, M. Acet, E. Wassermann, X. Moya, L. Mañosa, and A. Planes, Nat. Mater. **4**, 450 (2005).

[125] P. Bhobe, K. Priolkar, and A. Nigam, Appl. Phys. Lett. **91**, 242503 (2007).

[126] A. Pathak, M. Khan, I. Dubenko, S. Stadler, and N. Ali, Appl. Phys. Lett. **90**, 262504 (2007).

[127] V. Sharma, M. Chattopadhyay, and S. Roy, J. Phys. D: Appl. Phys. **40**, 1869 (2007).

[128] S. Aksoy, T. Krenke, M. Acet, and E. Wassermann, Appl. Phys. Lett. **91**, 241916 (2007).

[129] M. Chattopadhyay, V. Sharma, and S. Roy, Appl. Phys. Lett. **92**, 022503 (2008).

[130] A. Pathak, I. Dubenko, S. Stadler, and N. Ali, J. Phys. D: Appl. Phys. **41**, 202004 (2008).

[131] A. Planes, L. Mañosa, and M. Acet, J. Phys.: Condens. Matter. **21**, 233201 (2009).

[132] L. Manosa, D. González-Alonso, A. Planes, E. Bonnot, M. Barrio, J.-L. Tamarit, S. Aksoy, and M. Acet, Nat. Mater. **9**, 478 (2010).

[133] B. Hernando, J. Sánchez-Llamazares, J. Santos, L. Escoda, J. Suñol, R. Varga, D. Baldomir, and D. Serantes, Appl. Phys. Lett. **92**, 042504 (2008).

[134] B. Gao, F. Hu, J. Shen, J. Wang, J. Sun, and B. Shen, J. Appl. Phys. **105**, 083902 (2009).

[135] B. Hernando, J. Sánchez-Llamazares, J. Santos, V. Prida, D. Baldomir, D. Serantes, R. Varga, and J. González, Appl. Phys. Lett. **92**, 132507 (2008).

[136] B. Hernando, J. Sánchez-Llamazares, V. Prida, D. Baldomir, D. Serantes, M. Ilyn, and J. González, Appl. Phys. Lett. **94**, 222502 (2009).

[137] J. Sánchez-Llamazares, B. Hernando, V. Prida, D. Baldomir, D. Serantes, C. García, and J. González, Appl. Phys. A **xx**, xxxx (2010).

[138] V. Sharma, M. Chattopadhyay, R. Kumar, T. Ganguli, P. Tiwari, and S. Roy, J. Phys.: Condens. Matter. **19**, 496207 (2007).

[139] J. Sánchez-Llamazares, T. Sanchez, J. Santos, M. Pérez, M. Sanchez, B. Hernando, L. Escoda, J. Suñol, and R. Varga, Appl. Phys. Lett. **92**, 012513 (2008).

[140] J. Marcos, L. Mañosa, A. Planes, F. Casanova, X. Batlle, and A. Labarta, Phys. Rev. B **68**, 094401 (2003).

[141] J. Sánchez-Llamazares, B. Hernando, C. García, J. González, L. Escoda, and J. Suñol, Appl. Phys. Lett. **42**, 045002 (2009).

[142] S. Sun, Adv. Mater. **18**, 393 (2006).

[143] S. Sun, C. Murray, D. Weller, L. Folks, and A. Moser, Science **287**, 1989 (2000).

[144] U. Wiedwald, M. Spasova, E. Salabas, M. Ulmeanu, M. Farle, Z. Frait, A. Fraile-Rodriguez, D. Arvanitis, N. Sobal, M. Higendorff, et al., Phys. Rev. B **68**, 644241 (2003).

[145] C. Antoniak and M. Farle, Modern Physics Letters B **21**, 1111 (2007).

[146] N. Shukla, C. Liu, P. Jones, and D. Weller, J. Magn. Magn. Mater. **266**, 178 (2003).

[147] O. Iglesias and A. Labarta, Phys. Rev. B **63**, 184416 (2001).

[148] V. Salgueiriño-Maceira, L. Liz-Marzán, and M. Farle, Langmuir **20**, 6946 (2004).

[149] H. Gu, P.-L. Ho, K. Tsang, L. Wang, and B. Xu, J. Am. Chem. Soc. **125**, 15702 (2003).

[150] V. Salgueiriño-Maceira, M. Correa-Duarte, and M. Farle, Small **1**, 1073 (2005).

[151] X. Battle and A. Labarta, J. Phys. D: Appl. Phys. **35**, R15 (2002).

[152] D. Serantes, M. Spasova, D. Baldomir, M. Farle, and V. Salgueiriño-Maceira, Chem. Mater. **22**, 4103 (2010).

[153] U. Wiedwald, K. Fauth, M. Hebler, H.-G. Boyen, F. Weigl, M. Hilgendorff, M. Giersig, G. Schütz, P. Ziemann, and M. Farle, ChemPhysChem **6**, 2522 (2005).

[154] J. Nogues, J. Sort, V. Langlais, V. Skumryev, S. Suriñach, J. Muñoz, and M. Baró, Phys. Rep. **422**, 65 (2005).

[155] G. Salazar-Alvarez, J. Qin, V. Sepelak, I. Bergmann, M. Vasilakaki, K. Trohidou, J. Ardisson, W. Macedo, M. Mikhaylova, M. Muhammed, et al., J. Am. Chem. Soc. **130**, 13234 (2008).

[156] M. Holmes, D. Newman, and M. Wears, J. Magn. Magn. Mater. **315**, 39 (2007).

[157] P. Allia, M. Coisson, P. Tiberto, F. Vinai, M. Knobel, M. Novak, and W. Nunes, Phys. Rev. B **64**, 144420 (2002).